

The Distribution of Stellar Mass in Galaxy Clusters over Cosmic Time

Proefschrift

ter verkrijging van
de graad van Doctor aan de Universiteit Leiden,
op gezag van Rector Magnificus prof. mr. C.J.J.M. Stolker,
volgens besluit van het College voor Promoties
te verdedigen op woensdag 14 mei 2014
klokke 10:00 uur

door

Remco F.J. van der Burg
geboren te Leiderdorp
in 1986

Promotiecommissie

Promotor: Prof. dr. Koenraad Kuijken
Co-Promotor: Dr. Henk Hoekstra

Overige leden: Prof. dr. Michael Balogh (U. Waterloo)
Prof. dr. Marijn Franx
Prof. dr. Huub Röttgering
Prof. dr. Joop Schaye

*"Do not follow where the path may lead...
Go instead where there is no path, and leave a trail."*
- Muriel Strode

The cover shows a cluster-scale overdensity in the Millennium simulation at redshift $z=1.4$ (back cover), and at redshift $z=0$ (front cover).

Credit: Springel et al. (Virgo Consortium)
and the Max-Planck-Institute for Astrophysics.

The colour images show observations of cluster SpARCS-1613 at $z=0.87$ (back), and cluster Abell655 at $z=0.13$ (front), which are central to the work in this thesis.

Cover design: Remco F.J. van der Burg
Cover lay-out: Suzanne Taylor Muzzin

Contents

1	Introduction	1
1.1	The standard cosmological model	1
1.2	Structure formation in the Universe	3
1.3	The challenge of stellar masses	3
1.4	The world of galaxies	4
1.5	Galaxies in high-density environments	5
1.6	This Thesis	6
1.6.1	Galaxy clusters at $z \sim 1$	6
1.6.2	Galaxy clusters in the local Universe	8
1.6.3	Probing the early phases of star-formation	8
2	The environmental dependence of the stellar mass function at $z \sim 1$	9
2.1	Introduction	11
2.2	Sample & Data description	13
2.2.1	The GCLASS cluster sample	13
2.2.2	Spectroscopy	14
2.2.3	Photometric Data	16
2.2.4	UltraVISTA field reference	17
2.3	Analysis	18
2.3.1	Photometric redshifts	18
2.3.2	Stellar masses and completeness	19
2.3.3	Rest-frame colours	20
2.3.4	Cluster member selection	21
2.4	Results	25
2.4.1	The cluster stellar mass function	25
2.4.2	Cluster versus Field	27
2.4.3	Star-forming vs Quiescent galaxies	29

2.4.4	Normalisation of the SMF	30
2.5	Discussion	31
2.5.1	The shape of the galaxy SMF	31
2.5.2	A simple quenching model	33
2.6	Summary and Conclusions	38
2.A	Data processing and catalogue creation	40
2.A.1	Photometric data reduction	40
2.A.2	PSF homogenisation and colour measurements	41
2.B	Field SMF measurements from GCLASS	44
3	The Phase Space and Stellar Populations of Cluster Galaxies at $z \sim 1$	47
3.1	Introduction	49
3.2	Dataset	50
3.3	Galaxies in the Cluster Phase Space	51
3.4	Simulated Cluster Phase Space	53
3.5	SED fitting of Poststarburst Galaxies	58
3.6	Discussion	61
3.7	Summary and Outlook	63
4	A Census of Stellar Mass in 10 Massive Haloes at $z \sim 1$ from the GCLASS Survey	65
4.1	Introduction	67
4.2	GCLASS Data & Analysis	69
4.2.1	Total halo masses	71
4.2.2	Photometric redshifts and Stellar masses	72
4.2.3	Cluster membership correction	73
4.3	Central stellar mass versus halo mass	75
4.4	Total stellar mass versus halo mass	77
4.4.1	Comparison to other samples	80
4.5	Radial stellar density distribution	83
4.5.1	Discussion	85
4.5.2	Evolution towards lower redshift	86
4.6	Summary and Conclusions	88
5	The distribution of stellar mass in galaxy clusters at $z \sim 0.15$	91
5.1	Introduction	93
5.2	Data overview & processing	95
5.2.1	Photometry - MegaCam	96
5.2.2	Photometry - WFC	98
5.2.3	Catalogue construction	100
5.3	Analysis	104
5.3.1	Method 1 - statistical background subtraction	104

5.3.2	Method 2 - spectroscopic approach	106
5.4	Results and comparison at low- z	107
5.4.1	Galaxy number density profile	107
5.4.2	Stellar mass density profile	110
5.5	The evolving stellar mass distribution	113
5.5.1	Selection effects in GCLASS	116
5.6	Summary and Conclusions	119
5.A	Consistency checks	120
6	The UV galaxy Luminosity Function at $z=3-5$ from the CFHT Legacy Survey Deep fields	123
6.1	Introduction	125
6.2	Data & Samples	127
6.2.1	The CFHT Legacy Survey Deep	127
6.2.2	u -, g -, and r -dropout samples	127
6.2.3	Redshift distributions & Contamination fractions	128
6.3	Analysis - Survey completeness	129
6.3.1	Model galaxies	130
6.3.2	Eddington bias	131
6.3.3	Source injection and recovery	132
6.3.4	Effective volumes	133
6.4	Results	134
6.4.1	The UV Luminosity Function at $z=3-5$	134
6.4.2	The UV Luminosity Density and SFR Density	139
6.4.3	Robustness of our results	141
6.4.4	The evolving galaxy population	145
6.5	Comparison with previous determinations	145
6.5.1	Comparison at $z=3$	146
6.5.2	Comparison at $z=4$	148
6.5.3	Comparison at $z=5$	150
6.5.4	Comparison of the SFR density	150
6.6	Summary & Conclusions	150
	Bibliography	153
	Nederlandse Samenvatting	163
	Curriculum Vitae	169
	Nawoord	171

Chapter 1

Introduction

The Universe is a fascinating place, and our perception of it has changed over the centuries. Until no more than 25 human generations ago, the geo-centric world model, in which the Earth occupies the centre of the Universe, was our fiducial prescription of the cosmos. Since then, revolutionary insights have led to a very different picture, especially during the 20th century. The Universe is vastly larger than previously thought, and we humans do not seem to occupy a special place in it, nor are we made of the most common form of matter. Careful astronomical observations have been key in shaping our understanding of the cosmos. This thesis presents measurements on the stellar component in the most massive structures formed in the Universe, with the potential to test and further expand current physical models and thus our understanding of the cosmos. First, in this introduction, we summarise the sequence of scientific discoveries that led to the standard model of cosmology, and lay out open questions we are currently facing in the field of extragalactic astronomy.

1.1 The standard cosmological model

Determining the age, composition, and evolution of the Universe as a whole have been central goals in the study of cosmology. These questions have fascinated human minds for centuries, and in the 16th century the revolutionary Heliocentric model was formulated by (among others) Nicolaus Copernicus and Galileo Galilei. In this model, the planets were described to orbit a stationary Sun in the centre of the Solar system, and this led to an easier and more elegant mathematical description of the movement of the other planets. We now know that the Sun has properties similar to other stars in the firmament, although their distances to us are very different. Attempts to describe the position of the Sun within this vastness of stars led to a model called the Kapteyn Universe, in which our galaxy, the Milky Way, is an island Universe

of about 40,000 light years in size (Kapteyn 1922). Whereas astronomers in the 1920s agreed that the Sun does not occupy the centre of the Milky Way, the question whether the nebulae are of galactic nature was a topic of debate. Not much later, observations by Edwin Hubble (Hubble 1926) showed that most nebulae are galaxies beyond the Milky Way which move away from us, and this settled the debate. The velocities (or redshift) of these galaxies were found to be proportional to their distances (Hubble & Humason 1931). This result came as a big surprise, since it implies that the Universe is not static but expanding over time.

Galaxies are not distributed randomly in space, but are clustered on a range of scales such as galaxy groups, or even larger agglomerations called clusters. When Fritz Zwicky studied the movement of galaxies in the Coma cluster, he found that their relative velocities were significantly higher than what was expected from the matter observed in this cluster (Zwicky 1933). This was the first indication of a matter component we now call "dark matter", a type of matter that does not emit light but does interact through gravity. Measurements of the rotation velocity of stars in spiral galaxies by Rubin & Ford (1970) also showed that most of the gravitational matter in galaxies could not be observed, providing another sign of dark matter. Modern estimates suggest that all the elements covered by the periodic system that we were taught at school constitute less than 20% of the total matter content of the Universe (Bennett et al. 2013), and that the rest is in an unknown form of dark matter.

The discovery that the Universe on large scales is expanding motivated the Big Bang model, a picture in which the Universe originated from a singularity in space and time and has been expanding since. Whereas a logical thought is that the expansion speed is decreasing due to gravity, a study of distant supernovae in the late 1990s led to a surprising insight. The expansion of the Universe seems to be accelerating (Riess et al. 1998; Perlmutter et al. 1999), leading to the exotic term of dark energy. This form of energy may describe the vacuum energy density of space, and was first hypothesized by Albert Einstein who expressed it as the cosmological constant Λ . Altogether, no cosmological probe has been as constraining of our view of the cosmos as the observations of the Cosmic Microwave Background (CMB) (Gamow 1948; Hu & White 1996; Bennett et al. 2013). The CMB is the afterglow of the Big Bang revealing small ($dT/T \approx 10^{-5}$) temperature differences of the $\sim 380\,000$ year old Universe.

The Big Bang model, which has been tightly constrained by combining all cosmological probes, makes concrete predictions and thus far this model has passed every observational test. However, given that dark matter and dark energy make up the dominant energy content of the Universe in this model, substantial mysteries remain regarding the nature of these components. As long as their existence is only inferred indirectly, alternative cosmological theories remain to be considered.

1.2 Structure formation in the Universe

According to the cosmological standard model, just after the Big Bang, which happened about 13.8 Gyr ago, the matter in the Universe was remarkably homogeneously distributed. Due to the force of gravity, small initial perturbations in the primordial density field have been responsible for the rich diversity of structures we observe today. Whereas the protons and electrons in the young Universe were supported by thermal photons, the dark matter was able to collapse earlier, and this accelerated the formation of structures. Given the presumed collisionless nature of dark matter, the structure formation process can now be studied using large N-body simulations (e.g. Springel et al. 2005).

Although these simulations do not include baryonic physics, they make predictions on the matter distribution that have successfully passed some basic observational tests. For example, the 2-degree-Field Galaxy Redshift Survey (Colless et al. 2001) has shown a web-like structure in the distribution of galaxies that is similar to the distribution of dark matter haloes in N-body simulations. Also, just like in the mathematical model introduced by Press & Schechter (1974), the simulations suggest that small gravitationally bound structures form first, which subsequently merge to form galaxies, and larger ensembles such as groups and clusters of galaxies. This leads to a halo mass function that is dominated by low-mass haloes (e.g. Tinker et al. 2008). The luminosity distribution of galaxies (Schechter 1976) has a similar shape, although baryonic physics play a dominant role in determining the exact shape of the luminosity (or stellar mass) distribution. The radial density profile of dark matter haloes is found to be described by NFW profiles (Navarro et al. 1997), similar to what the distribution of galaxies in groups and clusters is observed to be (Lin et al. 2004; Muzzin et al. 2007; Budzynski et al. 2012). Although these simulations give results that qualitatively agree with the observations, an important goal in extragalactic astronomy today is to provide a complete understanding how baryonic structures form in this dark-matter dominated Universe.

1.3 The challenge of stellar masses

Although the majority of the baryonic mass in the Universe is in the form of gas, the presence of stars plays an important role in the overall cycle of baryons. Through stellar winds and supernova explosions, the gaseous medium is enriched by elements heavier than hydrogen and helium. These heavy elements have been important in the formation of the rocky planets in our solar system, and eventually provided the ingredients for life on Earth. To be able to constrain the build-up of the stellar component in the Universe, stellar mass measurements need to be quantified.

In the Milky Way, observations of binary stars have been used to measure the masses of stars with different spectral types. Simple scaling relations between the mass, temperature, luminosity, and lifetimes of stars have been obtained. For stars around a solar mass, the luminosity scales with mass roughly as $L \propto M^4$. In typical stellar populations, low-mass stars are substantially more abundant than high-mass stars. Whereas the total mass of a stellar population is thus dominated by the low-mass stars, the total energy output is dominated by high-mass stars. To relate the luminosity of a stellar population to its total stellar mass, we need to know its mass distribution (the Mass Function, MF). However, especially for distant galaxies the MF is not directly observable, and thus unknown to us.

Given that the lifetimes of high-mass stars are relatively short ($T \propto M^{-3}$), the MF of a stellar population evolves with age. If we consider a stellar population just after it formed (i.e. at zero-age), we refer to the MF as the Initial MF (IMF). A critical assumption in typical studies that involve stellar mass measurements is that the IMF has a universal shape (however see Bastian et al. (2010) for a review). Salpeter (1955) estimated that the IMF can be approximated by a power-law $\frac{dN}{dM} \propto M^{-\alpha}$, where α is typically ~ 2.35 . Recent studies (Miller & Scalo 1979; Kroupa 2001; Chabrier 2003) have suggested refinements of this simple power-law, leading to different relations between the luminosity and stellar mass of a zero-age stellar population. As of today, the shape of the IMF at low masses is the main systematic uncertainty on stellar mass estimates of galaxies.

Since high-mass stars are very luminous in the ultraviolet, the spectral energy distribution (SED) of a stellar population becomes redder as these stars cease to exist. The age of a stellar population can be estimated by considering its full SED, and once the age is known we can estimate the current MF from the assumed IMF. The mass-to-light ratio (M/L) of a galaxy is estimated from the MF, and thus a stellar mass can be estimated for a given luminosity.

A further complication for stellar mass estimates is that the SED of a galaxy is typically not well-described by a single-age stellar population. The stars may have formed following a general Star Formation History (SFH), leading to a more complicated MF. Also, the presence of dust can redden the SED, mimicking the effect of a higher age (e.g. Worthey 1994). Given that the SED of a galaxy is observed, the SFH and dust-attenuation of a galaxy can be estimated using a typical SED-fitting program such as FAST (Kriek et al. 2009).

1.4 The world of galaxies

By measuring properties of galaxies such as their stellar masses, colours and morphologies, they can roughly be divided in two distinct types, labelled early-types and late-types for historical reasons. Late-type (a.k.a. star-forming)

galaxies generally have a central concentration of old stars, and an extended disk in which stars are forming. Early-type (a.k.a. quiescent) galaxies are redder since they feature no (or very little) on-going star formation, and generally have ellipsoidal shapes compared to the spiral nature of late-type galaxies. Due to the advance of modern telescopes and instruments, galaxy studies have been expanded over the last decades, and measurements of the Luminosity Function (LF) and Stellar Mass Function (SMF) (e.g. Bell et al. 2003; Pérez-González et al. 2008; Ilbert et al. 2010) have been used as key observables of a population of galaxies. The LF and SMF describe the number density of galaxies as a function of their estimated luminosity and stellar masses, respectively, and are generally parameterized using the Schechter function (Schechter 1976).

By comparing the halo mass function with the SMF, we have learned that dark matter haloes of different masses have different stellar mass fractions (e.g. Behroozi et al. 2013). The inefficiency of low-mass haloes in forming stars is possibly due to supernova feedback (Efstathiou 2000; Dalla Vecchia & Schaye 2008), stellar winds, and the presence of a photo-ionizing background (Benson et al. 2002). In high-mass haloes, AGN feedback is expected to play a role in regulating the formation of stars (Schawinski et al. 2007; Fabian 2012).

Separating the SMF between late-type and early-type galaxies, observations have shown that the most massive galaxies are generally early-type. It is also shown that their abundance rises towards the present day compared to late-type galaxies. Contrary to what their names may suggest, late-type galaxies are thus regarded as the progenitors of early-type galaxies. Recent studies (Muzzin et al. 2013a) have measured and compared the universal SMF of the two galaxy types up to $z \sim 4$, and such measurements are fundamental observables for constraining the star-formation efficiency as a function of halo mass and redshift in physical models (e.g. Schaye et al. 2010; Henriques et al. 2012; Weinmann et al. 2012; Cen 2014). A relatively simple approach to this is the abundance matching technique (e.g. Behroozi et al. 2010; Moster et al. 2010; Behroozi et al. 2013; Moster et al. 2013), in which observables such as the SMF and cosmic star formation history are directly combined with merger trees from dark matter simulations to provide constraints on the processes that build up the stellar mass in the central galaxies of dark matter haloes.

1.5 Galaxies in high-density environments

It has been known for a long time now that the properties of galaxies do not only depend on the mass of the halo in which they live, but also correlate with the density of their environment (e.g. Dressler 1980). Galaxies in crowded regions generally show a higher quiescent fraction than galaxies in sparse environments. Several physical mechanisms have been proposed to explain these differences, but a consensus is still missing. The Sloan Digital Sky Survey (SDSS) has allowed substantial progress to be made in quanti-

ifying the relationship between galaxy environment and Star Formation Rate (SFR), morphology, stellar mass, and metallicity in the local Universe (e.g. Kauffmann et al. 2004; Baldry et al. 2006; Peng et al. 2010). However, surveys that have provided insight into the far-away Universe (e.g. COSMOS; Scoville et al. 2007) typically lack the volume to study the most extreme over-densities (i.e. galaxy clusters) at these redshifts since they observe relatively small areas on the sky.

Clusters of galaxies are the most massive gravitationally bound structures in the Universe, which typically contain ~ 1000 galaxies and have a total mass of $\gtrsim 10^{14} M_{\odot}$. Given their extreme over-densities at any epoch, we expect environmental effects on the evolution of galaxies to be most prominent in these systems. To separate these environmental effects from general redshift evolution, galaxy clusters also have to be studied at higher redshifts. In surveys that cover a large field-of-view, these systems can be detected by their hot X-ray emitting gas (e.g. Rosat), Sunyaev-Zel'dovich decrement (e.g. SPT, Planck), or galaxy over-density (e.g. SpARCS), and are then specifically targeted for follow-up observations.

Number density measurements of massive haloes as a function of redshift are also used to constrain cosmological parameters, as these haloes are a sensitive probe of the growth of structures. The two applications of cosmology and galaxy evolution are intimately related, since the presence of baryons can have a measurable effect on the shape of the matter power spectrum and the cluster mass function, and therefore on the determined cosmological parameters (e.g. van Daalen et al. 2011; Cusworth et al. 2013). In order to interpret abundance measurements of clusters in a cosmological context, a comparison with fitting functions obtained from simulations is required (e.g. Tinker et al. 2008). So far, these simulations are based on N-body codes, and thus do not include baryonic physics. In an era in which we aim to do precision cosmology, the influence of baryons can no longer be ignored in simulations and their assembly needs to be better constrained by observations.

1.6 This Thesis

In this thesis, we study the distribution of galaxies in galaxy clusters over cosmic time. Both the SMF and the spatial distribution of galaxies provide insights in the connection between dark matter and the stellar component, and the transformation of galaxies in high-density environments.

1.6.1 Galaxy clusters at $z \sim 1$

In order to assess the time evolution of galaxies in high-density environments, we study 10 clusters observed in the distant Universe in **Chapters 2-4**, when the Universe was about half its current age. This cluster sample is drawn from the Gemini Cluster Astrophysics Spectroscopic Survey (GCLASS), which

consists of 10 of the richest clusters in the redshift range $0.86 < z < 1.34$ selected from the 42 square degree SpARCS survey (Muzzin et al. 2009; Wilson et al. 2009; Demarco et al. 2010).

In **Chapter 2**, we present the galaxy SMF of the GCLASS clusters, and compare it directly to the SMF of field galaxies in the same redshift range to study the effect of environment on this fundamental observable at $z \sim 1$. Interestingly, when we distinguish photometrically between star-forming and quiescent galaxies, we find that the best-fitting Schechter parameters α and M^* are similar within the uncertainties for these galaxy types within the different environments. However, there is a significant difference in the shape and normalisation of the total SMF between the clusters and the field sample. This difference in the total SMF is primarily a reflection of the increased fraction of quiescent galaxies in high-density environments. At $z \sim 1$ the clusters are already completely dominated by quiescent galaxies. We employ and evaluate a quenching model based on Peng et al. (2010), which separates the quenching of galaxies by two distinct tracks dubbed mass-quenching and environmental quenching, and find that this model gives a reasonable description of the data.

The quenching model predicts the presence of galaxies that have recently been abruptly quenched. In **Chapter 3**, we follow this prediction by studying the transformation of galaxies at $z \sim 1$ in the GCLASS clusters. Using the deep spectroscopic data available for GCLASS, we identify a population of post-starburst galaxies with no on-going star-formation, but with spectra still indicative of young stellar populations. The fact that this type of galaxy is more abundant in the clusters than in the field (Muzzin et al. 2012) suggests that the responsible process depends on environment. We find that the post-starburst galaxies have a distinctive distribution in projected velocity vs. position phase space, possibly related to quenching processes that are dependent on environment. Using several zoom simulations of clusters, we find that this coherent distribution of post-starburst galaxies can be reasonably well reproduced using a simple quenching scenario. The phase-space distribution of these galaxies can be reproduced if satellite quenching occurs on a rapid timescale ($0.1 \lesssim T_q \lesssim 0.5$ Gyr) after they make their first passage of $R \sim 0.5R_{200}$, where R_{200} is defined as the radius at which the mean interior density is 200 times the critical density of the Universe.

In order to further constrain the relation between the assembly of stellar mass and dark matter in these systems, other observables can be exploited. In **Chapter 4**, we compare the halo masses of the GCLASS systems to the stellar mass measurements of the central galaxies, and to stellar mass measurement of the entire population of cluster galaxies. When we study the distribution of stellar mass in the ensemble GCLASS cluster, we find that it is well described by a projected NFW profile, but with a relatively high concentration parameter of $c \sim 7$. This result is intriguing because it shows that the stellar mass is significantly more concentrated than the dark matter in N-body simulations in

this mass and redshift regime. This is significantly different from the picture at lower redshift, when compared to studies in the literature. However, differences with analyses and data sets in the literature are a major concern and limitation.

1.6.2 Galaxy clusters in the local Universe

By extending the study described above towards lower redshift, we make the comparison across cosmic time more consistent and put the GCLASS measurements into context. **Chapter 5** describes a measurement of the stellar mass distribution in 10 clusters in the redshift range $0.07 < z < 0.26$, drawn from the Multi-Epoch Nearby Cluster Survey (MENeCS) and the Canadian Cluster Comparison Project (CCCP). The systems have dynamical masses of $M_{200,c} \simeq 10^{15} M_{\odot}$, which roughly matches the expected descendent population of the GCLASS sample. We find that the stellar mass distribution is well described by an NFW profile with concentration $c \sim 2$. The stellar mass distribution thus evolves significantly since $z \sim 1$, and this trend is opposite to what is seen in the evolution of the dark matter concentration in simulations. We consider different evolutionary scenarios and conclude that the build-up of stellar mass in the intracluster light and the central galaxy, combined with outside growth onto the clusters, could explain the observed evolution.

1.6.3 Probing the early phases of star-formation

Even in galaxy clusters at $z \sim 1$, the galaxy population is entirely dominated by quiescent galaxies. In **Chapter 6**, we turn our attention towards an epoch in which the star-forming fraction of galaxies was considerably higher. We use the *ugriz* data set of the CFHT Legacy Survey Deep, which spans a 4 square degree survey area, to measure the UV galaxy LF at $3 < z < 5$. The Lyman-Break Galaxies (LBGs) that we consider are star-forming galaxies that have many applications. They are identified relatively easily at this redshift range, by using multi-band optical photometry to probe the wavelength-position of the Lyman limit. Our study in **Chapter 6** is based on 100,000 LBGs, and given the large survey area compared to previous studies, this renders the systematic uncertainty on the LF caused by cosmic variance insignificant. Furthermore, we are able to measure the LF down to such bright (and therefore rare) galaxies that the intervening matter density distribution significantly alters the (Schechter) shape of the LF. With the knowledge of the intrinsic shape of the LF in hand, these LBGs can be used as sources in weak lensing magnification studies (e.g. Hildebrandt et al. 2013; Ford et al. 2013). Although the LBGs are too small to be spatially resolved in this data set, a magnification study only requires measurements of their fluxes. Since this relaxes the observational requirements substantially, it is a promising method for measuring the total masses of galaxy clusters at redshifts $z \gtrsim 1$, as shown by Hildebrandt et al. (2011) for the SpARCS cluster sample.

The environmental dependence of the stellar mass function at $z \sim 1$

We present the stellar mass functions (SMFs) of star-forming and quiescent galaxies from observations of 10 rich, red-sequence selected, clusters in the Gemini Cluster Astrophysics Spectroscopic Survey (GCLASS) in the redshift range $0.86 < z < 1.34$. We compare our results with field measurements at similar redshifts using data from a K_s -band selected catalogue of the COSMOS/UltraVISTA field. We construct a K_s -band selected multi-colour catalogue for the clusters in 11 photometric bands covering u - $8\mu\text{m}$, and estimate photometric redshifts and stellar masses using SED fitting techniques. To correct for interlopers in our cluster sample, we use the deep spectroscopic component of GCLASS, which contains spectra for 1282 identified cluster and field galaxies taken with Gemini/GMOS. This allows us to correct cluster number counts from a photometric selection for false positive and false negative identifications. Both the photometric and spectroscopic samples are sufficiently deep that we can probe the stellar mass function down to masses of $10^{10} M_\odot$. We distinguish between star-forming and quiescent galaxies using the rest-frame U-V versus V-J diagram, and find that the best-fitting Schechter parameters α and M^* are similar within the uncertainties for these galaxy types within the different environments. However, there is a significant difference in the shape and normalisation of the total stellar mass function between the clusters and the field sample. This difference in the total stellar mass function is primarily a reflection of the increased fraction of quiescent galaxies in high-density environments. We apply a simple quenching model that includes components of mass- and environment-driven quenching, and find that in this picture $45_{-3}^{+4}\%$

of the star-forming galaxies, which normally would be forming stars in the field, are quenched by the cluster. If galaxies in clusters and the field quench their star formation via different mechanisms, these processes have to conspire in such a way that the shapes of the quiescent and star-forming SMF remain similar in these different environments.

Remco F.J. van der Burg, Adam Muzzin, Henk Hoekstra, Chris Lidman, Alessandro Rettura, Gillian Wilson, H.K.C. Yee, Hendrik Hildebrandt, Danilo Marchesini, Mauro Stefanon, Ricardo Demarco, Konrad Kuijken
Astronomy & Astrophysics, **Volume 557**, A15 (2013)

2.1 Introduction

One of the missing parts in the theory of galaxy formation and evolution is a detailed understanding of the build up of stellar mass in the Universe. While the hierarchical growth of dark matter haloes has been studied in large N-body simulations (e.g. Springel et al. 2005), the baryonic physics that regulates the cooling of gas and formation of stars in these haloes is much harder to simulate and is not yet well understood. To understand which physical processes are dominant in shaping the stellar content of galaxies, models need good observational constraints. One of the most fundamental observables of a population of galaxies is their stellar mass function (SMF), which describes the number density of galaxies as a function of stellar mass. Measuring the SMF as a function of cosmic time provides useful constraints on the parameters in semi-analytic models, and these models have to match and predict the SMF for a range of redshifts and environmental densities.

Although models are tuned to match the observations at $z=0$, there is in general still a poor agreement between observations and theory at higher redshift. Models generally show an excess of galaxies with a stellar mass (M_*) $\sim 10^{10} M_\odot$ around $z=1-2$ compared to observational data (e.g. Bower et al. 2012; Weinmann et al. 2012). At higher redshifts the number of high-mass galaxies is generally underpredicted by the models. For a detailed comparison between models and the observed SMF also see Marchesini et al. (2009).

At low redshifts ($z \lesssim 0.2$) the SMF has been measured from wide field data and spectroscopic information (Cole et al. 2001; Bell et al. 2003), while at higher redshifts the SMF has been measured from deep surveys by making use of photometric redshift estimates (Pérez-González et al. 2008; Marchesini et al. 2009; Ilbert et al. 2010). The general consensus is that the total stellar mass density evolves slowly between $0 < z < 1$, which can also be inferred from the sharp decline of cosmic star formation in the Lilly-Madau diagram (Lilly et al. 1996; Madau et al. 1996) in this redshift range. The main evolution is in the normalisation of the SMF, whereas the shape does not show a substantial evolution since $z \sim 4$ (Pérez-González et al. 2008). However, since these deep surveys generally probe small volumes, the dominant source of random uncertainty is often cosmic variance (Somerville et al. 2004; Scoville et al. 2007; Marchesini et al. 2009), which is expected to not only have an effect on the normalisation but also on the shape of the observed SMF (Trenti & Stiavelli 2008). Observations over large areas, or a combination of multiple sight lines, are used to reduce this source of uncertainty.

Besides the general time evolution of the properties of galaxies, they are also observed to be strongly influenced by the density of their environment. In particular, galaxies in overdense regions show lower star formation rates, and a higher fraction of red galaxies. At low redshifts, the Sloan Digital Sky Survey has allowed us to quantify these correlations with high precision (Kauffmann

et al. 2004; Balogh et al. 2004; Blanton et al. 2005). The fraction of galaxies that are red is also a function of their stellar mass, with more massive galaxies being redder and forming fewer stars. The quenching fraction of galaxies being a function of both stellar mass and environmental density, some recent studies have suggested the processes of "mass quenching" and "environmental quenching" to be operating completely independently from each other (Peng et al. 2010; Muzzin et al. 2012), each operating on different time scales. Naively, we would expect the combination of these processes to affect the shape of the SMF.

A measurement of the SMF of galaxies as a function of environmental density therefore provides further constraints on the physical processes that are important in these dense regions. For example, galaxies falling into massive galaxy clusters are expected to be stripped of their cold gas component due to ram-pressure stripping, and a lack of new inflowing cold gas leads to a galaxy's star formation being turned off. Galaxies in groups and clusters are also expected to interact gravitationally through mergers and experience strong tidal forces as they fall towards the cluster centre.

Combining these measurements done over a range of redshifts and environments puts constraints on the way galaxies quench their star formation, since it allows one to separate between internally and externally driven processes. Some studies have attempted to measure the SMF as a function of local environment at $0.4 \lesssim z \lesssim 1.2$ (e.g. Bundy et al. 2006; Bolzonella et al. 2010; Vulcani et al. 2011, 2012; Giardini et al. 2012). A measurement of the SMF at the highest densities has not yet been achieved in this redshift range. This is partly because the deep (and therefore limited in area) surveys that have been used for SMF measurements (mostly the COSMOS and DEEP2 fields) do not contain the extreme overdensities corresponding to the most massive clusters of galaxies.

In this paper we present a measurement of the SMF of galaxies in 10 rich galaxy clusters at a range of redshifts ($0.86 < z < 1.34$). These clusters were detected using the red-sequence method on data from the Spitzer Adaptation of the Red-sequence Cluster Survey (SpARCS, see Muzzin et al. 2009; Wilson et al. 2009; Demarco et al. 2010), and have typical velocity dispersions of $\sigma_v = 700$ km/s which imply halo masses of $M_{200} \simeq 3 \times 10^{14} M_\odot$. We combine deep photometric data in 11 bands with the extensive deep spectroscopic coverage that we obtained from the Gemini Cluster Astrophysics Spectroscopic Survey (GCLASS, Muzzin et al. 2012). This allows us to estimate stellar masses for individual objects and quantify the amount of interlopers in the photo- z selected sample as a function of mass and projected clustercentric distance. We use the UVJ-diagram to photometrically separate between star-forming and quiescent galaxies, which is critical because the two galaxy types suffer from different observational difficulties and completenesses. We also provide a comparison between the cluster results and the SMF measured from

UltraVISTA/COSMOS field.

The structure of the paper is as follows. In Sect. 2.2 we give an overview of GCLASS, and the spectroscopic and photometric data that have been taken for this cluster sample. We also describe the data from the reference UltraVISTA survey. In Sect. 2.3 we present our measurements of photometric redshifts, stellar masses and rest-frame colours to distinguish between star-forming and quiescent galaxies. We also explain how we correct the photometric sample for incompleteness by making use of the spectroscopic data. In Sect. 2.4 we present our results and make comparisons between the two galaxy types, and between cluster environments and the field. In Sect. 2.5 we discuss our results in the context of galaxy evolutionary processes and in particular quenching in these massive clusters. We summarise and conclude in Sect. 2.6. Extra information considering colour measurements and calibration are presented in the Appendices. There we also compare the UltraVISTA field SMF with the field probed by GCLASS outside the clusters to test for possible systematics.

All magnitudes we quote are in the AB magnitudes system and we adopt Λ CDM cosmology with $\Omega_m = 0.3$, $\Omega_\Lambda = 0.7$ and $H_0 = 70 \text{ km s}^{-1} \text{ Mpc}^{-1}$.

2.2 Sample & Data description

2.2.1 The GCLASS cluster sample

The GCLASS cluster sample consists of 10 of the richest clusters in the redshift range $0.86 < z < 1.34$ selected from the 42 square degree SpARCS survey, see Table 2.1. Clusters in the SpARCS survey were detected using the cluster red-sequence detection method developed by Gladders & Yee (2000), where the $z' - 3.6\mu\text{m}$ colour was used to sample the 4000\AA break at these redshifts (see Muzzin et al. 2008). For an extended description of the SpARCS survey we refer to Muzzin et al. (2009), Wilson et al. (2009) and Demarco et al. (2010). The 10 clusters that were selected from the SpARCS survey for further study are described in Muzzin et al. (2012), and can be considered as a fair representation of IR-selected rich clusters within this redshift range.

We note that there is a possible selection bias in favour of systems with a high number of bright red galaxies. It is impossible to select clusters based on their total halo mass and therefore any cluster sample has potential selection biases, whether it is X-ray selected, SZ-selected, or galaxy-selected. We note that follow-up studies of X-ray or SZ-selected clusters in the same redshift range also show a significant over-density of red-sequence galaxies (e.g. Blakeslee et al. 2003; Mullis et al. 2005). Furthermore, the field SMF at $z=1$ shows (e.g. Muzzin et al. 2013a) that even in the field, the bright/massive end of the population is completely dominated by red galaxies. Therefore it seems unlikely that a red-sequence selection results in a significant selection bias, at

Table 2.1: The 10 GCLASS clusters selected from SpARCS for follow-up spectroscopic and photometric observations. These clusters form the basis of this study.

Name ^a	z_{spec}	RA J2000	Dec J2000	K _s -band PSF FWHM ["]	K _{lim} ^b [mag _{AB}]	M _{*,lim} ^c [M _⊙]	limit from bc03 ^d
SpARCS-0034	0.867	00:34:42.086	-43:07:53.360	1.01	21.53	10.42	10.43
SpARCS-0035	1.335	00:35:49.700	-43:12:24.160	0.40	23.60	9.92	9.95
SpARCS-0036 ^e	0.869	00:36:45.039	-44:10:49.911	1.23(J)	22.11(J)	10.53	10.50
SpARCS-0215	1.004	02:15:23.200	-03:43:34.482	1.00	21.73	10.45	10.46
SpARCS-1047 ^f	0.956	10:47:32.952	57:41:24.340	0.61	22.68	10.17	10.04
SpARCS-1051 ^f	1.035	10:51:05.560	58:18:15.520	0.86	22.96	9.99	9.99
SpARCS-1613	0.871	16:13:14.641	56:49:29.504	0.81	22.55	9.97	10.02
SpARCS-1616	1.156	16:16:41.232	55:45:25.708	0.84	22.65	10.33	10.20
SpARCS-1634	1.177	16:34:35.402	40:21:51.588	0.77	22.88	10.14	10.13
SpARCS-1638	1.196	16:38:51.625	40:38:42.893	0.66	23.00	10.13	10.09

^a For full names we refer to Muzzin et al. (2012).

^b 80% completeness limit for simulated sources.

^c Corresponding mass completeness limit based on the galaxy in UltraV-ISTA with the highest M/L fitted at this redshift at K_{lim}.

^d Mass limit from a synthetic spectrum with $\tau = 10\text{Myr}$ starting at age of universe at that redshift with no dust (Bruzual & Charlot 2003).

^e For SpARCS-0036 we used to J-band as the selection band since it is significantly deeper than the K_s-band. The image quality and magnitude limits refer to the J-band for this cluster.

^f Since the BCG is offset from the centre, this is a better approximation for the cluster centre (different from Muzzin et al. (2012)).

least for the most massive clusters at a given redshift such as the GCLASS sample.

2.2.2 Spectroscopy

The clusters in the GCLASS sample have extensive optical spectroscopy, which has been taken using the GMOS instruments on Gemini-North and -South. For details on these measurements, the target selection and an overview of the reduction of these data, we refer to Muzzin et al. (2012).

In summary, spectroscopic targets were selected using a combination of their $3.6\mu\text{m}$ fluxes, $z' - 3.6\mu\text{m}$ colours, and their projected clustercentric radii. The colour priority selection was chosen to be sufficiently broad so that there is no selection bias against blue galaxies within the cluster's redshift range. Because the mass-to-light ratio in the $3.6\mu\text{m}$ channel is only a weak function

Table 2.2: Properties of the 10 GCLASS clusters.

Name	z_{spec}	σ_v [km/s]	M_{200} [$10^{14} M_{\odot}$]	R_{200} [Mpc]
SpARCS-0034	0.867	700^{+90}_{-150}	$3.6^{+1.6}_{-1.9}$	$1.1^{+0.1}_{-0.2}$
SpARCS-0035	1.335	780^{+80}_{-120}	$3.9^{+1.3}_{-1.5}$	$0.9^{+0.1}_{-0.1}$
SpARCS-0036	0.869	750^{+80}_{-90}	$4.5^{+1.6}_{-1.4}$	$1.1^{+0.1}_{-0.1}$
SpARCS-0215	1.004	640^{+120}_{-130}	$2.6^{+1.7}_{-1.3}$	$0.9^{+0.2}_{-0.2}$
SpARCS-1047	0.956	660^{+70}_{-120}	$2.9^{+1.0}_{-1.3}$	$1.0^{+0.1}_{-0.2}$
SpARCS-1051	1.035	500^{+40}_{-100}	$1.2^{+0.3}_{-0.6}$	$0.7^{+0.1}_{-0.1}$
SpARCS-1613	0.871	1350^{+100}_{-100}	$26.1^{+6.2}_{-5.4}$	$2.1^{+0.2}_{-0.2}$
SpARCS-1616	1.156	680^{+80}_{-110}	$2.8^{+1.1}_{-1.2}$	$0.9^{+0.1}_{-0.1}$
SpARCS-1634	1.177	790^{+60}_{-110}	$4.4^{+1.1}_{-1.6}$	$1.0^{+0.1}_{-0.1}$
SpARCS-1638	1.196	480^{+50}_{-100}	$1.0^{+0.3}_{-0.5}$	$0.6^{+0.1}_{-0.1}$

of galaxy type, the targeting completeness is, to first order, a function of radial distance and stellar mass only. The assigned targeting priority is highest for massive objects near the cluster centres (see Muzzin et al. 2012, Fig. 4).

For these 10 clusters there are 1282 galaxies in total with redshifts, of which 457 are cluster members. For more than 90% of the targeted objects with stellar masses exceeding $10^{10} M_{\odot}$, the limiting mass of the photometric data, a redshift was measured with high confidence. Note that the targeting prioritization is known, we do not select against a particular type of galaxies, and we have a high success rate of obtaining redshifts over the stellar mass range we study. Therefore, although the spectroscopic sample is incomplete, it is a representative sample for the underlying population of cluster galaxies. The targeting completeness can be quantified, and in Sect. 2.3.4 we use the spectroscopic sub-sample to correct the full sample for cluster membership.

We have performed a dynamical analysis (Wilson et al., in prep) to study the distribution of line-of-sight (LOS) velocities of the spectroscopic targets. For all 10 clusters, the distribution of LOS velocities approximates a Gaussian profile, which is an indication that the clusters are (close to) virialised. From this distribution we measure the LOS velocity dispersion (σ_v) of the clusters. This leads to estimates of R_{200} , the radius at which the mean interior density is 200 times the critical density (ρ_{crit}), and M_{200} , the mass contained within R_{200} . The current analysis is done similar to Demarco et al. (2010), and is based on an expanded spectroscopic data set. Table 2.2 shows the cluster properties obtained from this analysis.

The clusters have typical velocity dispersions of $\sigma_v = 700$ km/s which imply halo masses of $M_{200} \simeq 3 \times 10^{14} M_{\odot}$. Note that SpARCS-1613 is much

more massive, with a velocity dispersion of $\sigma_v = 1350$ km/s. This high value is consistent with the X-ray temperature measured from a recent Chandra observation (see Ellingson, in prep.).

2.2.3 Photometric Data

Optical *ugriz* data for the six clusters observable from the Northern sky were taken with MegaCam at the Canada-France-Hawaii Telescope (CFHT). For the clusters in the South, *ugri* data were taken with IMACS at the Magellan telescopes, and the *z*-band data using the MOSAIC-II camera mounted on the Blanco telescope at the Cerro Tololo Inter-American Observatory (CTIO). There is J- and K_s -band imaging data from WIRCam at the CFHT for the Northern clusters, and from ISPI at the Blanco telescope or HAWK-I at the Very Large Telescope (VLT) UT4 for the Southern clusters. Note that these near-IR data were already presented and used in Lidman et al. (2012) to study the evolution of BCGs. The photometric data set also includes the 3.6, 4.5, 5.8 and $8.0\mu\text{m}$ IRAC channels from SWIRE (Lonsdale et al. 2003). For half of the clusters, including the four at the highest redshifts, we obtained deeper IRAC observations from the GTO programs PID:40033 and PID:50161. The measured depths and an overview of instruments that were used are listed in the Appendix in Table 2.5.

In Appendix 2.A we give a comprehensive description of the photometric data processing leading to a multi-wavelength coverage with a field of view of $10' \times 10'$ centred on the Southern clusters, and a $15' \times 15'$ field of view for the Northern clusters. This wide field view provides information up to several Mpc from the cluster centres at the respective cluster redshifts, even for clusters at the lowest redshifts.

Object detection

To measure the stellar mass function it is necessary to obtain a catalogue in which the galaxy sample is complete down to a known mass threshold, independent of their star-formation properties. In an IR-wavelength band the M/L varies little for different star formation histories, so that the luminosity in those bands is a good tracer for the total stellar mass of a galaxy.

Because the IRAC channels suffer from a large point spread function (PSF), separating objects on the sky is difficult. As a compromise between good image quality and detection in a red filter, we therefore choose the K_s -band as the selection band. We use SExtractor to detect all sources in the K_s -band that have 5 adjacent pixels with significance $> 2.5\sigma$ relative to the local background.

We obtain a clean catalogue by excluding regions near bright stars and their diffraction spikes, and separate stars from galaxies by using their observed colours. In the $u - J$ versus $J - K$ colour plane the distinction between stars

and galaxies is clear (see e.g. Whitaker et al. 2011), and we find that the following colour criterion can be used to select a sample of galaxies.

$$J - K > 0.18 \cdot (u - J) - 0.70 \cup J - K > 0.08 \cdot (u - J) - 0.40 \quad (2.1)$$

Colour measurements

To measure photometric redshifts and stellar masses for the galaxies, accurate colour measurements are necessary. The circumstances of the atmosphere and optical instruments change continuously, and therefore the shape and size of the PSF is different between telescopes, exposures and filters. Therefore it is non-trivial to measure colours of the same intrinsic part of a galaxy. A common approach is to degrade the PSF of the images in all filters to the PSF of the worst seeing, after which the colours are measured by comparing the flux in fixed apertures for all filters.

An alternative approach, proposed by Kuijken (2008), is to perform a convolution of the images in each filter with a position-dependent convolution kernel to make the PSF Gaussian, circular and uniform on each image. The images in the different filters are not required to share the same Gaussian PSF size. Fluxes are measured in apertures with a circular Gaussian weighting function, whose size is adapted to ensure that the same part of the source is measured. Because the weighting function approximately matches the galaxy profiles, this technique generally improves the S/N of the measurement compared to a normal top-hat shaped aperture, and we elaborate on this method in Appendix 2.A.2. Note that this technique is not suited for measurements of the total flux, only to obtain colours of a galaxy.

The photometric zeropoints are set based on standard-star observations. We improve the precision of the zeropoints in the *ugrizJK_s* filters by making use of the universality of the stellar locus (High et al. 2009) and comparing the measured stellar colours in our images with a reference catalogue (Covey et al. 2007). Further details can be found in Appendix 2.A.2.

2.2.4 UltraVISTA field reference

In this paper we compare the cluster results to measurements from a representative field at similar redshifts as the clusters. The last decade has seen substantial improvement in the depth and an increase in the field-of-view of ground-based NIR surveys. The most recent wide-field NIR survey is UltraVISTA (McCracken et al. 2012), which is composed of deep YJHK_s images taken using the VISTA telescope on a 1.6 square degree field that overlaps with COSMOS.

The field sample in this study is based on a K_s-selected catalogue of the COSMOS/UltraVISTA field from Muzzin et al. (2013b). The catalogue con-

tains PSF-matched photometry in 30 photometric bands covering the wavelength range $0.15\mu\text{m} - 24\mu\text{m}$ and includes the available *GALEX* (Martin et al. 2005), CFHT/Subaru (Capak et al. 2007), UltraVISTA (McCracken et al. 2012), and S-COSMOS (Sanders et al. 2007) datasets. Sources are selected from the DR1 UltraVISTA K_s -band imaging (McCracken et al. 2012) which reaches a depth of $K_s = 23.4$ at 90% completeness. A detailed description of the photometric catalogue construction, photometric redshift measurements, and stellar mass estimates is presented in Muzzin et al. (2013b). In the next section we estimate these properties for the galaxies selected in GCLASS in a similar way. In Appendix 2.B we show a comparison between the UltraVISTA field SMF and the SMF measured in GCLASS outside of the clusters. In general the agreement is good, even though the GCLASS data are much shallower and contain fewer filters. At the low-mass end of the SMF there are some small differences due to incompleteness of GCLASS. We use UltraVISTA to correct this and provide an unbiased measure of the Schechter parameters in the field.

2.3 Analysis

2.3.1 Photometric redshifts

We estimate photometric redshifts (photo- z 's) using the publicly available code EAZY (Brammer et al. 2008). This code was tested (Hildebrandt et al. 2010) and performs very well on simulated and real imaging data. Input to the code are fluxes in the 11 available bands and their errors.

We checked for possible systematic problems in the photometric calibration or photo- z code by comparing the estimated photometric redshifts with spectroscopic redshifts where the samples overlap, see Fig. 2.1. The performance is then quantified by the scatter, bias and outlier fraction of this comparison. First we calculate $\Delta z = \frac{z_{\text{phot}} - z_{\text{spec}}}{1 + z_{\text{spec}}}$ for each object with a reliable spectroscopic redshift. For historical reasons and to facilitate comparisons with other photo- z studies, we define outliers as objects for which $|\Delta z| > 0.15$. For the remaining measurements we measure the mean of $|\Delta z|$ and the scat-

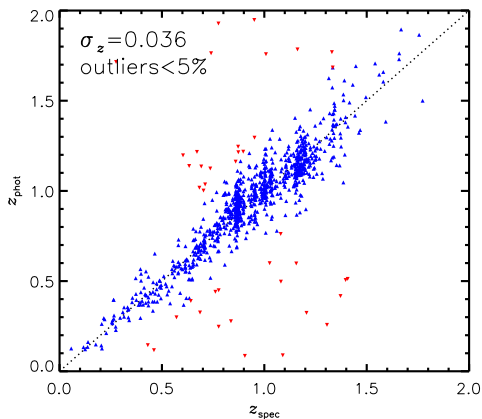


Figure 2.1: Spectroscopic versus photometric redshifts for the 10 GCLASS clusters. Outliers, objects for which $\Delta z > 0.15$, are marked in red. The outlier fraction is less than 5%, the scatter of the remaining objects is $\sigma_z = 0.036$.

ter around this mean, σ_z . We find the following typical values: a scatter of $\sigma_z = 0.036$, a bias of $|\Delta z| = 0.005$, and fewer than 5% outliers. Specifically, in the redshift range of the clusters ($0.867 < z < 1.335$), we find a scatter of $\sigma_z = 0.035$, a bias of $|\Delta z| < 0.005$, and about 8% outliers. We find that the scatter is in the range $0.031 < \sigma_z < 0.044$ for all 10 clusters, and therefore the differences in photo- z quality between the clusters is negligible.

Whereas these values are computed for the entire population of galaxies, a subdivision by galaxy type shows that photo- z estimates for quiescent galaxies are more precise ($\sigma_z = 0.030$) than for star-forming galaxies ($\sigma_z = 0.040$) because of the stronger 4000Å feature in the broad-band SEDs of quiescent galaxies, and the presence of emission lines and a larger diversity of intrinsic SEDs in the star-forming population. We therefore make the separation by galaxy type when correcting for cluster membership in Sect. 2.3.4. The scatter in photo- z estimates increases for fainter objects, however we take this effect into account when we correct for cluster membership.

2.3.2 Stellar masses and completeness

We estimate stellar masses for all objects using the SED fitting code FAST (Kriek et al. 2009). The redshifts are fixed at the measured spec- z , whenever available. Otherwise we use the photo- z from EAZY, and the stellar population libraries from Bruzual & Charlot (2003) are used to obtain the model SED that gives the best fit to the photometric data. We use a parameterization of the star formation history as $SFR \propto e^{-t/\tau}$, where the time-scale τ is allowed to range between 10 Myr and 10 Gyr. We also assume a Chabrier (2003) IMF, solar metallicity, and the Calzetti et al. (2000) dust law. These settings are identical to those used for the measurement of stellar masses in the UltraVISTA sample, in order to provide a fair comparison.

We estimate the mass completeness limits for each of the clusters in the following way. First we measure the depths of the K_s detection bands by performing simulations in which we add artificial sources to these images for a range of magnitudes. We then run SExtractor with the same settings as for the construction of the catalogue (Sect. 2.2.3). The recovered fraction as a function of magnitude for the simulated sources provides an estimate for the depth of the detection image. Note that the clusters at higher redshift were prioritized to have longer exposure times and therefore deeper detection bands, leading to more homogeneous detection limits in terms of absolute magnitude and stellar mass. Magnitude values corresponding to the 80% recovery limit, which are typically $\sim 22.5\text{mag}_{\text{AB}}$, are given in Table 2.1.

We estimate stellar mass limits that correspond to these 80% K_s -band completeness limits in two different ways. The first method uses the UltraVISTA catalogue, which is about a magnitude deeper than GCLASS in the K_s -band. For each cluster we select all galaxies from UltraVISTA with a photometric

redshift within 0.05 from the cluster redshift. By comparing the total K_s -band magnitudes with estimated stellar masses in this redshift range, we identify the galaxy with the highest mass around the limiting detection magnitude. This is the object with the highest mass-to-light ratio, corresponding to the reddest galaxy in UltraVISTA. All galaxies more massive than these mass limits, which are listed in Table 2.1, will be detected with a probability of $> 80\%$ in GCLASS.

Secondly, to provide a comparison, we also give the mass limit corresponding to a maximally old stellar population with no dust (Bruzual & Charlot 2003), at the redshift of the cluster with a flux equal to the detection limit. The mass limits resulting from this approach are also given in Table 2.1, and are similar to the first estimates to within several hundredths of a dex for most of the clusters.

Note that for cluster SpARCS-0036 we use the J-band as the detection band instead of the K_s -band because the K_s -band is of much lower quality. Because the seeing in the J-band is significantly better, a J-band selection leads to a stellar mass detection limit that is 0.3 dex lower than could be obtained with a K_s -selection. In Table 2.1 we therefore give the estimates corresponding to the J-band.

2.3.3 Rest-frame colours

In the following we make a separate comparison between the SMF for star-forming and quiescent galaxies, and correct each of the galaxy types for cluster membership. Wuyts et al. (2007), Williams et al. (2009) and Patel et al. (2012) have shown that the U-, V- and J-band rest-frame fluxes of galaxies can be combined into a UVJ diagram to distinguish quiescent galaxies from star-forming galaxies, even if the latter population is reddened by dust extinction.

After estimating redshifts for all objects in the photometric catalogue, we use EAZY to interpolate the input SED to obtain the U-V and V-J rest-frame colours for each galaxy. In Fig. 2.2 we plot those colours for all K_s -band selected objects with $M_\star > 10^{10} M_\odot$. The greyscale distribution shows the galaxies in GCLASS that are in the redshift range $0.85 < z < 1.20$, but are not part of the clusters, while the red points show the objects that are separated from the BCG by less than 2 arcmin, and have a photometric redshift within 0.1 from the cluster redshift. We select as the quiescent population galaxies with $(U - V) > 1.3 \wedge (V - J) < 1.6 \wedge (U - V) > 0.88(V - J) + 0.6$ (e.g. Whitaker et al. 2011). This dividing line is shown in the figure. For reference, the dust-reddening vector is also shown, indicative of a dust-independent separation of quiescent and star-forming galaxies.

Comparing the cluster and field galaxy populations, we find that 68% of the cluster galaxies in this mass range are quiescent, whereas only 42% of the field galaxies are quiescent. This shows that the cluster population is dominated by

quiescent galaxies, whereas the field has a more mixed population of galaxies. Note, however, that the distribution of colours due to dust-reddening within the separate galaxy types is similar for the two environments.

2.3.4 Cluster member selection

Due to the scatter in the photometric redshift estimates, selecting cluster galaxies based on photometric redshifts will result in the sample being contaminated by fore- and background galaxies. In this section we combine the photometric K_s -band selected multi-colour catalogue and the sub-sample of galaxies with spectroscopic information to select a complete sample of cluster members. We will use the following terminology. By "false positive" we refer to an object that is not part of the cluster, yet has a photo- z that is consistent with the cluster redshift. A "false negative" is an object that belongs to the cluster, but has a photo- z inconsistent with cluster membership. A "secure cluster" object is correctly classified as being part of the cluster based on the photo- z , while a "secure field" object is correctly identified as being outside of the cluster.

Given the relatively small fields in which we measure the cluster SMF, field-to-field variance complicates a full statistical interloper subtraction that is based solely on photometric data. However, owing to the extended spectroscopic coverage of GCLASS, we can estimate the field contamination from these data without having to rely on the statistical subtraction of an external field. This way we take account of both false positives and false negatives in the photometrically selected sample. The objects in the spectroscopic sample were prioritized by $3.6\mu\text{m}$ IRAC flux and proximity to the cluster core, see Sect. 2.2.2 and Muzzin et al. (2012). This selection leads to a targeting completeness that is, to first order, a function of radial distance and stellar mass only.

For these targets we measure the differences between photo- z 's and the redshift for each cluster, and between spec- z 's and the redshift of the cluster. A composite for all 10 clusters is shown in Fig. 2.3, after separating between quiescent and star-forming galaxies. This can be considered as a different representation of Fig. 2.1, where the data for all clusters have been folded on top of each other. Galaxies with $|\Delta z| < 0.05$ are selected as preliminary cluster members based on their photometric redshifts. The red crosses show false positives, orange crosses indicate false negatives. Green (blue) symbols show objects that are identified as secure cluster (field) galaxies. Note that, although we could have started with any cut on $|\Delta z|$, the $|\Delta z| < 0.05$ criterion conveniently yields a number of false positives that approximately equals that of false negatives.

For the objects in the photometric sample that do not have a spectroscopic redshift, we use these fractions of false positives and false negatives to correct the number counts for cluster membership. To make sure that the spec- z

Figure 2.2: Rest-frame U-V versus V-J colours for galaxies with stellar masses exceeding $10^{10} M_{\odot}$ to differentiate between quiescent and star-forming galaxies. The arrow indicates the reddening vector for dust. Combining both colours facilitates a distinction between both galaxy types, even when there is significant reddening by dust. In grey is the distribution of galaxies from GCLASS that are between $0.85 < z < 1.20$, but outside the clusters. A relative density scale is provided. The red points show photo- z selected cluster members with projected position less than 2 arcmin from the cluster centres.

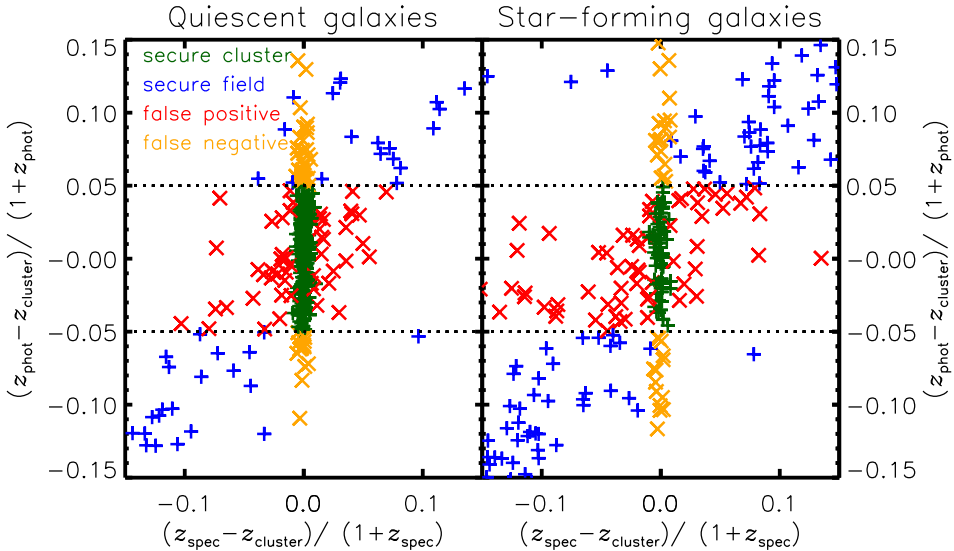
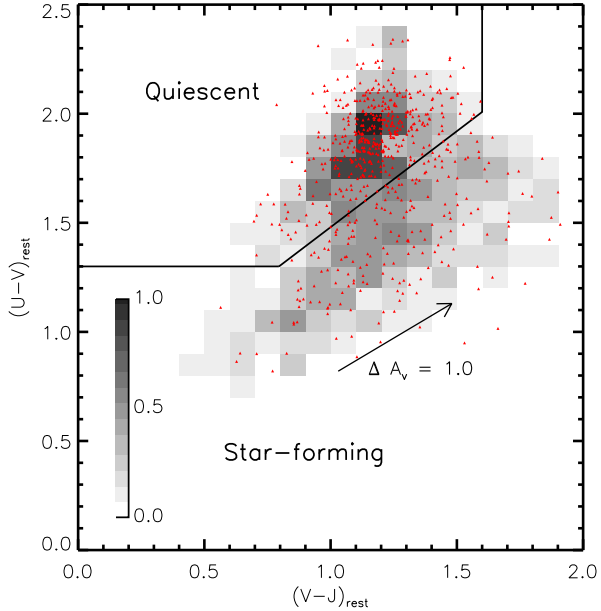


Figure 2.3: An adaptation of Fig. 2.1, showing a composite plot of the 10 clusters to measure the fraction of false positives and false negatives, after separating quiescent and star-forming galaxies. By plotting the difference with respect to the cluster redshift, all clusters are effectively plotted on top of each other. The z_{phot} measurements for star-forming galaxies have a larger scatter than the measurements for quiescent galaxies. What is not shown here, is how the purity fractions change as a function of mass and radial distance. In the analysis we also take account of this mass and radial dependence; see Fig. 2.4.

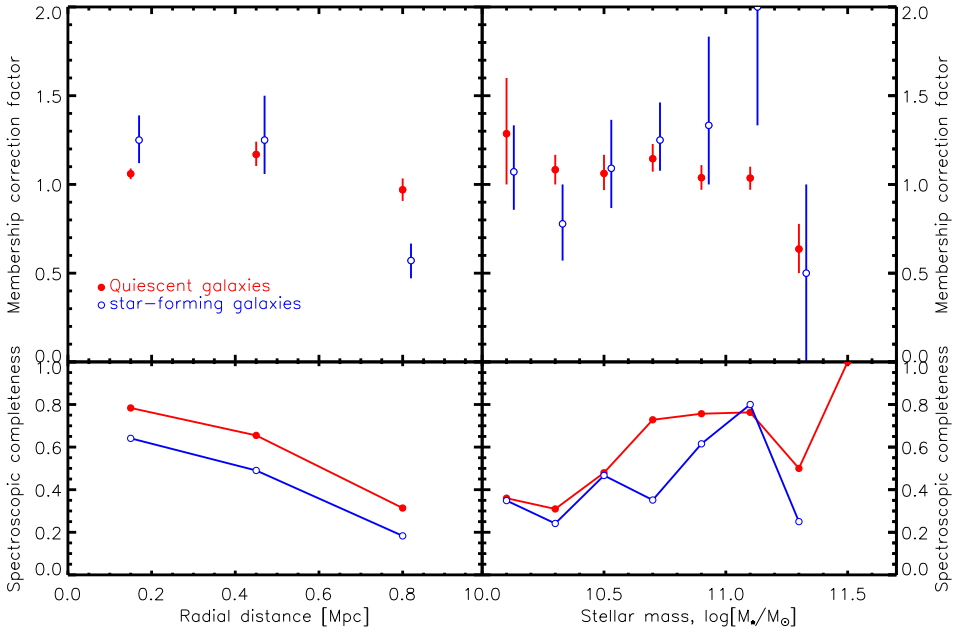


Figure 2.4: The correction factors for the photo- z selected members that have no spec- z information, estimated from the subsample of objects that do have spectroscopic overlap. A separation by radial distance and stellar mass is made, and these factors are multiplied to yield the total correction factor for each galaxy. A correction factor > 1 indicates that the number of false negatives exceeds the number of false positives in that bin. In the bottom panels the spectroscopic targeting completeness is shown.

subsample is representative of the photo- z sample, we have to estimate this correction as a function of radial distance and stellar mass. This separation ensures that we take account of the spectroscopic targeting completeness, the mass- and radially-dependent overdensity of the cluster compared to the field, and the flux dependence of the photo- z quality. In Fig. 2.4 we show the correction factors, as a function of radial distance (left panel) and as a function of stellar mass (right panel). Error bars give the 68% confidence regions estimated from a series of Monte-Carlo simulations in which we randomly draw a number for secure cluster members, false positives and false negatives from a Poisson distribution in each mass-, and radial bin. A correction factor > 1 indicates that the number of false negatives exceeds the number of false positives in that bin. Corrections are roughly constant with M_* , decreasing slightly at large radii, but the selection of photo- z members as objects with $|\Delta z| < 0.05$ ensures that the corrections are small in general. If we change the cut to 0.03, 0.07 or 0.10, this leads to different membership corrections. However, after these corrections have been applied, we find that these cuts give results that are consistent within the errors.

Down to the mass-completeness of the clusters there are 283 spectroscop-

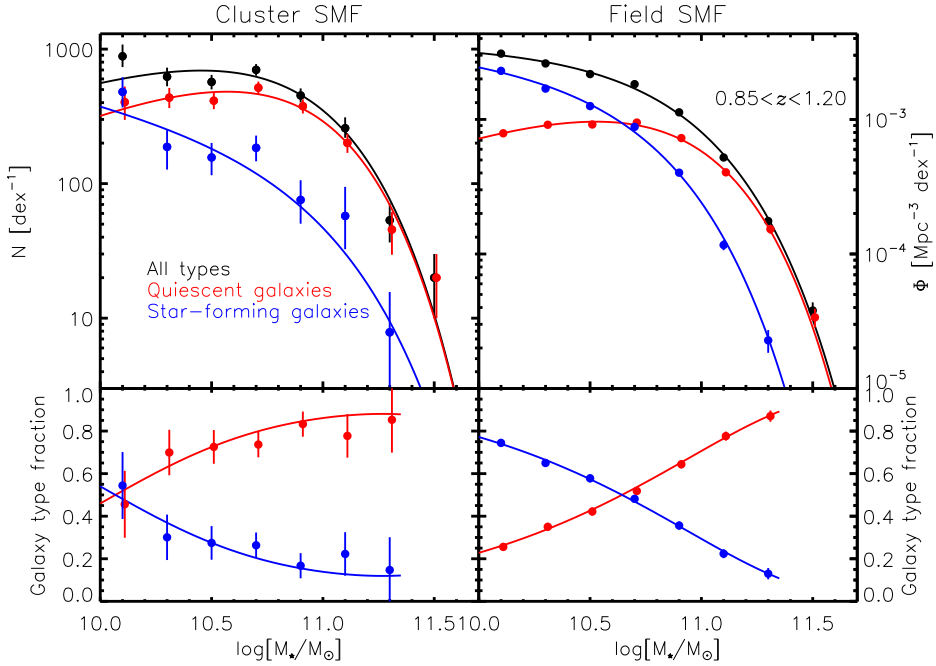


Figure 2.5: Comparing the cluster SMF (left panel) with a similar representation of the field SMF (right panel). The total SMFs (black points) are separated by galaxy type. Red points show the quiescent galaxies and the blue points show star-forming galaxies. The best-fitting Schechter functions are overplotted for each SMF sample. Note that the red points have been offset by 0.01 dex for better visibility. In the bottom panel we show the fractional contribution of quiescent and star-forming galaxies to the total population, and the curves show the fractional contributions of the Schechter functions. The relative contribution of quiescent galaxies is shown to be higher in the cluster than in the field. Note that the error bars on the field data are smaller than the data point symbols, because only Poissonian errors are taken into account.

ically confirmed cluster members. We divide the 255 photo- z members for which we do not have spectra over a 2-dimensional array of 3 radial bins and 8 stellar mass bins, and correct them for membership by multiplying with both the radial and mass-dependent correction factors (as shown in Fig. 2.4). Because the corrections are relatively small, the way we bin the data only has a minor effect on the results. The dominant source of uncertainty is of statistical nature.

Table 2.3: The values for the data points of the galaxy SMF that are shown in Fig. 2.5. These are the raw, membership-corrected, numbers of galaxies for the clusters. To obtain the units shown in the figures for the clusters, these values need to be multiplied by 5, since the binsize is 0.2 dex in stellar mass. Numbers in brackets show the total number of spectroscopic cluster members in each bin. Note that the spectroscopic completeness is highest in the high-mass bins. Errors represent 1σ uncertainties estimated from Monte-Carlo simulations for the cluster data, and Poissonian errors for the field data.

$\log(M_*)$ [M_\odot]	Cluster $z \sim 1$			Field $z \sim 1$		Mpc $^{-3}$
	Total	Quiescent	Star-forming	Total	Φ [10^{-5} dex $^{-1}$]	
10.10	176^{+39}_{-29} [24]	80^{+24}_{-21} [9]	96^{+27}_{-22} [15]	308.6 ± 5.1	78.9 ± 2.6	229.7 ± 4.4
10.30	124^{+20}_{-18} [20]	87^{+15}_{-14} [13]	37^{+12}_{-12} [7]	260.8 ± 4.7	91.3 ± 2.8	169.5 ± 3.8
10.50	114^{+14}_{-13} [46]	82^{+11}_{-11} [34]	31^{+8}_{-8} [12]	217.4 ± 4.3	91.7 ± 2.8	125.7 ± 3.3
10.70	140^{+14}_{-13} [78]	103^{+11}_{-10} [63]	36^{+8}_{-7} [15]	183.0 ± 3.9	94.9 ± 2.8	88.1 ± 2.7
10.90	90^{+11}_{-10} [63]	75^{+9}_{-8} [55]	15^{+6}_{-5} [8]	112.9 ± 3.1	72.7 ± 2.5	40.2 ± 1.8
11.10	51^{+7}_{-7} [33]	40^{+6}_{-6} [29]	11^{+7}_{-4} [4]	52.1 ± 2.1	40.5 ± 1.8	11.7 ± 1.0
11.30	10^{+3}_{-3} [8]	9^{+3}_{-2} [7]	1^{+1}_{-1} [1]	17.6 ± 1.2	15.3 ± 1.1	2.3 ± 0.4
11.50	4^{+2}_{-2} [4]	4^{+2}_{-2} [4]	[0]	3.8 ± 0.6	3.4 ± 0.5	0.4 ± 0.2

2.4 Results

2.4.1 The cluster stellar mass function

We measure the cluster galaxy SMF from the sample of galaxies in the 10 GCLASS clusters, obtained as described in Sect. 2.3.4. This is done by summing over the 3 radial bins so that we measure the SMF out to a projected radius of 1 Mpc. The summation is done separately for quiescent and star-forming galaxies, which were identified using the UVJ criterion (Sect. 2.3.3). The errors from the Monte-Carlo simulations that we discussed in Sect. 2.3.4 are propagated. Note however that the spectroscopic targets only contribute a Poissonian error, since these do not need to be statistically corrected for cluster membership.

The blue points in the left panel of Fig. 2.5 show the SMF for the star-forming galaxies in the 10 clusters, while the red points show the quiescent population in the clusters. The total galaxy SMF is the sum of the two galaxy types, and is shown in black. The fraction of quiescent and star-forming galaxies to the total number of galaxies is shown in the bottom panel. The data points are also given in Table 2.3. Note that the quiescent population dominates the SMF of the cluster galaxies over almost the entire mass range we study. The BCGs are not included in this plot, nor in the rest of the analysis in this paper. Although the satellites in the galaxy clusters are believed to originate from an infalling population of centrals in the field, the BCGs are the central galaxies in massive cluster haloes and do not have a field counterpart.

Consequently, BCGs do not follow the Schechter function that describes the rest of the cluster galaxies. For a study of the stellar mass evolution of BCGs we refer to Lidman et al. (2012).

Because the selection bands of some of the clusters are not sufficiently deep to probe the SMF down to $10^{10} M_{\odot}$ (see Table 2.1), the lowest two stellar-mass bins are composed of galaxies selected from 6 and 7 clusters, respectively. These two bins were scaled up by assuming the richnesses of the clusters are similar, i.e. multiplying their values with a factor of $\frac{10}{6}$ and $\frac{10}{7}$, respectively. A rough estimate of the richnesses of the individual galaxy clusters shows that these correction factors are accurate to within 10%.

We perform a small additional completeness correction based on a comparison of the field SMF measured from UltraVISTA and the parts of GCLASS that are outside the clusters (i.e. the field SMF from GCLASS; see Appendix 2.B). Because of the depth of its photometry, UltraVISTA is complete at $M_{*} > 10^{10} M_{\odot}$ in the redshift range $0.85 < z < 1.20$. We compare the field estimates in Appendix 2.B and find that there is a good quantitative agreement in both the shape and normalisation of the field SMF between the surveys at this stellar mass range, except for the lowest three mass points. This suggests that there may be residual incompleteness in GCLASS that affects the lowest mass points. Assuming that this incompleteness affects the cluster and field data of GCLASS in a similar way, we correct the GCLASS cluster SMF points for the star-forming and quiescent galaxies with small factors, up to 37% at the lowest mass bin for the quiescent galaxies. This correction changes the best-fit Schechter parameters for the cluster fits in the following way. M^{*} increases by 0.01, 0.10 and 0.08 dex and α becomes more negative by 0.07, 0.33 and 0.26 for the total, star-forming and quiescent population, respectively. These changes do not affect any of the qualitative results in this paper, nor change the conclusion in any way.

We fit a Schechter (Schechter 1976) function to the binned data points. This function is parameterized as

$$\Phi(M) = \ln(10)\Phi^{*} \left[10^{(M-M^{*})(1+\alpha)} \right] \cdot \exp \left[-10^{(M-M^{*})} \right], \quad (2.2)$$

with M^{*} being the characteristic mass, α the low-mass slope, and ϕ^{*} the total overall normalisation. Our data cannot rule out a different functional form at the low-mass end. Therefore we will discuss the differences in the SMFs between the cluster and field in the context of the Schechter function fit. A more quantitative assessment would require measurements at lower masses.

Because the number of sources in the brighter stellar mass bins is low, we are in the regime where errors cannot be represented by a Gaussian distribution and therefore ordinary χ^2 minimisation is not appropriate. Consequently, we take a general maximum likelihood approach where we use the probability functions on each data point obtained from the Monte-Carlo simulations. This

way we compute the likelihood function \mathcal{L} on a 3 dimensional grid of Schechter parameters. The best fitting parameters M^* and α , corresponding to \mathcal{L}_{\max} , are listed in Table 2.4 and the corresponding Schechter function is shown in the left panel of Fig. 2.5 (black curve). The Schechter function provides a reasonable fit to the data, with a Goodness of Fit (GoF) of 2.12. We also give the 68.3% confidence levels on each parameter after marginalising over the other two parameters. We take this confidence interval to be the region where $2 \ln(\mathcal{L}_{\max}/\mathcal{L}) \leq 1$. However, since these parameters are known to be degenerate, we show confidence regions in Fig. 2.7. The black curves correspond to 68.3% and 95.4% confidence levels after marginalising only over ϕ^* .

In general, uncertainties on individual mass measurements of the galaxies lead to a bias in the shape of the SMF and the best fitting Schechter parameters (Eddington 1913; Teerikorpi 2004). Especially for high masses, where the slope of the SMF is steep, the shape of the SMF can be biased because of galaxies scattering to adjacent bins. To study the magnitude of this effect on our analysis, we need to estimate the stellar mass scatter of galaxies in each bin of the SMF. To do this we created 100 Monte Carlo realisations of the photometric catalogue, in which we randomly perturb the aperture fluxes following the estimated statistical errors on these measurements. Then we estimate photo- z 's and stellar masses for the entries of these catalogues in a similar way as for the standard analysis. At the high-mass end, where the SED fitting is mostly supported by spec- z 's (see Fig. 2.4 or Table 2.3), the scatter is about 0.05 dex in stellar mass. For lower masses the scatter increases towards 0.08 (0.10) dex in stellar mass for quiescent (star-forming) galaxies. Even if all galaxies would scatter to higher masses, the bias in the Schechter parameter M^* would be 0.05 dex. In reality α might also change slightly due to Eddington bias (e.g. van der Burg et al. 2010), but we expect the bias of the combination of Schechter parameters to be substantially smaller than the size of the $1\text{-}\sigma$ statistical error contours in Fig. 2.7. Given also that the systematic uncertainties due to assumptions regarding the IMF, models on the stellar populations, star-formation histories and metallicity, are substantially larger (e.g. Marchesini et al. 2009), we do not attempt to correct for this bias in the current analysis.

2.4.2 Cluster versus Field

We compare the cluster results with the field galaxy SMF by selecting all galaxies with a photometric redshift in the range $0.85 < z < 1.20$ from the UltraVISTA survey. Since the UltraVISTA survey is superior in depth compared to GCLASS, the SMF can be measured down to $10^{10} M_{\odot}$ in this redshift range. The right panel of Fig. 2.5 shows the field total SMF in black, which is composed of 13633 galaxies in this mass and redshift range. The best fitting Schechter function for the field sample is found by minimizing χ^2 on a 3 dimen-

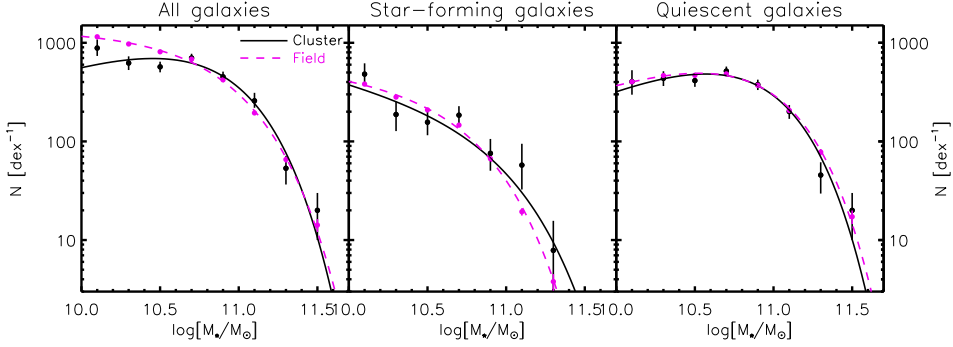


Figure 2.6: Galaxy SMFs for different galaxy types and environments. Left panel: the total galaxy population in the cluster (black) and the field (magenta). Middle panel: the cluster and field SMF for the subset of star-forming galaxies. Right panel: the subset of quiescent galaxies. The field data have been scaled vertically to match the cluster SMF at M^* of the cluster. Error bars show the 68% confidence regions from Monte-Carlo simulations (on the cluster data), or Poisson error bars (field data).

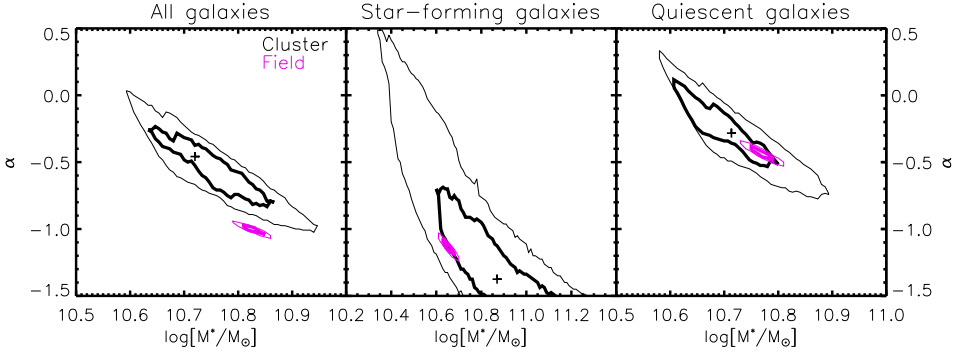


Figure 2.7: The 68% and 95% likelihood contours for the Schechter parameters M^* and α , after marginalising over the ϕ^* parameter. Black lines show the cluster contours, while magenta lines show the contours for the field data. $+$ -signs show the single best fit Schechter parameters. The regions corresponding to the cluster SMF were obtained using maximum-likelihood fitting of the Monte-Carlo simulated data.

Table 2.4: A comparison between the best fitting Schechter parameters and their 68% confidence intervals for the different galaxy types and environments.

Galaxy type	Environment	$\log[M^*/M_\odot]$	α	GoF^a
Total	Cluster	$10.72^{+0.09}_{-0.02}$	$-0.46^{+0.08}_{-0.26}$	2.12
Total	Field	$10.83^{+0.01}_{-0.02}$	$-1.01^{+0.04}_{-0.02}$	4.66
Star-forming	Cluster	$10.87^{+0.28}_{-0.18}$	$-1.38^{+0.38}_{-0.35}$	1.44
Star-forming	Field	$10.65^{+0.02}_{-0.01}$	$-1.13^{+0.02}_{-0.05}$	4.15
Quiescent	Cluster	$10.71^{+0.04}_{-0.10}$	$-0.28^{+0.33}_{-0.14}$	1.21
Quiescent	Field	$10.77^{+0.01}_{-0.01}$	$-0.43^{+0.02}_{-0.04}$	1.39

^a Goodness of Fit (GoF) defined as χ^2/dof for the field survey (we assumed Gaussian statistics owing to the large number counts in this survey). For the cluster fits we used an analogous expression from the Maximum likelihood fitting method.

sional grid of Schechter parameters, and is represented by the black curve in the right panel of Fig. 2.5. For a comprehensive comparison between the SMF from UltraVISTA and other field estimates we refer to Muzzin et al. (2013a). There it is shown that the SMF of the entire galaxy population, measured with this catalogue, is in good agreement with previous measurements.

To better compare the shape of the total SMF in the two environments, we refer to the left panel of Fig. 2.6, where the magenta points show the galaxy SMF from UltraVISTA, and the black points show the SMF for the cluster galaxies. The field data have been scaled such that the Schechter functions of the cluster and field intersect at the characteristic mass M^* of the cluster. The best fitting values for the α and M^* parameters are given in Table 2.4, with their 68.3% confidence levels. Because we only included Poissonian errors on the field SMF data, the GoF of the Schechter fits are rather high (up to 4.66 for the total galaxy population). At this level of detail it is also possible that the Schechter function is no longer an adequate description of the data. The magenta contours in the left panel of Fig. 2.7 show the 2-d confidence contours for the field.

2.4.3 Star-forming vs Quiescent galaxies

We separate the UltraVISTA galaxy catalogue between quiescent galaxies and star-forming galaxies by using their estimated rest-frame U-V and V-J colours, as was analogously done for the cluster galaxies in Sect. 2.3.3. We compare the shapes of the SMF for each galaxy type between the different environments.

In the middle panel of Fig. 2.6 we show the shape of the SMF for star-forming galaxies in the field (magenta) and the cluster (black), together with their best-fitting Schechter functions. The field data have been normalised so

that the Schechter functions intersect at the characteristic mass M^* for star-forming galaxies in the cluster. The corresponding 68% and 95% confidence regions for the Schechter parameters α and M^* are shown in the middle panel of Fig. 2.7. The best-fitting Schechter parameters and their error bars are also given in Table 2.4.

2.4.4 Normalisation of the SMF

The data points in Fig. 2.6 are arbitrarily normalised to provide for an easy comparison of the shapes of the SMF between the field and cluster samples. As a consequence, the ϕ^* parameters corresponding to the best fitting Schechter function have no direct meaning. Normalised by volume the cluster is, by definition, substantially overdense compared to the field. To be able to better interpret the differences of the SMF between the field and cluster environment in Sect. 2.5, we therefore normalise the SMF by the total amount of matter in each respective part of the Universe.

For the UltraVISTA field reference we take the total comoving volume within a redshift range $0.85 < z < 1.20$ and an unmasked survey area of 1.62 square degree (Muzzin et al. 2013b). After multiplying the volume corresponding to this area in this redshift range, $5.9 \cdot 10^6 \text{ Mpc}^3$, by the average matter density of the Universe, being $2.8 \cdot 10^{-30} \text{ g cm}^{-3}$ in our cosmology, we find that the total amount (i.e. dark matter + baryonic) of matter in this volume is about $2.4 \cdot 10^{17} \text{ M}_\odot$.

Given the values for M_{200} , which are presented in Table 2.2 and are based on the dynamical analysis of the GCLASS spectra, we estimate the concentration parameter corresponding to the NFW profiles (Navarro et al. 1997) for these systems from Duffy et al. (2008). We integrate these NFW profiles along the LOS and out to a projected radius of 1 Mpc, yielding a total mass of $5.6 \times 10^{15} \text{ M}_\odot$ for the 10 clusters. Since Sheldon et al. (2009) and Hoekstra et al. (2000) have shown that, although cluster centres are dominated by luminous matter, the mass to light ratio (M/L) of clusters within a distance of 1 Mpc is similar to the cluster M/L within larger distances, this ensures that we measure and normalise the SMF in a representative volume.

Fig. 2.8 shows the total SMF for the cluster and the field, after normalising by the total masses estimated above. Note that there is, per unit total mass, a strong overdensity of galaxies at all stellar masses we probe in the cluster environments. In the stellar mass range we study, the overdensity ranges from a minimum factor of 1.3 at 10^{10} M_\odot to a maximum factor of 3.2 at $10^{11.1} \text{ M}_\odot$. This shows that the clusters contain a very biased population of galaxies, where a relatively high fraction of the total baryonic mass is transformed into stars. The field, in contrast, contains regions such as voids, where the star formation efficiency is very low.

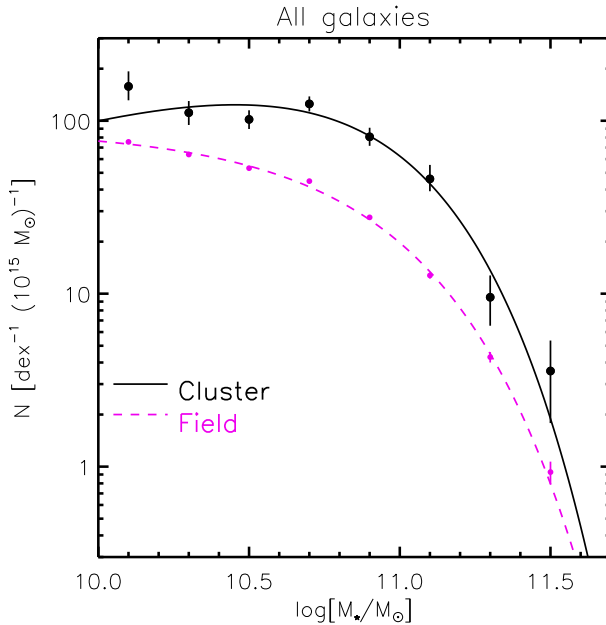


Figure 2.8: Same as the left panel of Fig. 2.6, but normalised by the total mass (dark matter + baryonic) in the field sample (magenta) and cluster sample (black). Per unit of total mass the cluster has a clear overdensity at all stellar masses we probe. Error bars show the 68% confidence regions from Monte-Carlo simulations (on the cluster data), or Poisson error bars (field data). In the left panel of Fig. 2.6 we provided an easier comparison of the shapes of the two SMFs.

2.5 Discussion

In this section we discuss the implications of the results from Sect. 2.4. We discuss in Sect. 2.5.1 the shape of the SMF for star-forming galaxies, quiescent galaxies, and the total galaxy population. We make a comparison between the cluster and field, and also compare our results to measurements from the literature. We proceed to apply a simple model that Peng et al. (2010) showed to give a good fit to the SMF measured at $z = 0$ from SDSS data. Peng et al. (2010) could not explore the area of high- z clusters with COSMOS and SDSS data, so we confront our results at $z = 1$ with the predictions of their model.

2.5.1 The shape of the galaxy SMF

Star-forming galaxies

Fig. 2.6 shows that the shape of the galaxy SMF for the subset of UVJ-selected star-forming galaxies is similar between the clusters from GCLASS and the field from UltraVISTA. Quantitatively, Fig. 2.7 indicates that the combination of best-fitting Schechter parameters differs by about 1σ . The low-mass slope α is $-1.38_{-0.35}^{+0.38}$ for the cluster versus $-1.13_{-0.05}^{+0.02}$ in the field. The characteristic mass M^* is $10.87_{-0.18}^{+0.28}$ and $10.65_{-0.01}^{+0.02}$ for the cluster and field, respectively.

We do not make a quantitative comparison between the literature and our measurements of the SMF for star-forming galaxies because the way these

star-forming samples are selected is different for different studies. Whereas we select a subset of star-forming galaxies based on the UVJ-diagram, most other studies use either a single colour or a morphological selection. Nonetheless, the finding that the shape of the star-forming SMF is independent of environment is qualitatively consistent with lower redshift measurements presented by e.g. Bolzonella et al. (2010). Note however that the clusters in GCLASS constitute much higher overdensities than the highest densities in the COSMOS fields used by Bolzonella et al. (2010). The shape of the star-forming galaxy SMF is also measured to be roughly constant with cosmic time (e.g. Ilbert et al. 2010; Brammer et al. 2011). This shows that, whatever processes are responsible for the quenching of star formation in galaxies, they have to operate in such a way that the SMF of star-forming galaxies does not change shape, even in the highest density environments. This is a fundamental assumption for the Peng et al. (2010) quenching model that we employ in Sect. 2.5.2.

Quiescent galaxies

Fig. 2.6 shows that for the selection of quiescent galaxies based on the UVJ criterion, the shape of the SMF for those galaxies is also similar in the different environments probed by GCLASS and UltraVISTA. The best fitting α for the clusters is $-0.28_{-0.14}^{+0.33}$ versus $-0.43_{-0.04}^{+0.02}$ in the field. Given the degeneracy between α and M^* , the combination of these Schechter parameters, as shown in Fig. 2.7, also agrees to better than 1σ between the field and cluster. It seems remarkable that, whatever quenching processes are responsible for the build-up of the quiescent population in these contrasting environments, they work in such a way that the resulting SMF for quiescent galaxies at $M_\star > 10^{10} M_\odot$ has a similar shape in both environments.

Rudnick et al. (2009) measured the cluster galaxy luminosity function of red sequence galaxies in the redshift range $0.4 < z < 0.8$ and compared their measurements with the field luminosity function. They also found little difference in the shape of the quiescent luminosity function between the two environments. Rudnick et al. (2009) also found a hint of a shallower low-mass slope in the cluster compared to the field. Note that they use a different selection of red galaxies, so that their red sequence selected sample might be contaminated by reddened star-forming galaxies.

The total galaxy population

Whereas the SMF for each of the galaxy types appears to be similar in the different environments probed by GCLASS and UltraVISTA, Figs. 2.6 & 2.7 show that the SMF for the total galaxy population is significantly different. This is because the *fraction* of quiescent galaxies is higher in the cluster. That makes the low-mass slope of the total SMF shallower in the cluster compared

to the field (see Fig. 2.6). This result is also consistent with the measurements shown for more moderate overdensities in the COSMOS field by Bolzonella et al. (2010). We compare our results to the literature results from the WINGS, ICBS and EDisCS clusters probed in Vulcani et al. (2013), although our sample is unique in this combination of redshift range and photometric depth.

Vulcani et al. (2013) assumed a Kroupa (Kroupa 2001) IMF, which yields stellar masses consistent with Chabrier to within several 0.01 dex. For the sample of WINGS clusters ($0.04 < z < 0.07$) they measure Schechter parameters $M^* = 10.82 \pm 0.13$ and $\alpha = -0.88 \pm 0.31$. Although the redshift distribution is very different from the GCLASS sample, they agree within $1 - \sigma$ with the contours shown in Fig. 2.7. The measured Schechter parameters for the ICBS clusters ($0.3 < z < 0.45$) are $M^* = 11.37 \pm 0.28$ and $\alpha = -1.29 \pm 0.41$. Note that this point lies in the direction of the correlation between M^* and α , as is shown in Fig. 2.7. The same is true for the EDisCS clusters ($0.4 < z < 0.8$), for which Vulcani et al. (2013) report Schechter parameters $M^* = 11.15 \pm 0.07$ and $\alpha = -1.03 \pm 0.08$.

Another fundamental observable of a population of galaxies, besides their SMF, is the distribution of specific star formation rates (sSFRs). Wetzel et al. (2012) studied the distribution of sSFRs for central and satellite galaxies as a function of stellar mass in a range of environments. They show that the distribution of sSFRs is clearly bimodal, with clear populations of active and passive galaxies. Interestingly, they show that the location and shape for each of the two peaks is independent of environment, and that only the relative amounts of star-forming and quiescent galaxies occupying the peaks differ as a function of environment. Likewise, Muzzin et al. (2012) show that for the GCLASS data the sSFR of star-forming galaxies in a given mass bin is also independent of environment. These results are analogous to our measurements for the SMF, which can also be considered as a sum of the quiescent galaxy SMF and the star-forming galaxy SMF. Having a different fraction of quiescent galaxies in opposing environments, the total galaxy SMF will look different whereas the SMF for each galaxy type is similar, analogous to what Wetzel et al. (2012) found for the distribution of sSFRs.

2.5.2 A simple quenching model

It has been known for several decades that the fraction of quiescent galaxies increases with both stellar mass and environmental density (e.g. Baldry et al. 2006). However, recent studies (e.g. Peng et al. 2010; Muzzin et al. 2012) have suggested that the quenching of star-forming galaxies can be fully separated in two distinct quenching tracks, dubbed "mass quenching" and "environmental quenching". The assumption that the shape of the galaxy SMF for star-forming galaxies is universal, which is supported by our measurements, places constraints on the way these quenching processes operate.

To interpret our observed data in this context we consider the simple model proposed by Peng et al. (2010). This model is based on the observed constancy in the shape of the SMF for star-forming galaxies with redshift. Peng et al. (2010) use a combination of mass quenching and environmental quenching, processes which they assume to act independently of each other, to build up the quiescent population. The basic descriptions for these quenching tracks are demanded to operate such that the shape of the SMF for star-forming galaxies is independent of environment.

Because star-forming galaxies are forming stars at a rate that scales roughly linearly with their stellar mass (the observed sSFR for this population is roughly independent of mass (Noeske et al. 2007)), mass quenching is supposed to preferentially quench high mass galaxies in order to keep the SMF for star-forming galaxies unchanged. Therefore the resulting galaxy SMF for this quenched population is expected to contain an excess of high mass galaxies and hence has a shallow low-mass slope. In high-density environments the fraction of quiescent galaxies increases compared to low-density environments. Peng et al. (2010) assume that this increase is caused by the process of environmental quenching. The environmental quenching efficiency is assumed to be independent of mass, so that the resulting SMF of the environmentally-quenched galaxies has the same shape as the star-forming galaxy SMF. With some additional quenching due to, what they presume to be, merger processes, Peng et al. (2010) showed that this model works very well at reproducing the SMF measured in the redshift range $0.02 < z < 0.085$ from SDSS DR7 (Abazajian et al. 2009) data. The regime of $z \sim 1$ clusters however has not yet been tested against their model, since this range is not probed by COSMOS.

The model, however, makes predictions for the SMF at higher redshifts over a range of environmental densities (Peng et al. 2010, Fig. 13), and we compare these predictions at $z = 1$ to the SMFs measured from GCLASS and UltraVISTA. The predictions from their model are separated by environmental density in four quartiles, with D1 (D4) corresponding to the lowest (highest) density quartile. The (especially environmentally) quenched galaxies contribute more substantially to the total galaxy population in D4 compared to D1, leading to a higher fraction of quiescent galaxies. The left panel of Fig. 2.9 compares the prediction of the highest environmental density quartile (D4) with the measurement of the cluster galaxy SMF from GCLASS. We fitted the total normalisation as a free parameter, but left the relative normalisations of star-forming and quiescent galaxies unchanged. Note that the GCLASS clusters constitute the most massive structures around $z = 1$ and therefore contain higher overdensities than the D4 reference. Nevertheless, the D4 model provides a reasonable fit to the data, where the quiescent fraction of galaxies between the model and the data is well matched. In future studies it would be interesting to compare the Peng et al. (2010) model for the upper 5% in environmental density to the cluster data, which would be a closer match

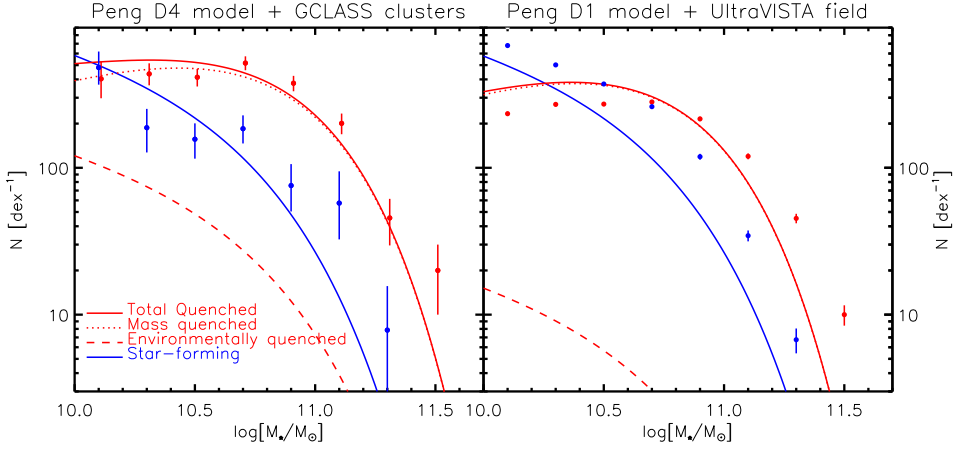


Figure 2.9: The left panel compares the Peng et al. (2010) model prediction in the environmental density quartile D4 with our GCLASS cluster SMF measurements, which were already presented in Fig. 2.5 and Table 2.3. A separation between the two quenching processes is made. The right panel makes a similar comparison between the model in quartile D1 with the UltraVISTA field data. Note that the relative normalisations of star-forming and quiescent populations are fixed, and that the populations are fitted simultaneously.

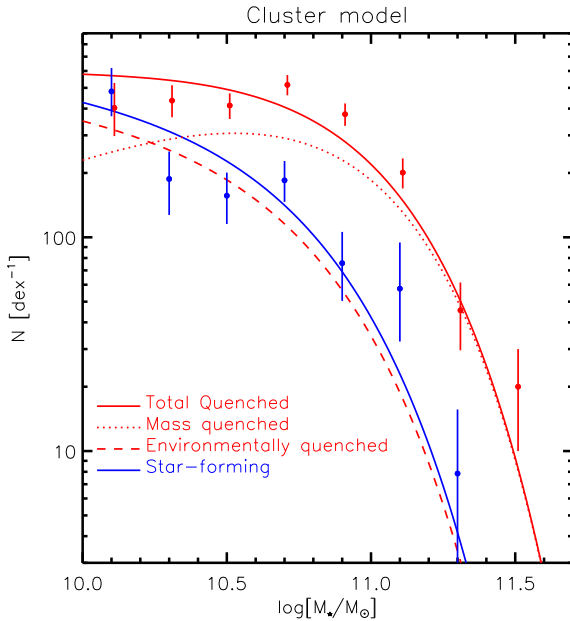


Figure 2.10: The cluster data, which were already given in Table 2.3, with the predictions from a simple quenching model based on Peng et al. (2010) in its most basic form, using UltraVISTA as a starting point. Mass quenching and environmental quenching are assumed to act independently. The blue Schechter function is the best fit to the star-forming galaxy population and the red solid line gives the best fit to the quiescent population. The red line is composed of a mass quenched population (dotted red line), and an environmentally quenched population (dashed line). This model needs 45% additional environmental quenching compared to the field to yield the best fit to the data. Note that the red points have been offset by 0.01 dex for better visibility.

to their density.

The UltraVISTA field is expected to contain a range of environmental densities. The measured SMF from these data should therefore be matched to a combination of the D1-D4 models. However, the right panel of Fig. 2.9 shows that even the lowest environmental density quartile D1 overpredicts the quiescent fraction of galaxies in the field of UltraVISTA at $z = 1$. The caveat is that the separation of star-forming and quiescent galaxies is done differently between the data and the model. Our sample of UVJ-selected star-forming galaxies includes star-forming galaxies that are seen edge-on and therefore reddened by dust, whereas a rest-frame (U-B) colour selection, as applied in Peng et al. (2010), identifies these objects as being on the red sequence.

To reconcile the apparent disagreement between the data and the Peng et al. (2010) model in predicting the quiescent fraction of galaxies, we consider the following simplified analytical model where we only assume mass quenching and environmental quenching, and no additional merging. We apply this simplified model, based on the same principles as Peng et al. (2010), to the GCLASS cluster data, but use the Schechter fits to the UltraVISTA data as a starting point. UltraVISTA is the limiting case where the dominant quenching process is mass-quenching.

We fit the cluster data by a combination of three functions that describe populations of star-forming galaxies, mass-quenched quiescent galaxies and environmentally-quenched quiescent galaxies. Two of these functions are given by the Schechter fits that were measured for the UltraVISTA field population. The quiescent population of UltraVISTA is expected to be primarily mass-quenched at the stellar mass range we study, so we take the shape of this SMF for the mass-quenched population and allow the normalisation to be adjusted by the fit. The SMF for star-forming galaxies is also taken from UltraVISTA, and since the functional form of this distribution is assumed to be independent of environment, we use the shape of this SMF and allow for a change in the normalisation. The third SMF, that describes the population of environmentally-quenched galaxies, is assumed to have the same shape as the SMF of star-forming galaxies, but the normalisation can be adapted in the fit. The sum of the functions for both quenched populations is fitted to the data points that describe the SMF for quiescent galaxies.

Now that the functional forms of the three populations that we fit are defined, the normalisations are adapted by fitting two free parameters in the following way. One free parameter x describes how the three functions move relative to each other, and constrains the percentage of star-forming galaxies that is environmentally quenched by the cluster. This gives rise to a population of environmentally-quenched galaxies with a normalisation of x compared to the star-forming galaxies. The star-forming galaxies are reduced by a factor of $(1 - x)$. We do not change the relative amount of mass-quenched galaxies. The second free parameter describes the total normalisation of these three

functions and has no direct meaning because the cluster and field are arbitrarily normalised with respect to each other.

We perform a maximum-likelihood fit to the data points for the star-forming and quiescent galaxies simultaneously, where we adapt these two parameters, and find a best fitting value of $x = 0.45_{-0.03}^{+0.04}$. Assuming this simple picture we therefore find that, besides the quenching processes that also happen in the field, the cluster environment has to quench an additional 45% of the galaxies to yield the best fit. In the Peng D4 model this environmental quenching fraction ranges from 0.17 at $10^{10} M_{\odot}$ to 0.22 at $10^{11} M_{\odot}$. Fig. 2.10 shows the best fit to the observed SMF in the cluster based on this simple model. The blue and red solid lines give the simultaneous best fit to both galaxy types, for the star-forming and quiescent populations respectively. The red line is composed of a mass-quenched population (dotted red line), and an environmentally-quenched population (dashed line). The quiescent population at high ($> 10^{10.2} M_{\odot}$) masses is dominated by mass-quenched galaxies, while the population at lower stellar masses is dominated by environmentally-quenched galaxies.

The best-fitting model does not yield a perfect representation of the data, since the model significantly overpredicts the number of quiescent galaxies in the low mass regime ($< 10^{10.6} M_{\odot}$). At intermediate masses around $10^{10.9} M_{\odot}$ the model predicts about 30% less galaxies than the data show. The overall Goodness-of-Fit for this model is 2.2 per degree of freedom. Peng et al. (2010) acknowledge that another term, due to merger quenching, is required to fit the data in SDSS and zCOSMOS.

We know that mergers occur in clusters (e.g. van Dokkum et al. 1999), and that the intra-cluster light builds up over time, probably by disruptions of relatively low mass galaxies (Martel et al. 2012). Also we know that BCGs have to grow in stellar mass over time (e.g. Lidman et al. 2012), likely by consuming infalling galaxies. It is possible that these merging processes are required to reconcile the disagreement between the data and this model.

The intriguing similarity in the shape of the quiescent SMF between the cluster and field environments at $z \sim 1$ suggests that there might be a simpler explanation than the Peng et al. (2010) model that does not involve a large amount of mergers. A similar internally-driven quenching mechanism might be responsible for the build-up quiescent population in both environments. We know that the age of a quiescent galaxy at a given stellar mass does not significantly depend on its environment (Thomas et al. 2010; Muzzin et al. 2012). However, for galaxies at a given stellar mass, their underlying dark matter (sub-)haloes at the time of formation might be different between the clusters and the field. "Environment quenching" could therefore refer to an internally driven process that is accelerated in cluster sub-haloes compared to the field. The finding that the cluster environment has already formed a large stellar mass content by $z \sim 1$ (see Fig. 2.8) compared to the field, and that the

fraction of quiescent galaxies is higher in the cluster than in the field, could be caused by a different evolution of the underlying dark matter haloes.

A detailed study of the evolution of the (sub-)halo mass function, compared between cluster and field, is required to look into the different quenching scenarios. It is required to trace back the (sub-)haloes that host the galaxies we study to investigate how their progenitors merge and accrete during their formation history. Such a study could be useful to better understand the process of environmental quenching.

2.6 Summary and Conclusions

In this paper we measured and compared the galaxy SMF at $z \sim 1$ in the high-density environments probed by GCLASS and the field environment from UltraVISTA. The GCLASS sample is composed of 10 rich, red-sequence selected clusters in the redshift range $0.86 < z < 1.34$. The K_s -band selected catalogue based on observations in 11 photometric filters allowed us to estimate photometric redshifts and stellar masses for galaxies in the studied redshift range down to a stellar mass of $10^{10} M_{\odot}$. The extensive spectroscopic sample of GCLASS covers the majority of the cluster members, and is critical to account for contaminants in the sample for which we only have photometric redshifts. Galaxies were separated by type (star-forming versus quiescent) based on their rest-frame U-V and V-J colours. For each galaxy in the photometric sample we estimated the probability that it is part of the cluster based on its type, stellar mass and clustercentric distance. This resulted in a statistically complete sample of cluster members to measure the SMF from.

As a reference field SMF we used UltraVISTA, which is a new NIR survey that overlaps with COSMOS, resulting in 30 band photometric coverage over 1.62 square degrees. Analogously to GCLASS, sources were selected from the K_s -band, and galaxies were separated between the star-forming and quiescent type using the rest-frame UVJ fluxes. This led to a measurement of the SMF for field galaxies at $0.85 < z < 1.20$ that is complete down to stellar masses of $10^{10} M_{\odot}$.

Under the assumption of a single Schechter function fit, we found that the shape of the SMF for star-forming galaxies is similar between the cluster and field environment, and that the combination of best-fitting Schechter parameters α and M^* agree to 1σ between the cluster and field. Furthermore, for the samples of quiescent galaxies we obtain a similar result. The shape of the SMF for quiescent galaxies is similar between the cluster and field at $M_{\star} > 10^{10} M_{\odot}$. The shape of the SMF for the total galaxy population is significantly different between the cluster and field. This is caused by a different fraction of quiescent galaxies in both environments. We find that there is a relative deficit of galaxies with low stellar masses in the cluster compared to the field. However,

when we normalise the SMF by the total amount of matter in each respective part of the Universe, we find that there is a strong excess of galaxies over the entire stellar mass range we probe. This indicates that the cluster environment must have been substantially more efficient in transforming mass into stars compared to the field. Note that this does not imply that field galaxies are less efficient, but rather it is the consequence of the fact that voids contain dark matter, but relatively few stars.

The similarity in the shape of the quiescent and star-forming SMF between the cluster and the field indicates that, if different processes are to be responsible for the quenching of star formation in different environments, these processes have to work in such a way that the shapes of the quiescent and star-forming SMF are similar in these different environments at $z = 1$. This poses a challenge to analytical models that attempt to explain the build-up of the quiescent population by a combination of mass quenching and environment quenching. A simple model suggests that $45_{-3}^{+4}\%$ of the star-forming galaxies which normally would be forming stars in the field, would be quenched by the cluster. Although the physical processes that cause galaxies to quench environmentally are not yet completely understood, it is clear that a process like environmental quenching at $z \sim 1$ is important.

Acknowledgements

We thank Gregory Rudnick, Marijn Franx and Simone Weinmann for discussions and helpful suggestions for this study. Further we thank Jean-Charles Cuillandre for providing information on the MegaCam amplifier drift problem, and Michael Balogh for general feedback on the paper draft.

R.F.J. van der Burg and H. Hoekstra acknowledge support from the Netherlands Organisation for Scientific Research grant number 639.042.814. C. Lidman is the recipient of an Australian Research Council Future Fellowship (program number FT0992259). H. Hildebrandt is supported by the Marie Curie IOF 252760, a CITA National Fellowship, and the DFG grant Hi 1495/2-1. R.D. gratefully acknowledges the support provided by the BASAL Center for Astrophysics and Associated Technologies (CATA), and by FONDECYT grant N. 1130528.

Based on observations obtained at the Gemini Observatory, which is operated by the Association of Universities for Research in Astronomy, Inc., under a cooperative agreement with the NSF on behalf of the Gemini partnership: the National Science Foundation (United States), the National Research Council (Canada), CONICYT (Chile), the Australian Research Council (Australia), Ministério da Ciência, Tecnologia e Inovação (Brazil) and Ministerio de Ciencia, Tecnología e Innovación Productiva (Argentina). Based on observations obtained with MegaPrime/MegaCam, a joint project of CFHT and CEA/DAPNIA, at the Canada-France-Hawaii Telescope (CFHT) which

is operated by the National Research Council (NRC) of Canada, the Institut National des Sciences de l'Univers of the Centre National de la Recherche Scientifique of France, and the University of Hawaii. Based on observations obtained with WIRCam, a joint project of CFHT, Taiwan, Korea, Canada, France, and the Canada-France-Hawaii Telescope (CFHT) which is operated by the National Research Council (NRC) of Canada, the Institut National des Sciences de l'Univers of the Centre National de la Recherche Scientifique of France, and the University of Hawaii. This work is based in part on observations made with the Spitzer Space Telescope, which is operated by the Jet Propulsion Laboratory, California Institute of Technology under a contract with NASA. Support for this work was provided by NASA through an award issued by JPL/Caltech. This paper includes data gathered with the 6.5 meter Magellan Telescopes located at Las Campanas Observatory, Chile. This work is based on observations obtained at the CTIO Blanco 4-m telescopes, which are operated by the Association of Universities for Research in Astronomy Inc. (AURA), under a cooperative agreement with the NSF as part of the National Optical Astronomy Observatories (NOAO). Based on observations that were carried out using the Very Large Telescope at the ESO Paranal Observatory. Based on data products from observations made with ESO Telescopes at the La Silla Paranal Observatories under ESO programme ID 179.A-2005 and on data products produced by TERAPIX and the Cambridge Astronomy Survey Unit on behalf of the UltraVISTA consortium.

2.A Data processing and catalogue creation

This Appendix is meant to give a more elaborate description of the data reduction steps (Sect. 2.A.1) and in particular the procedure for homogenising the PSF and measuring colours using Gaussian weighted apertures (Sect. 2.A.2). Because we combine photometric data over a wide range of wavelengths and for clusters that are both in the Northern and Southern sky, we necessarily have to combine data from different telescopes and/or instruments.

2.A.1 Photometric data reduction

The standard reduction steps include bias and flatfield corrections. Although the images have been flatfielded (e.g. by *Elixir* for the MegaCam data) to yield a uniform zeropoint for the source fluxes, there are still residual background patterns due to scattered light, fringe residuals, and amplifier drift (Cuillandre, private communication). These patterns are reasonably stable over time, and since most exposures in a given filter have been taken consecutively on the same night, we can subtract these background effects. We do this by using

the dithered pattern of observations to differentiate signals that are on a fixed position on the ccd array from sky-bound signals.

To remove cosmic rays from ccd images one usually compares different frames of the same part of the sky. However, since we only have a few deep exposures in some of the filters, the number of overlapping frames of our data set is not always sufficient to be able to identify all cosmic rays. Therefore we remove cosmic rays by using the Laplacian Cosmic Ray Identification method (van Dokkum 2001), which works on individual images. We optimise the parameters in the setup of the code such that we minimise the amount of false positives (bright stars) and false negatives. We do this by testing the code on a range of images with different seeing. The only parameter that has a significant influence on the fraction of false positives and false negatives is *objlim*, which we take to be 3.0.

We obtain astrometric and relative photometric solutions for each chip using SCAMP (Bertin 2006), where we use all exposures in a given filter for all clusters at once to effectively increase the source density, and obtain stable solutions. As a reference catalogue we use SDSS-DR7 data, or the USNO-B catalogue whenever a cluster falls outside the SDSS footprint. This leads to consistent astrometric solutions between the different filters with an internal scatter of about $0.05''$.

2.A.2 PSF homogenisation and colour measurements

Because the shape and size of the point spread function (PSF) are different between exposures and filters, it is non-trivial to measure accurate colours of a galaxy. The simplest approach would be to take the ratio of the total flux of a galaxy in different bands, but this requires very large photometric apertures: for background-limited observations these are very noisy.

However, a reliable colour measurement for the purpose of photometric redshift determination can also be made by taking the ratio of aperture fluxes in different bands, provided these apertures represent the same intrinsic part of the galaxy. We have followed this approach here, based on a modification of the Gaussian-aperture-and-PSF (GaaP) photometry method (Kuijken 2008).

The first step is to convolve each image with a suitable position-dependent kernel that modifies its PSF into a uniform size, circular and Gaussian. This kernel can be constructed using the shapelet (Refregier 2003; Kuijken 2006) formalism, as was done in the *local* approach described in Hildebrandt et al. (2012), with one modification: here we allow the resulting PSF size for each image to be different. Specifically, for each filter and field we choose the size of the resulting PSF to be slightly larger (ca. 10%) than the median gaussian radius of all bright stars in the images. To obtain a stable PSF in the stacked images for each filter we Gaussianise the PSF of the individual astrometrically corrected exposures before stacking.

Following Kuijken (2008) we then measure fluxes in the following way. Instead of using a function where the weight is either 0 or 1, as is the case for regular aperture photometry measured with a top-hat weighting function (e.g. by running `SExtractor` in dual image mode), we use a smooth weight function that makes use of the fact that the S/N for each pixel decreases away from the peak pixel. When the PSF in each filter follows a Gaussian profile, the choice to perform photometry using a Gaussian weight function is computationally convenient, as we show next.

Kuijken (2008) defines the "Gaussian-aperture-and-PSF" flux F_q as the Gaussian weighted flux a source would have if it were observed with a Gaussian PSF with the same width q as the weight function. Hence

$$F_q \equiv \int d\mathbf{r} e^{-r^2/2q^2} \int d\mathbf{r}' S(\mathbf{r}') \frac{e^{-(\mathbf{r}-\mathbf{r}')^2/2q^2}}{2\pi q^2}, \quad (2.3)$$

where S is the intrinsic light distribution of the source (i.e. before smearing with the PSF) and q is the scale radius of the weight function. It is straightforward to simplify Eq. 2.3 to

$$F_q = \int d\mathbf{r} \frac{1}{2} S(\mathbf{r}) e^{-r^2/4q^2}, \quad (2.4)$$

which shows that F_q is a Gaussian-aperture photometric measurement of the *intrinsic* galaxy.

After gaussianising the images, S has already been convolved with a Gaussian that has a constant dispersion g_{PSF} for each stacked image. The flux distribution on the ccd is therefore

$$I(\mathbf{r}) = \int d\mathbf{r}' S(\mathbf{r}') \frac{e^{-(\mathbf{r}-\mathbf{r}')^2/2g_{PSF}^2}}{2\pi g_{PSF}^2}. \quad (2.5)$$

Analytically we have an identical expression for F_q

$$F_q = \int d\mathbf{r}' I(\mathbf{r}') \frac{q^2}{2q^2 - g_{PSF}^2} e^{-(\mathbf{r}-\mathbf{r}')^2/2(2q^2 - g_{PSF}^2)}, \quad (2.6)$$

which thus shows that the same intrinsic aperture flux F_q can be measured from images with a range of Gaussian PSF sizes. Therefore, from our PSF-gaussianised images, we can measure colours of the same intrinsic part of the galaxy if we use Gaussian weight functions to measure fluxes. Note that it is no longer necessary that the stacks of the different filters have a PSF with the same Gaussian FWHM, as long as the weight function is adapted accordingly for each filter.

Table 2.5: The GCLASS photometric data set. The instruments used for the different clusters and filters are indicated. The limiting magnitudes reported are median 5- σ flux measurement limits for point sources measured with a Gaussian weight function.

Name ^a	u_{lim} [mag _{AB}]	g_{lim} [mag _{AB}]	r_{lim} [mag _{AB}]	i_{lim} [mag _{AB}]	z_{lim} [mag _{AB}]	J_{lim} [mag _{AB}]	$K_{s,\text{lim}}$ [mag _{AB}]	$3.6\mu\text{m}_{\text{lim}}$ [mag _{AB}]	$4.5\mu\text{m}_{\text{lim}}$ [mag _{AB}]	$5.8\mu\text{m}_{\text{lim}}$ [mag _{AB}]	$8.0\mu\text{m}_{\text{lim}}$ [mag _{AB}]
SpARCS-0034	23.1 ^b	25.3 ^b	24.4 ^b	24.3 ^b	23.9 ^c	22.5 ^e	22.2 ^e	21.4 ^g	21.2 ^g	19.7 ^g	19.6 ^g
SpARCS-0035	24.4 ^b	25.4 ^b	24.9 ^b	24.3 ^b	23.6 ^c	24.1 ^f	23.4 ^f	22.8 ^g	22.3 ^g	20.8 ^g	20.4 ^g
SpARCS-0036	22.9 ^b	25.1 ^b	24.4 ^b	23.7 ^b	23.5 ^c	22.7 ^e	21.5 ^e	21.2 ^g	21.1 ^g	19.9 ^g	19.6 ^g
SpARCS-0215	24.8 ^a	25.1 ^b	24.7 ^b	24.4 ^b	23.7 ^a	22.8 ^e	22.0 ^e	21.3 ^g	21.1 ^g	19.5 ^g	19.4 ^g
SpARCS-1047	25.5 ^a	25.7 ^a	25.0 ^a	24.7 ^a	23.8 ^a	23.1 ^d	22.3 ^d	21.6 ^g	21.3 ^g	19.7 ^g	19.7 ^g
SpARCS-1051	25.6 ^a	25.8 ^a	25.2 ^a	25.0 ^a	24.0 ^a	23.2 ^d	22.4 ^d	21.7 ^g	21.3 ^g	19.8 ^g	19.7 ^g
SpARCS-1613	25.5 ^a	26.0 ^a	25.4 ^a	24.7 ^a	24.0 ^a	23.1 ^d	22.7 ^d	22.7 ^g	22.6 ^g	21.2 ^g	20.9 ^g
SpARCS-1616	25.1 ^a	25.7 ^a	25.1 ^a	24.8 ^a	23.5 ^a	23.3 ^d	22.7 ^d	22.6 ^g	22.4 ^g	21.2 ^g	20.9 ^g
SpARCS-1634	25.6 ^a	26.1 ^a	25.6 ^a	25.1 ^a	24.4 ^a	23.7 ^d	23.1 ^d	23.2 ^g	23.2 ^g	21.6 ^g	21.3 ^g
SpARCS-1638	25.4 ^a	25.9 ^a	25.4 ^a	25.1 ^a	24.2 ^a	23.4 ^d	22.8 ^d	23.0 ^g	23.1 ^g	21.3 ^g	21.3 ^g

^a MegaCam, Canada-France-Hawaii Telescope (CFHT)

^b IMACS, Magellan Telescope

^c MOSAIC-II, Blanco Telescope, Cerro Tololo Inter-American Observatory (CTIO)

^d WIRCam, Canada-France-Hawaii Telescope (CFHT)

^e ISPI, Blanco Telescope, Cerro Tololo Inter-American Observatory (CTIO)

^f HAWK-I, Very Large Telescope (VLT) UT4

^g IRAC, Spitzer Space Telescope

We adjust q to ensure the aperture roughly matches each galaxy's size, to optimise the S/N. We base our choice for q on the SExtractor parameter FLUX_RADIUS measured in the K_s -band image, such that $q = 0.85 \cdot \text{FLUX_RADIUS}$. The factor of 0.85 is chosen to optimise the S/N of a source with a circular Gaussian PSF-profile. Further we make sure that q is chosen such that $q > g_{PSF}$ in all filters.

This method is applied to measure fluxes in the $u - K_s$ -bands, but since the IRAC data suffer from a much larger PSF we work in a two stage process to incorporate the IRAC fluxes in a way that reduces the problems from confusion. We construct a 2-stage multi-colour catalogue where we multiply the IRAC flux measured in the bigger aperture with the fractional difference of the K_s -band flux measured in the small and bigger aperture. This way we effectively correct the IRAC flux for blending with nearby objects by assuming these neighbours have the same (K_s -IRAC) colour as the source. For contaminating galaxies this is often the case. To verify that any residual blending in the IRAC bands does not affect our results, we repeated the analysis while excluding the IRAC data in all SED fits. We find no bias in the stellar mass estimates, and even for the lowest masses ($M_\star = 10^{10} M_\odot$), 68% of the estimated stellar masses differ by less than 0.05 dex from our fiducial analysis.

We calibrate the photometric zeropoints on a catalogue basis by making use of the universality of the stellar locus (High et al. 2009). We use stellar data from Covey et al. (2007), containing 600,000 point sources selected from the SDSS and 2MASS surveys. By applying linear colour terms we compare these colours to stars measured with the filter sets in the telescope we used. Note that these data are especially favourable to calibrate the zeropoints using the stellar locus since the amount of galactic dust is very low in these fields. We adapt the zeropoints of the $ugrizJK_s$ filters to bring the colours of stars in our data in line with the reference catalogue. Corrections are typically on the order of 0.05 magnitudes. To account for uncertainties in the absolute zeropoint of IRAC, we included a 10% systematic error to the IRAC fluxes.

After gaussianisation, the background noise in the images is correlated between pixels. Therefore we estimate the errors on the flux measurements in the stacks of each filter by measuring the fluctuations in the flux values measured from apertures that are randomly placed on the images. We take account of the non-uniform exposure time over the image stacks. Table 2.5 shows an overview of the median $5\text{-}\sigma$ flux measurements for point sources in each filter and each cluster.

2.B Field SMF measurements from GCLASS

Thanks to the relatively wide areas that were observed to obtain the GCLASS multi-colour catalogues ($15' \times 15'$ centred on the clusters in the Northern sky,

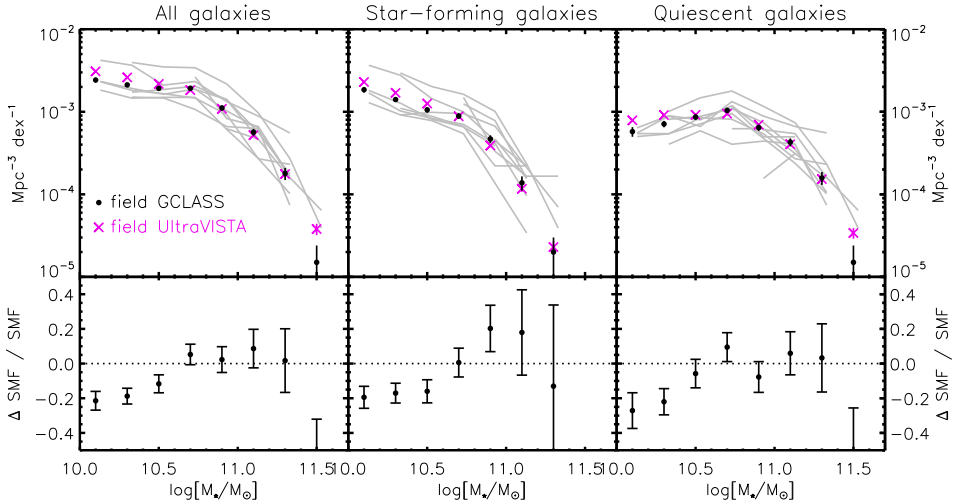


Figure 2.11: The UltraVISTA (magenta) versus GCLASS (black) field measurements. Left panel: the total galaxy population in both fields. Middle panel: the SMF for the subset of star-forming galaxies. Right panel: the subset of quiescent galaxies. Error bars show the 68% confidence regions for Poisson error bars. The grey curves show the 10 contributions to the field SMF around the GCLASS clusters, which differ because of cosmic variance due to the small volumes probed in these individual fields. Also the fields contribute only down to a particular mass respecting the varying depths of the GCLASS fields. Bottom panels: the fractional differences between the two field measurements, given by $\frac{\text{GCLASS} - \text{UltraVISTA}}{\text{UltraVISTA}}$, together with the estimated errors.

and $10' \times 10'$ for the clusters in the Southern sky), these data can also be used to study galaxies outside the clusters and hence to measure the SMF of the general field. In this appendix we measure the field SMF from GCLASS in the redshift range $0.85 < z < 1.20$ and compare this to the field SMF measured from UltraVISTA.

Since the UltraVISTA sample is based on a relatively deep (compared to GCLASS) 30-band photometric catalogue, it is complete in the mass range ($M_* > 10^{10} M_\odot$) at this redshift range. A comparison between GCLASS and UltraVISTA may reveal possible systematic differences in the stellar mass catalogues, and any residual incompleteness in GCLASS.

To minimise the contamination by cluster galaxies in the sample, we use a conservative selection of field galaxies in GCLASS. A galaxy is considered as part of the field when it is separated from the cluster centre by more than the angular distance that corresponds to 1.5 Mpc at the redshift of the cluster. Furthermore we require a field galaxy to have a photometric redshift $|z_{\text{phot}} - z_{\text{cluster}}| > 0.05$. After taking account of the areas masked by bright stars, this results in a total probed volume of the field that is ~ 6 times smaller

in GCLASS compared to UltraVISTA. Since the 10 GCLASS pointings have different depths, we have to take account of the estimated mass-completeness of the detection bands. This is measured similarly as Sect. 2.3.2, but using a redshift limit of 1.20 in each field (instead of the individual cluster redshifts). This way we correct for Malmquist bias in a similar way as in the $1/V_{\max}$ weighting method.

Fig. 2.11 shows a comparison of the field SMF measured in the GCLASS (black) and UltraVISTA (magenta) surveys. The curves are normalised with respect to the total volume subtended by these surveys. The grey curves show the contributions to the field SMF of the 10 individual GCLASS fields. These contributions differ between the pointings because their depths are different, and also the area surrounding the cluster that is part of the field differs. The differences in the grey curves are further caused by cosmic variance. The field in the SpARCS-1047 image for example is significantly overdense in the redshift bin $0.85 < z < 1.20$. Note however that, when these 10 independent sight-lines of GCLASS are combined, the uncertainty due to cosmic variance is greatly reduced (Somerville et al. 2004).

There is generally a good agreement between the field SMF measurements from GCLASS and UltraVISTA, especially at the high-mass end. This indicates that there are no substantial systematic differences between the two catalogues this study is based on. At the low-mass end of the SMF there are some systematic differences in both the star-forming and quiescent population, increasing to several $\sim 10\%$ in the lowest mass bins. In Sect. 2.4.1 we explained that we corrected the GCLASS cluster SMF data by these completeness correction factors. That way we can not only compare the cluster and field qualitatively, but have a more realistic view on the absolute Schechter parameters. Note that this additional completeness correction does not change any of the qualitative statements in this paper, nor affects the conclusions of this paper in any way.

The Phase Space and Stellar Populations of Cluster Galaxies at $z \sim 1$

We investigate the velocity vs. position phase space of $z \sim 1$ cluster galaxies using a set of 424 spectroscopic redshifts in 9 clusters drawn from the GCLASS survey. Dividing the galaxy population into three categories: quiescent, star-forming, and poststarburst, we find that these populations have distinct distributions in phase space. Most striking are the poststarburst galaxies, which are commonly found at small clustercentric radii with high clustercentric velocities, and appear to trace a coherent “ring” in phase space. Using several zoom simulations of clusters we show that the coherent distribution of the poststarbursts can be reasonably well-reproduced using a simple quenching scenario. Specifically, the phase space is best reproduced if satellite quenching occurs on a rapid timescale ($0.1 < \tau_Q < 0.5$ Gyr) after galaxies make their first passage of $R \sim 0.5R_{200}$, a process that takes a total time of ~ 1 Gyr after first infall. The poststarburst phase space is not well-reproduced using long quenching timescales ($\tau_Q > 0.5$), or by quenching galaxies at larger radii ($R \sim R_{200}$). We compare this quenching timescale to the timescale implied by the stellar populations of the poststarburst galaxies and find that the poststarburst spectra are well-fit by a rapid quenching ($\tau_Q = 0.4^{+0.3}_{-0.4}$ Gyr) of a typical star-forming galaxy. The similarity between the quenching timescales derived from these independent indicators is a strong consistency check of the quenching model. Given that the model implies satellite quenching is rapid, and occurs well within R_{200} , this would suggest that ram-pressure stripping of either the hot or cold gas component of galaxies are the most plausible candidates for the physical mechanism. The high cold gas consumption rates at $z \sim 1$ make

it difficult to determine if hot or cold gas stripping is dominant; however, measurements of the redshift evolution of the satellite quenching timescale and location may be capable of distinguishing between the two.

Adam Muzzin, Remco F.J. van der Burg, Sean L. McGee, Michael Balogh, Marijn Franx, Henk Hoekstra, Michael J. Hudson, Allison Noble, Dan S. Taranu, Tracy Webb, Gillian Wilson, H. K. C. Yee
The Astrophysical Journal, submitted

3.1 Introduction

It is well known that galaxies in high-density environments such as galaxy groups and clusters (i.e., satellite galaxies) exhibit a higher fraction of quiescent galaxies at a fixed stellar mass than more isolated “field” galaxies (i.e., central galaxies). This is true both in the local universe (e.g., Baldry et al. 2006; van den Bosch et al. 2008; Peng et al. 2010; Wetzel et al. 2012; Rasmussen et al. 2012; Haines et al. 2013), and at $z \sim 1$ (e.g., Patel et al. 2009; Cooper et al. 2010; Sobral et al. 2011; Muzzin et al. 2012; Raichoor & Andreon 2012; van der Burg et al. 2013; Mok et al. 2013; Woo et al. 2013; Nantais et al. 2013; Kovač et al. 2014). While the correlation between galaxy quiescence and environment is well-established, and heuristic models that can explain the quenching rates and timescales exist (e.g., Peng et al. 2010; Wetzel et al. 2012), at present there is little direct observational evidence linking the satellite quenching mechanism to a specific physical process that occurs in clusters/groups such as ram-pressure stripping of cold gas (e.g., Gunn & Gott 1972) or hot gas (e.g., “strangulation”, Larson et al. 1980; Balogh et al. 1999), mergers, or harassment (e.g., Moore et al. 1996). One way to make further progress in identifying the dominant satellite quenching mechanism will be to better constrain both the timescale over which quenching occurs, and its location within the cluster/group (e.g., Treu et al. 2003; Moran et al. 2007).

Semi-analytic models are physically motivated and recent works have argued that in order to properly reproduce the fraction of quiescent galaxies as a function of clustercentric radius, long quenching timescales, of order 3 - 7 Gyr, are necessary (e.g., Weinmann et al. 2010; McGee et al. 2011; De Lucia et al. 2012). Taken at face value, these long timescales are difficult to reconcile with observations, where a weak dependence of the specific star formation rates (SSFRs) of star-forming galaxies on environment is found (e.g., Kauffmann et al. 2004; Peng et al. 2010; Vulcani et al. 2010; Muzzin et al. 2012; Wetzel et al. 2013). Indeed, the observations suggest a rapid quenching timescale (e.g., Muzzin et al. 2012; Wetzel et al. 2013; Mok et al. 2013, although see Taranu et al. 2012 for evidence of longer timescales), and this hypothesis is supported by an abundance of poststarburst galaxies found in clusters at higher redshifts (e.g., Poggianti et al. 2004; Tran et al. 2007; Poggianti et al. 2009; Balogh et al. 2011; Muzzin et al. 2012; Mok et al. 2013; Wu et al. 2013). Interestingly, hydrodynamical simulations predict much faster quenching timescales than semi-analytic models (e.g., McCarthy et al. 2008; Bahé et al. 2013; Cen 2014), and similar to the observations, they do not see the strong dependence of SSFR on environment. It has been argued by Wetzel et al. (2013) that one way to reconcile the long quenching timescales required by semi-analytic models with the short quenching timescales required by observations is to have a “delayed-then-rapid” quenching, where galaxies experience a $\sim 2 - 4$ Gyr delay after infall into a cluster where they behave as normal star-forming galaxies

before quenching in < 1 Gyr.

While some progress towards defining the timescale of satellite quenching is being made, there are still few observational constraints on where within the cluster/group the process begins, and this is key information for identifying the physical processes involved (e.g., Treu et al. 2003). Our previous work on $z \sim 1$ clusters showed that poststarbursts are more common in the cluster core than in the outskirts (Muzzin et al. 2012); however, most previous studies simply compared the poststarburst fraction between cluster and field. A better way of identifying populations within the cluster is to use the velocity vs. position phase space of clusters (e.g., Biviano et al. 2002; Mahajan et al. 2011; Haines et al. 2013; Oman et al. 2013). Recently Noble et al. (2013) performed such an analysis on the most massive cluster in the GCLASS sample, and showed that this combined space is a more effective way of identifying sub-populations within the cluster than simply using clustercentric radius. In particular, they showed that while properties such as SSFR and $D_n(4000)$ show little dependence on clustercentric radius, once galaxies are separated in phase space there is a dependence of those properties as a function of environment.

In this paper we continue the phase space analysis approach of Noble et al. (2013) using the full GCLASS sample and examine the location of cluster galaxies at $z \sim 1$ in phase space. In particular, we focus on the poststarburst population in order to try and identify the satellite quenching timescale and location at $z \sim 1$. Throughout the paper we assume a cosmology with $H_0 = 70 \text{ km s}^{-1} \text{ Mpc}^{-1}$ and $\Omega_m = 0.3$, $\Omega_\Lambda = 0.7$.

3.2 Dataset

Our analysis is based on a spectroscopic sample of 424 cluster galaxies in 9 clusters at $z \sim 1$ from the GCLASS survey (see Muzzin et al. 2012). The GCLASS clusters were selected from the 42 deg² SpARCS survey (Muzzin et al. 2009; Wilson et al. 2009) using an optical/IR adaptation of the red-sequence method (Gladders & Yee 2000) that is discussed in Muzzin et al. (2008). The clusters have halo masses between $M_{200} \sim (1.0 - 20.0) \times 10^{14} M_\odot$ (van der Burg et al. 2014, G. Wilson et al., in preparation) which have been inferred from the cluster line-of-sight velocity dispersion (σ_v).

We classify each galaxy in the spectroscopic sample as either star-forming, quiescent, or poststarburst¹ using the [OII] emission line and $D_n(4000)$ as diagnostics. Star-forming galaxies are classified as those galaxies with detected [OII] emission, where the detection limit is $\sim 1 - 3\text{\AA}$ equivalent width (EW),

¹In this paper, following convention, we refer to these galaxies as "poststarbursts". In fact, we will show later that these galaxies are well-fit by rapidly-truncated star-formation with no secondary "burst". They could also be considered as "recently quenched" galaxies, but we keep the poststarburst designation for consistency with previous work.

depending on signal-to-noise. Quiescent galaxies are defined as those without detected [OII] emission. Similar to Muzzin et al. (2012), poststarburst galaxies are defined as the subset of quiescent galaxies that have $D_n(4000) < 1.45$ (i.e., those that are quiescent but have young stellar populations). This is somewhat different than the more typical $EW(H_\delta) > 3 - 5\text{\AA}$ definition used for K+A galaxies in many studies (e.g., Dressler et al. 1999; Balogh et al. 1999; Poggianti et al. 2009); however, as discussed in Muzzin et al. (2012), H_δ is a weak line and is difficult to measure consistently in all spectra at $z \sim 1$, and a weak $D_n(4000)$ serves as a good proxy for strong H_δ in galaxies without [OII] emission. The average stacked spectrum of our poststarburst definition does have $EW(H_\delta) > 5\text{\AA}$ (Muzzin et al. 2012, see also § 5), and strong Balmer lines, so on average our selection of poststarbursts is comparable to the K+A selection criteria.

We note that the poststarburst classification may not be 100% complete for all galaxies with strongly truncated star formation. One population that would be missed are old galaxies that experienced a recent rejuvenation of star formation and then a subsequent truncation of that star formation. If the total stellar mass formed in that event was modest, they will have $D_n(4000) > 1.45$ and remained classified as quiescent. It is unclear if such a population exists in clusters at $z \sim 1$; however, if so, then it would be absent from the current sample.

3.3 Galaxies in the Cluster Phase Space

In the left panel of Figure 3.1 we plot the velocity vs. projected clustercentric radius phase space (hereafter referred to simply as “phase space”) for all 9 clusters. The clusters are combined by normalizing each relative to its σ_v and R_{200} (see van der Burg et al. 2014, Table 1).

Figure 3.1 shows that there is a segregation in phase space between quiescent galaxies (red triangles) and star-forming galaxies (blue triangles). Quiescent galaxies are typically found at smaller clustercentric radii, and lower clustercentric velocities; whereas the star-forming population is more extended in both position and velocity. A similar segregation between these types in phase space has also been seen in lower-redshift cluster samples (e.g., Carlberg et al. 1997c; Biviano et al. 2002). What is surprising about Figure 3.1 is the phase space location of the poststarburst galaxies (green stars with circles). Similar to the quiescent galaxies, these tend to lie at smaller clustercentric radii; however, they typically have higher velocities. Most strikingly, these galaxies seem to avoid the “core” region in phase space, where the majority of the quiescent galaxies are located. Indeed, they appear to form roughly a coherent “ring” structure around the core in phase space, although some of the population does extend as far out as $R \sim R_{200}$.

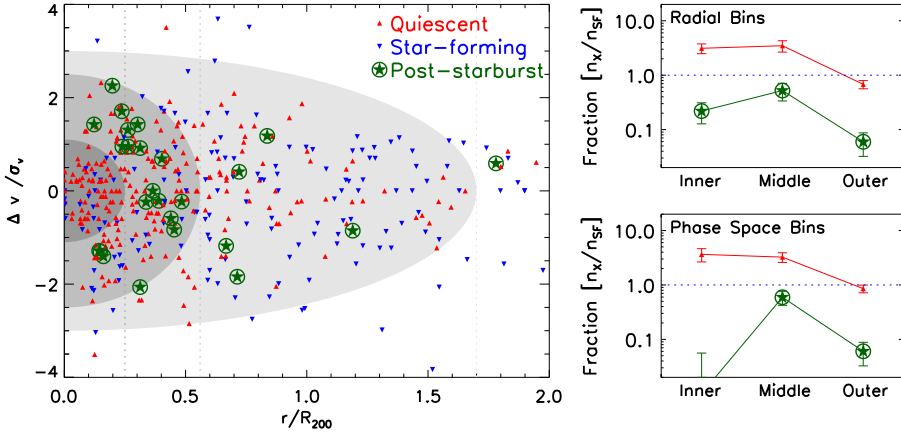


Figure 3.1: Left panel: The velocity vs. clustercentric radius phase space of galaxies in the 9 GCLASS clusters. The velocities are in units relative to the individual cluster velocity dispersions and the radii are relative to the position of the brightest cluster galaxy scaled by the R_{200} of the cluster. The shaded regions are arbitrarily defined but are indicative of increasing time since infall (see text). Quiescent galaxies (red triangles), star forming galaxies (blue triangles) and poststarburst galaxies (green stars) all occupy distinct locations in phase space. Right panels: The ratio of quiescent and poststarburst galaxies compared to star-forming galaxies separated into the three radial bins marked by the dotted lines (top panel), and the three phase space bins marked by the shaded regions (bottom panel). The error bars are 1σ Poisson errors. Poststarburst galaxies are distributed fairly uniformly in the cluster by radius (top panel), with a peak in the middle bin; however, in phase space they are most prevalent in the middle bin and completely absent in the inner bin (bottom panel).

The phase space segregation is illustrated in the top right panel of Figure 3.1, where we plot the number of quiescent and poststarburst galaxies relative to the number of star-forming galaxies in three radial bins (dotted lines in the left panel), and the bottom right panel, where we plot these ratios in three phase space bins (shaded ring-shaped regions in the left panel). The shaded regions in Figure 3.1 have been arbitrarily defined to enhance the contrast of the poststarbursts in phase space; however, they are similar to the variable-slope “chevrons” that have been shown to correlate with the infall histories of galaxies in N-body simulations (see e.g., Mahajan et al. 2011; Taranu et al. 2012; Oman et al. 2013). Within the main region of phase space they are also similar to the “trumpet”-shaped curves of constant $r/R_{200} \times v/\sigma_v$ that have been shown to correlate with infall times by Noble et al. (2013) based on simulated accretion histories from Haines et al. (2012). Therefore, while the precise definition of the phase space regions is arbitrary (i.e., rings, chevrons, or curves), all three are quite similar and correlate with time since infall into the cluster, making them physically-motivated demarcations.

The right panels of Figure 3.1 show that the trend for the fraction of

quiescent galaxies to increase towards the inner bin is roughly the same in both the phase space and radial bins. In radial bins, the fraction of poststarburst galaxies has a peak in the middle bin; however, in phase space bins there are no poststarbursts in the core region, and the majority are confined to the middle phase space bin, with many being at low radii and high velocities.

In order to test if the three populations have distributions in phase space that are different, and that the difference is statistically significant, we perform a 2 dimensional Kolmogorov-Smirnov test of the distribution (hereafter the “2D-KS” test). Comparing the 2 dimensional distribution of poststarbursts to the quiescent and star-forming galaxies we find a P-values of 0.038, and 0.009, respectively. We therefore reject the null hypothesis that they are likely to be drawn from the same distribution at $\sim 2\sigma$ and 3σ , respectively. This demonstrates that the poststarbursts have a distribution that is distinctive compared to the other galaxy types in phase space.

3.4 Simulated Cluster Phase Space

The coherent distribution of the poststarburst galaxies in phase space suggests that it may be possible to use their distribution to constrain the location and timescale of satellite quenching. In this section we use a set of dark-matter-only zoom simulations of clusters to test if the phase-space distribution of the poststarbursts can be described using a simple quenching model.

Our approach is to assume that satellite quenching may begin at a particular clustercentric radius. We then follow the evolution of cluster subhalos in phase space after they make their first crossing of that radius to test if at some time step (hereafter T) later they resemble the phase space of the observed poststarburst galaxies. If so, this timestep would be indicative of the satellite quenching timescale (hereafter τ_Q). For this simple experiment we use three possible clustercentric radii where quenching could begin: the first time a subhalo passes $R = 0.25, 0.5,$ and $1.0 R_{200}$. These radii roughly correspond to first passage of the cluster core, first passage of the dense intra-cluster medium (ICM), and first passage of the virial radius. We follow the galaxies in time steps of $\Delta T = 0.2$ Gyr up to 1.1 Gyr after crossing the quenching location. This time is approximately the longest time that we can expect to detect the poststarburst signature in galaxies (e.g., Balogh et al. 1999; Poggianti et al. 1999).

We stress that while these models are based on cosmological simulations and therefore the orbits and infall rates may be correct, they are extremely simplified toy models for the satellite quenching process. The satellite quenching process is almost certainly more complex, likely with multiple timescales, locations, and even a dependence on galaxy properties such as stellar mass; all of which is neglected in the current analysis. Furthermore, some of the

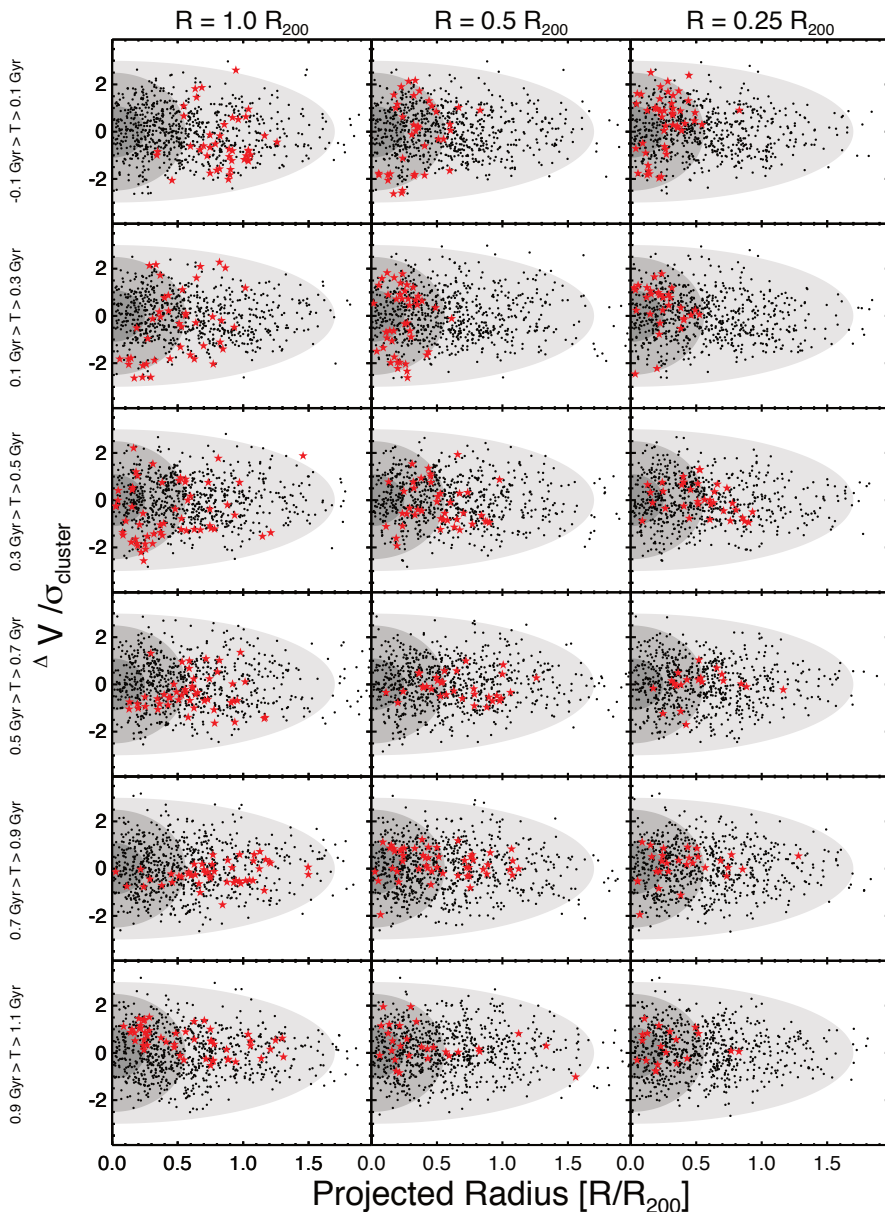


Figure 3.2: The average projected phase space of subhalos in the combined dark-matter-only N-body zoom simulations of four clusters in different time steps. The black points show all subhalos and the red stars in the three columns follow subhalos after they have made their first crossing of $R = 1.0, 0.5,$ and $0.25 R_{200}$. Each row is a timestep of 0.2 Gyr after first crossing of that radius. Similar to the observed poststarbursts (Figure 3.1), a ring structure can be seen in the subhalos for the shortest timesteps ($T < 0.5$ Gyr) after subhalos have crossed the smaller radii ($R < 0.5R_{200}$). This suggests that the quenching timescale for the poststarbursts is likely to be short, and occur in the inner part of the cluster.

poststarbursts found at larger radii are almost certainly falling in to the cluster already quenched in the field, and we have not attempted to account for “pre-quenched” galaxies. The goal of this modeling is not to make a comprehensive descriptive model of phase space and quenching, but simply to test if the coherent distribution of the poststarburst galaxies in phase space can be reproduced at all, and if so, what it may imply for the location and timescale for satellite quenching.

For the models we use a set of N-body zoom simulations of four clusters that were first presented in Taranu et al. (2012). We refer the reader to that paper for a detailed description of the simulations. In brief, the clusters were selected for re-simulation from a larger low-resolution simulation covering $512h^{-1} \text{ Mpc}^3$. Each re-simulation has 12.5 million particles with a mass of $6.16 \times 10^8 M_\odot$, and resolves Milky-Way-like halos with ~ 1000 particles and Magellanic-Cloud-like halos with ~ 30 particles. The simulated clusters have virial masses of $M_{vir} \sim 0.9 - 1.8 \times 10^{15} M_\odot$ at $z = 0$, and therefore are comparable to massive clusters such as Coma. Their masses are a factor of a few smaller at $z \sim 1$, making them an excellent match in halo mass to the GCLASS clusters.

In order to make a fair comparison between the phase space of the models and the observations, a correction for the incompleteness of the spectroscopic sample must be applied. The GCLASS sample has a high spectroscopic completeness overall; however, there is still a spectroscopic targeting bias, with galaxies near the core being targeted more frequently, and more massive galaxies also being targeted more frequently (see Figure 4 of Muzzin et al. 2012, for the spectroscopic completeness corrections). Rather than correct the observations for completeness, we have made the simulations “incomplete” in the same way as the observations, so as to match the observed phase space. For simplicity, the stellar mass in the simulations has been assigned by assuming a uniform stellar-mass-to-halo-mass ratio of 0.1 and the halo mass is the mass of the subhalo before it is accreted.

In Figure 3.2 we plot the projected phase space of all galaxies (black points), as well as those galaxies that first crossed the three quenching radii (the three columns of Figure 3.2) at $T = 0$ (red stars) and follow their evolution through various time steps. We work in projected phase space so to match the observational data. Generally speaking, the marked galaxies in Figure 3.2 follow similar orbital histories. Most are falling directly into the cluster, likely because they are accreted through filaments in this early stage of cluster formation. Once they pass the chosen radius they continue to pick up velocity and make a close passage of the cluster core (i.e., first pericenter). As would be expected, the passage of the cluster core happens earlier for subhalos that we mark at smaller clustercentric radii (~ 0.1 Gyr after crossing $0.25R_{200}$ and ~ 0.4 Gyr after crossing R_{200}). During their first core passage they tend to be found at high projected velocities, and small clustercentric radii. Because of this they are not found in the central “core” region of the cluster phase space at low

velocities and small clustercentric radii where many of the massive quiescent galaxies reside in the observations (e.g., Figure 3.1). Once they make a high velocity crossing of the core they tend to backsplash out to larger radii, as far out as $R \sim R_{200}$. After another ~ 0.5 Gyr they begin to fall back in and appear to be much more mixed in phase space with the rest of the population. In particular, some galaxies manage to penetrate into the low-velocity, small-radius core region in phase space.

We make a quantitative comparison between the red stars in the 18 panels of Figure 3.2 with the poststarbursts in Figure 3.1 using the 2D-KS test. All but four of the snapshots have $P < 0.05$ and hence we can reject the null hypothesis that they are drawn from the same distribution at $\sim 2\sigma$. The four radii/timescales that have $P > 0.05$ and are therefore consistent with being drawn from the same distribution as the poststarbursts are for $R = 0.5R_{200}$ at $T = 0.0$ and 0.4 , and for $R = R_{200}$ at $T = 0.2$ and 0.4 . In both cases a short timescale is favored, and quenching outside the cluster core is favored. Interestingly, there is no long timestep from any radius where the distribution of subhalos resembles the poststarburst distribution. This appears to rule out the possibility of long quenching times ($\tau_Q > 0.5$ Gyr) no matter what the quenching radius. This may have been expected, as the poststarburst distribution appears coherent, and coherent structures will become mixed and eventually washed out in phase space on the order of a dynamical time.

Formally, the quenching radii and timescales listed above are the most representative of the overall distribution of poststarbursts, which extends out to larger radii; however, from examination of Figure 3.2 it appears that the quenching at $R = R_{200}$ panels do not reproduce the inner ring structure of the poststarbursts particularly well. They are likely statistically acceptable distributions because they get the overall radial distribution reasonably correct, not the ring structure. As discussed earlier, some of the poststarburst population at larger radius is likely to have been accreted from the field “pre-quenched”. The poststarburst fraction in the field at this redshift is $\sim 1 - 3\%$, (Yan et al. 2009; Muzzin et al. 2012), which for ~ 400 cluster members implies a maximum of 4 - 12 galaxies may be infalling already quenched. This number is of order the total number of poststarbursts seen at $R > 0.5 R_{200}$ (see Figure 3.1). If the poststarbursts at larger clustercentric radii are pre-quenched, then it may be that the inner ring of poststarbursts is the primary signature of satellite quenching, and is the distribution that should be matched in the simulation.

Given this, we used the 2D-KS test to determine in which timesteps the distribution of subhalos is consistent with the distribution of the poststarburst population using only subhalos and galaxies at $R < 0.5R_{200}$, where the ring structure is strongest. These results are quite different from the overall 2D-KS test. The two timesteps for $R = R_{200}$ that were favored by the full 2D-KS test have much smaller P values when only galaxies at $R < 0.5R_{200}$ are considered ($P = 0.06$ and 0.05), and are rejected at the $\sim 2\sigma$ level. The only timesteps that

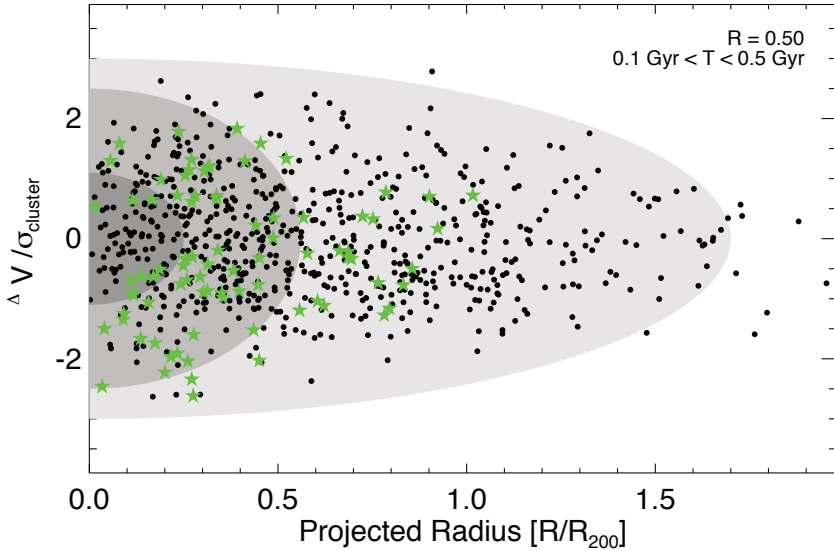


Figure 3.3: The phase space of the simulations with the same phase space contours as in Figure 3.1. Green stars show galaxies that first crossed $R = 0.5R_{200}$ within the last $0.1 < T < 0.5$ Gyr. This is the only quenching timescale and location that passes a 2D-KS test for both in the inner and outer regions and therefore have a distribution that is consistent with having been drawn from the poststarburst distribution in Figure 3.1

are consistent with the observations are for quenching at $R = 0.5R_{200}$ at $T = 0.1, 0.3,$ and $0.5,$ and for $R = 0.25R_{200}$ at $T = 0.1$. The strong ring structure from these panels can also be seen quite clearly by eye in Figure 3.2. The reason some of these are not formally the good descriptions of the data in the full 2D-KS test is simply because they fail to reproduce the few poststarburst galaxies at larger radii that are seen in the observations. Therefore, this may actually make these the most likely candidates for the location and timescale of the dominant satellite quenching process, even though several of them fail to reproduce the full phase space distribution of phase space.

Ignoring this possibility for the moment, and attempting match both the inner ring and the overall distribution of the poststarbursts with a single model, we combined a few of the timescales to produce the best-possible description of the observations. This is shown in Figure 3.3 where we plot the distribution of galaxies quenched at $R = 0.5R_{200}$ on a timescale of $0.1 < T < 0.5$. A 2D-KS test applied to that dataset provides values of $P = 0.358$ and 0.185 for all galaxies, and galaxies at $R < 0.5R_{200}$, respectively, and hence is the only model that has acceptable P-values for both the overall distribution and the

inner ring structure. We therefore adopt it as our best overall model for the location and timescale of satellite quenching.

3.5 SED fitting of Poststarburst Galaxies

The phase space modeling suggests that satellite quenching occurs on a timescale of roughly $0.1 \text{ Gyr} < \tau_Q < 0.5 \text{ Gyr}$ after galaxies make their first passage of $R \sim 0.5R_{200}$. The simulations imply that the median time it takes for an accreted galaxy to travel from $2.0R_{200}$ to $0.5R_{200}$ is $\sim 0.7 \pm 0.2 \text{ Gyr}$, where the uncertainty is the 1σ rms dispersion in infall times. This scenario is qualitatively similar to the “delayed-then-rapid” quenching model proposed by Wetzel et al. (2013), where the quenching time appears to be roughly similar, but the delay time may be a factor of $\sim 2 - 4$ faster at $z \sim 1$. We note that this comparison of delay time is qualitative, because our delay time is inferred since first passage of $2.0R_{200}$, whereas the Wetzel et al. (2013) delay time is measured as the time since a galaxy is identified as a subhalo of a parent halo in an N-body simulation using friends-of-friends linking. It is therefore not immediately clear how these two definitions are related. Although qualitative, it is unlikely that the longer end of the delay time proposed by Wetzel et al. (2013) (e.g., $3 - 4 \text{ Gyr}$) could be supported by the data at $z \sim 1$ for two reasons. Firstly, because the simulations show that almost all subhalos would have already made a passage of $R = 0.5R_{200}$ and hence should be quenched based on our model, and secondly, because this long delay time is approaching the age of the universe at $z = 1$ ($\sim 6 \text{ Gyr}$) which would require clusters to form at very high redshift ($z > 3$).

If the timescales in our phase space model are correct, they place constraints on the ages of the stellar populations of both the poststarburst galaxies and their star-forming progenitors. Poststarburst galaxies should have star formation histories that are consistent with this rapid quenching timescale, and cluster star-forming galaxies should be at least old enough that they have had time to migrate from the cluster outskirts to $R = 0.5R_{200}$ while maintaining active star formation.

In order to test the consistency of the phase space model and the stellar populations of the galaxies, we fit the spectra of both the star-forming galaxies and the poststarbursts, with the assumption that the cluster star forming galaxies are the progenitor population of the poststarburst population. Our methodology is as follows: we fit the age of the star-forming galaxies to define the initial age of the poststarburst galaxies once quenching began, defined as t_1 . We then fit the poststarburst spectrum starting from this age and fit for two parameters, τ_Q , the timescale over which quenching occurred, and t_2 , the age of the galaxy since it was fully quenched. This fiducial star-formation history (SFH) is illustrated in the bottom left panel of Figure 3.4, and is, again,

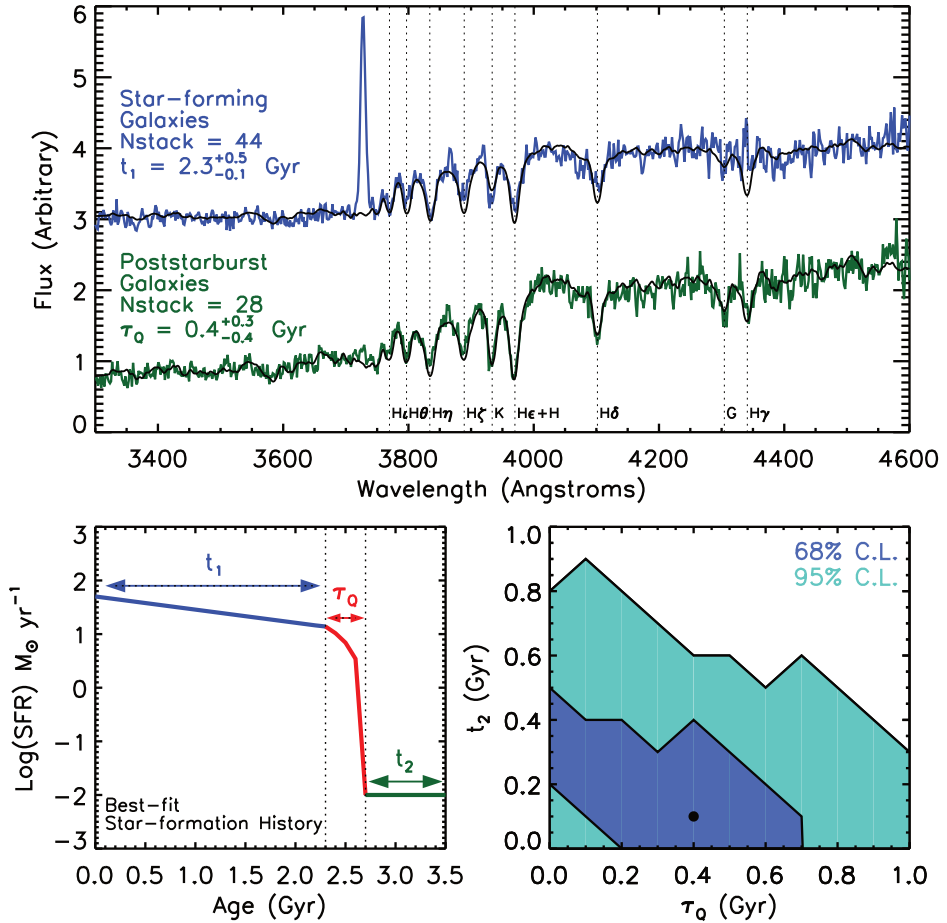


Figure 3.4: Top panel: Mean stacked spectrum of star-forming (blue) and poststarburst (green) galaxies in the GCLASS clusters with prominent absorption features labelled. The overlaid black spectra show the best-fit Bruzual & Charlot (2003) spectrum for these types assuming the star-formation history in the lower left panel. The most constraining feature in the star-forming spectrum is the Calcium K line, which implies the population is somewhat evolved. The most constraining features in the poststarburst spectrum are Calcium K and the G-band which also imply a more evolved population, but also the deep H δ absorption which implies a recent end to the star-formation. Bottom left panel: The best-fit star formation history assuming the poststarburst galaxies are descendants of the star-forming galaxies and undergo a quenching process. Bottom right panel: Confidence intervals on the quenching timescale (τ_Q) and time since star formation ended (t_2). These timescales are consistent with those derived from the phase space analysis.

schematically similar to the “delayed-then-rapid” SFH proposed by (Wetzel et al. 2013, see their Figure 12)

We begin by stacking the spectra of all star-forming galaxies (details of the stacking process are discussed in Muzzin et al. 2012), with an additional cut requiring that $D_n(4000) < 1.45$. There are relatively few star-forming galaxies with $D_n(4000) > 1.45$; however, given that this cut is a requirement for the poststarburst selection, it is impossible that star forming galaxies with $D_n(4000) > 1.45$ can be the progenitors of the poststarburst population. The top panel of Figure 3.4 shows the mean stacked spectrum of the star-forming galaxies with prominent absorption features labelled.

To fit the spectrum we employ the high-resolution models from Bruzual & Charlot (2003) assuming solar metallicity, a Calzetti et al. (2000) dust law ($A_v = 0 - 4$), and a Chabrier (2003) IMF. We degrade the spectral resolution of the models to match that of the data which is 17\AA in the observed frame, and corresponds to $\sim 9\text{\AA}$ rest-frame). We assume a declining SFH based on the decline of the global star-formation rate (SFR) from $z = 3$ to $z = 0$ compiled by Bouwens et al. (2012). We also tried a SFH with a constant SFR; however, this continued high level of star formation cannot reproduce the strength of the Calcium K absorption line in the star-forming galaxies even at old ages and therefore some form of a declining SFH is required. The Bruzual & Charlot (2003) models do not contain emission lines, so the [OII] emission line is not fit by the model.

The black solid line in Figure 3.4 shows the best-fit model to the star-forming population which has a time since star-formation began of $t_1 = 2.3_{-0.1}^{+0.5}$ Gyr. This implies a mass-weighted age of the stellar population of $1.5_{-0.1}^{+0.2}$ Gyr. The strongest constraint on the age comes from the relatively strong Calcium K line, which cannot be reproduced by a very young stellar population. This intermediate-age population is old enough that it would be continuously forming stars over the infall time from $R = 2.0R_{200}$ to $R = 0.5R_{200}$, and therefore is consistent with the delay time implied by the simulation.

To fit the poststarburst population, we create a set of new model grids with the same range of ages and dust extinctions as the declining SFH of the star-forming galaxies. We then add a linear quenching of star formation at $t_1 = 2.3$ Gyr, and create 11 new grids with τ_Q ranging from 0 - 1.0 Gyr in steps of 0.1 Gyr, where τ_Q is the time between when star formation starts to decline and $\text{SFR} = 0$ (see Figure 3.4). We then fit the poststarburst spectrum to each of these grids and fit for t_2 (the time since $\text{SFR} = 0$) and A_v . We then find the minimum χ^2 across the 11 grids which gives us a best fit τ_Q , t_2 , and A_v .

The best fit model for the SFH of the poststarbursts ($t_1 = 2.3_{-0.1}^{+0.5}$ Gyr, $\tau_Q = 0.4_{-0.4}^{+0.3}$ Gyr, $t_2 = 0.1_{-0.1}^{+0.4}$ Gyr) is plotted in Figure 3.4 as the black model on top of the green spectrum. The best fit reproduces the line strengths of the Calcium K line, the G-band, and H_δ impressively well. This is remarkable in the sense that Calcium K and the G-band are typical of older stellar

populations, whereas strong H_δ is from recently-quenched galaxies. It would be difficult to reproduce such a spectrum with any form of a SFH other than that in Figure 3.4.

Remarkably, the implied SFH, τ_Q , and best-fit ages of the stellar populations inferred from the spectral fitting are consistent with the timescales implied by the phase space modeling. It is possible that the SFH and ages could be fit by a wider range of models which we have not explored in exhaustive detail; however, the consistency between the two with basic modeling is encouraging. It is particularly encouraging considering that the stellar population measurements of the satellite quenching timescale are completely independent of the velocities and positions of the galaxies within the cluster.

3.6 Discussion

The overall picture of satellite quenching that arises from the modeling is that star-forming galaxies at $z \sim 1$ are not immediately quenched once they are accreted by a cluster/group. Instead, they evolve as normal star-forming galaxies as they fall into the central regions of the cluster. Based on the N-body simulation, it takes ~ 0.7 Gyr for a galaxy to first cross $R \sim 0.5R_{200}$, and this is where satellite quenching begins. Once the satellite quenching process starts, it proceeds on a short timescale $0.1 < \tau_Q < 0.5$ Gyr. Moreover, not only is the quenching timescale short, but most of the observed poststarbursts are consistent with having their star formation fully ended only recently. This observation of most poststarbursts having been recently quenched is not a selection effect, as our selection criteria for the poststarbursts of $D_n(4000) < 1.45$ and $[OII] < 3\text{\AA}$ could select galaxies as old as $\sim 1.0 - 1.5$ Gyr, depending on the τ_Q .

This scenario and the inferred timescales are remarkably similar to that presented by Smith et al. (2010b) for the Coma cluster. They found that galaxies with asymmetric UV morphologies were concentrated within the central 500 kpc (i.e., $R \sim 0.25 R_{200}$) of the Coma cluster. With numerical modeling they showed that this population could be explained if they were quenched at $R \sim 1$ Mpc (i.e., $R \sim 0.5 R_{200}$) and they were viewable for ~ 0.5 Gyr after quenching began. This quenching location and timescale are nearly identical to that derived from the phase space analysis at $z \sim 1$.

Our inferred timescale is also consistent with the quenching timescale at $z \sim 1$ proposed by Mok et al. (2013) based on their analysis of the fraction of red, blue, and “green” galaxies in groups. They showed that in order to properly reproduce the fractions of these galaxy types, delay times before quenching begins of < 2 Gyr were required along with a $\tau_Q < 1$ Gyr. Our quenching timescale is also similar to the quenching timescale proposed by Wetzel et al.

(2013) at $z = 0$ ($\tau_Q = 0.2 - 0.8$ Gyr); however, it appears that the delay time before quenching may be a factor of 2 – 4 longer at $z = 0$.

One potential issue with the proposed scenario for satellite quenching is that we have pre-selected only poststarburst galaxies as our tracer of the quenched/ quenching population. If there are galaxies that quench on very long timescales, they will have been omitted from this analysis. While we cannot formally rule this out, we note that a significant number of studies have shown that the SSFR of star-forming galaxies has little dependence on clustercentric radius at both high and low redshift (e.g., Patel et al. 2009; Vulcani et al. 2010; Muzzin et al. 2012; Wetzel et al. 2013). Although this does not rule out some population of slow quenching satellite galaxies, it strongly suggests that slow quenching cannot be the dominant type of quenching for satellites.

It is remarkable that the quenching timescales determined from four independent methods (Smith et al. 2010b; Wetzel et al. 2013; Mok et al. 2013, and the current phase space analysis) are consistent. The phase space constraints are particularly useful because they also provide an additional constraint on where within the cluster/group the satellite quenching begins. With both an inferred location and timescale, we can attempt to infer the physical process that may be responsible.

We first consider the location within the cluster where quenching begins. As derived by Treu et al. (2003) and Moran et al. (2007), quenching from mergers or high-speed galaxy interactions (“harassment”) occurs preferentially at $R > R_{200}$, which is inconsistent with our derived quenching radius. Likewise, tidal processes such as halo stripping or disruption occur close to the cluster core ($R < 0.25 R_{200}$), and also seem inconsistent with our data, where the implied quenching radius is $R \sim 0.5R_{200}$. Hot halo gas stripping (“strangulation”) and cold gas stripping (“ram-pressure”) are most effective where the ICM is dense, at roughly $R < 2.0R_{200}$ and $R < 0.5R_{200}$, respectively (e.g., Bahé et al. 2013). Based on the location where we expect quenching to occur, these appear to be the best candidates for the physical process.

If the timescale for quenching is considered at face value, it would suggest that complete removal of the galaxy cold gas via ram-pressure stripping will be necessary to quench galaxies so rapidly. However, Carilli & Walter (2013) have compiled the latest measurements of gas fractions (i.e., $f_{gas} = M_{gas}/(M_{gas}+M_{star})$) of galaxies at $z \sim 1$ and these are of order 0.3. Our measurements of the SSFRs of galaxies in the GCLASS sample (see Muzzin et al. 2012) show that galaxies with stellar masses of a few times $10^{10} M_{\odot}$ (the typical stellar mass of the poststarburst galaxies) have $\text{Log}(\text{SSFRs}) \sim -8.8$, which implies that if they were cut off from their hot gas supply completely, they would consume their cold gas in ~ 0.5 Gyr. This is consistent with the long end of quenching timescale that we derive; and therefore it means that we cannot formally rule out hot gas stripping as a plausible mechanism for quenching the poststarbursts in the cluster.

It is also worth considering that the cold gas consumption timescales tend to evolve to longer values at lower redshift. This is simply because SSFRs decline faster than f_{gas} with decreasing redshift (e.g., Carilli & Walter 2013). This evolution of the cold gas consumption timescale is fairly weak (evolving from ~ 0.5 Gyr at $z \sim 1$, to ~ 1 Gyr at $z \sim 0$); however, it is potentially measurable. If cold gas stripping (i.e., ram-pressure) is the dominant satellite quenching process, we might expect that the satellite quenching timescale may not evolve with redshift. However, if hot gas stripping dominates then the evolution of the cold gas consumption timescale would suggest that the satellite quenching timescale may also evolve to longer values at lower redshift. Therefore, measuring the redshift evolution of the satellite quenching timescale may be a useful approach for identifying whether hot or cold gas stripping is the dominant physical process for satellite quenching. Interestingly, lower redshift studies such as Wetzel et al. (2013) seem to suggest slightly longer quenching timescales ($\tau_Q = 0.2 - 0.8$ Gyr), although this has significant overlap with the timescale derived at $z \sim 1$ ($\tau_Q = 0.1 - 0.5$ Gyr). If this could be shown to be statistically significant, then it would imply that hot gas stripping is likely the most important satellite quenching process. However, given the large uncertainties at present this clearly requires more detailed investigation. It would also benefit from a comparison of timescales measured using similar techniques to avoid systematic errors.

3.7 Summary and Outlook

In this paper we have shown that the population of poststarburst galaxies in clusters at $z \sim 1$ has a distribution in phase space that is distinctive from both the quiescent and star-forming cluster galaxy populations. Using a set of dark-matter-only zoom simulations of clusters we showed that this distribution can be recovered if galaxies quench on a rapid timescale ($0.1 < \tau_Q < 0.5$ Gyr) after first passage of $R \sim 0.5R_{200}$. The simulations also show that longer quenching timescales ($\tau_Q > 0.5$ Gyr), or quenching at $R \sim R_{200}$ provide poor descriptions of the poststarburst phase space distribution. Fitting of the stacked spectra of the star-forming and poststarburst galaxies shows that the SFH, τ_Q , and ages of their stellar populations are consistent with the timescales derived from the phase space analysis, and the similarity between these independent indicators provides the strongest consistency check of the overall model.

The derived quenching location and timescale suggest that gas stripping processes are most likely responsible for quenching the satellite population; however, the current constraints are not strong enough to distinguish between hot or cold gas stripping as the dominant quenching mechanism. Measurement of the evolution of the quenching timescale and possibly the location could be extremely valuable for determining the dominant physical process. Cluster

samples with high-quality spectroscopic data exist at lower redshift, and so this is a tractable problem for the future.

An additional conclusion of this work is that the approach of using phase space and simulations to constrain the location and timescale of satellite quenching seems to be a promising new way forward on this problem (see also Noble et al. 2013). We note that better constraints at $z \sim 1$ using this approach could be made with larger samples of spectroscopic cluster members. The results of most of the 2D-KS tests in this work provide constraints on the timescales at the $\sim 2\sigma$ level, with the limitation being the total number of poststarbursts in the sample (only 28 galaxies out of 424 cluster members). Increasing the number of spectra of poststarbursts by a factor of a few would allow constraints at $\sim 3\sigma$ level or better, which would be useful for further refining the quenching model. Also, more detailed modeling of the infalling process that includes tracking self-quenching of the infalling field population would be useful for understanding the population of poststarbursts are larger radii and putting tighter constraints on the quenching timescale. This will be addressed in future papers.

Acknowledgements

We acknowledge the work of Chris Power and Brad Krane in developing the N-body simulations used in this analysis. AM and MF acknowledge support from an NWO Spinoza grant. RFJvdB and HH acknowledge support from the Netherlands Organisation for Scientific Research grant number 639.042.814. MLB acknowledges support from an NSERC Discovery Grant, and from NOVA and NWO visitor grants that supported his sabbatical at Leiden Observatory, where this work was completed. MJH acknowledges support from an NSERC Discovery Grant.

A Census of Stellar Mass in 10 Massive Haloes at $z \sim 1$ from the GCLASS Survey

We study the stellar mass content of massive haloes in the redshift range $0.86 < z < 1.34$, by measuring (1) the stellar mass in the central galaxy versus total dynamical halo mass, (2) the total stellar mass (including satellites) versus total halo mass, and (3) the radial stellar mass and number density profiles for the ensemble halo. We use a K_s -band selected catalogue for the 10 clusters in the Gemini Cluster Astrophysics Spectroscopic Survey (GCLASS), with photometric redshifts and stellar masses measured from 11-band SED fitting. Combining the photometric catalogues with the deep spectroscopic component of GCLASS, we correct the cluster galaxy sample for interlopers. We also perform a dynamical analysis of the cluster galaxies to estimate the halo mass M_{200} for each cluster based on a measurement of its velocity dispersion. (1) We find that the central galaxy stellar mass fraction decreases with total halo mass and that this is in reasonable, quantitative agreement with measurements from abundance matching studies at $z \sim 1$. (2) The total stellar mass fractions of these systems decrease with halo mass, indicating that lower mass systems are more efficient at transforming baryons into stars. We find the total stellar mass to be a good proxy for total halo mass, with a small intrinsic scatter. When we compare these results from GCLASS with literature measurements, we find that the stellar mass fraction at fixed halo mass shows no significant evolution in the range $0 < z < 1$. (3) We measure a relatively high NFW concentration parameter $c_g \sim 7$ for the stellar mass distribution in these clusters, and debate a possible scenario for explaining the evolution of the stellar mass distribution

from the GCLASS sample to their likely descendants at lower redshift. The stellar mass measurements in the $z \sim 1$ haloes provided by GCLASS puts constraints on the stellar mass assembly history of clusters observed in the local Universe. A simple model shows that the stellar mass content of GCLASS can evolve in typical distributions observed at lower redshifts if the clusters primarily accrete stellar mass onto the outskirts.

Remco F.J. van der Burg, Adam Muzzin, Henk Hoekstra, Gillian Wilson, Chris
Lidman, H.K.C. Yee
Astronomy & Astrophysics, **Volume 561**, A79 (2014)

4.1 Introduction

One of the main objectives in the field of extragalactic astronomy is to understand the connection between galaxies and the distribution of the underlying dark matter. The growth of dark matter structures has been studied in large N-body simulations (e.g. Springel et al. 2005; Boylan-Kolchin et al. 2009; Navarro et al. 2010). From these simulations, the density profiles of collapsed structures have been found to be well represented by NFW-profiles (Navarro et al. 1997). These profiles are described by two parameters: the halo mass and the halo concentration parameter. The dependence of the concentration parameter c on the halo mass, formation time and redshift has been studied with N-body simulations (e.g. Wechsler et al. 2002; Neto et al. 2007; Duffy et al. 2008; Gao et al. 2008). These have shown that c , for the dark matter, is higher for lower mass haloes, higher for haloes that collapse early, and higher for haloes at lower redshift.

How baryons affect the distribution of the dark matter is still under debate (Dolag et al. 2009; van Daalen et al. 2011; Newman et al. 2013). Baryons in the gas phase can cool and form stars at the bottom of the potential wells in the dark matter (sub-)haloes. The efficiency with which this happens depends on the properties of the halo (see e.g. Kravtsov & Borgani 2012; Planelles et al. 2013). To constrain the physics behind these processes, there are a number of key observables that can be exploited. In this paper we concentrate on three of these, which we introduce in turn below, and measure at $z \sim 1$ for a sample of ten cluster sized haloes.

First, to constrain the build up of stellar mass in central galaxies, we measure the stellar mass present in the central galaxies of GCLASS and compare it to direct measurements of their total halo masses. Behroozi et al. (2013) estimate the stellar mass in central galaxies versus total halo mass over a range of redshifts and halo masses in a *statistical* way using the abundance matching technique. In this technique observables, such as the stellar mass function and cosmic star formation history, are combined with merger trees from dark matter simulations to provide constraints on the processes that build up the stellar mass in central galaxies. The stellar content of central galaxies, or brightest cluster galaxies (BCGs) in the case of clusters, can grow by star formation in the galaxy itself or by merging with other galaxies. Given the significant growth of stellar mass in BCGs as a function of redshift (Lin & Mohr 2004; Lidman et al. 2012), this build-up is likely to occur through mainly dry mergers. However, the mass assembly has been shown (Lidman et al. 2012) to increase more slowly than is expected from semi-analytic models (De Lucia & Blaizot 2007), but in good agreement with more recent simulations (Laporte et al. 2013). Since the main halo also accretes matter while the central galaxy is building up its stellar content, studies have focussed on the relationship between those processes. The Behroozi et al. (2013) estimates at $z = 1.0$ cover a

range of halo masses from $10^{11.3} < M_h/M_\odot < 10^{14.2}$, and are consistent with predictions from other abundance matching analyses (e.g. Moster et al. 2010, 2013). In general the highest central stellar mass fraction is found in haloes of around $10^{12} M_\odot$. By combining *direct* measurements of total mass and stellar mass in the same haloes, we test the results from abundance matching studies at $z \sim 1$.

Second, a key measurement for understanding the interplay between the growth of large scale structure and the formation and accretion of galaxies is to compare the total stellar mass as a function of halo mass. For a sample of groups selected at $0.1 < z < 1.0$ from COSMOS, Giodini et al. (2009) show that their stellar mass fraction is a decreasing function of halo mass. Similar results are found by Gonzalez et al. (2007, 2013), Andreon (2010) and Hilton et al. (2013) for samples of clusters around $z = 0.1$, $z < 0.1$ and $z = 0.5$, respectively. Given that the most massive haloes are expected to grow by accreting lower mass systems, which have a higher stellar mass fraction, one would naively expect the stellar mass fraction of massive haloes to grow with cosmic time, even in the absence of in situ star-formation processes. Consequently, measurements on the stellar mass fraction in these haloes are used to constrain the progenitor population that form the building blocks of these haloes (Balogh et al. 2008; McGee et al. 2009). Due to the major caveats in comparing measurements from different studies with inhomogeneous data and different analyses, the relation itself is hard to constrain observationally (Leauthaud et al. 2012a; Budzynski et al. 2013). So far little evolution with redshift has been found (Giodini et al. 2009; Lin et al. 2012).

Third, the spatial distribution of the stellar mass component of satellites within the main halo is intimately related to accretion processes, and eventually the growth of the central galaxy. While the sub-haloes in pure gravitational N-body simulations get destroyed by tidal disruptions, the galaxies that have formed inside of them are more resistive to those forces (e.g. Budzynski et al. 2012). The NIR luminosity and number density profiles are found to be described by NFW profiles for group-sized haloes (e.g. Giodini et al. 2009; Tal et al. 2013), and clusters (e.g. Carlberg et al. 1997b; Lin et al. 2004; Muzzin et al. 2007). Budzynski et al. (2012) measured the radial distribution of galaxies from the SDSS around Luminous Red Galaxies in a redshift range $0.15 < z < 0.4$, and found that this distribution is also well described by an NFW profile. However, they found that the concentration parameter c is lower for the galaxies than for the underlying dark matter. They found that the concentration is independent of mass, but that there is a hint of a mild dependence of the stellar mass concentration on redshift. A comparison of the radial stellar mass density distribution of clusters over a range of redshifts, linking high- z systems to their likely descendants, yields insights in the evolution of the galaxy distribution. In this study we will extend the redshift baseline of these comparisons towards $z = 1$.

We perform the aforementioned key measurements in an unexplored combination of redshift and halo mass range using the GCLASS survey, which contains deep 11-band photometry and spectroscopy for 10 rich clusters at $0.86 < z < 1.34$. This paper builds further on the results presented in several papers on the GCLASS sample. Muzzin et al. (2012, hereafter M12) present the spectroscopic sample, which is critical in this study to correct the photometrically selected galaxies by cluster membership. van der Burg et al. (2013, hereafter vdB13) measure the stellar masses of the galaxies in the sample and present their stellar mass function (SMF). We will use the stellar masses estimated in this work for the current study. Lidman et al. (2012) identifies and studies the BCGs of GCLASS clusters as part of their analysis on the central galaxy stellar mass growth. The total GCLASS halo masses are estimated based on the velocity dispersions estimated in Wilson et al. (in prep.). To describe the masses of the clusters, we will use R_{200} and M_{200} , which are defined as the radius at which the mean interior density is 200 times the critical density of the Universe, and the mass enclosed within this radius, respectively.

The structure of this paper is as follows. In Sect. 4.2 we present the GCLASS cluster sample, the available photometric and spectroscopic data, and give the results from a dynamical analysis to estimate the total halo masses. We also show how we obtain photometric redshifts and stellar mass estimates by summarizing the analysis from vdB13. We further show how the spectroscopic data are used to correct the full photometric catalogue for cluster membership. In Sect. 4.3 we compare the stellar mass in the central galaxies with their halo masses. In Sect. 4.4 we present results on the total stellar mass versus halo mass relation of the clusters. In Sect. 4.5 we show how the galaxies are distributed radially and compare this to the expected dark matter profiles for these systems. Further, we discuss a possible evolutionary model to connect the $z \sim 1$ measurements to their likely descendants at lower redshift. In each section we compare the results with the literature and discuss how they are affected by possible systematics. We summarise and conclude in Sect. 4.6.

All magnitudes we quote are in the AB magnitudes system and we adopt Λ CDM cosmology with $\Omega_m = 0.3$, $\Omega_\Lambda = 0.7$ and $H_0 = 70 \text{ km s}^{-1} \text{ Mpc}^{-1}$. For stellar mass estimates we assume the Initial Mass Function (IMF) from Chabrier (2003).

4.2 GCLASS Data & Analysis

The GCLASS cluster sample consists of 10 rich clusters in the redshift range $0.86 < z < 1.34$ selected with the red-sequence selection method (Gladders & Yee 2000) using the $z' - 3.6\mu\text{m}$ colour from the 42 square degree SpARCS survey (Muzzin et al. 2009; Wilson et al. 2009). These 10 clusters, which are amongst the richest at $z \sim 1$ in this survey area, are described in M12, and can

Table 4.1: The 10 GCLASS clusters selected from SpARCS that form the basis of this study, with their dynamical properties.

Name ^a	z_{spec}	RA ^b J2000	DEC ^b J2000	σ_v^c [km/s]	M_{200}^d [$10^{14} M_{\odot}$]	R_{200}^d [Mpc]	Spec- z Members
SpARCS-0034	0.867	00:34:42.06	-43:07:53.41	700^{+90}_{-150}	$2.4^{+1.0}_{-1.2}$	$0.9^{+0.1}_{-0.2}$	45
SpARCS-0035	1.335	00:35:49.70	-43:12:24.20	780^{+80}_{-120}	$2.5^{+0.9}_{-1.0}$	$0.8^{+0.1}_{-0.1}$	20
SpARCS-0036	0.869	00:36:45.03	-44:10:49.91	750^{+80}_{-90}	$2.9^{+1.0}_{-0.9}$	$1.0^{+0.1}_{-0.1}$	47
SpARCS-0215	1.004	02:15:24.00	-03:43:32.15	640^{+120}_{-130}	$1.7^{+1.1}_{-0.8}$	$0.8^{+0.2}_{-0.2}$	48
SpARCS-1047	0.956	10:47:33.43	57:41:13.30	660^{+70}_{-120}	$1.9^{+0.7}_{-0.9}$	$0.8^{+0.1}_{-0.2}$	31
SpARCS-1051	1.035	10:51:11.21	58:18:03.17	500^{+40}_{-100}	$0.8^{+0.2}_{-0.4}$	$0.6^{+0.1}_{-0.1}$	34
SpARCS-1613	0.871	16:13:14.63	56:49:29.95	1350^{+100}_{-100}	$16.9^{+4.0}_{-3.5}$	$1.8^{+0.1}_{-0.1}$	92
SpARCS-1616	1.156	16:16:41.32	55:45:12.44	680^{+80}_{-110}	$1.9^{+0.7}_{-0.8}$	$0.8^{+0.1}_{-0.1}$	46
SpARCS-1634	1.177	16:34:38.22	40:20:58.36	790^{+60}_{-110}	$2.9^{+0.7}_{-1.0}$	$0.9^{+0.1}_{-0.1}$	50
SpARCS-1638	1.196	16:38:51.64	40:38:42.91	480^{+50}_{-100}	$0.6^{+0.2}_{-0.3}$	$0.5^{+0.1}_{-0.1}$	44

^a For full names we refer to Muzzin et al. (2012).

^b Coordinates of the BCGs, as identified by Lidman et al. (2012).

^c Velocity dispersions estimated by Wilson et al., in prep.

^d Dynamical properties estimated using the relation between σ_v and M_{200} from Evrard et al. (2008).

be considered as a fair representation of IR-selected rich clusters within this redshift range. It is always a question how representative a cluster sample is of the full distribution of massive haloes, as it is impossible to select a sample based on halo mass. Each selection method has potential biases, whether it is X-ray selected, SZ-selected or galaxy-selected. However, especially at the high-mass end of the distribution, these selection methods are unlikely to cause significant biases in favour of particular types of galaxy clusters. Specifically, as e.g. Blakeslee et al. (2003) and Mullis et al. (2005) show, X-ray and SZ-selected clusters also show significant over-densities of red-sequence galaxies. We will discuss a possible selection bias further in Sect. 4.5.1. An overview of the GCLASS sample is given in Table 4.1.

The BCGs of these clusters have been identified and studied in Lidman et al. (2012). In general the identification of the BCGs is straightforward, being the brightest cluster member in the K_s -band, and we will use the same identification as done in Lidman et al. (2012). In the cases of SpARCS-1051 and SpARCS-1634, Lidman et al. (2012) found that the BCGs are off-set from the approximate cluster centre by about 250kpc (projected).

The photometric data set consists of imaging in $ugrizJK_s$ and 4 IRAC channels for each cluster. For details on the data reduction, and a description of the catalogue, we refer to vdB13. In summary, the catalogues contain ob-

jects detected in the K_s -band, with Gaussian-weighted aperture fluxes in 11 filters to constrain the SEDs of the objects, and to separate stars from galaxies by combining their $u - J$ and $J - K$ colours. The depth of the images, and therefore the completeness of the catalogues, differs slightly from cluster to cluster. The median photometric completeness limit (80%), in terms of stellar mass, is $10^{10.16} M_\odot$ for the 10 clusters in the GCLASS sample.

Each cluster has substantial spectroscopic coverage provided by the GMOS instruments on Gemini North and Gemini South. The targets for spectroscopic follow-up were prioritized by their $3.6\mu\text{m}$ flux and their projected cluster-centric distance, as explained in M12. The membership of the massive galaxies that constitute most of the stellar mass in the clusters are thus confirmed spectroscopically. Since the targeting completeness is well understood, we can use the sub-sample for which we have spectra to statistically correct the full catalogue for cluster membership. How this is done is outlined in vdB13 (Sect. 3.4), and expanded on in Sect. 4.2.3.

4.2.1 Total halo masses

Using the sample of spectroscopically identified cluster galaxies, totalling 457 members for 10 clusters, we perform a dynamical analysis to estimate masses for each cluster. From the line-of-sight velocity distributions, which show approximately Gaussian profiles, the velocity dispersions are measured (Wilson et al., in prep.) using standard methods such as the shifting gapper and the bi-weight estimator (Beers et al. 1990; Girardi et al. 1993; Fadda et al. 1996), see Table 4.1. Since we do not measure the velocity dispersion from dark matter particles but from subhaloes (or galaxies), several dynamical effects render this an imperfect tracer of the gravitational potential (e.g. Saro et al. 2013). In an attempt to take account of these biases (which also depend on the spectroscopic target selection), various scalings between the velocity dispersion and halo mass (M_{200}) have been proposed in the literature (e.g. Carlberg et al. 1997a; Evrard et al. 2008; Munari et al. 2013). These are of the form

$$\sigma_{1D} = A_{1D} \left[\frac{h(z) M_{200}}{10^{15} M_\odot} \right]^\alpha \text{ km s}^{-1}, \quad (4.1)$$

where A_{1D} and α are parameters that are different for each study (Fig. 4.1).

In order to determine which scaling relation gives the best halo mass estimate for the measured velocity dispersions in GCLASS, we consider a sample of clusters which were originally studied as part of the Canadian Network for Observational Cosmology (CNOC, Yee et al. 1996). A weak-lensing study has been performed for these systems, which provides for independent mass estimates (Hoekstra 2007; Hoekstra et al. 2012, revised in Hoekstra et al., in prep.). For 13 of the clusters in this sample, velocity dispersions have been

measured from spectroscopic targets that were chosen in a similar way as the targets selected in the GCLASS sample (Borgani et al. 1999; Girardi & Mezzetti 2001). Fig. 4.1 compares the weak-lensing masses (M_{200}) to the line-of-sight cluster velocity dispersions. We fit a linear relation in this logarithmic plane, while fixing the slope to $\alpha = \frac{1}{3}$, and allow for the presence of intrinsic scatter in the fit. The black line shows the best-fitting scaling relation to the data points ($A_{1D} = 972_{-52}^{+60} \text{ km s}^{-1}$), and we find a significant amount of intrinsic scatter around this relation ($\log(\sigma_{\sigma_v|h(z) \cdot M_{200}}) = 0.07_{-0.02}^{+0.03} \text{ dex}$).

The best-fitting scaling relation is very similar to the relation suggested by Evrard et al. (2008). To estimate halo masses of the GCLASS clusters, we will therefore use the Evrard et al. (2008) scaling relation. This relation was also used by a recent dynamical study on the ACT cluster sample (Sifón et al. 2013), which simplifies a comparison with the results from this sample (e.g. Hilton et al. 2013) in the rest of this paper. Values of M_{200} and R_{200} are shown in Table 4.1. Statistical uncertainties are given (propagated from uncertainties on the velocity dispersion), but note that there is also a significant systematic uncertainty ($\sim 20\%$), corresponding to the choice of scaling relation, and indicated by the substantial amount of intrinsic scatter. Note that the R_{200} values have a smaller fractional uncertainty, since

$$R_{200} \propto M_{200}^{1/3}.$$

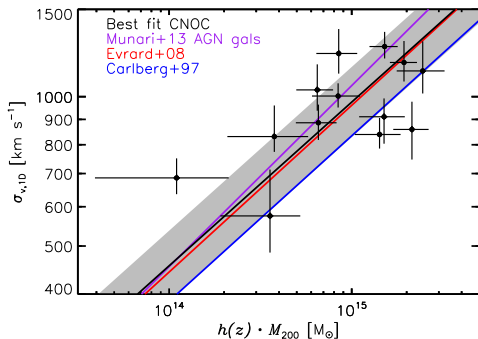


Figure 4.1: Measured velocity dispersion versus halo mass ($h(z) \cdot M_{200}$). Data points are measurements on the CNOC sample. Lensing masses are from Hoekstra et al. (2012) (which are revised in hoekstra et al., in prep.), whereas velocity dispersions are obtained from Borgani et al. (1999) and Girardi & Mezzetti (2001). Although there is a substantial amount of intrinsic scatter (grey region indicates $\pm 1\text{-}\sigma$ intrinsic scatter around the relation), the best fit to these data (black line) is very close to the Evrard et al. (2008) scaling relation (red).

4.2.2 Photometric redshifts and Stellar masses

We estimate photometric redshifts for all galaxies in the K_s -band selected catalogue using the EAZY code (Brammer et al. 2008). In vdB13 we assessed the performance by comparing the photo- z estimates to spec- z measurements for the galaxies that have been observed spectroscopically. We found a scatter of $\sigma_z = 0.036$ in $\frac{\Delta z}{1+z}$, a negligible bias and fewer than 5% outliers.

After fixing the redshift for each object at its spec- z , or the photo- z when a spec- z is not available, we estimate stellar masses using FAST (Kriek et al. 2009). The stellar population libraries from Bruzual & Charlot (2003) are used

to obtain the model SED that gives the best fit to the photometric data. We use a parameterization of the star formation history as $SFR \propto e^{-t/\tau}$, where the time-scale τ is allowed to range between 10 Myr and 10 Gyr. We also assume a Chabrier (2003) IMF, solar metallicity, and the Calzetti et al. (2000) dust law. For estimates on the stellar-mass completeness of the catalogues, we refer to vdB13. To approximate the statistical uncertainty on each stellar mass measurement, we perform 100 Monte-Carlo simulations in which we perturb the photometric aperture flux measurements within their estimated errors. Each realisation of the catalogue gives a slightly different SED fit, and therefore the mass-to-light ratio (M_*/L) is different. We translate the obtained scatter in M_*/L into an approximate uncertainty on the stellar mass, after including uncertainties on the spectral templates themselves. We find typical uncertainties on M_*/L of 0.21 dex at $M_* \sim 10^{10} M_\odot$, and 0.13 dex at $M_* \sim 10^{11} M_\odot$.

4.2.3 Cluster membership correction

Fig. 4.2 shows the distribution of total stellar mass contained in galaxies with a given stellar mass. The best-fitting Schechter function to the total galaxy population from vdB13 is also shown. The points with error bars are the measurements of the SMF presented there, and are integrated masses over the SMF in each bin, i.e. $\int_{M_{\min}}^{M_{\max}} \Phi(M) \cdot M \cdot dM$, where $\Phi(M)$ represents the number density of galaxies as a function of stellar mass. With the characteristic mass of the Schechter function around $M_* = 10^{11} M_\odot$, galaxies around this mass contribute most to the total stellar mass of the cluster. For the galaxies with stellar masses around $M_* = 10^{11} M_\odot$, the completeness is high ($\geq 50\%$). For measurements within R_{500} the completeness is even higher. For that reason, the measurements of the total stellar mass of the clusters are based mostly on spectroscopic redshifts, and are robust with respect to how we correct the photometric sample for completeness.

We use the limited number of galaxies in the fields that have been targeted spectroscopically to estimate the probability that a galaxy is part of the cluster

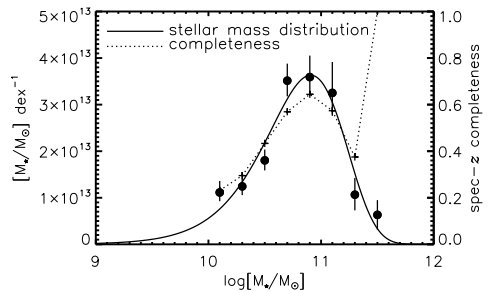


Figure 4.2: Solid line: the distribution of total stellar mass contained in galaxies with a given stellar mass. The points with error bars are the measurements of the SMF presented in van der Burg et al. (2013), but integrated over the mass bins. Dotted line: the spectroscopic completeness for galaxies with projected distances from the BCG less than R_{200} . For the galaxies that constitute most of the stellar mass in the clusters, the spectroscopic completeness is high ($\gtrsim 50\%$).

for the objects that do not have a measured spectroscopic redshift. For objects with stellar masses exceeding $\sim 10^{10} M_{\odot}$ that were targeted, the success rate of obtaining a reliable spec- z is higher than 90% (M12). Given that the targeting prioritization is known (M12), we can correct the photometrically selected sample for cluster membership using the sub-sample of spectroscopic targets. To do this we take a similar approach as outlined in vdB13 (Sect. 3.4), but with a few adaptations.

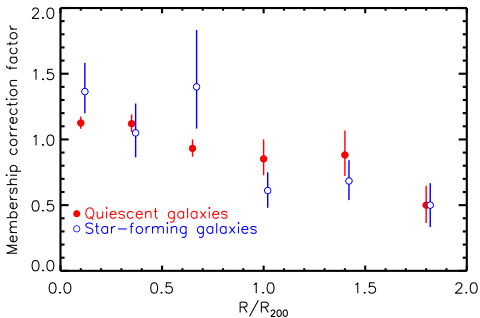


Figure 4.3: Correction factors as a function of radius, scaled by R_{200} , for the cluster ensemble. Error bars represent uncertainties estimated from Monte-Carlo simulations. Further away from the projected centres, the correction factors go down because galaxies are increasingly more likely to be part of the field.

The radial distance of each galaxy is rescaled to units of R_{200} , instead of physical distance. Then we measure for the cluster ensemble, in bins of radial distance and stellar mass, the fraction of correctly identified cluster galaxies based on their photo- z . Comparing this number to the total number of spec- z selected cluster members in this bin, we obtain membership correction factors that are used to correct the photometrically selected numbers for membership. The correction factors as a function of radial distance are shown in Fig. 4.3. The membership correction factors are a decreasing function of distance, since the clusters are less overdense further away from their cluster centre. The blue (red) points represent the population of star-forming (quiescent) galaxies. For the correction factors as a function of stellar mass we refer to vdB13 (Fig. 4).

To further improve the estimates on the total stellar mass associated with each cluster, we estimate the contamination by field galaxies for each individual cluster. This minor correction to the photo- z selected sample for each cluster is due to cosmic variance, slight differences in photometric redshift quality between the fields, and also the dependence of angular size associated with R_{200} on the cluster mass and redshift. To estimate this overdensity parameter we 1) apply the correction factors that we use on the photometric sample (e.g. Fig. 4.3 and vdB13 (Fig. 4)) on all spectroscopically targetted galaxies, then 2) use this to estimate the number of cluster members in this sample, and 3) divide the actual number of spectroscopic cluster members by the estimated number of cluster members to give the correction factor. This cluster overdensity parameter is by construction around 1.0 and ranges from 0.86 to 1.22 for the clusters in our sample.

4.3 Central stellar mass versus halo mass

In Fig. 4.4 we show the stellar mass of the central galaxy as a function of dynamical halo mass. Stellar masses are measured based on M_*/L 's estimated with FAST, multiplied with the total flux in the K_s -band. Since brightest cluster galaxies (BCGs) generally have extended light profiles, their flux measured with SExtractor in Kron elliptical apertures is under-estimated. To account for the total flux of the BCGs in the K_s -band, we use GALFIT to fit Sérsic profiles to these galaxies. We make sure that we carefully mask any nearby satellite galaxies and perform 10 different fits where we convolve the profiles with different stars to approximate uncertainties due to the PSF. We compare the integrated flux in these Sérsic profiles with the SExtractor magnitudes in Table 4.2. The values show the median values and the maximum and minimum values for the 10 different GALFIT runs, after rejecting the highest and lowest value. The difference between the GALFIT and SExtractor measurements is typically about 0.2 mag, and depends mainly on the shape of the profile, which is described by the Sérsic parameter n . To obtain the total stellar masses of the central galaxies we multiply the total flux in the K_s -band with the M_*/L estimated using FAST, and include both the flux-error and the error on M_*/L (which is the dominant source of uncertainty).

Table 4.2: K_s -band magnitudes for the BCGs identified in Lidman et al. (2012) for the GCLASS clusters. The last column gives the stellar masses corresponding to the GALFIT total integrated magnitude, and the errors also include the statistical uncertainty on M_*/L .

Name	MAG_AUTO [mag _{AB}]	GALFIT [mag _{AB}]	GALFIT Sérsic - n	$M_{*,BCG}$ [$10^{11} M_\odot$]
SpARCS-0034	16.59 ± 0.01	16.51 ^{+0.04} _{-0.03}	3.68 ^{+0.36} _{-0.37}	3.56 ^{+0.36} _{-0.54}
SpARCS-0035	17.27 ± 0.01	17.06 ^{+0.01} _{-0.01}	3.77 ^{+0.13} _{-0.13}	4.61 ^{+0.97} _{-0.60}
SpARCS-0036	16.40 ± 0.01	16.10 ^{+0.01} _{-0.04}	3.82 ^{+0.30} _{-0.37}	6.92 ^{+0.30} _{-1.25}
SpARCS-0215	17.05 ± 0.01	16.86 ^{+0.02} _{-0.02}	3.02 ^{+0.14} _{-0.13}	3.36 ^{+0.47} _{-0.94}
SpARCS-1047	17.29 ± 0.01	17.03 ^{+0.01} _{-0.03}	4.35 ^{+0.22} _{-0.41}	2.42 ^{+0.29} _{-0.58}
SpARCS-1051	17.11 ± 0.02	16.73 ^{+0.03} _{-0.04}	6.87 ^{+0.97} _{-0.93}	4.49 ^{+0.15} _{-0.72}
SpARCS-1613	15.67 ± 0.01	15.50 ^{+0.00} _{-0.01}	3.25 ^{+0.10} _{-0.15}	10.91 ^{+0.44} _{-2.40}
SpARCS-1616	17.01 ± 0.01	16.96 ^{+0.01} _{-0.02}	3.03 ^{+0.18} _{-0.15}	3.24 ^{+0.26} _{-0.13}
SpARCS-1634	17.41 ± 0.01	17.42 ^{+0.01} _{-0.01}	0.83 ^{+0.01} _{-0.01}	1.89 ^{+0.23} _{-0.21}
SpARCS-1638	17.71 ± 0.02	17.43 ^{+0.01} _{-0.01}	5.23 ^{+0.12} _{-0.12}	2.36 ^{+0.47} _{-0.40}

Considering the GCLASS data in Fig. 4.4, we find mild evidence for a correlation between the BCG stellar mass and halo mass, with a Spearman

rank coefficient $\rho = 0.49$. The fraction of mass contained in stellar form in the BCG is approximately 0.001 of the halo mass.

Behroozi et al. (2010) and Behroozi et al. (2013) estimated the stellar mass versus virial halo mass relation over a range of redshifts and halo masses using the abundance matching technique. At the high mass end we make a comparison between their estimates and our observations, which are based on direct measurements of the total halo masses and stellar masses of centrals in the same systems. We multiply the Behroozi halo masses by factor 1.11 to account for the difference between their virial halo masses and M_{200} (Bryan & Norman 1998). We show the Behroozi et al. (2010) (Behroozi et al. (2013)) prediction for $z = 1$ by the light (dark) shaded area in Fig. 4.4. Although the allowed areas are large because of including statistical and systematic uncertainties, the results from Behroozi et al. (2010) seem to be in better agreement with the GCLASS data than the results from Behroozi et al. (2013). What is different in both abundance matching studies is the specific treatment of intra-cluster light (ICL) in Behroozi et al. (2013). When a galaxy merger occurs in this new model, the stars associated with the satellite galaxy may either be deposited onto the central galaxy or be ejected into the ICL. Since Behroozi et al. (2013) estimate the ICL to be of a significant contribution to the total stellar mass at $z = 1$, this is potentially related to an under-prediction of the stellar mass in the central galaxies.

To increase the dynamic range in terms of cluster halo mass, in order to constrain the power-law slope of this relation, we compare our results to those from Hilton et al. (2013), which were obtained from a sample of ACT SZ-selected clusters. To be able to compare the results directly, we reduce the stellar masses estimated from Hilton et al. (2013) by 0.24 dex to account for differences in the adopted IMF. Note that Hilton et al. (2013) did not fit the SED of the BCG with a model to constrain M_*/L , but rather assumed a single burst stellar population that has a formation redshift $z_f = 3$. For the purpose of estimating BCG stellar masses the difference between these approaches is small (< 0.1 dex), because the BCGs contain relatively old stellar populations. The M_{200} measurements for this cluster sample are taken from Sifón et al. (2013). Fig. 4.4 shows a clear relation between the BCG stellar mass and total halo mass from GCLASS and Hilton et al. (2013).

When we fit a slope to the combined set of data points, we have to account for intrinsic scatter in the relation to ensure that we do not give too much weight to precise measurements that are far off the mean relation. We follow the approach outlined in Hoekstra et al. (2011) to perform a three parameter fit to these data points. Besides the parameters describing the power-law relation, the intrinsic scatter is assumed to be described by a log-normal distribution, for which we fit the dispersion σ . The intrinsic scatter is best described by $\log(\sigma_{M_{BCG}|M_{200}}) = 0.12^{+0.03}_{-0.02}$ dex, and the best-fitting relation is $\log(M_{BCG}) = (11.66 \pm 0.03) + 0.42^{+0.06}_{-0.07} \cdot [\log(M_{200}) - 14.5]$. This relation is plotted in

Fig. 4.4 and indicates that the BCG stellar mass fraction is lower for higher mass haloes. The fit shows that there is a significant amount of intrinsic scatter in the relation between central galaxy stellar mass and halo mass, which is consistent with the finding of e.g. Leauthaud et al. (2012b).

Note that our data do not allow for measurements of the intracluster light (ICL), and therefore the contribution of intracluster stars to the central stellar mass is neglected. Formally the measured values are therefore lower limits, but Burke et al. (2012) show that the contribution of intracluster stars to the total stellar mass at $z \sim 1$ is expected to be significantly smaller than at lower redshifts. In contrast, Behroozi et al. (2013) suggest a picture in which a significant fraction of the ICL has already been formed at $z \sim 1$. There is, however, slight tension between their statistical study and our observations of the stellar mass in the central galaxy (which is related to the build-up of the ICL component) in Fig. 4.4.

Lidman et al. (2012) measure the BCG stellar mass versus halo mass for a sample of 160 BCGs in the redshift interval $0.03 < z < 1.63$. Besides the different redshift range they study, their analysis is slightly different from ours. Lidman et al. (2012) constrain the M_*/L of the BCGs with J-, and K_s -band data and do not use GALFIT to probe the extended light profiles of the BCGs. The slope fitted by Lidman et al. (2012) is $M_{200} \propto M_{\text{BCG}}^{1.6 \pm 0.2}$. The reciprocal of this is consistent with our slope to within $2\text{-}\sigma$.

4.4 Total stellar mass versus halo mass

We make a comparison between the halo masses and the total stellar mass in the halo, including the satellites. We will perform all measurements both within R_{200} and within R_{500} to provide a reference and facilitate the comparison with literature measurements. When necessary, we will convert between R_{200} and R_{500} by applying the concentration parameter estimated from Duffy et al. (2008). For the mass and redshift range of the GCLASS clusters, Duffy et al. (2008) find a typical concentration of $c = 2.7$, which is consistent with a stacked weak-lensing measurement of clusters at $z \sim 1$ (Sereno & Covone 2013). Corresponding to this concentration parameter, we will use the relationships $R_{500} = 0.632 \cdot R_{200}$ and $M_{500} = 0.631 \cdot M_{200}$.

For each cluster we sum the stellar mass contained in galaxies with a spectroscopic redshift consistent with the cluster that exceed the mass completeness limit of the cluster. The K_s -band flux limits were simulated for each cluster, and corresponding stellar mass completeness limits were estimated and presented in vdB13 (Table 1). To this we add the photo- z selected sources that we correct for cluster membership using the method explained in Sect. 4.2.3, provided that their projected radii from the BCG are less than R_{200} (or R_{500}). Since the overdensity of the cluster with respect to the field is different for

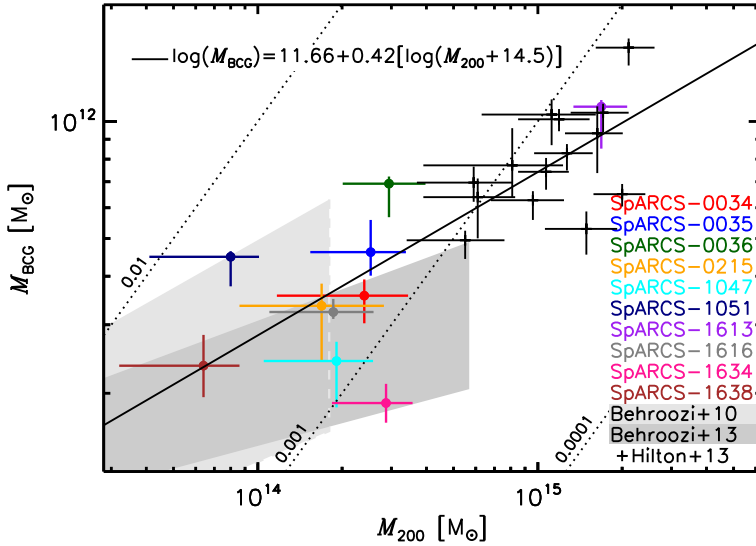


Figure 4.4: BCG stellar mass versus total halo mass. Black dots show lines of constant stellar mass fractions of 0.0001, 0.001 and 0.01. '+'-signs show the results from Hilton et al. (2013). The relation is the best fit to the combined data set of Hilton et al. (2013) and the current study. Estimates from Behroozi et al. (2010) and Behroozi et al. (2013) are indicated by the shaded regions.

each cluster, as explained in Sect. 4.2.3, we correct the total stellar mass of the photometric sample with the cluster overdensity parameter for each cluster.

The stellar mass is now measured within a projected radius of R_{200} (or R_{500}), but to estimate the stellar mass fraction and be able to compare to results in the literature we have to deproject the stellar mass onto a sphere with radius r_{200} (or r_{500}), since the halo mass M_{200} (or M_{500}) is defined in that way. Assuming a concentration parameter $c = 2.7$ and integrating the NFW profile along the line of sight, we find that 74% of the mass in the cylinder also lies within the sphere with radius R_{200} (and 69% when we make this comparison for R_{500}). We therefore multiply the stellar mass estimates by a factor 0.74 (0.69 for R_{500}).

Since so far we only considered galaxies with stellar masses exceeding the mass completeness limits, we have to estimate the stellar mass contained in lower mass galaxies. We measured the Schechter parameters of the SMF in vdB13, and although these parameters were constrained by galaxies with stellar masses exceeding $10^{10} M_{\odot}$, we use the integral of this Schechter function for masses below the stellar mass completeness limits to correct for these lower mass galaxies. Fig. 4.2 shows that the total stellar mass contained in low-mass galaxies is small. The percentage by which we correct the stellar mass

depends on the stellar mass completeness and ranges from 4% for SpARCS-0035 to 25% for SpARCS-0036. Given the size of these correction factors, they do not have a significant effect on the results, especially because the depth in terms of stellar mass is independent of the redshift or halo mass of the clusters. Total stellar masses are listed in Table 4.3.

In Fig. 4.5 we show the total stellar mass versus total halo mass compared within R_{200} and R_{500} (left and right panels, respectively) for the GCLASS systems. Error bars in the vertical direction include statistical uncertainties on individual stellar mass measurements, and uncertainties on the estimated probabilities that a photometrically selected galaxy is part of the cluster. The latter uncertainty, which dominates, includes the error on the overdensity parameter for each cluster. The GCLASS data show a clear correlation, with Spearman coefficient $\rho = 0.65$ (within R_{200}), and $\rho = 0.62$ (within R_{500}).

We fit a power-law relation to the GCLASS data points, with the amount of intrinsic scatter as a free parameter, and described by a log-normal distribution with scatter σ . We find the following best-fitting parameters for the comparison within R_{200} ; $\log(\sigma_{M_{200,*}|M_{200}}) = 0.08_{-0.05}^{+0.04}$ dex, and the relation $\log(M_{200,*}) = (12.44 \pm 0.04) + (0.59 \pm 0.10) \cdot [\log(M_{200}) - 14.5]$. When we perform the fit to the data within R_{500} we find; $\log(\sigma_{M_{500,*}|M_{500}}) = 0.11_{-0.04}^{+0.05}$ dex, and the relation $\log(M_{500,*}) = (12.44_{-0.06}^{+0.05}) + (0.62 \pm 0.12) \cdot [\log(M_{500}) - 14.5]$. Both relations are shown in Fig. 4.5. The slope of the relation is consistent with the slope found by Lin et al. (2012), who measured it to be 0.71 ± 0.04 for a sample of redshift $z < 0.6$ clusters. The small amount of intrinsic scatter in the relation between total stellar mass and halo mass indicates that stellar mass is a good proxy for total halo mass (albeit with large measurement uncertainties on individual clusters), as was also suggested by Andreon (2012).

For 6 X-ray selected galaxy clusters at $z \sim 1$, Burke et al. (2012) show that the contribution of the ICL to the total J-band flux within R_{500} is about 1-4%. Since this contribution is much (factor $\sim 2-4$) smaller than the contribution of the ICL at low- z , our measurements should be close to the actual mass in stars.

Given that this tight relation between total stellar mass and halo mass already exists at $z \sim 1$, and that the stellar mass fraction is decreasing with increasing halo mass, one would naively expect the stellar mass fraction of these massive haloes to increase towards lower redshifts. That is because the likely systems that will be consumed by these haloes are those with a high stellar mass fraction (McGee et al. 2009). In this simple picture the stellar mass fraction would increase, even in the absence of in-situ star formation. Given this naive expectation, it is therefore interesting to make a comparison of the stellar mass content of haloes at lower redshifts.

Table 4.3: Total stellar masses projected onto spheres with radii R_{200} and R_{500} for the GCLASS clusters.

Name	$M_{200,*}$ [$10^{12} M_{\odot}$]	$M_{500,*}$ [$10^{12} M_{\odot}$]	$M_{500,*}(3.6\mu\text{m})^a$ [$10^{12} M_{\odot}$]
SpARCS-0034	$2.40^{+0.16}_{-0.15}$	$2.10^{+0.14}_{-0.14}$	-
SpARCS-0035	$1.89^{+0.22}_{-0.20}$	$1.50^{+0.18}_{-0.16}$	$5.43^{+2.92}_{-1.90}$
SpARCS-0036	$3.30^{+0.16}_{-0.15}$	$2.74^{+0.14}_{-0.13}$	-
SpARCS-0215	$2.86^{+0.25}_{-0.23}$	$1.55^{+0.15}_{-0.14}$	-
SpARCS-1047	$1.45^{+0.15}_{-0.13}$	$0.94^{+0.09}_{-0.08}$	-
SpARCS-1051	$1.00^{+0.07}_{-0.07}$	$0.60^{+0.06}_{-0.06}$	-
SpARCS-1613	$7.35^{+0.60}_{-0.55}$	$5.68^{+0.42}_{-0.39}$	$18.72^{+9.65}_{-6.37}$
SpARCS-1616	$3.29^{+0.20}_{-0.19}$	$2.75^{+0.16}_{-0.15}$	$7.14^{+2.19}_{-1.68}$
SpARCS-1634	$1.88^{+0.13}_{-0.12}$	$1.38^{+0.11}_{-0.10}$	$3.37^{+2.58}_{-1.46}$
SpARCS-1638	$1.13^{+0.14}_{-0.13}$	$0.92^{+0.13}_{-0.11}$	$2.33^{+1.56}_{-0.93}$

^a Taking the background subtracted flux in IRAC $3.6\mu\text{m}$ and assuming the same M_*/L for every galaxy in each cluster, based on a single burst stellar population with $\tau = 0.1$ Gyr formed at $z_f = 3$.

4.4.1 Comparison to other samples

We compare our measurements to others in the literature (mostly performed at low- z) for R_{500} , since this radius was used by most studies that estimate the halo masses with X-ray data. However, there are several important caveats to make before we can make a fair comparison. The adopted M_*/L is a major systematic uncertainty in any study and depends on the assumed IMF due to differences in the contribution of low mass stars to the total mass. We transform the results from other studies to the Chabrier IMF by subtracting 0.24 dex in mass for a Salpeter IMF, or adding 0.04 dex to the mass for a Kroupa IMF. The M_*/L depends on galaxy type, but due to the lack of multi-wavelength photometry, it is often assumed that all cluster galaxies are composed of the same stellar population. If one assumes an old stellar population (and therefore a high M_*/L), the mass of the late-type galaxies (and thus the cluster as a whole) is over-estimated. Such an effect will be more pronounced at higher redshift because of the higher number density of late-type galaxies in high- z clusters (M12, vdB13). We will point out possible issues for each of the comparison samples below.

An obvious study to compare our results to is based on an SZ-selected cluster sample from the ACT, with a redshift range overlapping with GCLASS and a median redshift of $z = 0.50$ (Hilton et al. 2013). A complication is that

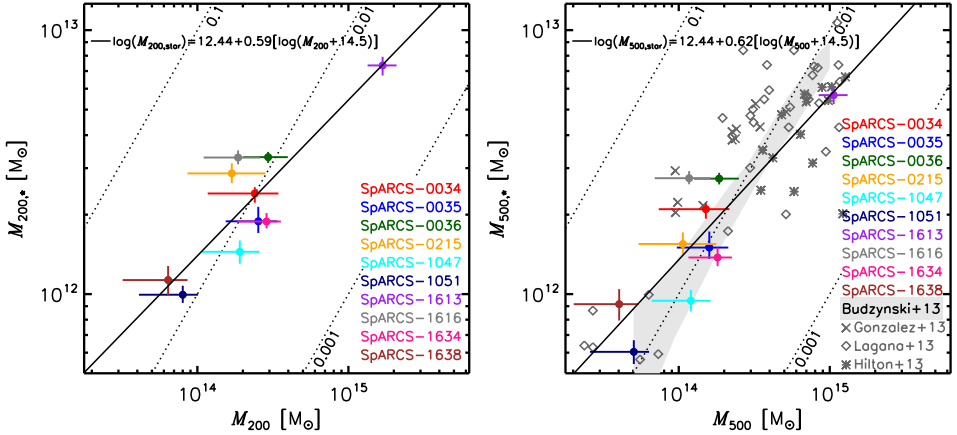


Figure 4.5: Total stellar mass versus halo mass within a sphere with radius R_{200} and R_{500} (left and right panels, respectively). Error bars represent uncertainties on individual mass measurements and uncertainties on the membership correction for galaxies we do not have spectra for. Dotted lines show locations with constant stellar mass fractions. The literature measurements (right panel) are measured over a range of redshifts, and are based on different analyses. When possible, the data points are corrected for differences in IMF and M_*/L 's, as explained in the text.

Hilton et al. (2013) estimated cluster stellar masses based on the total IRAC $3.6\mu\text{m}$ flux measured after a statistical background subtraction. Instead of fitting a M_*/L for each galaxy based on SED modelling, they assume a stellar population that is formed at $z_f = 3$, following a $\tau = 0.1$ Gyr single burst model and the Bruzual & Charlot (2003) stellar population synthesis model. To estimate the effects of these assumptions and see if this creates a bias, we follow the method described by Hilton et al. (2013) to obtain the background subtracted IRAC $3.6\mu\text{m}$ flux within R_{500} for the 5 GCLASS clusters for which we have deep IRAC data (vdB13), and estimate the total stellar mass based on the described stellar population. Table 4.3 compares these estimates with the total stellar mass in the clusters obtained by the full SED fitting analysis. The approach with a fixed M_*/L over-estimates the stellar mass in all clusters by at least a factor of 2, and this difference seems to be largest for the highest redshift cluster. This is consistent with the notion that the blue fraction, and therefore the fraction of galaxies with relatively low M_*/L , increases with redshift (cf. Butcher & Oemler 1978). It is also possible that the stellar population assumed by Hilton et al. (2013) has a formation redshift ($z_f = 3$) that is too high. After correcting the stellar masses from Hilton et al. (2013) to a Chabrier IMF, we divide them by an additional factor of 2 as an approximate correction for the M_*/L explained above. These data points are overplotted in Fig. 4.5 (right panel, \ast -symbols), and lie around the relation that is the best fit to the

GCLASS data. Note that since we used the red-sequence selected GCLASS sample to measure this bias, the real bias might be even larger if the SZ-selected sample contains a lower fraction of quiescent galaxies.

To study a possible evolution in the stellar mass content of clusters we consider Laganá et al. (2013), who measure the stellar mass content in a sample of $z < 0.3$ clusters. Estimates for M_{500} are obtained from X-ray observations. To measure the total stellar mass from the available SDSS data, the galaxy population is separated between early-type and late-type galaxies using the $(u - i)$ colour. Exploiting the M_*/L from Kauffmann et al. (2003) in the i -band for these galaxy types, Laganá et al. (2013) estimate stellar masses. Since the Kauffmann et al. (2003) M_*/L 's are based on the Kroupa IMF, we subtract 0.04 dex to compare their results to ours, and overplot them in Fig. 4.5 (right panel, \diamond -symbols).

Another nearby cluster sample is the one studied by Gonzalez et al. (2007), which is in the range $0.03 < z < 0.13$, and these measurements are revised in Gonzalez et al. (2013). In these studies, a single M_*/L was used for each galaxy, irrespective of their type. From a dynamical analysis of the SAURON project, they estimate the average M_*/L in the i -band, which they found to be lower than the M_*/L based on an assumed Salpeter IMF. We correct their M_*/L to a Chabrier IMF by subtracting 0.12 dex, and overplot the points from Gonzalez et al. (2013) in Fig. 4.5 (right panel, \times -symbols). The stellar mass fractions they find are in approximate agreement with the stellar mass fractions of the GCLASS clusters, although they find a somewhat shallower slope of 0.52 ± 0.04 when they fit a relation to only their data set. Given that the fraction of red (with a large M_*/L) galaxies depends on halo mass, it is possible that this slope is biased due to the assumption of a single M_*/L for the sample.

To increase the dynamic range of the comparison samples, we make a comparison to the measurements from Budzynski et al. (2013), who measured the stellar mass fraction across a wide range of masses in the group and cluster regime from the SDSS. Their stacked measurement of over 20,000 optically selected systems at $0.15 < z < 0.4$ is shown by the shaded region in Fig. 4.5. Since their analysis is very similar to our, we do not have to correct their measurements for differences in e.g. M_*/L . Both the normalisation and their slope of 0.89 ± 0.14 are consistent with the relation we find for GCLASS. When they stack original SDSS images to measure the contribution from the ICL to the stellar mass in their sample, they find a slope that is even steeper.

We note that there are caveats that arise when comparing different cluster samples, as was also pointed out by several other studies (e.g. Leauthaud et al. 2012a; Budzynski et al. 2013). Performing the analysis described by Hilton et al. (2013) on the GCLASS data shows that there is a bias in the total stellar mass when a single M_*/L is assumed for all cluster galaxies, especially at high- z . This bias in the stellar mass can be larger than the

evolution expected in the redshift range $0 < z < 1$. This shows that it is important to analyse the full SED of each galaxy to estimate its stellar mass. Thanks to the spectroscopic coverage of the GCLASS sample, which is more than 50% complete within R_{200} for the galaxies that dominate the total stellar mass content, membership assignment is relatively straight-forward. In other analyses, where a statistical background subtraction is performed, this can be a major uncertainty for individual systems. We attempted to correct for differences in the analyses between literature studies to be able to compare the total stellar mass fractions between different epochs. Within the uncertainties there seems to be a good agreement between the studies over this redshift range, showing that there is no significant evolution in the stellar mass fraction at fixed halo mass in the redshift range $0 < z < 1$. To tighten the constraints on a possible evolution of this relation, a large and more homogeneous dataset and analysis are required.

4.5 Radial stellar density distribution

Measurements of the evolution of the spatial galaxy number density and stellar mass density distributions are a key to understand how stellar mass accretes onto massive haloes. We perform these measurements in GCLASS by dividing the sample in radial bins. We do this by stacking the cluster ensemble at the location of the BCGs, and scaling the clusters by their respective R_{200} . We measure the area in each bin by masking the locations on the images that are contaminated by bright stars. Also, since we do not take the stellar mass of the BCGs into account in this study, we mask the location of the central galaxies since this location does not allow for the detection of typical cluster members.

The number density distribution is shown in Fig. 4.6, where in each radial bin the number of spec- z identified cluster members and the membership-corrected photo- z members with stellar masses exceeding $10^{10.2} M_{\odot}$ are combined. Errors on each point are a combination of Poisson sampling errors, and errors propagated from the membership correction which we estimated from a series of Monte-Carlo simulations. We used the area-weighted position to plot the data points in the horizontal direction. The '+'-signs show the innermost point including the BCGs. The bottom panel of Fig. 4.6 shows the spectroscopic targeting completeness as a function of radial distance, which shows that -as designed- the completeness is higher for objects near the projected cluster centres. Further away from the cluster centre, the errors that arise from membership estimates are dominant.

The radial distribution of stellar mass in the ensemble cluster is shown in Fig. 4.7. Besides Poisson counting errors and errors that arise from cluster membership corrections, the error bars include stellar mass measurement errors on individual galaxies. Compared to the number density profile, the

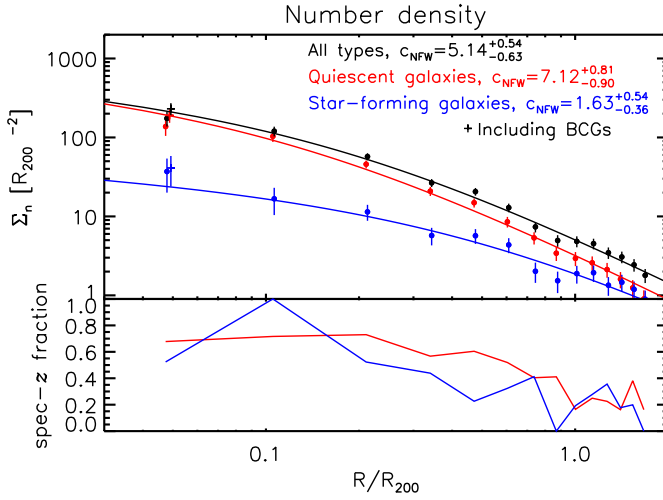


Figure 4.6: The number density of galaxies with stellar masses $> 10^{10.2} M_{\odot}$ in the 10 GCLASS clusters as a function of radial distance. The total galaxy population (black) is separated between star-forming (blue) and quiescent (red) galaxies. Thick points show the membership-corrected number density, where the error bars represent the uncertainties that arise from membership correction. The points are fitted by projected NFW functions (lines), with different concentration parameters. The lower panel shows the fraction of galaxies in each bin with a spectroscopic redshift.

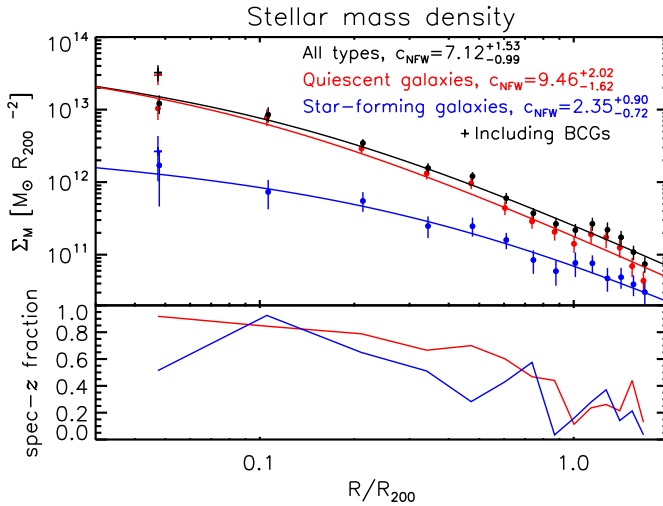


Figure 4.7: The stellar mass density distribution in galaxies with stellar masses $> 10^{10.2} M_{\odot}$ of the composite cluster as a function of radial distance. Comparing these distributions to those shown in Fig. 4.6, we find that the stellar mass distributions are peaked more strongly than the number density distribution. That is an indication for mass segregation of quiescent galaxies in these systems. The lower panel shows the fraction of stellar mass in galaxies with a spectroscopic redshift.

spectroscopic targeting completeness is higher due to the selection of spectroscopic targets by their $3.6\mu\text{m}$ flux.

Table 4.4: Best-fitting NFW parameters to the radial density distributions. Reduced χ^2 values are given (12 degrees of freedom).

	c_{NFW}	$\chi^2/d.o.f.$
$\Sigma_{\text{M,all}}$	$7.12^{+1.53}_{-0.99}$	0.94
$\Sigma_{\text{n,all}}$	$5.14^{+0.54}_{-0.63}$	0.84
$\Sigma_{\text{M,quiescent}}$	$9.46^{+2.02}_{-1.62}$	1.07
$\Sigma_{\text{n,quiescent}}$	$7.12^{+0.81}_{-0.90}$	0.92
$\Sigma_{\text{M,star-forming}}$	$2.35^{+0.90}_{-0.72}$	0.36
$\Sigma_{\text{n,star-forming}}$	$1.63^{+0.54}_{-0.36}$	0.73

We fit projected NFW (Navarro et al. 1997) profiles to the data points, excluding the BCGs, to be able to interpret the results in the context of the NFW concentration parameter. Using χ^2 minimization, taking account of the 2D annulus-shaped bins, we find the best fitting functions, which give good representations of the data (see the reduced χ^2 values in Table 4.4). We give the best-fitting concentration parameters and their marginalized errors in the table for both the number density and the stellar mass density profiles. The best-fitting profiles are shown in the corresponding figures.

From both the number density and the stellar mass density profiles we find that the quiescent galaxy population is concentrated more strongly than the star-forming population, which is consistent with the view that the star-forming population is accreted more recently by the cluster (for a measurement at low- z , cf. Biviano et al. 2002).

We also find that the stellar-mass distribution of quiescent galaxies is concentrated more strongly than their number density profile, which is an indication that more massive galaxies are situated closer towards the cluster centres than lower mass galaxies. This is likely caused by dynamical friction of the cluster members, which is more efficient for massive galaxies. Note that this effect is observed without taking account of the BCGs.

4.5.1 Discussion

We measured the galaxy concentration parameters in the ensemble GCLASS cluster, and it may be that a subset of these systems is driving the concentration to this relatively high value. To investigate this we perform different stacks using subsets of the GCLASS sample. We separate the sample in 3

bins, and to make sure the statistics in each bin are sufficiently high, we rank order the clusters by total stellar mass and fill the bins by 6, 3, and 1 cluster(s), respectively. We find that the best-fitting stellar mass concentrations for these 3 ensembles are in the range $6.0 < c < 9.0$, and agree to within 2σ of their measurement errors. This suggests that the stellar mass in each of the GCLASS clusters is likely to be distributed with a concentration parameter around $c \sim 7$.

This high concentration parameter for the stellar matter suggest that the stellar mass is concentrated more strongly than the dark matter is expected to be. For the GCLASS haloes Duffy et al. (2008) estimates a concentration parameter around $c = 2.7$ from simulations that only contain dark matter. Although this value is the median value for massive haloes at $z = 1$, the distribution of concentrations is found to be distributed by a log-normal distribution with a scatter $\sigma(\log(c)) = 0.15$. It is possible that the red-sequence selection method is biased towards systems with highly concentrated red-sequence galaxies. However, given the large difference in concentration between the stellar mass and dark matter, and the relatively small scatter in the distributions, it is unlikely that this difference is merely an effect of the selection method. Note that it is possible that the inclusion of baryonic physics in simulations will alter the dark matter distribution, as recent studies have suggested (e.g. van Daalen et al. 2011). This might bring the dark matter and stellar mass concentrations better in agreement. We checked that the results shown in Fig. 4.5 are only marginally affected if we change the concentration to $c = 7$.

The composite cluster sample is obtained after stacking the individual clusters on the locations of their BCGs. In some cases the identification of the BCG is ambiguous. For SpARCS-1051 and SpARCS-1634 the identified BCGs are separated by ~ 250 kpc from the approximate projected cluster centres. We test what the effect of possible mis-centring is on the concentration of the measured radial density profiles. We find that, if the intrinsic cluster profiles are described by a $c = 10$ NFW profile, and 10 clusters are stacked with a mis-centring sampled from a Gaussian distribution with $\sigma = 0.1r_{200}$, the measured concentration would be $c = 7$. Any misalignment with the "true" cluster centre would result in a concentration that is biased low. Given these tests, it is likely that the stellar mass is concentrated even more strongly than indicated by the NFW fits to the cluster ensemble.

4.5.2 Evolution towards lower redshift

From numerical simulations (Wechsler et al. 2002) we know that massive haloes are likely to grow by a factor of ~ 2.5 between $z = 1.0$ and $z = 0.3$. This suggests that the GCLASS cluster sample, with typical halo masses of $M_{200} \simeq 2 \times 10^{14}$, is the likely progenitor population of the clusters observed in the CNOC survey (Yee et al. 1996; Carlberg et al. 1996), which have typical

halo masses of $M_{200} \simeq 7 \times 10^{14}$. The concentration of the underlying dark matter distribution is expected to increase by $\sim 10\%$ in this redshift interval (Duffy et al. 2008). Muzzin et al. (2007) measured the K-band luminosity and number density profiles for 15 of the CNOC1 clusters, and showed that the K-band luminosity distribution is well described by a projected NFW profile with concentration parameter $c = 4.28 \pm 0.57$. Although the luminosity in the K-band is a good proxy for the stellar mass, the mass-to-light ratio in this filter depends on galaxy type. Since we find a different distribution of stellar mass in quiescent and star-forming galaxies (Fig. 4.7), this suggests that the K-band luminosity profile differs from the stellar mass density profile. Indeed, if we scale the star-forming galaxies in GCLASS by a factor of 2 to account for the rough difference in M_*/L , we measure a luminosity profile with a concentration $c < 6$. Although the difference between GCLASS and CNOC1 is thus not as extreme, these results suggest that the dark matter and stellar mass density distributions evolve in distinct ways. This is also suggested by Budzynski et al. (2012), who based their study on a sample of groups and clusters in the redshift range $0.15 < z < 0.4$ from the SDSS. For this sample Budzynski et al. (2012) found that the concentration of the number density profile is lower than the dark matter prediction. There are several caveats, and possible explanations for the observed evolution of the stellar mass distribution.

First, since we do not take account of the stellar mass present in the central galaxies when fitting NFW profiles, accretion of galaxies onto the central galaxy might change the distribution of stellar mass in satellites, and therefore the concentration parameter, over time. Mergers play a dominant role in the build-up of stellar mass in BCGs (Lidman et al. 2013; Burke & Collins 2013). Massive galaxies that are close to the centre are expected to merge with the BCG on a relatively short timescale (Bildfell et al. 2012; Lidman et al. 2013), thereby rendering the BCG an increasingly statistically different population compared to cluster satellite galaxies. An indicator for this process is an increase in the luminosity gap between the BCG and the second brightest cluster galaxy (e.g. Smith et al. 2010a). However, given the shallow slope of the central stellar-halo mass relation (Sect. 4.3), BCGs are expected to grow only by a factor of 1.5 in the redshift range $1.0 > z > 0.3$ (see also Lidman et al. (2012)). If the supply of this stellar mass growth is obtained from galaxies near the centre, the concentration parameter of the satellite galaxy population would go down.

We perform a simple simulation in which we reduce the stellar mass in satellite galaxies within $0.5 \cdot R_{200}$ in accordance with a BCG growth of a factor of 1.5, and this shows that this is not sufficient to explain the dramatic decrease in the concentration parameter (c decreases from 7.0 to 6.0). Nevertheless, it is possible that the build-up of the ICL component towards lower redshift plays a role in lowering the concentration parameter of stellar mass in satellites.

Second, as clusters get larger, the dynamical friction timescale of a galaxy

with a given mass increases, so that it takes longer for galaxies to sink to the centre of the potential well. This is also hinted at when we compare the relation between central stellar and halo mass (Sect. 4.3), and between total stellar mass and halo mass (Sect. 4.4). Given that the latter slope is steeper, the fraction of stellar mass in satellite galaxies is higher in more massive haloes. It is possible that galaxies that are accreted onto the cluster at a later time are situated closer to the outskirts of the clusters due to the same process, and thus are less concentrated than the population that was accreted earlier.

We perform a simple test in which we increase the mass of the ensemble cluster by a factor 2.5 by adding stellar mass that is distributed following an NFW distribution with a given concentration. If we vary the concentration parameter of the population that we add, we find that, in order to end up with a concentration of $c = 4.0$ by $z = 0.3$ (i.e., similar to the concentration measured in CNOC), we have to add satellites with a concentration parameter of $c = 2.8$ to the stellar mass density distribution observed in GCLASS. This scenario could potentially explain the difference with the results from Budzynski et al. (2012), who find that at low- z the stellar mass is concentrated more strongly than the dark matter, and suggests that the stellar mass content mostly grows by accreting stellar mass onto the cluster outskirts.

4.6 Summary and Conclusions

In this paper we provide three key measurements concerning the stellar content in 10 clusters at $z \sim 1$ from the GCLASS survey. GCLASS benefits from 11 band photometric coverage and deep spectroscopic coverage to provide a full census of stellar mass in cluster members down to about $M_{\star} = 10^{10.2} M_{\odot}$. Combining these observations with measurements at lower redshifts we hope to provide constraints on the way baryons cool and form stars in galaxies in high density environments.

In Sect. 4.3 we presented a comparison of the central stellar mass with total halo mass, and found a correlation that suggests that the fraction of mass in the central galaxy is a decreasing function of halo mass, and about 0.001 for the mass range probed by GCLASS. We confirmed the trend predicted using abundance matching techniques, both in a qualitative as quantitative sense.

Sect. 4.4 showed a comparison of the total stellar masses (including satellites) with the dynamical halo masses, both within R_{200} and R_{500} . We found that the total stellar mass increases with halo mass, and that the fraction is around 0.01 for our sample and appears to decrease towards higher halo masses. A comparison of this relation with samples at other redshifts can yield insights on the way these systems accrete their stellar mass, but is difficult due to inhomogeneous sample selections and analyses. Especially inaccurate estimates on the stellar mass-to-light ratio are a source of confusion. After correcting

the reference studies for differences in their analyses, we found no significant evolution with redshift in the stellar mass fraction at fixed halo mass.

In Sect. 4.5 we studied the radial number density and stellar mass density profiles of galaxies in the sample, and found that these are represented by projected NFW profiles. The stellar mass density distribution is concentrated more strongly than the galaxy number density distribution, which shows that more massive galaxies are situated closer to the cluster cores (i.e. mass segregation). The stellar mass density profile has an NFW concentration parameter ($c = 7$) that is significantly higher than the dark matter distribution is expected to be ($c = 2.7$) from numerical simulations. Comparison of the concentration parameter with the CNOC1 survey at $z = 0.3$ suggests that the stellar mass concentration should decrease towards lower redshift. A simple simulation showed that stellar mass growth of the BCG alone is not enough to explain the evolution between GCLASS and CNOC1, and that the clusters are likely to accrete more stellar mass on the cluster outskirts as they grow by a factor of 2.5 in total mass from $z = 1$ to $z = 0.3$. Also the build-up of the ICL can play a role in the observed evolution.

We note that comparisons of our results with other studies are complicated due to inhomogeneous samples and different analyses. In order to draw firm conclusions regarding the evolution of the baryonic content, and in particular stellar mass, observational data need to be homogenized. We have also seen that the assumption of a single stellar mass-to-light ratio is inadequate to measure the total stellar mass content of galaxy clusters. Rather, one should fit the full Spectral Energy Distributions (SEDs) to estimate the stellar masses for individual galaxies. Moreover, since the galaxies with a high mass-to-light ratio are generally more concentrated in the cluster cores, measurements of the K-band luminosity profile and stellar mass density profile should not be taken as equivalent measurements. Thanks to the advance of large optical and near-infrared imaging facilities over the past decades, these multi-wavelength data are relatively easy to obtain, so that we will soon expect to be able to compare consistent stellar mass measurements with full SED fitting over a large redshift baseline.

Acknowledgements

We thank Marcello Cacciato, Dennis Just, Rob Crain, Anthony Gonzalez, Michael Balogh and Ivo Labbé for valuable discussions that improved the quality of this work.

R.F.J. van der Burg and H. Hoekstra acknowledge support from the Netherlands Organisation for Scientific Research grant number 639.042.814. C. Lidman is the recipient of an Australian Research Council Future Fellowship (program number FT0992259).

The distribution of stellar mass in galaxy clusters at $z \sim 0.15$

We study the radial galaxy and stellar mass density distributions in a sample of 10 galaxy clusters at $0.07 < z < 0.26$ selected from two surveys; the Multi-Epoch Nearby Cluster Survey (MENeCS) and the Canadian Cluster Comparison Project (CCCP). Deep *ugri*-band imaging is used to estimate photometric redshifts and stellar masses, and then statistically subtract foreground and background sources using data from the COSMOS survey. This procedure performs well, given that identical results are obtained for the ensemble cluster by considering the ~ 3000 spectroscopically confirmed member galaxies which make up the bulk of the stellar mass. We find that the radial distribution of stellar mass is well-described by an NFW distribution with concentrations in the range $0.8 < c < 5.6$, and an ensemble averaged value of $c = 1.92 \pm 0.19$ ($1\text{-}\sigma$ statistical). We estimate an intrinsic scatter of $\sigma_{c,\text{int}} = 0.70_{-0.22}^{+0.33}$ (or $\sigma_{\log_{10}c,\text{int}} = 0.25 \pm 0.05$ dex), which is likely caused by a combination of centroiding uncertainties, a range of different halo assembly histories, and different orientations on the sky.

The halo masses, which range from $4.8 \times 10^{14} M_{\odot}$ to $2.3 \times 10^{15} M_{\odot}$ (M_{200c}), match the approximate descendent population of the GCLASS cluster sample at $z \sim 1$, for which a stellar mass concentration of $c = 7.12_{-0.99}^{+1.53}$ was estimated. A comparison of these results shows that the spatial distribution of stellar mass evolves substantially towards low- z , a trend that is opposite to what is found for the dark-matter distribution in N-body simulations. We compare the stellar mass density distributions at $z \sim 1$ and $z \sim 0.15$ in the same physical units, showing that the stellar mass density in the cluster cores ($R < 0.2$ Mpc) decreases since $z \sim 1$. This may be related to the build-up of the ICL+BCG component over cosmic time. We also find that the clusters at $z \sim 1$ have

to grow in stellar mass at larger radii to match the descendent population. Comparisons with simulations have the potential to provide constraints on the stellar mass content of haloes falling into these clusters, and the dynamical friction time-scale that is applied in semi-analytic models.

Remco F.J. van der Burg, Henk Hoekstra, Adam Muzzin, Cristóbal Sifón, Sean McGee,
Michael Balogh
In preparation

5.1 Introduction

A key open question in the field of extragalactic astronomy today is to understand how galaxies form in our dark-matter dominated Universe (e.g. Guo et al. 2010). To learn about the baryonic physics that govern complex processes such as the cooling of gas, formation of stars and several feedback modes, models need to be tailored to match the observations. Observational probes such as the luminosity function and stellar mass function (e.g. Bell et al. 2003; Pérez-González et al. 2008; Ilbert et al. 2010; Muzzin et al. 2013a) have been used as fundamental observables to constrain physical models (e.g. Henriques et al. 2012; Weinmann et al. 2012), or test results from hydrodynamical simulations (e.g. Schaye et al. 2010; Cen 2014). Galaxies are not randomly distributed in space, and properties such as the star-formation rate (SFR), morphology, stellar mass, and metallicity of galaxies are dependent on their environment (Dressler 1980; Kauffmann et al. 2004; Baldry et al. 2006; Muzzin et al. 2012; Woo et al. 2013; van der Burg et al. 2013). Central galaxies and satellite galaxies, the latter of which are typically lower mass galaxies that are part of the same halo, evolve in different ways and are thus studied separately (Peng et al. 2010, 2012; Knobel et al. 2013).

The observed abundance and spatial distribution of satellite galaxies provide further constraints on galaxy formation models. A comparison between the outcomes of numerical N-body simulations and observations has revealed a problem known as the 'missing satellites problem' (Klypin et al. 1999; Bullock 2010). The number of satellite galaxies in the local group is significantly lower than predicted by the Λ CDM model. A possible interpretation of this is the inefficiency of low-mass haloes in forming stars, possibly due to supernova feedback (Efstathiou 2000; Dalla Vecchia & Schaye 2008), stellar winds, and the presence of a photo-ionizing background (Benson et al. 2002). It may also hint at a fundamental problem with our fiducial Λ CDM model, such that simulated haloes have more substructure (i.e. sub-haloes) than haloes in the actual Universe (Boylan-Kolchin et al. 2011).

Given the (nearly) self-similar properties of dark matter haloes, we can test the Λ CDM model by studying more massive haloes such as galaxy groups and clusters. Sub-haloes in these systems are correspondingly more massive, which makes them more efficient at forming stars, and thus easier to identify through observations. However, on the theory side this comparison also has limitations. Most studies are based on large N-body simulations (Springel et al. 2005), and dark matter haloes falling into larger haloes experience tidal forces leading to the stripping of their constituent particles (Ghigna et al. 2000; Binney & Tremaine 2008), also see Natarajan et al. (2002); Gillis et al. (2013) for an observational study. As a sub-halo falls into the main halo, it will continuously lose mass through the process of tidal stripping, and it may eventually fall below the mass resolution of the simulation. The sub-halo is

then no longer identified as such, its mass is deposited on the central galaxy or dispersed between the galaxies, and its orbit is no longer defined. For this reason, the radial distribution of sub-haloes is less concentrated than the dark matter in N-body simulations (Nagai & Kravtsov 2005). While the sub-haloes in these dissipationless simulations are eventually destroyed, the galaxies that have formed inside of them are expected to be more resistive to tidal forces. In semi-analytic models of galaxy formation, which are based on merger trees from these simulations, the more concentrated baryonic parts of galaxies are followed analytically after the sub-halo is dispersed (Bower et al. 2006; De Lucia & Blaizot 2007). A dynamical friction time-scale is generally applied, which determines when the galaxy is deposited onto the central galaxy, and how the intra-cluster light is building up (Contini et al. 2013). Measurements of the growth of brightest cluster galaxies (BCGs) (Lin & Mohr 2004; Lidman et al. 2012, 2013) and the intracluster light (ICL) (Gonzalez et al. 2013) can be used to constrain this time-scale, as the build-up of these components are directly related to the in-fall of satellite galaxies.

The radial number and stellar mass density distribution of satellite galaxies directly probe the abundance of sub-haloes, and can also be used to constrain the dynamical friction time-scale. These distributions are observed to be well described by NFW (Navarro et al. 1997) profiles for group-sized haloes and clusters from the local Universe to $z \sim 1$ (Carlberg et al. 1997a; Lin et al. 2004; Muzzin et al. 2007; Giodini et al. 2009; Budzynski et al. 2012; van der Burg et al. 2014). Each observational study however is based on a different data set and analysis, and presents results in a different form. Lin et al. (2004) and Budzynski et al. (2012) study the number density of galaxies, but due to mergers and interactions between galaxies, the number density distribution of galaxies can be different for galaxies with different luminosities or stellar masses. Their results are therefore dependent on the depth of their data set. Giodini et al. (2009) measure the number density distribution of generally lower mass systems from the COSMOS field. Carlberg et al. (1997a) and Muzzin et al. (2007) measure the luminosity density distribution in the r -band and K-band, respectively, for the CNOC1 (Yee et al. 1996) cluster sample. The advantage of this measurement is that, provided the measurements extend significantly below the characteristic luminosity L^* , it is almost insensitive to the precise luminosity cut. That is because the total luminosity in each radial bin is dominated by galaxies around L^* . However, especially in the r -band it is not straightforward to relate the luminosity distribution to a stellar mass distribution due to differences in mass-to-light-ratio between different galaxy types, and because the distributions of these types vary spatially. Inconsistencies between all these studies prevent us from drawing firm conclusions on comparisons between them.

The number density (down to galaxies with stellar mass $10^{10.2} M_{\odot}$) and stellar mass density distribution of galaxies in the GCLASS cluster sample at

$z \sim 1$ have been measured by van der Burg et al. (2014, hereafter vdB14). They find that both distributions are significantly more concentrated than the simulated distribution of dark matter in N-body simulations, and also more concentrated than a stacked weak-lensing measurement of $z \sim 1$ clusters (Sereno & Covone 2013). The only local measurement this study could compare to is the K-band luminosity distribution measured by Muzzin et al. (2007) for the CNOC1 clusters, which are approximate descendants of the GCLASS cluster by halo mass (estimated given the evolution of haloes in N-body simulations). Also the K-band luminosity is a good probe of the stellar mass of galaxies (Bell & de Jong 2001), especially in the local Universe where the clusters are dominated by galaxies with old stellar populations. The comparison suggests that the stellar mass density distribution evolves significantly since $z \sim 1$, and that the distribution becomes less concentrated over cosmic time.

In this paper we present a measurement of the radial galaxy number density and stellar mass density from a sample of approximate descendants of the GCLASS sample, but at a lower redshift of $0.07 < z < 0.26$. We measure these in a way that is as consistent as possible with the GCLASS measurement. In the discussion presented in vdB14 we suggest that the growth of the ICL or the accretion of galaxies onto the outskirts of the cluster could explain the significant evolution between the measurements in GCLASS and CNOC1. In this paper we revisit this discussion by also including the new measurements at $z \sim 0.15$.

The structure of this paper is as follows. In Sect. 5.2 we give an overview of the cluster sample, the available spectroscopic data set and the photometric catalogues based on *ugri*-band photometry. Section 5.3 presents the measurement of the radial density profiles, based on two independent analyses that we will compare for robustness tests. The results are presented in Sect. 5.4, and put into context against low- z literature measurements. In Sect. 5.5 we discuss the observed evolution and suggest possible scenarios to explain the differences between $z \sim 1$ and the local study. We summarise and conclude in Sect. 5.6.

All magnitudes we quote are in the AB magnitudes system (unless explicitly mentioned otherwise) and we adopt Λ CDM cosmology with $\Omega_m = 0.3$, $\Omega_\Lambda = 0.7$ and $H_0 = 70 \text{ km s}^{-1} \text{ Mpc}^{-1}$. For stellar mass estimates we assume the Initial Mass Function (IMF) from Chabrier (2003).

5.2 Data overview & processing

The sample we study is drawn from two large X-ray selected cluster surveys, the Multi-Epoch Nearby Cluster Survey (MENeCS) and the Canadian Cluster Comparison Project (CCCP). A substantial number of spectroscopic redshifts in these cluster fields are available from the literature, specifically the Cana-

dian Network for Observational Cosmology Survey (CNOC; Yee et al. 1996), the Sloan Digital Sky Survey Data Release 10 (SDSS DR10; Ahn et al. 2013), and the Hectospec Cluster Survey (HeCS; Rines et al. 2013). We searched the NASA/IPAC Extragalactic Database (NED)¹ to obtain additional spectroscopic information for galaxies that have not been targeted by these surveys.

In addition to the determination of cluster membership these redshifts allow us to estimate dynamical masses. We refer to Sifón et al. (in prep.) for details. In summary, cluster membership and velocity dispersions are determined using the standard shifting gapper approach (Fadda et al. 1996), see also Sifón et al. (2013). To relate the velocity dispersion σ_v to estimates of R_{200} , the radius at which the mean interior density is 200 times the critical density (ρ_{crit}), and M_{200} , the mass contained within R_{200} , the Evrard et al. (2008) scaling relation is used. See vdB14 (Sect. 2.1) for the application of this scaling relation to the GCLASS cluster sample.

This is a pilot study of 10 clusters which were drawn from those ME-NeaCS and CCCP clusters that were observed with MegaCam (as opposed to the older CFH12k camera) in the g - and r -bands and have additional u - and i -band photometry to allow for a cleaner cluster galaxy selection. The 10 clusters are listed in Table 5.1, and were selected from the larger sample following several criteria. Firstly, they have high dynamical masses to ensure that they are significantly over-dense compared to the field, which will lead to a clean background subtraction. Secondly, they have a large number of spectroscopic members to test the photometric background subtraction method by only considering the spectroscopically confirmed cluster members. Thirdly, we prioritize fields with low amounts of Galactic dust for a cleaner photometric calibration by exploiting the stellar locus. And finally, in order to not underestimate the concentration of the stellar mass distribution, we exclude known major mergers such as Abell 520 (Mahdavi et al. 2007; Clowe et al. 2012).

Figure 5.1 suggests that this is (within a factor of ~ 2) the mass regime of the likely descendants from GCLASS in the local Universe. Curves in this figure connect haloes selected from the Millennium simulation (Springel et al. 2005) at fixed comoving number density, and are thus approximate growth curves. We also show that the CNOC1 cluster sample, studied by Muzzin et al. (2007), is on this approximate evolutionary sequence, and we will also compare our results to theirs in this paper.

5.2.1 Photometry - MegaCam

Each of these clusters is covered by deep photometric data taken through the g -, and r -filters using MegaCam mounted at the Canada-France-Hawaii Telescope (CFHT), which is a 36 CCD imaging array covering a full 1×1

¹<http://ned.ipac.caltech.edu/>

Table 5.1: The 10 Abell clusters selected from MENeaCS and CCCP that form the basis of this study, with their dynamical properties.

Name	z_{spec}	RA ^a J2000	DEC ^a J2000	σ_v^b [km/s]	M_{200}^b [$10^{14} M_{\odot}$]	R_{200}^b [Mpc]	Spec- z Total (Members)
A655	0.127	08:25:29.02	47:08:00.10	934 ± 67	8.7 ± 1.9	1.9 ± 0.1	594 (304)
A1033	0.122	10:31:44.31	35:02:28.71	761 ± 85	4.8 ± 1.6	1.5 ± 0.2	496 (171)
A1068	0.139	10:40:44.46	39:57:11.41	1054 ± 138	12.4 ± 4.8	2.1 ± 0.3	621 (134)
A1835	0.252	14:01:02.04	02:52:42.96	1324 ± 104	23.2 ± 5.5	2.5 ± 0.2	690 (273)
A1914	0.167	14:25:56.69	37:49:00.12	962 ± 83	9.4 ± 2.4	1.9 ± 0.2	700 (264)
A2029	0.078	15:10:56.12	05:44:40.81	1103 ± 64	14.6 ± 2.5	2.3 ± 0.1	800 (315)
A2069	0.114	15:24:08.44	29:52:54.59	1026 ± 76	11.6 ± 2.6	2.1 ± 0.2	821 (347)
A2111	0.228	15:39:40.44	34:25:27.48	964 ± 72	9.1 ± 2.0	1.9 ± 0.1	780 (243)
A2142	0.090	15:58:20.08	27:14:01.11	1105 ± 37	14.6 ± 1.5	2.3 ± 0.1	1869 (1061)
A2261	0.226	17:22:27.16	32:07:57.36	976 ± 197	9.5 ± 5.7	1.9 ± 0.4	644 (214)

^a Coordinates of the BCGs.

^b Dynamical properties estimated by Sifón et al. (in prep.).

square degree. The data are pre-processed using the *Elixir* pipeline (Magnier & Cuillandre 2004). For MENeaCS, photometric data in the two bands have been taken for these clusters, with a significant dither pattern, and a cadence of several weeks to allow for the detection of type Ia supernovae in these clusters. Data for CCCP have been taken consecutively under the best seeing conditions to facilitate weak-lensing measurements. For the cluster Abell 655 we further retrieved archival MegaCam data in the u -, and i -bands.

The approach we take to process these data further is largely laid out in van der Burg et al. (2013, hereafter vdB13, Appendix A), and leads to deep image stacks to measure accurate and precise colours for the purpose of estimating photometric redshifts and stellar masses. We homogenise the PSF of each exposure before stacking, as opposed to homogenising the stack. The former approach leads to a final deep image with a cleaner PSF, especially given that the MENeaCS data have been taken under varying conditions and with substantial dithers. The spatially dependent convolution kernel has been chosen such that the PSF in the final stack has the shape of a circular Gaussian. By applying a Gaussian weight function for aperture fluxes we then optimise colour measurements in terms of S/N (see vdB13 (Appendix A); Kuijken 2008).

Given the large number and the range in image quality of the (2 minute deep) MegaCam exposures for the MENeaCS clusters, we stack only the 20 exposures with the best image quality (IQ, FWHM of the seeing disk) for each cluster and filter. If there are more than 20 exposures with $\text{IQ} < 0.8''$, we combine all exposures that satisfy this limit.

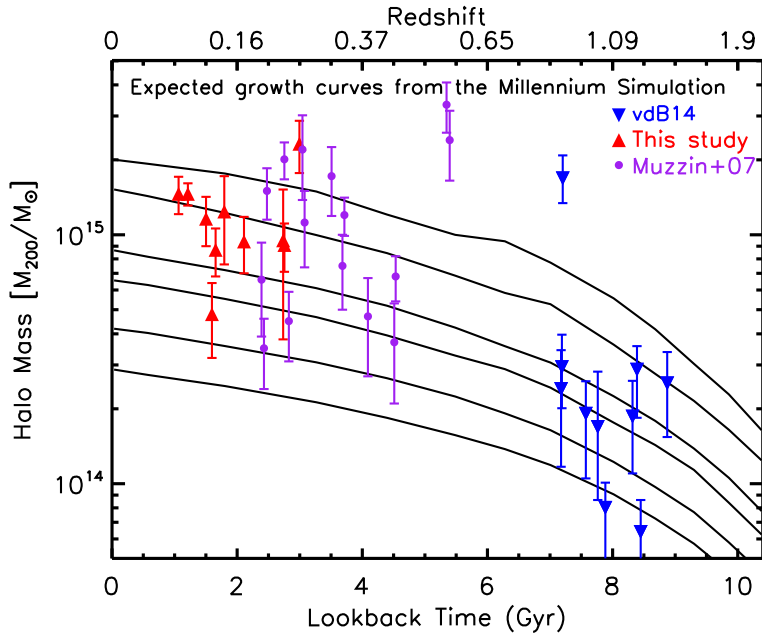


Figure 5.1: Lines: Expected growth curves as a function of cosmic time (or redshift) for massive haloes based on the Millennium simulation (Springel et al. 2005), in which we followed these haloes at fixed comoving number density. Blue: The GCLASS cluster sample studied in vdB14. Red: Low redshift cluster sample studied here. Purple: The CNO1 cluster sample studied by Muzzin et al. (2007). The cluster samples are linked by the evolutionary growth curves.

5.2.2 Photometry - WFC

The Wide-Field Camera (WFC) is an optical mosaic camera consisting of 4 chips, which is mounted on the Isaac Newton Telescope (INT) on La Palma. Its field-of-view (FoV) is roughly 30×30 arcmin, which includes spaces between chips, see the upper left panel of Fig. 5.2. The FoV of the mosaic is smaller than MegaCam, and also does not entirely cover the full extent of the low- z clusters within their projected virial radii. In order to study the distribution and properties of galaxies that extend at least up to the cluster virial radii, we apply a dithered pointing strategy. The angular size of the virial radius depends both on the cluster total mass and its angular diameter distance (through redshift). Our approach is to take 7, 9 or 12 pointings per cluster, depending on their angular sizes. Based on an automated test of 80,000 different pointing configurations we found that these can be combined to cover $>98\%$ of the area contained within projected radii of $1000''$, $1200''$ and $1400''$ (respectively) from their centres to a stacked depth of at least 3 pointings, see Fig. 5.2. By

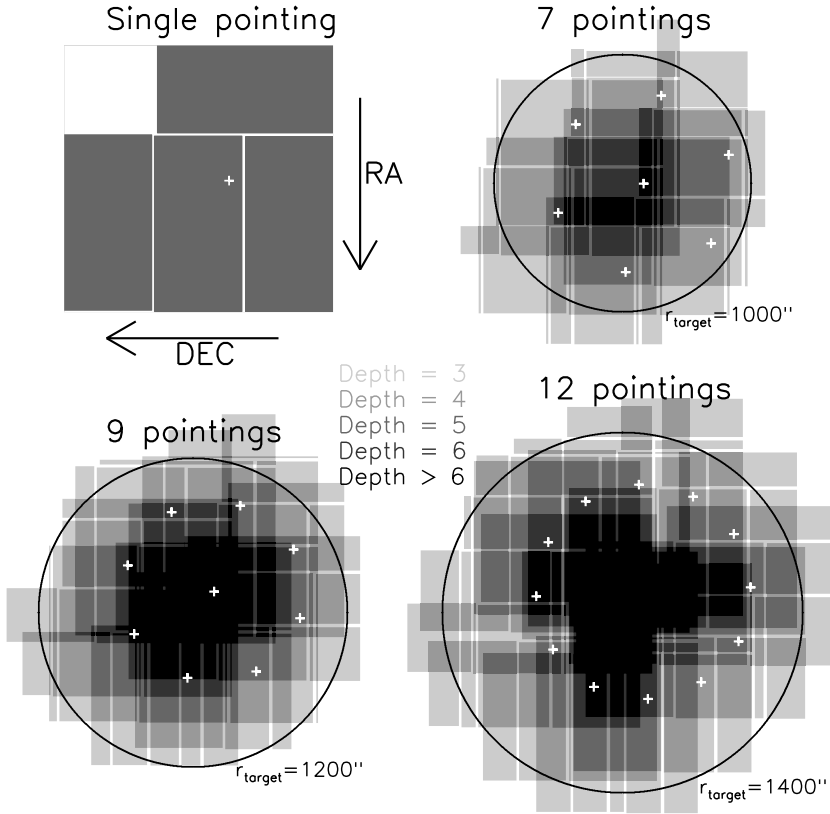


Figure 5.2: Upper left panel: Four CCDs in the WFC mosaic, showing gaps between chips. Other panels: Our optimised pointing strategy (other angular scale than upper left panel), showing how we cover the area within the estimated virial radius by using 7, 9 or 12 dithers. The area where the depth is at least 3 pointings, corresponding to a 1200s integration, is marked.

using exposure times of 400s in the u - and i -band, we reach a depth of at least 1200s over (practically) the entire cluster virial radius. Near the cluster centres there are more overlapping pointings which further enhance the depth. Since the MENeCS and CCCP cluster samples are spread in RA, we have to combine data from observing runs in different seasons. We compiled a data set, totalling 53 nights, see Table 5.2.

Whereas we used pre-processed MegaCam data from the *Elixir* pipeline, there is no similar alternative for WFC. We therefore composed our own reduction pipeline aimed at producing images to measure fluxes in the u -, and i -bands with high photometric accuracy and precision. In summary, we construct calibration frames for each run to subtract the bias, divide through

Table 5.2: Scheduled observations on the Isaac Newton Telescope (INT) in La Palma, using the Wide Field Camera (WFC) for a total of 53 nights.

Year	Month	Days	Number of nights
2010	Jan	5-13	9
2010	Apr	14-18	5
2010	May	6-15	10
2010	Oct	7-14	8
2010	Nov	8-14	7
2011	Apr	4-7, 30	5
2011	May	1-9	9
Total			53

flat-fields, and remove fringing patterns from the *i*-band. We identify and mask pixels that have a nonlinear response to incoming flux, and further remove cosmic rays by using the Laplacian Cosmic Ray Identification method (van Dokkum 2001). We construct a World Coordinate System (WCS) for each image by comparing with catalogues constructed using the MegaCam data for these cluster fields. The astrometric residuals have a low scatter that is typically 0.03-0.15", consistent with statistical uncertainties in centroid determination. We perform a chip-by-chip background subtraction after masking all detected objects.

Similar to what was done for the MegaCam data, we convolve the images with a position-dependent kernel to homogenize the PSF to a circular Gaussian. The FWHM size of this Gaussian for the WFC data is larger than for the MegaCam images, typically around 2". Relative scaling of the photometric zero point between exposures is determined by considering objects that are imaged on overlapping parts between exposures. After these steps, we achieve a systematic uncertainty on flux measurements smaller than 1% in the two bands.

5.2.3 Catalogue construction

Thus far, the photometric flux measurements have been scaled to yield a uniform zero point for each filter. To convert the flux measurements in different filters to the same relative photometric scale, we exploit the universal properties of the stellar locus. This method is described in High et al. (2009), and we also applied this calibration technique to the GCLASS data (see vdB13, Appendix A). Figure 5.3 demonstrates this technique for the four bands available to us, after selecting stars based on their measured flux and angular size.

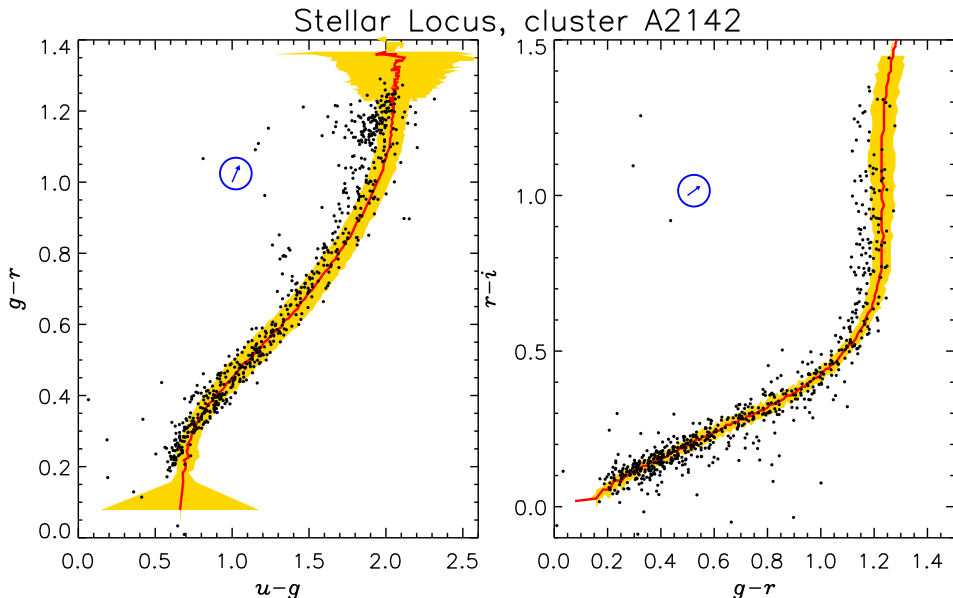


Figure 5.3: The stellar locus in 2 panels, combining the ugr (left panel) and gri (right panel) aperture fluxes of stars. *Red lines and orange contours:* colours of stars and $1\text{-}\sigma$ region of intrinsic scatter in the Covey et al. (2007) catalogue, converted to the CFHT filter set. *Black points:* colours of stars in the field of Abell 2142 after calibration. *Blue arrow:* Galactic dust reddening vector for this field.

The red line and associated $1\text{-}\sigma$ region of intrinsic scatter (orange) are based on the Covey et al. (2007) catalogue of stellar colours. Since this reference stellar catalogue is based on the SDSS filter system, we use linear colour terms to convert it to the CFHT filter set². Colour terms result in rotations and transformations of the stellar locus in this colour-colour plane, and can therefore be obtained from the distribution of stellar colours itself. We estimate the following linear colour term to put the WFC measurements onto the MegaCam photometric system.

$$u_{\text{MegaCam}} = u_{\text{WFC}} - 0.150 \cdot (u_{\text{WFC}} - g_{\text{MegaCam}}) \quad (5.1)$$

$$i_{\text{MegaCam}} = i_{\text{WFC}} - 0.120 \cdot (r_{\text{MegaCam}} - i_{\text{WFC}}) \quad (5.2)$$

We use maps from Schlegel et al. (1998) to find the average extinction caused by dust in the Milky Way that is obscuring each cluster. Since the flux extinction is wavelength dependent, we estimate the extinction in each band

²<http://www3.cadc-ccda.hia-ihp.nrc-cnrc.gc.ca/megapipe/docs/filters.html>

separately and correct the fluxes for this effect. The complication is that the stars in the field will have a range of distances to Earth, and thus stars that are further away have a larger amount of dust obscuration. Since we consider stars in a fixed window of apparent magnitude (e.g. $18 < \text{mag}_r < 20$), we expect the redder stars to be more nearby and thus be mostly in front of the dust column. Bluer stars on the other hand have a higher luminosity and therefore are typically at a larger distance from Earth. In Fig. 5.3 the dust reddening vector is indicated in both panels, and the stars at the red (upper right) part of the stellar locus have been over-corrected for Galactic dust extinction. However, the extragalactic sources in which we are interested are corrected properly for dust. In fields that are not significantly obscured by Galactic dust (i.e. when at high Galactic latitude) the stellar locus calibration technique works best, since the shape of the stellar locus will be least affected.

The MegaCam r -band is calibrated in absolute terms with respect to standard star fields, and most of these data are taken under photometric conditions. Therefore we adjust the u -, g -, and i -band zero-points to bring the stars in the field in line with the stellar locus, and we keep the r -band zero-point unchanged. We can test the robustness of the r -band absolute calibration in the following way. We correct the zero-points in each WFC exposure for differences in exposure time and airmass (using as reference 400s and an airmass of 1.3). This gives an indication of the atmospheric transmission, which we plot as a function of time (JD). Since many clusters were observed in the same night, and in most nights the conditions changed very gradually, outliers in these diagrams are indicative of problems in absolute calibration. For example, if for a given cluster the estimated atmospheric transmission is systematically off-set for all exposures in both filters, this is a strong indication of a calibration problem. We use this information to fine-tune the zero-points further. For fields that suffer from a large Galactic dust column this is our main method for photometric calibration. The apparent magnitude after atmospheric extinction is given by $m = m_1 + k_\lambda \times (\text{airmass} - 1)$, where m_1 is the magnitude for a reference airmass of 1, and k_λ is the wavelength dependent extinction coefficient. The atmospheric extinction coefficients in the u -, and i -band we find to be 0.50 and 0.06, respectively.

Because of the excellent image quality and depth in the MegaCam r -band stacks, we use these as our detection images. For galaxies with redshift $z \lesssim 0.4$ the r -band filter probes the rest-frame SED redward of the 4000\AA break, which makes the observed r -band flux a reasonable proxy for stellar mass. We measure aperture fluxes in the seeing-homogenized images using a Gaussian weight function, which we adjust in size to account for different PSF sizes. To estimate errors on these measurements, we randomly place apertures with the same shape on the seeing-homogenized images and measure the dispersion in the background. Since the flux measurements of our faint sources are background-noise limited, this way we probe the dominant component of the aperture flux

Table 5.3: The photometric data set used in this study. Unless indicated otherwise, u -, and i -band photometry is obtained using the Wide Field Camera at the INT, and g -, and r -band photometry comes from MegaCam at the CFHT. The limiting magnitudes reported are median $5\text{-}\sigma$ flux measurement limits for point sources measured with a Gaussian weight function. For all clusters apart from A655, we had to expand the size of the Gaussian aperture weight function substantially to accommodate the INT image quality.

Name	u_{lim} [mag _{AB}]	g_{lim} [mag _{AB}]	r_{lim} [mag _{AB}]	i_{lim} [mag _{AB}]
A655	25.9 ^a	26.0	25.5	25.0 ^a
A1033	24.0	25.0	24.4	22.9
A1068	24.8	25.1	24.4	23.6
A1835	24.5	24.8	24.4	23.6
A1914	24.0	25.1	24.5	23.2
A2029	24.2	24.6	24.0	23.4
A2069	24.0	25.1	24.5	23.2
A2111	24.4	25.2	24.6	23.1
A2142	24.3	24.8	24.2	22.5
A2261	24.3	25.0	24.4	21.8
COSMOS	26.6 ^a	26.3 ^b	26.4 ^b	26.0 ^b

^a MegaCam, Canada-France-Hawaii Telescope (CFHT)

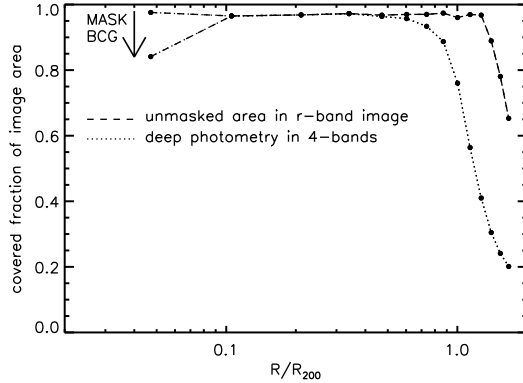
^b SuprimeCam, Subaru

error. For the WFC data we compare aperture flux measurements for each source in the individual exposures and (through sigma-clipping) combine this into a flux measurement and error. Using these estimated errors we give the median depth of each image in Table 5.3, considering only positions where the image depth is at least 1200s. Note that the $5\text{-}\sigma$ depth in these apertures is also affected by the seeing in the WFC images, since the sizes of the apertures need to be expanded proportionally to the images with inferior IQ. Note that for cluster Abell 655 we have deep 4-band coverage with CFHT MegaCam.

We mask stars brighter than $V=15$ (automatically selected from the Guide Star Catalog II (GSC-II Lasker et al. 2008)) and their diffraction spikes and haloes in the images, which typically cover a few percent of the area. The dashed line in Fig. 5.4 shows the imaged fraction of the ensemble cluster (i.e. 10 clusters combined) on the detection images as a function of radial extent from the BCG, as scaled with the virial radius R_{200} (Table 5.1). The detection images cover an area (excluding locations with bright stars) larger than the virial radius for each cluster. We also show the fractional area covered with 4-band photometry (depth at least 1200s in each band). The inner bin is

partly covered by the BCG, which does not allow for the detection of satellite galaxies, and this area is therefore also masked.

Figure 5.4: Fractionally covered area of the ensemble cluster as a function of radial distance from the BCG. *Dashed line:* imaged fraction of the ensemble cluster (i.e. 10 clusters combined) on the detection images. This excludes locations with bright stars. *Dotted line:* fractional area covered with 4-band photometry (depth at least 1200s in each band). The effective area in the inner bin is reduced due to the pixels covered by the BCG.



5.3 Analysis

We perform two parallel and (largely) independent analyses to measure the radial stellar mass distribution in the ensemble cluster. We then compare results from these analyses as a robustness test.

5.3.1 Method 1 - statistical background subtraction

The first approach is to estimate a photometric redshift for every galaxy in the cluster images, apply a cut in redshift space ($z < 0.3$) and statistically subtract galaxies in the fore-, and background by applying the same redshift cut to the reference COSMOS field. We use *ugri* photometric data in both our cluster fields and the COSMOS field to estimate photometric redshifts using the EAZY (Brammer et al. 2008) photometric redshift code. We use an *r*-band selected catalogue from the COSMOS field which has been constructed in the same way as the K-band selected catalogue of Muzzin et al. (2013b). The field has an effective area of 1.62 deg², and we only use data in the *ugri*-filters to provide a fair reference to our cluster sample.

Because our bluest band is the *u*-band, it is difficult to constrain the location of the 4000Å-break for galaxies at low ($z \lesssim 0.15$) redshift, since the break is then located in this filter. Like many redshift codes, EAZY applies a flux-, and redshift-based prior, which gives the redshift probability distribution for a galaxy of a given *r*-band flux $P(z,r)$. This prior has a strong effect in estimating the most probable redshift of a galaxy when the *u-g* colour loses its constraining power (as is the case for redshifts $z \lesssim 0.15$). In the low redshift

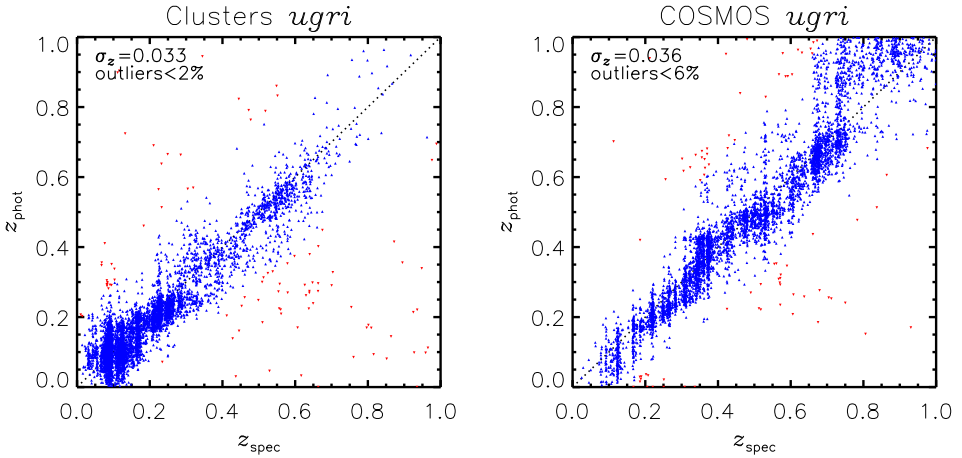


Figure 5.5: *Left panel:* Spectroscopic versus photometric redshifts for the 10 clusters in this study. Outliers, objects for which $\frac{\Delta z}{1+z} > 0.15$, are marked in red. The outlier fraction is less than 2%, the scatter (in $\frac{\Delta z}{1+z}$) of the remaining objects is $\sigma_z = 0.033$. *Right panel:* Same for the COSMOS field, but only using the *ugri*-filters. The outlier fraction and scatter are slightly larger as a result of deeper spectroscopic data (also at higher redshift where the *ugri* filters lose their constraining power).

regime ($z \lesssim 0.3$), the comoving volume element $dV_c/dz/d\Omega$ is a strong function of redshift (e.g. Hogg 1999), but the luminosity function does not evolve strongly in this redshift range (e.g. Muzzin et al. 2013a). Therefore the prior in this regime is decreasing rapidly towards $P(z,r)=0$ for $z = 0$, independently of the r -band flux. Consequently, according to the prior, it is much more likely to find a galaxy at $z = 0.2$ compared to e.g. $z = 0.1$. Once a field is centred on a massive cluster at low redshift, this prior is no longer applicable since the probability of finding a galaxy to be at the cluster redshift is significantly increased. Besides the general redshift and flux-dependence of the prior, one should therefore include information on e.g. the galaxy’s distance to the cluster centre to the prior. This however, is beyond our requirements, since we subtract the field statistically, and the volume (and therefore the number of contaminating galaxies) in the fields is small below $z < 0.3$. A correction on the prior will only affect redshifts at lower redshift, and will therefore not change which galaxies survive the redshift cut. For galaxies with a photometric redshift below $z_{\text{EAZY}} = 0.16$ we apply a simple correction of the form $\text{photo-}z = 0.16 \cdot (z_{\text{EAZY}} - 0.10)/0.06$ to the EAZY output, and plot a comparison between spec- z ’s and photo- z ’s in Fig. 5.5. We apply the same correction to the EAZY output on the COSMOS catalogue.

Since the distance modulus is a strong function of redshift in this regime, a small uncertainty in photometric redshift will result in a relatively large un-

certainty in luminosity (or stellar mass) of a galaxy. Given that the cluster redshift is well-known, we will assign the distance modulus of the cluster to every galaxy in the cluster fields. In order to properly subtract contaminating fore- and background galaxies, we also assign this distance modulus to each galaxy in the reference COSMOS field (after applying the redshift cut). We then use the SED-fitting code FAST (Kriek et al. 2009) to estimate the stellar-mass-to-light ratio (M/L) (in the r -band) for each galaxy. For this we again assume the same redshift and distance modulus (corresponding to the cluster) for each galaxy. Then in each of the radial bins (which are scaled by the size R_{200} of each cluster) we measure the area (in angular size) that is not masked by bright stars (which is also different for each cluster through its angular diameter distance) and estimate the expected number of sources in this area in the COSMOS field. We estimate the total stellar mass and corresponding error for those sources by performing a series of 10,000 Monte-Carlo realisations of the background, by randomly drawing sources from the COSMOS catalogue. We subtract the estimated field values from the raw number counts to obtain the cluster stellar mass density profile. In Appendix 5.A we perform a consistency check of this method by considering the stellar mass distribution of galaxies located far away from the cluster centre and comparing this to the field stellar mass distribution. We find no significant systematic difference between the field probed around the cluster and the reference COSMOS field, which strengthens our confidence in this method.

5.3.2 Method 2 - spectroscopic approach

In the method described above, we subtract the galaxies in the fore-, and background statistically based only on the photometric data. However, as discussed in Sect. 5.2, we can use a substantial amount of spectroscopic redshifts in the cluster fields from the literature. In this second approach we measure the stellar mass contained in spectroscopically confirmed cluster members to provide a lower limit to the full stellar mass distribution.

Since the spectroscopic data set is obtained after combining several different surveys, the way the spectroscopic targets have been selected is not easily reconstructed. Fig. 5.6 shows the spectroscopic completeness for all galaxies with a photometric redshift $z < 0.3$ as a function of stellar mass (assuming the same distance modulus as the cluster redshift), and for different radial bins. For stellar masses $M_* > 10^{11} M_\odot$, the completeness is very high ($> 80\%$). Since these objects constitute most of the total stellar mass distribution (see vdB14 (Fig. 2) for this argument), we can get a fairly complete census of stellar mass by just considering the galaxies for which we have a spectroscopic redshift. Note however that the stellar mass contained in the spectroscopically confirmed members is a lower limit to the total, but since the spectroscopic completeness is not a strong function of radial distance, we expect to miss

a similar stellar mass fraction at different distances. We obtain stellar mass estimates for these spectroscopically confirmed cluster galaxies using the SED fitting code FAST. We run 10,000 Monte-Carlo realisations in which we randomly draw spectroscopic members in each bin to estimate the $1-\sigma$ statistical uncertainty on each data point.

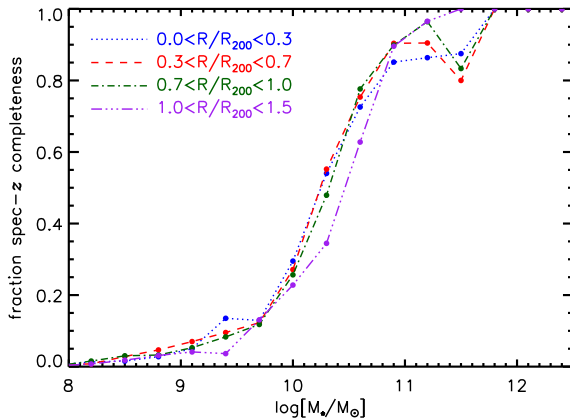


Figure 5.6: Spectroscopic completeness for sources with a photometric redshift $z < 0.3$ as a function of stellar mass (assuming the same distance modulus as the cluster redshift). The four lines show different radial bins. The completeness is similar for each bin, and is larger than 80% for stellar masses $M_* > 10^{11} M_\odot$.

5.4 Results and comparison at low- z

In this section we present the galaxy number and stellar mass density distributions of the 10 clusters we study, based on the two independent analyses described in Sect. 5.3. We compare these results to literature measurements at comparable redshifts ($z < 0.3$). In Sect. 5.5 we discuss a possible evolutionary scenario by comparing these results to measurements at higher redshifts.

5.4.1 Galaxy number density profile

Ignoring baryonic physics, the galaxy number density distribution in cluster haloes can be compared to the distribution of sub-haloes in N-body simulations as a test of Λ CDM. Due to mergers and interactions between galaxies, the number density distribution of galaxies may be different for galaxies with different stellar masses. Figure 5.7 shows the projected galaxy number density distribution for galaxies with stellar masses exceeding $M_* > 10^9 M_\odot$ (left panel), and $M_* > 10^{10} M_\odot$ (right panel) in the ensemble cluster. These cuts are chosen to facilitate comparisons with literature measurements of different depths. Before stacking the 10 clusters, their radial distances to the BCGs are scaled by R_{200} , but the BCGs themselves are not included. The blue points show the raw number counts, including the field. After the field (red points) is subtracted, we obtain the black data points as our estimate for the cluster.

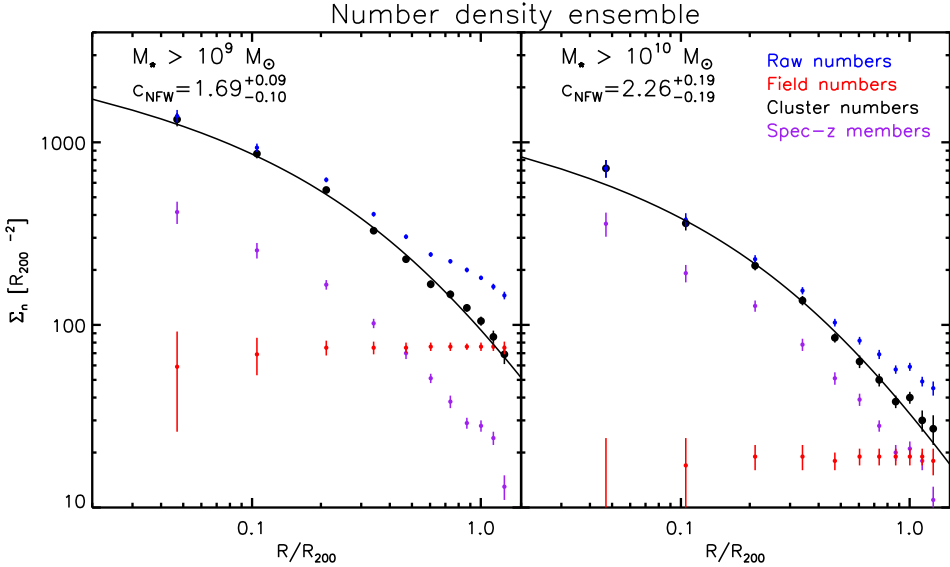


Figure 5.7: Galaxy number density distributions in the mass range $M_* > 10^9 M_\odot$ (left panel), and $M_* > 10^{10} M_\odot$ (right panel) for the ensemble cluster at $z \sim 0.15$. Error bars give Poisson sampling errors. Black points with the best fitting projected NFW functions are our best estimate for the cluster number counts. Purple points indicate the number of spectroscopically confirmed cluster members.

We fit projected NFW profiles to the data points, minimizing the χ^2 value and using the area-weighted centres of the 2D annulus-shaped bins. The best fitting functions give reasonable fits to the data (see the reduced χ^2 values in Table 5.4). We give the best-fitting concentration parameters and their marginalized errors in the table, and show the best-fitting functions in Fig. 5.7. The purple points show the numbers of spectroscopically confirmed member galaxies.

We find a significant difference in the best fitting concentration ($1.69^{+0.09}_{-0.10}$ versus $2.26^{+0.19}_{-0.19}$) between the different (though overlapping) mass bins ($M_* > 10^9 M_\odot$ and $M_* > 10^{10} M_\odot$, respectively), indicating that the more massive galaxies are more strongly concentrated in the cluster ensemble. The effect of dynamical friction, which is more efficient for massive galaxies, can be the cause of this mass segregation.

The number density profiles in the literature that we can compare with have been measured on shallower data. Lin et al. (2004) study the average number density profile of a sample of 93 clusters at $0.01 < z < 0.09$ with 2MASS K-band data. They are able to measure down to a magnitude limit (Vega) of $K_{s,\text{lim}} = 13.5$, which corresponds to $M_* \approx 10^{10} M_\odot$ at $z = 0.05$ (Bell & de Jong 2001). Although they study systems with a lower mass range than

Table 5.4: Parameters describing the best fitting NFW profile to the radial density distributions. Reduced χ^2 values are given (10 to 12 degrees of freedom per cluster).

Cluster	Stellar Mass density		Number density $M_\star > 10^9 M_\odot$		Number density $M_\star > 10^{10} M_\odot$	
	c_{NFW}	$\chi^2/d.o.f.$	c_{NFW}	$\chi^2/d.o.f.$	c_{NFW}	$\chi^2/d.o.f.$
A655	$2.83^{+0.76}_{-0.66}$	1.19	$3.78^{+0.52}_{-0.47}$	1.53	$3.68^{+0.90}_{-0.71}$	0.65
A1033	$5.53^{+2.42}_{-1.71}$	1.08	$3.49^{+0.76}_{-0.67}$	1.39	$4.16^{+1.52}_{-1.19}$	0.83
A1068	$1.07^{+0.71}_{-0.47}$	0.76	$1.21^{+0.57}_{-0.38}$	2.13	$1.16^{+0.57}_{-0.43}$	1.01
A1835	$3.35^{+0.90}_{-0.71}$	1.73	$1.97^{+0.29}_{-0.28}$	3.42	$3.25^{+0.71}_{-0.57}$	1.67
A1914	$5.44^{+2.28}_{-1.85}$	0.95	$3.02^{+0.48}_{-0.47}$	2.27	$4.35^{+1.33}_{-1.14}$	0.77
A2029	$0.88^{+0.43}_{-0.24}$	0.63	$1.21^{+0.19}_{-0.19}$	0.46	$1.40^{+0.38}_{-0.38}$	0.84
A2069	$1.74^{+0.62}_{-0.48}$	1.29	$1.40^{+0.24}_{-0.28}$	1.10	$2.07^{+0.71}_{-0.52}$	0.98
A2111	$3.87^{+1.28}_{-1.04}$	0.82	$2.45^{+0.43}_{-0.38}$	0.26	$2.73^{+0.81}_{-0.57}$	0.57
A2142	$0.93^{+0.28}_{-0.24}$	0.33	$0.83^{+0.14}_{-0.14}$	0.88	$1.21^{+0.33}_{-0.28}$	0.90
A2261	$1.69^{+0.43}_{-0.29}$	0.84	$1.88^{+0.29}_{-0.19}$	0.89	$2.21^{+0.52}_{-0.43}$	0.59
ensemble	$1.92^{+0.19}_{-0.14}$	0.81	$1.69^{+0.09}_{-0.10}$	1.74	$2.26^{+0.19}_{-0.19}$	1.40

we probe, they find a number density concentration of $c = 2.90^{+0.21}_{-0.22}$, which is comparable to the value of $c = 2.26^{+0.19}_{-0.19}$ that we find for the high mass galaxies ($M_\star > 10^{10} M_\odot$).

Budzynski et al. (2012) measure the radial distribution of satellite galaxies in groups and clusters in the range $0.15 < z < 0.40$ from the SDSS DR7. For the satellite galaxies they apply a magnitude limit of $M_r = -20.5$. This corresponds to about $M_\star = 10^{10.5} M_\odot$ for galaxies with a high M/L. The best fitting concentration parameter of $c \sim 2.6$ they find is also consistent with our measurement for the high-mass sample. They find that the concentration of satellites falls slightly as their brightness increases, but note that they compared satellites in a higher luminosity range with respect to our study.

vdB14 measure the number density distribution of the GCLASS cluster ensemble at $z \sim 1$ down to a stellar mass of $M_\star = 10^{10.2} M_\odot$. They measure an NFW concentration parameter of $c = 5.14^{+0.54}_{-0.63}$, which is significantly higher than the value we find for the low- z sample. A comparison between the number density distribution and the stellar mass density distribution presented in vdB14 suggests that the more massive galaxies are situated closer towards the cluster centres than lower mass galaxies, which is qualitatively consistent with the trend we find here.

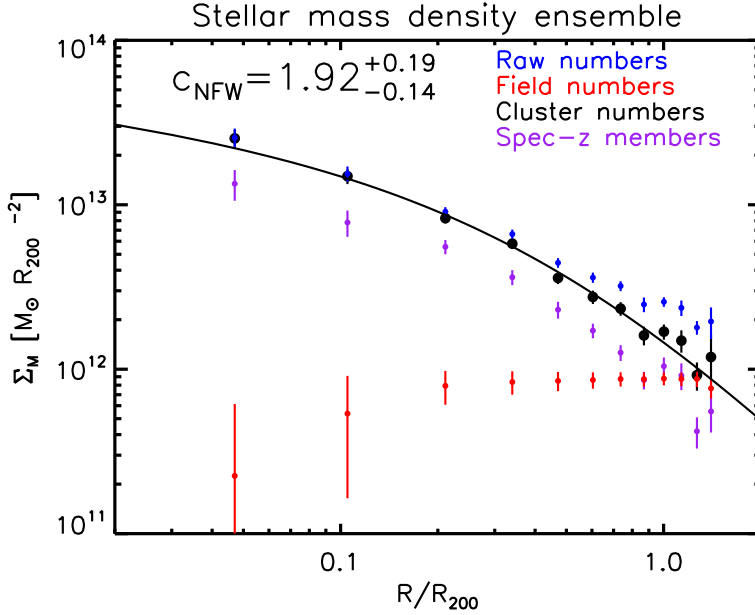


Figure 5.8: Stellar mass density distribution of the ensemble cluster at $z \sim 0.15$. Black points with corresponding Poisson sampling errors are our best estimate for the cluster stellar mass distribution. The best fitting projected NFW function is also shown. The purple points give the stellar mass distribution in spectroscopically confirmed cluster members.

5.4.2 Stellar mass density profile

Whereas the number density of galaxies can change as a result of mergers, the stellar mass density is not immediately affected by such processes if we ignore the build-up of ICL and stellar mass in the central galaxies, because these components are not included in these profiles. Figure 5.8 shows the radial distribution of stellar mass in the ensemble cluster. Radial distances are normalised by the clusters' scale radii R_{200} . Black data points give the background-subtracted (i.e. blue minus red) cluster stellar mass distribution. Errors are Poisson sampling errors, compared to which the stellar mass errors of individual galaxies can be ignored. The purple points show the numbers of spectroscopically confirmed member galaxies. The spectroscopic completeness in terms of total stellar mass is larger than 50%, and does not significantly depend on radial distance (cf. Fig. 5.6). Stellar mass distributions for individual clusters are presented in Figs. 5.9 & 5.10.

We fit a projected NFW profile to the black data points, minimizing the χ^2 value and using the area-weighted centres of the 2D annulus-shaped bins. The best fitting function gives a reasonable fit to the data (see the reduced χ^2 value

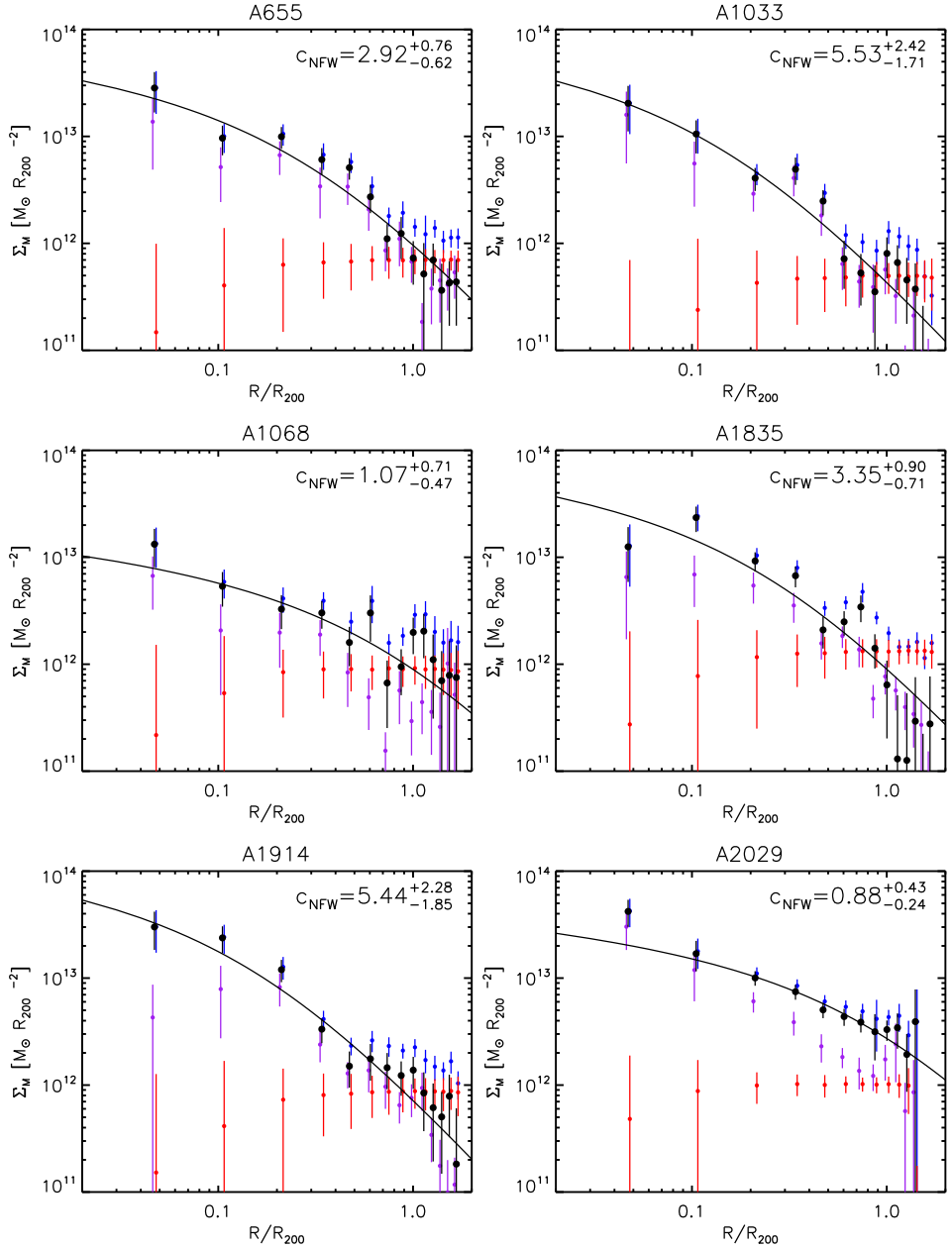


Figure 5.9: Stellar mass density distribution of the individual clusters. Black points with corresponding Poisson sampling errors are our best estimate for the cluster stellar mass distribution. The best fitting projected NFW functions are also shown. The purple points give the stellar mass distribution in spectroscopically confirmed cluster members.

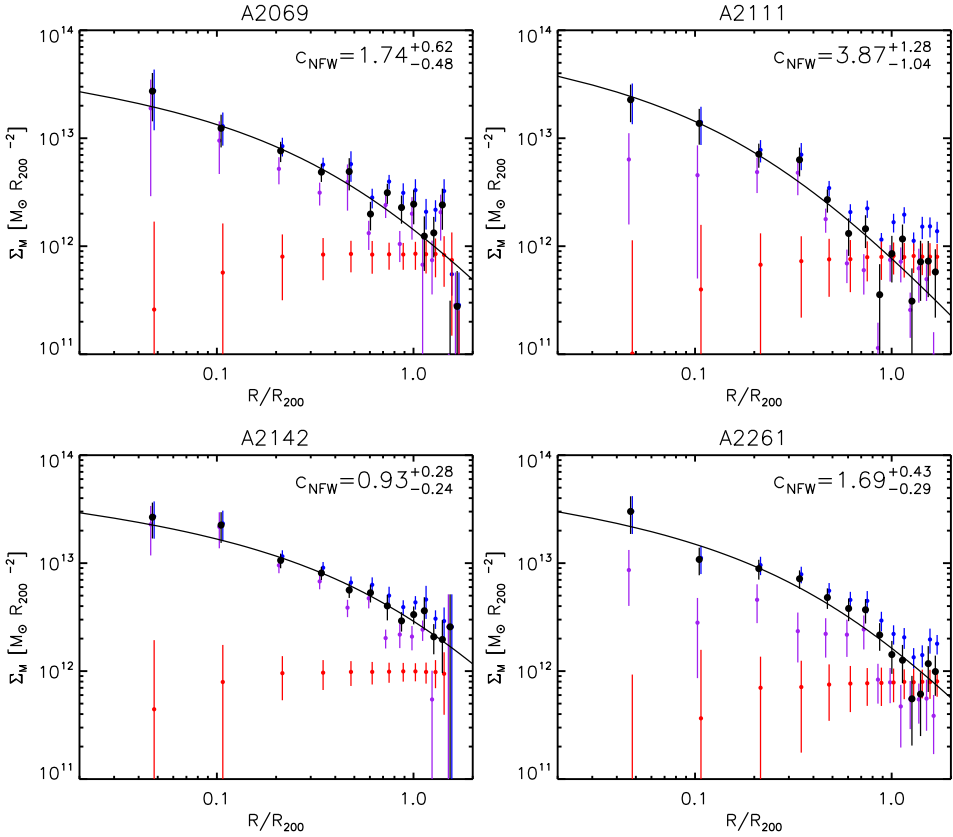


Figure 5.10: Figure 5.9 continued...

in Table 5.4). The best fitting concentration parameter for the ensemble is $c = 1.92^{+0.19}_{-0.14}$. Errors on this parameter are marginalized over the normalisation, and the best fitting NFW profile is shown in Fig. 5.8. When we fit a projected NFW profile to the spectroscopic data (purple points) we find $c = 2.21^{+0.19}_{-0.28}$, which agrees to within $1\text{-}\sigma$ with the photometric estimate. The normalisation is different by 0.22 dex. The fact that the background subtraction method yields the same concentration parameter is a strong robustness test.

We also fit projected NFW profiles to the stellar mass distributions for the individual clusters (Figs. 5.9 & 5.10), and present the best-fitting concentration parameters in Table 5.4. Although the uncertainties on the concentration parameters are relatively large due to lower number statistics compared to the ensemble, the scatter between the individual measurements seems to be larger than the measurement errors. Some sources of this intrinsic scatter may be different orientations on the sky, centroiding uncertainties and different halo

mass assembly histories for the clusters. We measure the intrinsic scatter in the concentration parameter by minimizing the log-likelihood

$$-2 \ln \mathcal{L} = 2 \sum_{i=1}^n \ln w_i + \sum_{i=1}^n \left(\frac{c_i - c_{\text{ensemble}}}{w_i} \right)^2, \quad (5.3)$$

where index i runs over the 10 clusters in our sample, and where w_i is a combination of statistical uncertainties on each individual measurement and a Gaussian intrinsic scatter $\sigma_{c,\text{int}}$, such that $w_i = \sqrt{\sigma_{c,i}^2 + \sigma_{c,\text{int}}^2}$. See also Hoekstra et al. (2011) for a comprehensive description of this method to estimate the intrinsic scatter. We find an intrinsic scatter in the concentration parameter of $\sigma_{c,\text{int}} = 0.70^{+0.33}_{-0.22}$ (or $\sigma_{\log_{10}c,\text{int}} = 0.25 \pm 0.05$ dex).

Muzzin et al. (2007) measure the K-band luminosity profiles for a stack of 15 CNOC1 (Yee et al. 1996) clusters in the redshift range $0.2 < z < 0.5$. In this redshift range, the luminosity in the K-band is expected to be a good proxy for stellar mass. They find a concentration of the luminosity density of $c = 4.28 \pm 0.70$. Although the redshift range of the CNOC1 sample is different from ours, they are approximate progenitors of the sample we study (see Fig. 5.1).

In vdB14 we present the stellar mass density distribution of the GCLASS cluster sample at $z \sim 1$, and find a relatively high concentration of $c = 7.12^{+1.53}_{-0.99}$. These systems are likely to grow into clusters that are only a factor of ~ 2 less massive than the low- z clusters studied in this paper. Comparisons among these results indicate that the stellar mass distribution in clusters evolves significantly over cosmic time.

5.5 The evolving stellar mass distribution

We have performed a measurement of the stellar mass distribution in clusters in the local ($0.07 < z < 0.26$) Universe. In Fig. 5.11 we compare this measurement to results from the GCLASS and CNOC1 surveys, which suggests that the stellar mass distribution evolves significantly between $z \sim 1$ and the local Universe.

We note that the concentration parameters we are comparing are defined with respect to the cluster scale radii R_{200} , which correspond to a physical size of ~ 1 Mpc for GCLASS, and $R_{200} \sim 2$ Mpc for the low- z sample. If the critical density ρ_{crit} , with respect to which the scale radii are defined, evolves, the measured concentrations will change, even if the physical profile remains constant over time (pseudo-evolution, e.g. Diemer et al. 2013). Nonetheless, clusters in this mass regime ($10^{14} < M_{200}/M_{\odot} < 10^{15}$) are expected to grow by a factor of ~ 3.0 between $z = 1$ and $z = 0$ (Wechsler et al. 2002; Springel et al. 2005). In Fig. 5.12 we compare the cluster stellar mass density profiles at the

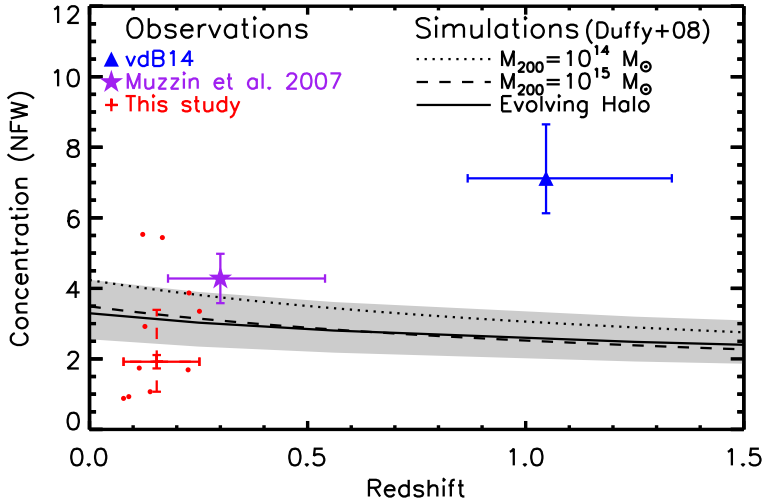


Figure 5.11: *Black lines:* The NFW concentration in the sample of relaxed haloes from Duffy et al. (2008) as a function of redshift. *Dotted and dashed:* Haloes of a given mass as a function of redshift. *Solid:* NFW concentration of a halo that is evolving in mass, with scatter given by the shaded region. The full sample from Duffy et al. (2008) has a slightly lower average concentration, but a larger scatter. *Blue:* Stellar mass density concentration in GCLASS from vdB14. *Purple:* K-band luminosity density concentration in CNOC1 from Muzzin et al. (2007). *Red:* Stellar mass density concentration for the clusters used in this study. The dashed error bar on the mean represents the best-fit log-normal intrinsic scatter on the concentration. Red points give measured concentrations for the individual clusters in MENaCS/CCCP.

same physical scale, so that we circumvent the effect of pseudo-evolution, and study directly how the profiles of these clusters evolve since $z \sim 1$. Given that the current low- z sample is a factor ~ 1.7 more massive than the descendants from GCLASS are expected to be (see Fig. 5.1), and the relation between stellar mass and halo mass $M_* \propto M_{500}^{0.71 \pm 0.04}$ from Lin et al. (2012) (also see vdB14 (Fig.5)), we multiplied the low- z profile by a factor of 0.7 to better resemble the expected descendant sample from GCLASS. The exact value of this correction factor does not have a significant impact on the interpretation.

Figure 5.12 suggests that, although the total stellar mass of these clusters grows substantially since $z \sim 1$, the stellar mass density in the cluster core ($R < 0.2$ Mpc) drops significantly during the same period. Since in our analysis we did not take account of the ICL component, and excluded the BCGs from the fit, the build-up of stellar mass in these components may be responsible for the observed evolution.

Massive galaxies close to the BCG are expected to merge with the central galaxy on a relatively short time-scale, and play a dominant role in the build-

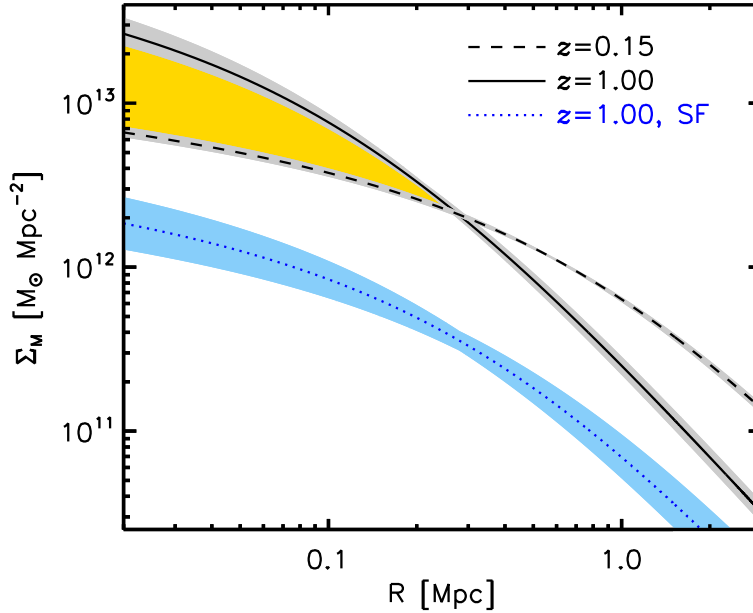


Figure 5.12: *Black solid:* The average stellar mass density profile of GCLASS, in physical units. *Black dashed:* The stellar mass density profile at low- z , at the same physical scale. *Blue solid:* The average stellar mass density profiles of the star-forming galaxies in GCLASS, which is the most recently accreted population of galaxies. Shaded regions mark 1- σ uncertainty regions on the NFW parameters. The orange region marks the part of the $z \sim 1$ profile that is in excess of the $z \sim 0.15$ profile.

up of stellar mass in the BCG (e.g. Burke & Collins 2013; Lidman et al. 2013). Several studies have found that the stellar mass in central galaxies is related to the halo mass of the system (e.g. Lidman et al. 2012; Behroozi et al. 2013, vdB14), with a relation that is approximately $M_{\text{BCG}} \propto M_{200}^{0.5}$ in this mass and redshift regime. If we integrate the mass enclosed in the $z \simeq 1$ profile that is in excess of the $z \simeq 0.15$ profile (i.e., the orange region in Fig. 5.12), we find that this is on average about $2 \times 10^{11} M_{\odot}$ per cluster. Given that the BCGs in the GCLASS clusters have typical stellar masses of $M_{\star, \text{BCG}} \simeq 3 \times 10^{11} M_{\odot}$ (vdB14, Table 2), and the halo masses are expected to grow by a factor of ~ 3 since $z \sim 1$, we find that the growth of the stellar mass in the central galaxies can readily explain the decreasing profile.

Furthermore, dynamical interactions between galaxies in the cluster may lead to a build-up of the ICL component. Gonzalez et al. (2013) measure the contribution of the BCG+ICL component to the total luminosity of a sample of galaxy groups and clusters at $z \sim 0.1$ (for estimates of the ICL component, also see Zibetti et al. 2005; Sand et al. 2011). Gonzalez et al. (2013) find that

the BCG+ICL fraction is a decreasing function of system mass (or velocity dispersion), and is about 30% of the total luminosity within R_{500} for systems with $\sigma = 1000 \text{ km s}^{-1}$. Around $z \sim 1$, the stellar mass fraction in the ICL is expected to be significantly lower (Burke et al. 2012) (this trend is also reproduced with semi-analytic models, Contini et al. (2013)). The development of an ICL component may therefore also contribute to an evolution in the observed stellar mass density profile.

Substantial growth onto the outskirts of the clusters is also required to explain the observed evolution since $z \sim 1$. In Fig. 5.12 we show the stellar mass density profile of the star-forming galaxies in GCLASS, which are expected to be accreted from the field relatively recently compared to the more concentrated quiescent population (vdB14). Given that this population is described by a radial distribution that is similar in shape to the total stellar mass distribution at lower redshift, a continuation of star-formation and accretion at these locations could explain the stellar mass density evolution on the outskirts.

Under the assumption that galaxies populate sub-haloes and that these systems are accreted onto the clusters since $z = 1$, it is expected that dark-matter haloes also accrete matter onto the outskirts. This effect is indeed observed in N-body simulations (Duffy et al. 2008), if these simulations are compared on the same physical scale. The substantial difference between the concentration simulated with N-body codes and the observed distribution of stellar mass may be reconciled by modifying the stellar mass fraction of infalling haloes in semi-analytic models. The observed evolution of the stellar mass distribution is also a stringent test for existing and future hydrodynamical simulations (e.g. Schaye et al. 2010; Cen 2014).

5.5.1 Selection effects in GCLASS

Given the significant evolution that is observed between the GCLASS sample and the low- z descendant sample, we have to consider the possibility that this inferred evolution is caused by the way these samples are selected. Since it is impossible to select a cluster sample based on halo mass, different selection methods (X-ray, SZ-, or galaxy selections) potentially result in a biased sample of clusters.

The GCLASS sample consists of 10 clusters drawn from the 42 degree Spitzer Adaptation of the Red-sequence Cluster Survey (SpARCS, Muzzin et al. 2009; Wilson et al. 2009; Demarco et al. 2010). Clusters in SpARCS were detected using the red-sequence detection method developed by Gladders & Yee (2000), and expanded on in Muzzin et al. (2008). In summary, this detection method was applied to the optical+InfraRed data in SpARCS, so that the $z' - 3.6\mu\text{m}$ colour was used to detect clusters at redshifts $z > 0.8$ after convolving the galaxy number density maps with an exponential kernel (see

Gladders & Yee 2000, Eq. 3). Richnesses were measured in fixed apertures with a radius of 500 kpc, after which the richest systems were considered for follow-up photometry and spectroscopy. Muzzin et al. (2012) describes how this GCLASS follow-up sample was drawn from the richest systems after optimising the redshift baseline and ensuring a spread in RA for observational convenience. The fixed aperture of 500 kpc makes the richness selection independent on concentration. However, we have to explore the possibility that richness and concentration are correlated quantities such that a richness selection indirectly biases our sample towards high/low concentrations.

The statistics in the GCLASS sample are insufficient to study a possible trend between richness and concentration at $z \sim 1$. Therefore we examine this using the low- z sample, for which we are able to measure a concentration for each individual cluster. Although the current sample of 10 clusters is limited, we find a hint of a correlation between richness (measured by counting all galaxies more massive than $M_* > 10^{10} M_\odot$ within a radius of $1.2 R_{200}$, background subtracted) and concentration, with a Spearman rank coefficient of $\rho = -0.62$. This negative correlation may not come as a surprise given the known mass-concentration relation (e.g. Comerford & Natarajan 2007; Mandelbaum et al. 2008), and mass-richness relation (e.g. Andreon & Hurn 2010; Bauer et al. 2012). Specifically, the two richest systems (A2142 and A2029) appear to have the lowest concentrations. Therefore, if the same is true at higher redshift, the current sample does not support the idea that a richness selection would result in a cluster sample with stellar mass distributions that are highly concentrated. We will expand the sample to 30-40 clusters, which will allow us to study a possible correlation between richness and concentration for clusters in similar (dynamical) mass bins.

In this thesis, we proceed to test a potential bias in the selection of GCLASS by comparing the dynamical masses of the GCLASS sample to the Tinker et al. (2008) cumulative halo mass function based on a WMAP7 cosmology, which we do in Fig. 5.13. Given the effective area of 41.9 square degrees we estimate the effective volume of the SpARCS survey (from which GCLASS was selected) in the redshift slice $0.86 < z < 1.34$ and normalise the cumulative number density of the GCLASS clusters over this volume. At the high-mass end of the distribution we expect Poisson scatter, and there is scatter in the mass-richness relation to be considered. The ten GCLASS systems are therefore not necessarily the most massive ones. Based on this comparison, we estimate that in GCLASS we probe around 10% of the clusters in the SpARCS volume around the median mass of the GCLASS sample ($M_{200} \simeq 10^{14.3} M_\odot$).

We consider the possibility that the clusters probed by GCLASS are the 10% with the highest concentrations in the simulation. Figure 5.14 shows the GCLASS ensemble average stellar mass concentration with a Gaussian probability distribution around $c = 7.12$. The Duffy et al. (2008) log-normal concentration distribution for cluster-sized haloes in N-body simulations are

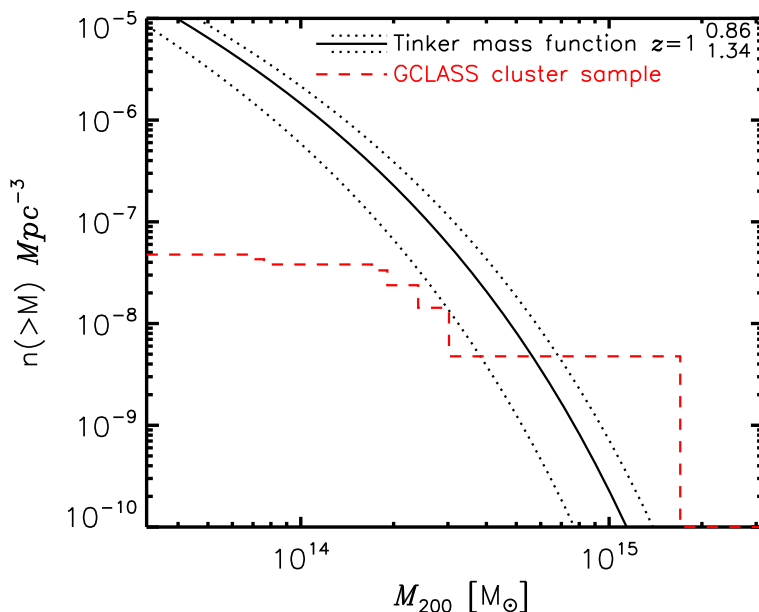
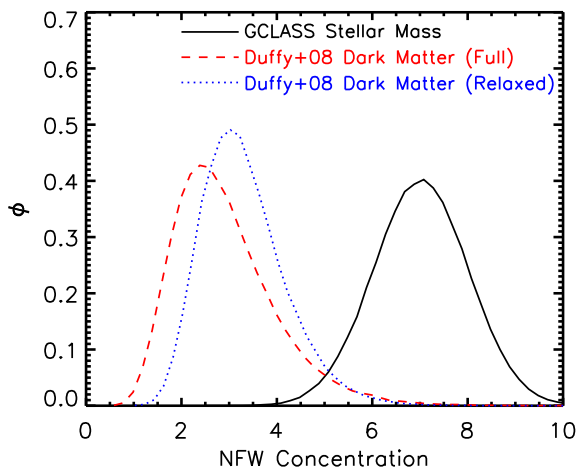


Figure 5.13: *Black solid line:* Tinker et al. (2008) cumulative mass function at $z = 1$ for WMAP7 cosmology. *Black dotted lines:* Tinker et al. (2008) cumulative mass functions at $z = 0.86$ and $z = 1.34$, which are the redshift limits within which the GCLASS clusters are selected. *Red dashed line:* cumulative mass function of the 10 GCLASS clusters, normalised by the total volume of SpARCS.

Figure 5.14: *Black solid line:* GCLASS ensemble average stellar mass concentration with a Gaussian probability distribution around $c = 7.12$. Also shown are the log-normal concentration distribution for clusters with the same mass and redshift as the GCLASS sample for the relaxed haloes in Duffy et al. (2008) (*Blue dotted line*), and their full sample (*Red dashed line*).



also shown, both for their relaxed and full sample (haloes were categorized based on the distance between the most bound particle and the centre of mass in the simulation). The relaxed sample has a slightly higher concentration of $c=3.30$ compared to $c=2.84$ for the full sample, but has a smaller scatter ($\sigma(\log_{10}c)=0.11$ dex versus 0.15 dex for the full sample). Where the Duffy et al. (2008) distributions overlap with the GCLASS probability distribution, these two distributions are similar.

We perform a simple test in which we randomly sample 100 concentrations from the Duffy et al. (2008) relations. We do this for 1000 different realisations and each time average the 10 most concentrated ones. In only 3% of the realisations we find a larger average than the measured concentration from GCLASS ($c = 7.12_{-0.99}^{+1.53}$), taking account also of the error on this measured concentration. Therefore, even under the most conservative assumption that a richness selection is completely biased towards the most concentrated galaxy clusters, there is only a 3% probability that we measure an average concentration for GCLASS of $c = 7.12_{-0.99}^{+1.53}$. Moreover, as we argued in vdB14, the measured concentration of $c \simeq 7.12$ is a lower limit if we include uncertainties arising from misalignments between the BCGs and the "true" cluster centres. Given these arguments, it is unlikely that both the observed evolution since $z \sim 1$, and the difference between the predictions from N-body simulations and observations at this redshift, are only an effect of the way the GCLASS sample is selected.

5.6 Summary and Conclusions

In this paper we study the radial galaxy number density and stellar mass density in a sample of 10 galaxy clusters at $0.07 < z < 0.26$. These clusters are drawn from the Multi-Epoch Nearby Cluster Survey (MENeACS) and the Canadian Cluster Comparison Project (CCCP). Approximately 3000 member galaxies in these clusters have been identified by several spectroscopic surveys in the literature. We compiled catalogues of *ugri*-band photometry to estimate photometric redshifts and stellar masses for each cluster field.

We measure the galaxy number density distribution in two (overlapping) stellar mass bins, and find that the higher mass galaxies ($M_{\star} > 10^{10} M_{\odot}$) are concentrated more strongly ($c = 2.26_{-0.19}^{+0.19}$) than galaxies with masses $M_{\star} > 10^9 M_{\odot}$ ($c = 1.69_{-0.10}^{+0.09}$). This observed mass segregation is expected from the process of dynamical friction. We find a qualitative agreement between these measurements and the literature measurements of galaxy distributions in low- z clusters.

We measure the radial stellar mass density profile in two ways, finding similar results (within 1- σ uncertainty). The statistical subtraction method relies exclusively on the photometric information. For the spectroscopic approach

we use the photometry only to measure stellar masses for the spectroscopically identified cluster members. The stellar mass distribution in the ensemble cluster is well fitted by a projected NFW profile with concentration $c = 1.92_{-0.14}^{+0.19}$. From the measured concentrations for the individual systems, we estimate an intrinsic scatter of $\sigma_{c,\text{int}} = 0.70_{-0.22}^{+0.33}$ (or $\sigma_{\log_{10}c,\text{int}} = 0.25 \pm 0.05$ dex). Some sources that may contribute to this intrinsic scatter are different orientations on the sky, centroiding uncertainties and different halo mass assembly histories for the clusters.

The cluster sample we study is close in halo mass to the likely descendant population of the $z \sim 1$ GCLASS cluster sample (vdB14), for which a stellar mass concentration of $c = 7.12_{-0.99}^{+1.53}$ was estimated. A comparison with these measurements suggests that there is significant evolution in the stellar mass density distribution since $z \sim 1$. We compare the stellar mass density distributions between the two epochs on the same physical scale, showing that the stellar mass density in the cluster cores ($R < 0.2$ Mpc) has to decrease since $z \sim 1$. We argue that this may be related to the build-up of the ICL+BCG component over cosmic time.

A build-up of stellar mass onto the outskirts ($R > 0.3$ Mpc) is further required to match the observed stellar mass distribution in the descendant population. Given that the dark matter haloes in N-body simulations are also found to accrete matter onto the outer parts, a comparison between observations and simulation has the potential to constrain the stellar mass fraction of haloes that are being accreted by the clusters.

Acknowledgements

Based on observations made with the Isaac Newton Telescope through program IDs I10AN006, I10AP005, I10BN003, I10BP005, I11AN009, I11AP013. We thank Malin Velander, Emma Grocutt, Lars Koens and Catherine Heymans for help in acquiring the data. The Isaac Newton Telescope is operated on the island of La Palma by the Isaac Newton Group in the Spanish Observatorio del Roque de los Muchachos of the Instituto de Astrofísica de Canarias.

5.A Consistency checks

We compare the SMF of galaxies in the COSMOS field, as estimated using photometry in the *ugri*-bands, with the SMF of galaxies in the outermost areas of the cluster fields. Since the distance to the cluster centre is larger than the virial radius (or R_{200}), the cluster is expected to only be marginally over-dense compared to the field in that regime. Thus we use this comparison as a consistency check between the different surveys and filter sets.

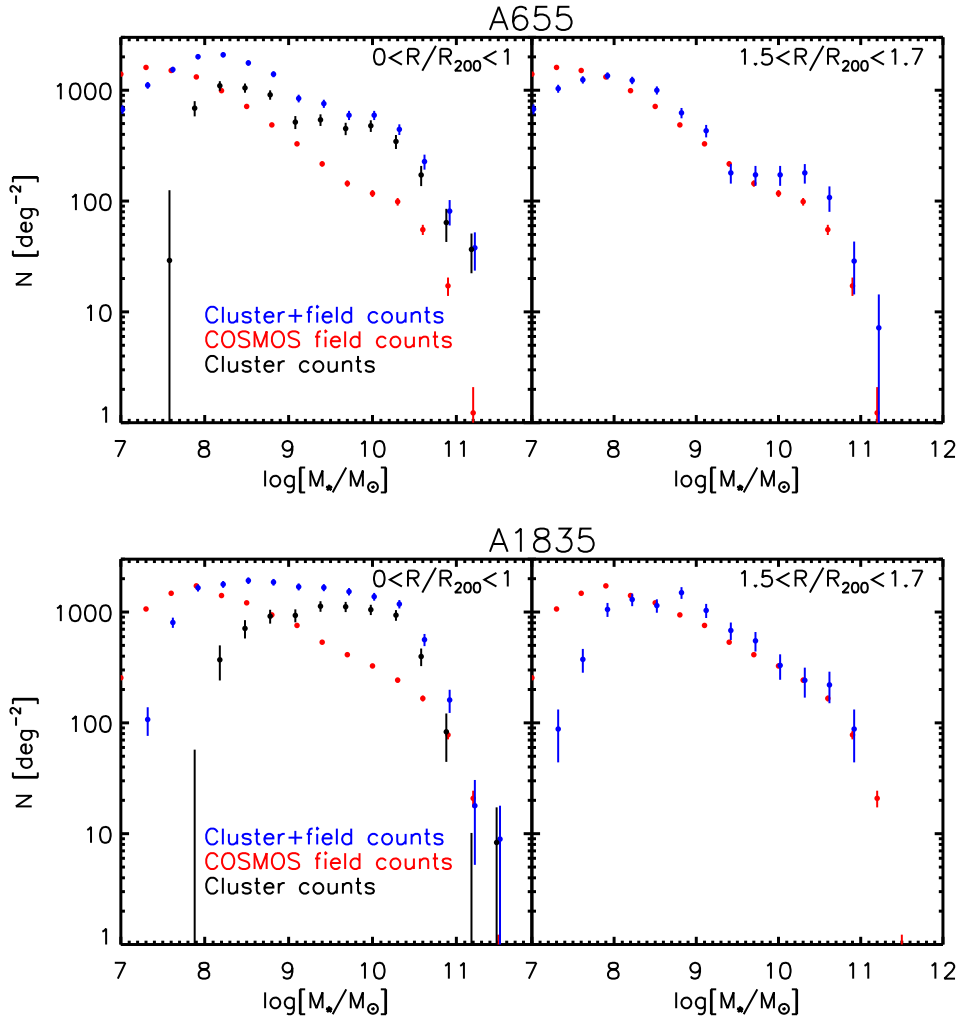


Figure 5.15: The SMF of A655 (*top*) and A1835 (*bottom*) in two radial bins. *Left:* The cluster inner part ($R < R_{200}$). *Right:* the outer part $1.5R_{200} < R < 1.7R_{200}$. The expected background (field) counts from the COSMOS survey are indicated in red, and the black points are the background subtracted values. The outer radial bin shows only a mild over-density of counts compared to the field values.

We obtain the stellar masses from the SED-fitting code FAST, where we fix the redshift to the median redshift of the cluster. This is thus no proper field SMF, since all distance moduli are equal to the clusters'. However, upon subtracting the COSMOS field value from the cluster-field counts, we obtain the stellar mass function in this outer radial bin of the cluster. The photometric data of the COSMOS field is substantially ($\sim 1-2$ mags) deeper than our cluster data, leading to a different stellar mass completeness limit (see the difference in the drop in galaxy counts at the low-mass end of the SMF for the different surveys). For the work presented in this paper, the incompleteness in that regime does not significantly affect the stellar mass distribution (nor the number density distribution for sources with stellar mass exceeding 10^9). For the measurement of the cluster galaxy stellar mass function in this cluster sample (van der Burg et al., in prep), we will perform a series of simulations to assess and correct for the stellar mass incompleteness at lower masses.

The UV galaxy Luminosity Function at $z=3-5$ from the CFHT Legacy Survey Deep fields

We measure and study the evolution of the UV galaxy Luminosity Function (LF) at $z=3-5$ from the largest high-redshift survey to date, the Deep part of the CFHT Legacy Survey. We also give accurate estimates of the SFR density at these redshifts. We consider $\sim 100\,000$ Lyman-break galaxies at $z \approx 3.1, 3.8$ & 4.8 selected from very deep *ugriz* images of this data set and estimate their rest-frame 1600\AA luminosity function. Due to the large survey volume, cosmic variance plays a negligible role. Furthermore, we measure the bright end of the LF with unprecedented statistical accuracy. Contamination fractions from stars and low- z galaxy interlopers are estimated from simulations. From these simulations the redshift distributions of the Lyman-break galaxies in the different samples are estimated, and those redshifts are used to choose bands and calculate k-corrections so that the LFs are compared at the same rest-frame wavelength. To correct for incompleteness, we study the detection rate of simulated galaxies injected to the images as a function of magnitude and redshift. We estimate the contribution of several systematic effects in the analysis to test the robustness of our results. We find the bright end of the LF of our *u*-dropout sample to deviate significantly from a Schechter function. If we modify the function by a recently proposed magnification model, the fit improves. For the first time in an LBG sample, we can measure down to the density regime where magnification affects the shape of the observed LF

because of the very bright and rare galaxies we are able to probe with this data set. We find an increase in the normalisation, ϕ^* , of the LF by a factor of 2.5 between $z \approx 5$ and $z \approx 3$. The faint-end slope of the LF does not evolve significantly between $z \approx 5$ and $z \approx 3$. We do not find a significant evolution of the characteristic magnitude in the studied redshift interval, possibly because of insufficient knowledge of the source redshift distribution. The SFR density is found to increase by a factor of ~ 2 from $z \approx 5$ to $z \approx 4$. The evolution from $z \approx 4$ to $z \approx 3$ is less eminent.

6.1 Introduction

The formation and evolution of galaxies rank among the big questions in astronomy and still await a complete explanation. According to current theory, the formation of dark matter haloes by gravitational instabilities is an essential first step in the formation of galaxies (Eggen et al. 1962). Stars are believed to form when gas cools at the centres of these haloes (White & Rees 1978), and make up the part of the galaxy that we can observe. A number of physical processes strongly affect this baryonic mass assembly, like the hydrodynamics of the gas, feedback processes by supernovae and stellar winds, possibly magnetic fields, the role of AGN, or the effects of galaxy-galaxy interactions and mergers. For these reasons the modelling of galaxy formation depends on many free parameters and is not very well constrained.

Over the past decade the high redshift universe has become accessible observationally through the use of photometric techniques. By detection of the spectral discontinuity due to the redshifted Lyman-break in a multi-wavelength filter set, large and clean samples of high redshift star-forming galaxies can be selected (Steidel et al. 1996, 1999; Giavalisco 2002), with low amounts of contamination. These samples can be used to study several properties of the early universe. For example, by measuring the correlation function of these Lyman-break Galaxies (LBGs) and comparing it with the correlation of dark matter, the characteristic mass of their haloes can be determined (e.g. Giavalisco & Dickinson 2001; Ouchi et al. 2004b; Hildebrandt et al. 2005, 2007, 2009). Hubble Space Telescope observations of LBGs are used to study how certain morphological types evolve with time (Pirzkal et al. 2005). A study of the evolution of the UV Luminosity Function (LF) (Steidel et al. 1996, 1999; Sawicki & Thompson 2006; Bouwens et al. 2007), which is the measure of the number of galaxies per unit volume as a function of luminosity, is another fundamental probe in galaxy formation and evolution, because of its close relation to star formation processes.

Several techniques can be used to estimate the star formation rate (SFR) in galaxies, mostly based on the existence of massive, young stars, indicative of recent star formation. A commonly used way to probe the existence of massive stars is the H α luminosity (Kennicutt 1983), because H α photons originate from the gas ionized by the radiation of massive stars. A second star formation indicator is the infrared (IR) luminosity originating from dust continuum emission (Kennicutt 1998; Hirashita et al. 2003). The absorption cross section of dust is strongly peaked in the UV, and therefore the existence of UV emitting, i.e. massive, stars is probed indirectly. Thirdly, the UV continuum is used as a star formation probe, with the main advantages being that the UV-emission of the young stellar population is *directly* observed, unlike in H- α and IR studies. Furthermore, this technique can be applied from the ground to star-forming galaxies over a wide range of redshifts. Hence, it

is still the most powerful probe of cosmological evolution of the SFR (Madau et al. 1996). However, information about the initial mass function (IMF), and particularly the extinction by dust are required to estimate the total star formation rate.

In this paper we estimate the UV LF at redshifts $z=3-5$ from the Canada-France-Hawaii-Telescope Legacy Survey (CFHTLS) Deep, a survey covering 4 square degrees in four independent fields spread across the sky. Since our samples, at different redshifts, are all extracted from the same dataset, this gives an excellent opportunity to study a possible evolution of the LF in this redshift interval. Several systematic effects that need to be considered when comparing results at different redshifts from different surveys (e.g. source extraction, masking, PSF-modelling, etc.) can be avoided when the different redshift samples are extracted from the same survey. Due to the large volumes we probe with our 4 square degree survey, the influence of cosmic variance on the shape of the estimated LF is negligible (Trenti & Stiavelli 2008), as we expect cosmic variance to affect our number counts only at the 1-5% level (Somerville et al. 2004). We can study the bright end of the LF with unprecedented accuracy, as these objects are rare and we are able to measure down to very low densities. This allows us to study the effect that magnification has on the observed distribution (see recent results by Jain & Lima 2010), and study a possible deviation from the commonly used Schechter function. Furthermore, given the depth of the stacked images, we can probe the faint end of the luminosity function with comparable precision as the deepest ground based surveys have done before (Sawicki & Thompson 2006).

The structure of this paper is as follows: In Sect. 6.2 we describe the data set we use, the LBG selection criteria as well as the simulations that lead to the redshift distributions and contamination fractions. In Sect. 6.3 the survey's completeness and the effective survey volumes are estimated. In Sect. 6.4 we proceed with the resulting estimated LFs, present the best-fitting Schechter parameters, and show how a simple magnification model can significantly improve the quality of the fit. The UV luminosity densities (UVLD) and SFR densities (SFRD) are estimated based on the measured LFs. We also elaborate on the robustness of our results. In Sect. 6.5 we compare these to previous determinations of the UV LF and SFRD from the literature. In Sect. 6.6 we finish with a summary and present our conclusions.

We use the AB magnitudes system (Oke & Gunn 1983) throughout and adopt Λ CDM cosmology with $\Omega_m = 0.3$, $\Omega_\Lambda = 0.7$ and $H_0 = 70 \text{ km s}^{-1} \text{ Mpc}^{-1}$.

6.2 Data & Samples

6.2.1 The CFHT Legacy Survey Deep

For this work we make use of publicly available data from the CFHTLS Deep, a survey using MegaCam mounted at the prime focus of the CFHT which covers four independent fields of 1 square degree each. Images are taken in the filters *ugriz* and are pre-processed using the Elixir system (Magnier & Cuillandre 2004). Image reduction is done using the THELI pipeline (Erben et al. 2005; Hildebrandt et al. 2006), leading to approximate 5σ point source limits of 27.5, 27.9, 27.9, 27.7 and 26.5 for the *ugriz* bands, respectively. The limits for each of the fields lie within 0.2 mag from these average values.

Source Extractor (Bertin & Arnouts 1996) is used to create a multi-colour catalogue. Total *i*-band magnitudes are measured in Kron-like apertures (Kron 1980) using SExtractor’s AUTO magnitudes. Every image is smoothed by convolution with a Gaussian filter to match the seeing of the image with the worst seeing value (typically the *u*-band). These corrections are typically small - all bands have a seeing below 1 arcsec. The dual-image mode of SExtractor is then used with the unconvolved *i*-band for source detection and isophotal magnitudes from the convolved bands to estimate colours. An extensive description of the data reduction and catalogue creation is given in Erben et al. (2009) and Hildebrandt et al. (2009).

6.2.2 *u*-, *g*-, and *r*-dropout samples

Clean samples of *u*-, *g*-, and *r*-dropouts are selected based on the following selection criteria (Hildebrandt et al. 2009):

$$\begin{aligned} u\text{-dropouts} & : 1.0 < (u - g) \wedge -1.0 < (g - r) < 1.2 \wedge \\ & 1.5 \cdot (g - r) < (u - g) - 0.75, \end{aligned} \quad (6.1)$$

$$\begin{aligned} g\text{-dropouts} & : 1.0 < (g - r) \wedge -1.0 < (r - i) < 1.0 \wedge \\ & 1.5 \cdot (r - i) < (g - r) - 0.80, \end{aligned} \quad (6.2)$$

$$\begin{aligned} r\text{-dropouts} & : 1.2 < (r - i) \wedge -1.0 < (i - z) < 0.7 \wedge \\ & 1.5 \cdot (i - z) < (r - i) - 1.00. \end{aligned} \quad (6.3)$$

Furthermore, it is required that all LBGs have a SExtractor CLASS_STAR parameter of CLASS_STAR < 0.9, that *g*-dropouts are not detected in *u*, and that *r*-dropouts are neither detected in *u* nor in *g*. Note that the colour selection criteria of the *u*-dropout sample in Hildebrandt et al. (2009) are pretty conservative. We relaxed the *u* - *g* cut slightly to make the selection more comparable to e.g. Steidel et al. (2003), Steidel et al. (2004) and Sawicki & Thompson (2006).

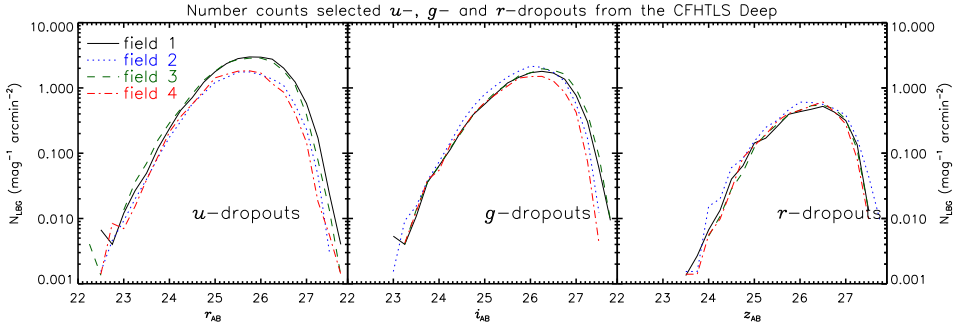


Figure 6.1: From left to right the number counts of the u -, g -, and r -dropouts in the CFHTLS Deep, as selected by the colour criteria of Eqs. 6.1-6.3.

This results in the selection of 50880 u -, 36226 g -, and 11411 r -dropouts in total over the four fields. Their magnitude distributions are shown in Fig. 6.1. Note the differences in depth of the individual fields.

6.2.3 Redshift distributions & Contamination fractions

The majority of the selected sources is too faint to make a spectroscopic redshift determination possible, and the brighter candidates have not spectroscopically been observed yet. For this reason Hildebrandt et al. (2009) estimated the redshift distributions by means of photometric redshifts and simulations.

Throughout this paper we will use the mean redshift values from simulations based on synthetic templates by Bruzual A. & Charlot (1993), being $\langle z \rangle \cong 3.1$, 3.8 and 4.7 for the u -, g -, and r -dropouts respectively. We estimate the uncertainty in the mean redshifts to 0.1 for the three dropout samples.

In order to address the amount of contamination in our LBG samples, Hildebrandt et al. (2009) consider the possibilities of stars and low- z galaxies scattering in the selection boxes. Galaxies are simulated based on templates from the library of Bruzual A. & Charlot (1993), while the colours of stars in the fields are estimated based on the TRILEGAL galactic model (Girardi et al. 2005). Contamination fractions are shown graphically in Fig. 6.2.

Stellar contamination is negligible for the brighter objects, as the selection boxes steer away from the stellar locus. For faint objects in the u -, and g -dropout samples, the stellar contamination increases as a result of photometric scatter.

The contamination by low- z galaxies is negligible in the u -dropout sample, as the Lyman break for a $z \sim 3$ galaxy is still blue-ward of the $z \sim 0$ Balmer/4000Å break. For higher redshifts this ceases to be the case, so that the g -, and r -dropout samples suffer from a significant contamination fraction

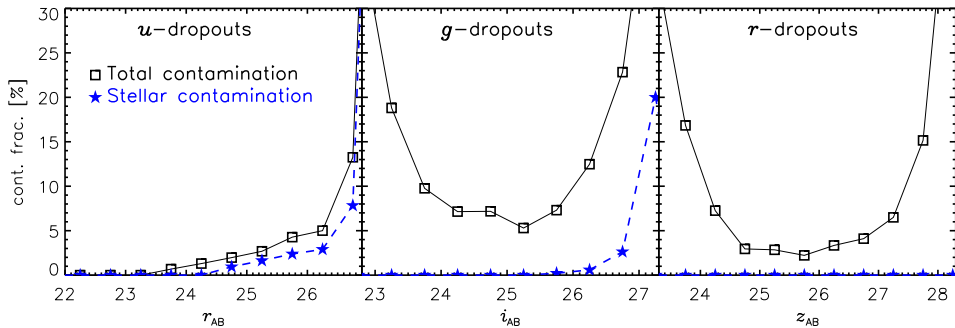


Figure 6.2: Contamination fractions of stars and low- z galaxies in the dropout samples. Blue \star -symbols connected by a dashed line show the stellar contamination fraction based on a galactic model. Black squares connected by the solid line show the total contamination fraction from Hildebrandt et al. (2009).

at the bright end, where the LBG population is sparse. Faint low- z objects are likely to scatter into the selection box in each of the samples, so that the contamination fractions are increased here.

Since the contamination fractions are low at the bright end of the u -dropouts, we have the potential to probe the LF to very low LBG galaxy densities. We inspect the 80 brightest objects ($r_{AB} < 23.2$) in the u -dropout sample by eye and remove obvious spurious sources, 30 in total. A strong, but certainly slightly subjective, rejection criterion is the size of the region in which the flux is measured, i.e. the half-light radius (13 objects rejected). Sources that are clearly blended by a bright neighbour (2 objects), as well as sources that have a too large apparent size (3 objects). Also an asteroid track has been removed.

In the g -, and r -dropout sample we do not probe these low ($\lesssim 0.01 \text{ mag}^{-1} \text{ arcmin}^{-2}$) LBG galaxy densities, since these points are unreliable due to the high contamination fractions from low- z objects (see Fig. 6.2). This prohibits a study of the bright end of the LF for the g -, and r -dropouts until the nature of the individual sources has been verified.

6.3 Analysis - Survey completeness

We use a detailed modelling approach to estimate the completeness of the survey as a function of magnitude and redshift, for each of the dropout samples. We add artificial objects to our images, with colours representative of star-forming galaxies, and try to recover them following the same source extraction and colour selection criteria as for the real data. We investigate how the increasing scatter in the colours for fainter objects influences the completeness

as a function of magnitude. Furthermore, one expects that, for fainter dropout objects, the redshift distribution of these objects broadens due to the same effect. Hence we will also model this as a function of redshift.

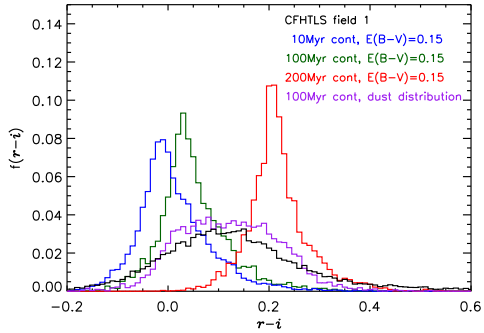
We describe our fiducial model SEDs, sizes and shapes of the simulated objects below. The assumptions we make, are tested in Sect. 6.4.3 to estimate the robustness of the results.

6.3.1 Model galaxies

The Bruzual A. & Charlot (1993) stellar population synthesis library is used to set up our fiducial galaxy SED model; a 100 Myr old galaxy template with constant star formation. A Miller & Scalo (1979) IMF is assumed. The optical depth of neutral hydrogen, as a function of redshift, is modelled according to Madau (1995).

This template is reddened by the starburst extinction law from Calzetti et al. (2000), with a distribution in $E(B - V)$. This distribution we choose such that the UV-continuum slopes that we measure from the data are matched when we use our fiducial template as a base. To measure the UV-continuum slopes, we use a colour redward of 1600 rest-frame, i.e. the $r - i$ colour for the u -dropouts and the $i - z$ colour for the g -dropouts. For the r -dropouts we can not perform a similar measurement because we do not have observations in a band redward of the z -band. Therefore we will use the same distribution of dust as we find for the g -dropouts.

Figure 6.3: The distribution of UV-continuum slopes for the u -dropouts as measured by the $r - i$ colour from the CFHT data (black) compared with the outcomes from simulations. The colour is measured in a part of the spectrum without strong features, redward of 1600. Both an older template and a higher amount of dust result in a redder UV colour. The amount of dust we need to add therefore depends on the age of the base template. For the u -dropouts we find that a uniform distribution of dust with $0.1 < E(B - V) < 0.4$ gives a good fit to the data, when the template is 100 Myr old with a constant amount of star formation (purple).



For the u -dropouts we find that a uniform dust distribution with reddening between with $0.1 < E(B - V) < 0.4$ gives a good fit to the data, see Fig. 6.3. For the g -dropouts we measure a larger spread in UV-continuum slopes, and find a reasonable fit when using a uniform dust distribution with reddening

between $0.0 < E(B - V) < 0.5$. It should be noted that the age and amount of dust attenuation of the template are highly degenerate, so that different combinations of these parameters fit the UV-continuum slopes in the data. It is especially important to correctly match the distribution of the UV-continuum slopes from the data with the model galaxies, since an increase (decrease) in the age of the galaxy model template has a similar effect on the LF as an increase (decrease) of the amount of dust. We will elaborate on this in Sect. 6.4.3. If we measure the UV-continuum slopes in our data for different magnitude bins, we do not find a significant evolution. Therefore we will use a distribution of dust attenuation in our simulations that is independent of magnitude.

LBGs have typical half-light radii of $r_{1/2} \sim 0.1''\text{-}0.3''$ (Giavalisco et al. 1996) and thus are unresolved by the CFHT and can be treated as point sources. As the size of the PSF in the CFHT images is strongly position dependent, we have to adapt the injected sources accordingly. We parametrize the PSF by a Moffat profile,

$$I = I_0 \left[1 + (2^{1/\beta} - 1) \cdot \left(\frac{R}{R_0} \right)^2 \right]^{-\beta}, \quad (6.4)$$

in which β and R_0 are the parameters that we adapt to adjust the shape and size of the profile respectively. I_0 represents the flux normalisation.

In order to measure the PSF as a function of position for the different filters and fields, we first select several hundred stars based on their magnitudes and half-light radii, in each field and each filter. We measure the 50% and 90% flux radii of these stars, r_{50} and r_{90} , using SExtractor. The ratio of these flux radii uniquely determines the Moffat- β parameter, which, in combination with either one of the flux radii, gives the Moffat profile radius R_0 for each star. We find that the Moffat- β parameter is fairly constant over the fields and filters ($\beta \approx 4.0$) and only R_0 changes significantly. To model R_0 as a function of position, we fit a 2-dimensional polynomial function to the SExtracted values for r_{50} . This constrains the PSF size on every position, for every field and filter.

We find that there is a $\sim 30\%$ difference in R_0 between the image center and boundaries. As this, in our ground-based wide-field survey, is by far the dominating effect in the apparent surface brightnesses of our sources, we do not assume an intrinsic size distribution for the sources in the main simulations of this paper.

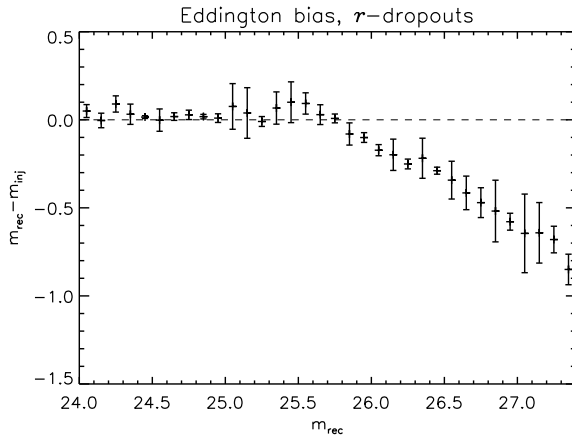
6.3.2 Eddington bias

If we consider a certain intrinsic magnitude distribution of galaxies, the recovered distribution after source extraction and colour selection will look different due to statistical fluctuations in the measurement. In our analysis we attempt to correct for this effect called Eddington bias (Eddington 1913; Teerikorpi

2004). It is hard to estimate this bias analytically because the size of the magnitude scatter is an increasing function of magnitude. Also, when approaching the completeness limit of the survey, only the brighter objects will be detected. What generally happens is that intrinsically faint objects will on average look brighter than they are.

The Eddington bias can be estimated by comparing the intrinsic magnitudes of the injected sources to the recovered magnitudes. Such a comparison is shown in Fig. 6.4, stressing the importance of that effect for faint magnitudes.

Figure 6.4: The difference between recovered and injected source magnitudes as a function of recovered magnitude for the r -dropouts. Similar trends appear in the other dropout samples. The error bars reflect the scatter from the four fields. A similar effect as shown around $m_{\text{rec}} = 25.3$, namely an increase of $m_{\text{rec}} - m_{\text{inj}}$, is found by Bouwens et al. (2006, Fig.19), where observations were used rather than simulations.



We want to inject sources with the same magnitude distribution as the intrinsic distribution, to get an unbiased result. As the bias is expected to be largest for fainter sources, it is especially important to correctly model the faint-end of the intrinsic distribution. Here we adopt a LF that is consistent with the deepest LBG survey, conducted by Bouwens et al. (2007).

6.3.3 Source injection and recovery

Following this adopted intrinsic distribution we inject 20 000 sources in each of the images, for 60 equal redshift steps between $z = 0.0$ and $z = 6.0$. To verify that the injected sources do not significantly influence each other by blending, nor that the background is influenced significantly, we perform the following tests. We inject the same 20 000 sources in 4 stages, 5000 sources each, and do a third analysis where we inject 100 000 sources in total. In Fig. 6.5 the recovered fractions of sources that also satisfy our g -dropout criteria are shown as a function of magnitude, for one particular redshift step. Only for faint magnitudes does the 100 000 curve deviate from the other ones, which are identical in this regime. In Fig. 6.6 the distribution of recovered g -dropouts with an intrinsic magnitude of $m = 25.0$ is shown as a function of recovered magnitude. We conclude that the injection of 20 000 sources does not influence

the images such that the photometry would be perturbed significantly. A similar behaviour is expected for the u - and r -dropout samples.

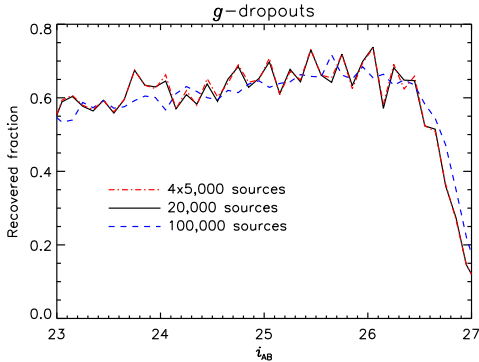


Figure 6.5: The recovered fraction of injected sources that also satisfy the g -dropout criteria, as a function of i -band magnitude, for 1 redshift step. Three curves are given for different amounts of injected sources, to see whether, and how, the presence of these sources influences the photometry of the analysis.

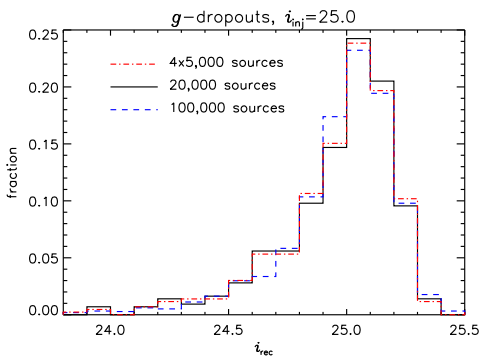


Figure 6.6: The distribution of measured source magnitudes for a population of injected simulated sources with intrinsic i -band magnitude=25.0, for 1 redshift step. Three curves are given for different amounts of injected sources, to see whether, and how, the presence of these sources influences the photometry of the analysis.

The clustering of LBGs is not taken into account. We assume this effect to be insignificant for estimating completeness, as the correlation length, which is typically around 5 Mpc (Hildebrandt et al. 2009), is very small compared to the survey volume. Therefore we spread our simulated sources uniformly over the images.

6.3.4 Effective volumes

Next we define the function $p(m, z)$ to be the number of sources recovered with an observed magnitude in the interval $[m; m + \Delta m]$, and are selected as dropouts, divided by the number of injected sources with an intrinsic magnitude in the same interval $[m; m + \Delta m]$ and a redshift in the interval $[z; z + \Delta z]$. Note that the definition of $p(m, z)$ is slightly different compared to the one used in e.g. Sawicki & Thompson (2006), as they do not take Eddington bias into account. In our definition, $p(m, z)$ could potentially be > 1 as a result of this bias correction.

The effective volumes (V_{eff}) of our survey are given by

$$V_{\text{eff}}(m) = A_f \int \frac{dV_C}{dz} p(m, z) dz, \quad (6.5)$$

where A_f is the field area in square arcminutes, and $\frac{dV_C}{dz}$ is the comoving volume per square arcminute, which depends on the adopted cosmology.

The magnitude is measured in the r -, i -, and z -bands for the u -, g -, and r -dropout samples, respectively. These bands probe flux at approximately 1600Å rest-frame of the sources at the expected mean redshifts, so that only a minor k-correction will be sufficient to compare the results for the different epochs directly, see the upper panel of Fig. 6.7. We transform the apparent magnitudes to absolute magnitudes and perform a k-correction to a rest-frame wavelength of 1600Å using the mean redshifts for each of the dropout samples, i.e. we assume all sources to be at the same redshift.

The uncertainties in the mean redshifts¹ are expected to be approximately 0.1 for the three dropout samples, as argued in Sect. 6.2.3. This leads to uncertainties in both distance modulus and k-correction, resulting in a systematic error in the absolute magnitudes of our estimated LF, see the lower panel of Fig. 6.7. The final uncertainties are about 0.07, 0.05 and 0.04 in the absolute magnitude for the u -, g -, and r -dropout samples, respectively.

6.4 Results

6.4.1 The UV Luminosity Function at $z=3-5$

After dividing the number counts by V_{eff} , which corrects for incompleteness and Eddington bias, and subtracting the distance modulus and the k-correction from the apparent magnitudes, we obtain the LF in absolute magnitudes at 1600.

Results from the four fields are binned to $\Delta\text{mag}=0.3$, combined, and shown in Fig. 6.8 and Table 6.1. Uncertainties in the magnitude direction are due to uncertainties in the redshift distribution of source galaxies. The four independent analyses of the fields allow us to estimate field-to-field variations for each of the data points. Vertical error bars reflect either this uncertainty, or

¹Note that we make use of two different redshift distributions in our analysis. To estimate both the k-correction and the effective volumes we use the distribution given by the simulations described in Sect. 6.3, while we use the distribution from the simulations from Hildebrandt et al. (2009) to shift the LF in the magnitude direction. The redshift distribution from the latter simulations are expected to be more reliable because they take a wide variety of template galaxy models into account, but we cannot use them for effective volumes & k-corrections because of computational constraints. Rather we have to simulate those with a single template.

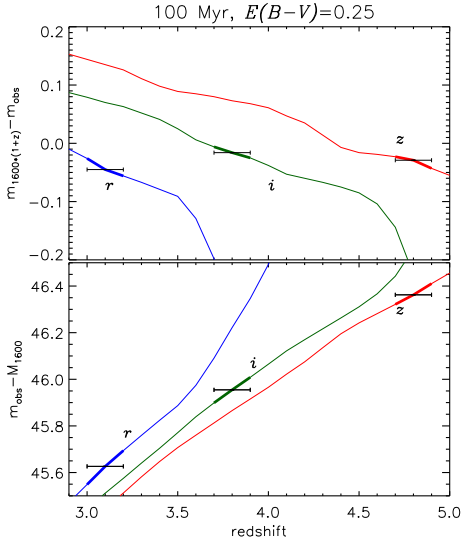


Figure 6.7: Upper panel: k-correction to 1600\AA for the MegaCam *riz* filters, as a function of redshift based on the 100 Myr old continuously star-forming template with a dust attenuation of $E(B - V)=0.25$. The average redshifts from the simulations and their uncertainties are represented by horizontal error bars. This leads to a corresponding error in the k-correction. Lower panel: Shifts from apparent magnitudes in the MegaCam *riz* filters, to absolute magnitudes at 1600\AA . The Distance Modulus and k-correction are taken into account. The uncertainties in the average redshifts of the samples lead to uncertainties in the absolute magnitudes.

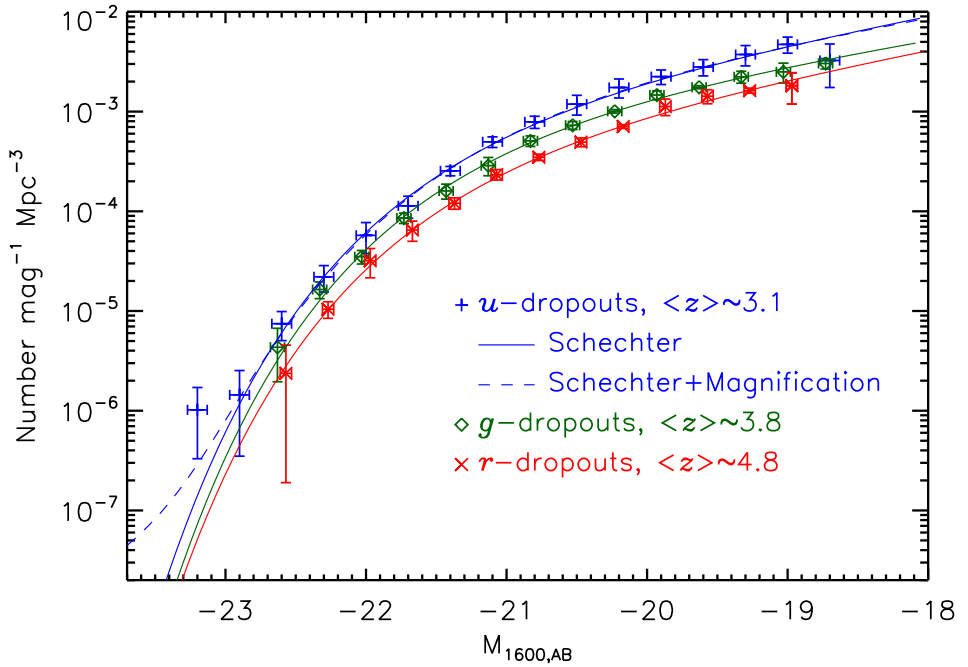


Figure 6.8: The LFs of LBGs in the CFHTLS-Deep fields. Data points and best-fitting Schechter functions are shown for the *u* (blue)-, *g* (green)-, and *r* (red)-dropouts. For legibility we applied a small offset on the x-axis values of the *g*-, and *r*- dropouts. The dashed blue curve shows the best fitting Schechter function for the *u*-dropouts after magnification effects have been included, as described in Sect. 6.4.1.

Table 6.1: The estimated LFs from the CFHTLS Deep.

$M_{1600,AB}$	u -dropouts	g -dropouts	r -dropouts
	$\phi_k [10^{-3} \text{ Mpc}^{-3} \text{ mag}^{-1}]$	$\phi_k [10^{-3} \text{ Mpc}^{-3} \text{ mag}^{-1}]$	$\phi_k [10^{-3} \text{ Mpc}^{-3} \text{ mag}^{-1}]$
-23.20	0.001 ± 0.001	-	-
-22.90	0.001 ± 0.001	-	-
-22.60	0.007 ± 0.002	0.004 ± 0.002	0.002 ± 0.002
-22.30	0.022 ± 0.007	0.016 ± 0.003	0.010 ± 0.002
-22.00	0.057 ± 0.020	0.035 ± 0.005	0.032 ± 0.010
-21.70	0.113 ± 0.028	0.086 ± 0.010	0.065 ± 0.015
-21.40	0.254 ± 0.027	0.160 ± 0.027	0.121 ± 0.016
-21.10	0.497 ± 0.061	0.287 ± 0.060	0.234 ± 0.028
-20.80	0.788 ± 0.110	0.509 ± 0.061	0.348 ± 0.025
-20.50	1.188 ± 0.267	0.728 ± 0.067	0.494 ± 0.050
-20.20	1.745 ± 0.377	1.006 ± 0.040	0.708 ± 0.030
-19.90	2.240 ± 0.373	1.465 ± 0.147	1.123 ± 0.211
-19.60	2.799 ± 0.519	1.756 ± 0.063	1.426 ± 0.229
-19.30	3.734 ± 0.863	2.230 ± 0.305	1.624 ± 0.095
-19.00	4.720 ± 0.866	2.499 ± 0.564	1.819 ± 0.630
-18.70	3.252 ± 1.508	3.038 ± 0.370	-

the Poisson noise term, whichever is largest. Usually the field-to-field variance dominates. As a consequence of the way these are computed, Poisson noise is always taken into account.

We fit a Schechter function (Schechter 1976) to the binned data points,

$$\phi(M)dM = 0.4 \ln(10) \phi^* 10^{0.4(\alpha+1)(M^*-M)} \exp(-10^{0.4(M^*-M)}), \quad (6.6)$$

with M^* being the characteristic magnitude, α being the faint-end slope, and ϕ^* being the overall normalisation.

Using χ^2 statistics on a three dimensional grid of 500³ different Schechter parameter combinations, we find the minimal value (χ^2_{\min}) for each of the dropout samples yielding the best fit values. To estimate the errors in the fitted parameters, we project the 3-dimensional distribution of χ^2 to 3 planes by taking the minimum χ^2 along the projected dimension. In Fig. 6.9 the 68.3% and 95.4% confidence levels are shown, which correspond to a $\Delta\chi^2=2.3$ and 6.17 with respect to χ^2_{\min} . In Table 6.2 we give the 68.3% confidence levels on each individual parameter, corresponding to $\Delta\chi^2=1.0$.

Note, however, that this error estimate assumes Gaussian errors, and that the errors on the data points are independent. Especially for the u -dropouts this is probably not the case. The normalisation of the LF seems to be systematically slightly different for each of the fields (see also Fig. 6.1), giving

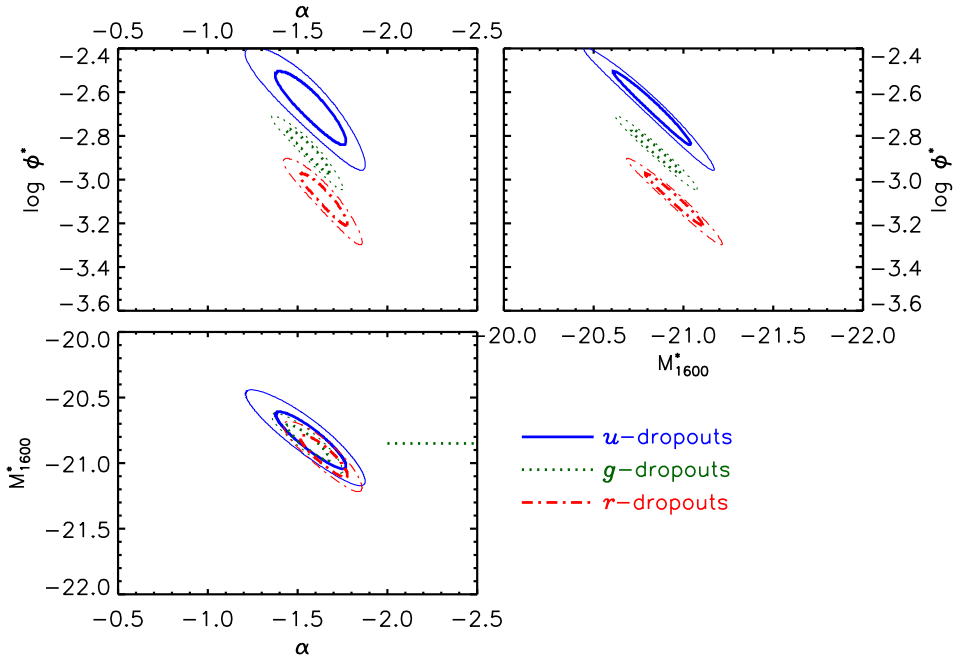


Figure 6.9: The 68% and 95% likelihood contours for different Schechter parameter combinations. Shown are the results for the u -dropouts at $z \sim 3$ (blue, solid), the g -dropouts at $z \sim 4$ (green, dots), and the r -dropouts at $z \sim 5$ (red, dash-dots). The u -dropout contours represent the best Schechter parameters when we include magnification effects, as described in Sect. 6.4.1.

a systematic uncertainty in ϕ^* of about 30%. For the u -dropouts this effect is largest because of a slightly more uncertain flux calibration in the u -band compared to the g - and r -bands. The effective filter throughput changes with time in the UV as the atmosphere is changing, and also the camera is less sensitive in this wavelength regime resulting in larger shot-noise.

Magnification contribution at low densities

Due to inhomogeneities in the matter distribution between distant sources and the observer, paths of photons get slightly perturbed. This results in a distortion of the shape and a magnification of distant sources. When a source is magnified by a factor μ , the flux gets boosted by the same amount. One can relate an intrinsic luminosity distribution to an observed distribution if the magnification distribution is known, as was shown by Jain & Lima (2010). Hilbert et al. (2007) estimate magnification distributions for different source redshifts by shooting random rays through a series of lens planes created from

Table 6.2: A comparison between the best fitting Schechter parameters and their 68% confidence intervals for the u -, g -, and r -dropouts.

Sample	M_{UV}^* ^a	ϕ^* [10^{-3} Mpc^{-3}]	α	χ^2/dof
u	$-20.94^{+0.14}_{-0.13}$	$1.79^{+0.51}_{-0.38}$	$-1.65^{+0.12}_{-0.11}$	0.52
g	$-20.84^{+0.09}_{-0.09}$	$1.36^{+0.23}_{-0.20}$	$-1.56^{+0.08}_{-0.08}$	0.36
r	$-20.94^{+0.10}_{-0.11}$	$0.83^{+0.15}_{-0.14}$	$-1.65^{+0.09}_{-0.08}$	0.19
u^b	$-20.84^{+0.15}_{-0.13}$	$2.11^{+0.63}_{-0.45}$	$-1.60^{+0.14}_{-0.11}$	0.41

- ^a Due to uncertainties in the redshift distributions there is an additional error component of 0.07, 0.05, and 0.04 in the estimated M_{UV}^* for the u -, g -, and r -dropout samples, respectively.
- ^b Best-fitted Schechter parameters for a model where the function is modified with a magnification distribution.

the Millennium Simulation. The width of the magnification distribution is found to increase with increasing source redshift, and the peak position of the distribution decreases slightly with increasing source redshift.

Magnification can account for a strong deviation from a Schechter function where the slope of the intrinsic luminosity distribution is very steep, see Jain & Lima (2010). We stress again that we measure the LF from a volume that is much larger than has been used before. The bright end of our g -, and r -dropout samples suffers from increasing amounts of contamination. Only for the u -dropouts we probe the distribution of u -dropouts at the bright end down to a density of $10^{-6} \text{ mag}^{-1} \text{ Mpc}^{-3}$. We use the magnification distribution for a source redshift of $z = 3.1$ that was kindly provided by Stefan Hilbert to improve our model to the data.

Writing the LF as a function of magnitude, we use the following equation to correct the Schechter function for magnification effects. It is equivalent to the expression used by Jain & Lima (2010).

$$\phi(m_{obs}) = \int d\mu P(\mu) \phi^*(m_{obs} + 2.5 \log(\mu)), \quad (6.7)$$

where ϕ^* is the Schechter function defined by Eq. 6.6. The new function yields a slightly better fit to the bright end of the LF, reducing the formal χ^2/dof from 0.52 to 0.41. Find the new Schechter parameters, together with their 68.3% confidence levels in Table 6.2, and their 2-dimensional 68.3% and 95.4% confidence contours plotted in Fig. 6.9. The best fitting function is the dashed curve in Fig. 6.8.

As the bright selected u -dropouts are likely to be significantly magnified, we expect them to appear close to a massive foreground galaxy or group of galaxies that acts as a lens. We inspected the brightest ($r_{AB} < 23.2$) u -dropouts by eye and find that this is indeed the case for many of them. Note that the model is still uncertain as the Millennium simulation does not include baryonic matter, and assumes $\sigma_8 = 0.9$ (Springel et al. 2005), where recent estimates indicate a lower value around 0.8 (Komatsu et al. 2010). Also, in the magnification probability distribution the possibility of multiply imaged systems is ignored. To rule out contamination in the LBG sample at the bright end of the LF, the nature of each bright object has to be verified spectroscopically.

A statistically much better sample can be selected from the CFHT Legacy Survey Wide, consisting of 170 square degree imaging in $ugriz$ of shallower depth. We leave this for future studies.

6.4.2 The UV Luminosity Density and SFR Density

Next we estimate the UV luminosity density (UVLD) at the different epochs. To be able to compare our results with the results from previous studies, we will integrate the data points down to $L = 0.3L_{z=3}^*$, where $L_{z=3}^*$ ($= 9.4 \times 10^{28}$ erg s^{-1} Hz $^{-1}$ at 1600Å) is the characteristic luminosity of our u -dropout sample. Results are shown in the odd-numbered rows of Col. 3 in Table 6.3. However, for steep faint-end slopes of $\alpha < -1.6$, more than 50% of the UV luminosity is expected to be emitted by lower luminosity sources. Therefore we will make a second estimate of the UV luminosity density by integrating the best-fitting Schechter function over all luminosities. This results in

$$\rho_{UV} = \phi^* L^* \Gamma(\alpha + 2), \quad (6.8)$$

where Γ is Euler's Gamma function. Although this full integral of the LF depends strongly on uncertainties in the faint-end slope, we use it to provide an upper limit to the UVLD. The results are shown in the even-numbered rows of Col. 3 in Table 6.3.

The effective extinction in the UV is a strong function of the amount of dust. At these high redshifts ($z \gtrsim 3$) the only estimate for the amount of dust is based on a measure of the UV continuum slope. Note however that there is a strong degeneracy between the age and the amount of dust in the template if the rest-frame IR is not covered, see e.g. Papovich et al. (2001).

Bouwens et al. (2009) recently measured the UV-continuum slope of LBGs at high redshifts from deep HST data, from which the amount of dust obscuration could be estimated as a function of LBG magnitude. The values they find at the characteristic magnitudes of our samples are $E(B - V) = 0.15$ for $z = 3, 4$, and $E(B - V) = 0.10$ for the $z \sim 5$ sample. Bouwens et al. (2009) find a decreasing amount of dust for fainter magnitudes. For consistency we

Table 6.3: The ρ_{UV} and ρ_{SFR} for the different dropout samples. The first lines for each sample correspond to sums over the data points down to $L = 0.3L_{z=3}^*$ while the second lines correspond to integrals over the best-fit Schechter functions.

Sample	Integral limit	$\rho_{UV} [10^{26}$ $\text{erg s}^{-1} \text{Hz}^{-1} \text{Mpc}^{-3}]^a$	ρ_{SFR} $[\text{M yr}^{-1} \text{Mpc}^{-3}]^{a,b}$
u	$L > 0.3L_{z=3}^*$	1.73 ± 0.09	$0.129_{-0.036}^{+0.064}$
	Schechter	4.41	0.154
g	$L > 0.3L_{z=3}^*$	1.07 ± 0.03	$0.078_{-0.019}^{+0.032}$
	Schechter	2.62	0.092
r	$L > 0.3L_{z=3}^*$	0.80 ± 0.03	$0.027_{-0.007}^{+0.013}$
	Schechter	2.19	0.038

^a Due to uncertainties in the redshift distributions, there is an additional error component of $\sim 7\%$, $\sim 5\%$, and $\sim 4\%$ in the estimated ρ_{UV} and ρ_{SFR} values for the u -, g -, and r -dropout samples, respectively.

^b Corrected for dust extinction using the luminosity dependent correction factors from Bouwens et al. (2009). Systematic errors as a result from the age-dust degeneracy are also included.

will use the relationships they estimate to correct for dust extinction in our data, and not the values from Sect. 6.3.1.

Meurer et al. (1999) find a relation between the UV-continuum slope and the extinction by dust. Bouwens et al. (2009) use this relation and find, upon integrating down to $L = 0.3L_{z=3}^*$, density correction factors of $6.0_{-1.4-1.6}^{+1.8+2.1}$, $5.8_{-0.7-1.5}^{+0.8+2.1}$, and $2.7_{-0.5-0.7}^{+0.7+1.0}$ for the three redshift samples, respectively. Both random errors and systematic errors are quoted (Bouwens et al. 2009).

We now convert the UV luminosity density into the star formation rate density, ρ_{SFR} , at the different epochs using (Madau et al. 1998),

$$L_{UV} = 8.0 \times 10^{27} \left(\frac{\text{SFR}}{\text{M}_{\text{yr}^{-1}}} \right) \text{erg s}^{-1} \text{Hz}^{-1}. \quad (6.9)$$

This relation assumes a 0.1-125M Salpeter IMF and a constant star formation rate of $\gtrsim 100$ Myr. The resulting estimates of ρ_{SFR} are shown in Col. 4 of Table 6.3, where we have corrected for dust extinction. In Sect. 6.5.4 we compare these estimates to values reported in previous studies.

Note, however, that some sources like AGN, which might be included in our dropout samples, add to the total UV luminosity density in the Universe, though do not contribute to the SFRD.

6.4.3 Robustness of our results

Our fiducial template model is a 100 Myr old continuously star-forming galaxy with a uniform distribution of dust centred around $E(B - V)=0.25$. This dust distribution was chosen such that the distribution of UV-continuum slopes of the recovered simulated sources matches the distribution of UV-continuum slopes in the real data (see Fig. 6.3). We test some of the assumptions we made in Sect. 6.3.1 by checking their influence on the final LFs.

As a reference SED we use a 100 Myr old galaxy model with constant star formation and a single dust attenuation value of $E(B - V)=0.25$. We consider redder (bluer) templates by either increasing (decreasing) the age of the star-forming period, or increasing (decreasing) the amount of dust. In Fig. 6.10 the colours of these alternative templates, as they would be measured by the MegaCam *ugriz* filter set, are shown as a function of redshift. As the quality of the Schechter fit is high in all cases ($\chi^2/\text{dof} < 1.0$), we present the differences by comparing the Schechter parameters:

- The faint-end slope α depends on the colour of the spectral template. In the *g*-, and *r*-dropout samples, redder templates tend to give steeper α than bluer templates. The reason for this is as follows, with the *g*-dropouts as an example. Sources in the selection box have red observed $g - i$ colours. For faint magnitudes (note that the reference magnitude is measured in the *i*-band), the *g*-band magnitude exceeds the limiting magnitude of the survey. Only a lower limit on $g - r$ can then be given and the source moves out of the dropout selection box. The magnitude at which this happens depends on the $g - i$ colour of the template. As the average $g - i$ colour in the selection box is redder for red templates (Fig. 6.10), the detection rate of red sources is suppressed at faint magnitudes. This argument holds for any red template in the *g*-, and *r*-dropout samples. Fig. 6.10 indicates that the opposite effect happens in the *u*-dropout sample as the $u - r$ colour is generally bluer (redder) for redder (bluer) templates in the selection box. This effect is indeed also inferred from the simulations. There is an additional effect due to the requirement that *g*-dropouts are not detected in *u*, and that *r*-dropouts are neither detected in *g* nor in *u*. This suppresses the detection of bright *g*-, and *r*-dropouts, especially at low redshifts. The bluer the $u - i$ colour for the *g*-dropouts (i.e. the bluer the template), the stronger this effect is. A similar argument holds for the *r*-dropouts. Therefore the V_{eff} 's are higher in the faint magnitude regime, so that the LFs are lower at this end. The ranges of best-fitted α values, for the template spectra we considered, are $-1.82 < \alpha < -1.38$ for the *u*-, $-1.82 < \alpha < -1.42$ for the *g*-, and $-2.14 < \alpha < -1.40$ for the *r*-dropout sample.
- The characteristic magnitude, M^* , does not sensitively depend on the

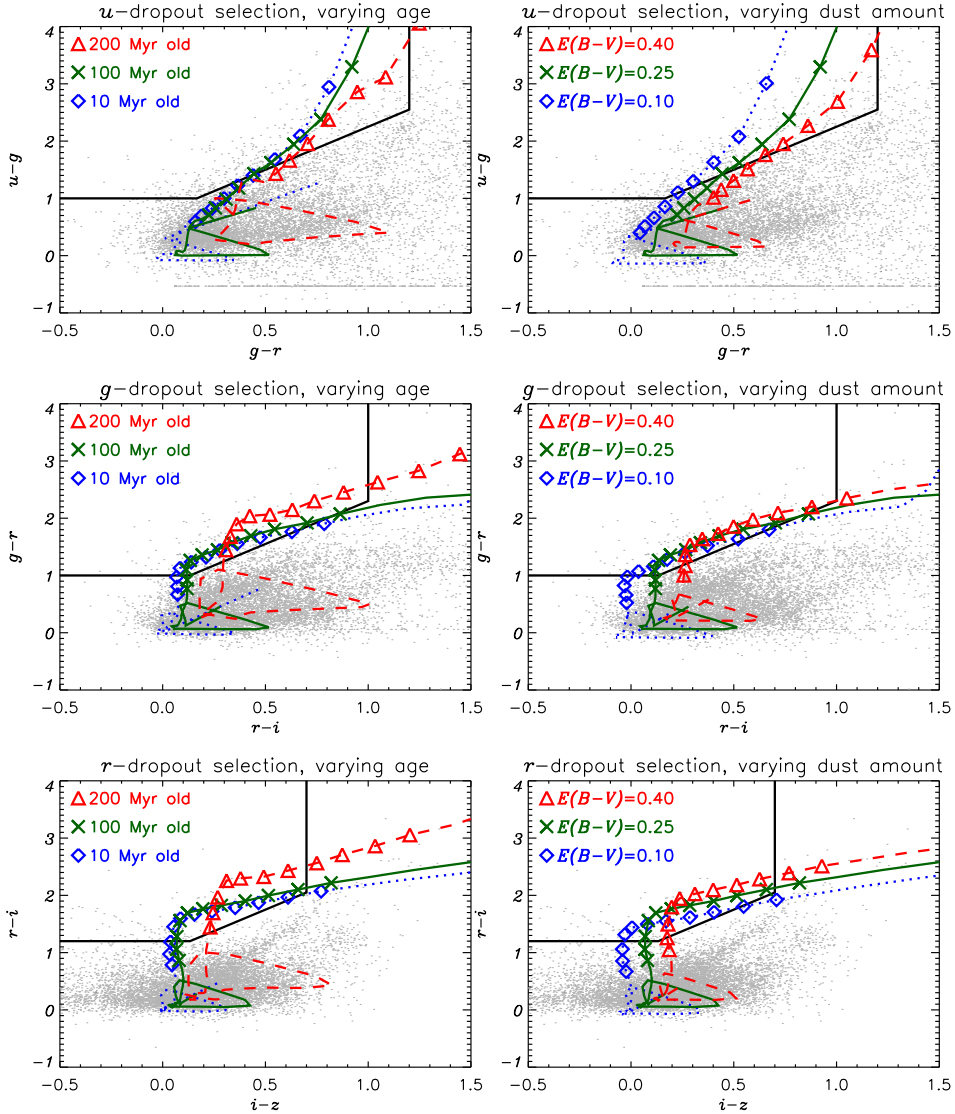


Figure 6.10: The grey points represent the colours of 10,000 objects in field 1 of the CFHTLS Deep. The black boxes are defined by Eqs. 6.1-6.3 and are used to select u - (top panels), g - (middle panels), and r - (bottom panels) dropouts. The coloured tracks represent the colours of a template galaxy as a function of z . They are evaluated at intervals of $\Delta z=0.1$. The symbols mark redshifts from 2.5 to 3.5, from 3.2 to 4.2 and from 4.2 to 5.2 for u -, g -, and r -dropouts respectively. The green curve with \times -symbols represents a reference model, a 100 Myr old continuously star-forming template with a dust attenuation of $E(B-V)=0.25$. In the left panels we consider redder (bluer) templates by increasing (decreasing) the template age, see the red (blue) curves and the \triangle (\diamond)-symbols. In the right panels we consider redder (bluer) templates by increasing (decreasing) the amount of dust in the template, see the red (blue) curves and the \triangle (\diamond)-symbols. Note that we use a distribution of dust in our fiducial analysis (see Sect. 6.3.1).

template spectrum chosen. The ranges of best-fitted M^* values, for the template spectra we considered, are $-20.88 < M^* < -20.72$ for the u -, $-21.06 < M^* < -20.74$ for the g -, and $-21.26 < M^* < -20.88$ for the r -dropout sample. However, another systematic uncertainty in this parameter is due to the unknown redshift distribution of source galaxies, see Fig. 6.7, which depends on the mix of templates used by Hildebrandt et al. (2009).

- The normalisation ϕ^* decreases (increases) when the faint-end slope becomes steeper (shallower). The best-fit Schechter parameters move then in the direction of the degeneracy of the ellipse in the upper left part of Fig. 6.9. The ranges of best-fitted ϕ^* values [10^{-3} Mpc^{-3}], for the template spectra we considered, are $1.36 < \phi^* < 2.89$ for the u -, $0.76 < \phi^* < 1.74$ for the g -, and $0.39 < \phi^* < 1.12$ for the r -dropout sample.

Some studies (e.g. Sawicki & Thompson 2006) make use of a starburst template instead of a continuously star-forming model. The stellar population in a starburst template is older on average, and therefore the colours will be redder. However, for a template age of 100 Myr the difference in colours is very small. We compare the Schechter parameters that we measure after using our reference model (i.e. a 100 Myr continuously star-forming template with a dust reddening of $E(B - V)=0.25$) with a model where we change the star-formation law to a starburst. We find the Schechter parameters to change in the directions that are expected for a redder template, as explained above. However the differences are insignificant since they are much smaller than the statistical errors on the Schechter parameters.

We stress again that we use a mix of dust amounts in our standard analysis to match the UV-continuum slope distribution that is measured from the data. Especially for the u -, and g -dropouts this puts strong constraints on the combination of the age and the amount of dust in the model template, so that we can reduce the systematic error to a minimum.

To justify the assumptions we make regarding the shapes of our simulated sources we also estimated the systematic error on the LF due to this component. Because we expect similar results in the three dropout samples, we only run these simulations for the g -dropouts. We inject sources that are 0.05" larger than the measured position-dependent PSF, and compare values of Moffat parameter $\beta = 3.0$ and $\beta = 5.0$ with our fiducial $\beta = 4.0$ parameter. We find the following:

- As expected, α becomes steeper for more extended sources (i.e. increasing the R_0 or decreasing β), as this causes the peak surface brightness to drop. This only significantly affects the V_{eff} 's at the faint end of the LF. Estimations of α range from $-1.94 < \alpha < -1.36$. A similar change is

expected for the u -, and r - dropout studies. The other Schechter parameters, ϕ^* and M^* , then also change slightly as they move in the direction of the degeneracy in Fig. 6.9.

Furthermore we find that, based on the different template spectra, the estimated UV luminosity density varies. The ranges are, upon integration down to $L < 0.3L_{z=3}^*$, in units [$10^{26} \text{erg s}^{-1} \text{Hz}^{-1} \text{Mpc}^{-3}$], $1.30 < \rho_{\text{UV}} < 1.98$ for the u -, $0.92 < \rho_{\text{UV}} < 1.15$ for the g -, and $0.80 < \rho_{\text{UV}} < 0.92$ for the r -dropouts.

In order to illustrate the effect that the Eddington bias can have on LF estimations we repeat our analysis with slightly changed $p(m, z)$. In the completeness simulations we bin the recovered sources by their intrinsic magnitude instead of their recovered magnitude. Doing so leaves the Eddington bias uncorrected. We find that the Schechter fit to the resulting LFs are not as good as for our standard analysis, especially for the g -, and r -dropouts, where we find that $\chi_{\text{min}}^2/\text{dof}$ would be 1.0 and 3.0, respectively. For the u -dropouts the best-fitting parameters are not changed significantly, but for the g -, and r -dropouts the faint-end slope steepens while the normalisation of the Schechter function decreases.

Note that we did not account for the presence of Lyman- α emission in our simulations, although this line clearly contributes to broadband fluxes. Shapley et al. (2003) measured the contribution of this line in the spectra of $z \sim 3$ LBGs and concluded that only $\sim 25\%$ of the sample showed significant Ly α emission such that $\text{EW}(\text{Ly}\alpha) > 20$, see also Reddy et al. (2008). Although the relative contribution of this line is thought to increase towards higher redshift and fainter continuum luminosity, this has not been quantified yet. We will therefore describe possible biases due to the presence of this line in the measurement of the LF only qualitatively.

If the line appears in emission, it contributes to the flux in the CFHT g -band for redshifts of about $2.5 < z < 3.5$, in the r -band for redshifts of about $3.7 < z < 4.6$, in the i -band for redshifts of about $4.8 < z < 5.9$, and in the z -band for redshifts of about $z > 5.8$. Following the redshift distributions from Hildebrandt et al. (2009), we expect that the line predominantly contributes to the middle band in a two colour selection for the u -, and r - dropout samples, moving the source to the upper left in Fig. 6.10. This effect causes the effective volumes to rise, thereby lowering the LF measurement. If the line indeed gets stronger at faint magnitudes, this would bias the LF measurement and results in a shallower alpha. In our g -dropout sample the line is expected to contribute to the flux in both the r - and i -band, depending on the redshift of the particular source. In the case where the line falls in the r -band, the effective volumes rise and the LF we measured is too high. For the redshifts where the line falls in the i -band, the sources would move to the right in Fig. 6.10 so that the effective volumes are decreased and the LF increases. To estimate which effect prevails,

the redshift distribution needs to be measured spectroscopically. Some objects show Ly- α in absorption rather than emission, which would give the opposite effect.

Note that Bouwens et al. (2007) model the contribution of Ly α in the measurement of their LF, by using a simple model where 33% of the $z \sim 4 - 5$ LBGs have $\text{EW}(\text{Ly } \alpha) = 50$, independent of the continuum luminosity. They find that this affects the normalisation of the LF by only $\sim 10\%$. However, we stress again that the measure of α might be biased if the strength of the line depends on the continuum luminosity.

6.4.4 The evolving galaxy population

Although we can measure the UV luminosity density with great accuracy, an estimate of the SFR Density depends sensitively on the dust extinction correction. Using the prescription from Bouwens et al. (2009), we find that the SFR Density shows a significant increase by a factor of 4-5 between $z \sim 5$ and $z \sim 3$.

We find a strong increase in ϕ^* between $z \sim 5$ and $z \sim 3$ by a factor of 2.5, which is a robust result. The characteristic magnitude, M_{UV}^* , however is not very well constrained by our data set. This is due to uncertainties in the redshift distributions of the source galaxies, as there are no spectroscopic data available. Our data are consistent with a non-evolving M_{UV}^* (~ -20.9) between $z \sim 5$ and $z \sim 3$. Our data do not show an evolution of the faint-end slope, and indicate $\alpha \sim -1.6$ in this epoch.

6.5 Comparison with previous determinations

Before we compare our results from each of the samples with Schechter parameters reported from previous determinations in the literature, there are a few things that should be noted. We will compare results at redshifts of *around* 3, 4 and 5. The LBGs are generally selected from different surveys and filter sets, and therefore intrinsically slightly different galaxies may be selected, studied and compared. Also the rest-frame wavelength at which the LF is estimated, varies. We compared the LFs at 1600Å, while e.g. Sawicki & Thompson (2006) measured the LF at 1700Å, and e.g. Giavalisco et al. (2004) did their analysis at 1500Å. Some of the studies described below make use of identical or partially overlapping datasets. Our analysis, on the contrary, is completely independent from previous determinations, except for the dust extinction correction in our SFR density estimate. Furthermore the errors of several other studies could be underestimated because only the Poisson noise component is taken into account, as other noise components (e.g. cosmic variance) are difficult to estimate with the typical small survey volumes of other surveys.

Also note that we compare our 2-dimensional error ellipses with 1-dimensional error bars that were attained after marginalizing over the two other Schechter parameters. This dilutes information on degeneracies between Schechter parameters. For these reasons the comparisons in this section will be rather qualitative, and are meant to put our results into context. Comparisons of the Schechter parameters are shown in Table 6.4, and in Figs. 6.11, 6.12 & 6.13, and will be discussed below.

Table 6.4: Our estimated Schechter parameters compared with values reported in the literature, for the three dropout samples.

Reference	M_{UV}^*	ϕ^* [10^{-3} Mpc^{-3}]	α
<i>u</i> -dropouts			
This work, Schechter	$-20.94^{+0.14}_{-0.13}$	$1.79^{+0.51}_{-0.38}$	$-1.65^{+0.12}_{-0.11}$
This work, Schechter+Magnification	$-20.84^{+0.15}_{-0.13}$	$2.11^{+0.63}_{-0.45}$	$-1.60^{+0.14}_{-0.11}$
Reddy & Steidel (2009)	-20.97 ± 0.14	1.71 ± 0.53	-1.73 ± 0.13
Sawicki & Thompson (2006)	$-20.90^{+0.22}_{-0.14}$	$1.70^{+0.59}_{-0.32}$	$-1.43^{+0.17}_{-0.09}$
Arnouts et al. (2005)	-21.08 ± 0.45	1.62 ± 0.90	-1.47 ± 0.21
Poli et al. (2001)	-20.84 ± 0.37	2.3	-1.37 ± 0.19
Steidel et al. (1999)	-21.04 ± 0.15	1.4	-1.60 ± 0.13
<i>g</i> -dropouts			
This work	-20.84 ± 0.09	$1.36^{+0.23}_{-0.20}$	-1.56 ± 0.08
Bouwens et al. (2007)	-20.98 ± 0.10	1.3 ± 0.2	-1.73 ± 0.05
Yoshida et al. (2006)	$-21.14^{+0.14}_{-0.15}$	$1.46^{+0.41}_{-0.35}$	-1.82 ± 0.09
Sawicki & Thompson (2006)	$-21.0^{+0.4}_{-0.5}$	$0.85^{+0.53}_{-0.45}$	$-1.26^{+0.40}_{-0.36}$
Giavalisco (2005)	-21.20 ± 0.04	1.20 ± 0.03	-1.64 ± 0.10
Ouchi et al. (2004a)	-21.0 ± 0.1	1.2 ± 0.2	-2.2 ± 0.2
Steidel et al. (1999)	-21.05	1.1	-1.6 (fixed)
<i>r</i> -dropouts			
This work	$-20.94^{+0.10}_{-0.11}$	$0.83^{+0.15}_{-0.14}$	$-1.65^{+0.09}_{-0.08}$
Bouwens et al. (2007)	-20.64 ± 0.13	1.0 ± 0.3	-1.66 ± 0.09
Oesch et al. (2007)	-20.78 ± 0.16	0.9 ± 0.3	-1.54 ± 0.10
Iwata et al. (2007)	-21.28 ± 0.38	$0.41^{+0.29}_{-0.30}$	$-1.48^{+0.38}_{-0.32}$
Yoshida et al. (2006)	$-20.72^{+0.16}_{-0.14}$	$1.23^{+0.44}_{-0.27}$	-1.82 (fixed)
Giavalisco (2005)	-21.06 ± 0.05	0.83 ± 0.03	-1.51 ± 0.18
Ouchi et al. (2004a)	-20.3 ± 0.2	2.4 ± 1.0	-1.6 (fixed)

6.5.1 Comparison at $z=3$

We compare the results from our *u*-dropout sample with several Schechter parameters reported in the literature. Sawicki & Thompson (2006) estimated the LF from the Keck deep fields, from $U_n GR$ -selected star-forming galaxies. Their

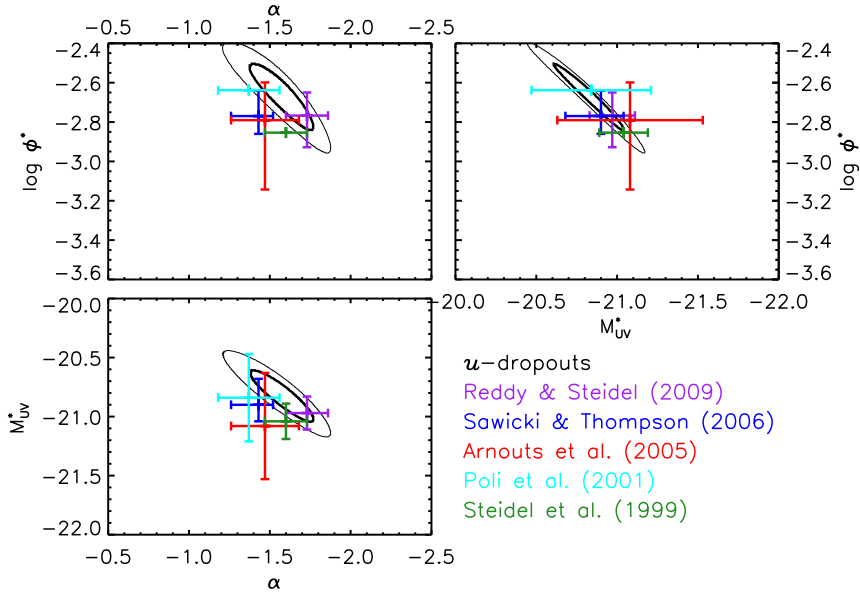


Figure 6.11: Comparison at $z \sim 3$. The ellipses represent the 68% and 95% confidence contours for different Schechter parameter combinations, based on our study. The error bars reflect the 68% confidence limits on the results from previous studies. Our results agree within the $1\text{-}\sigma$ level with most of the other determinations.

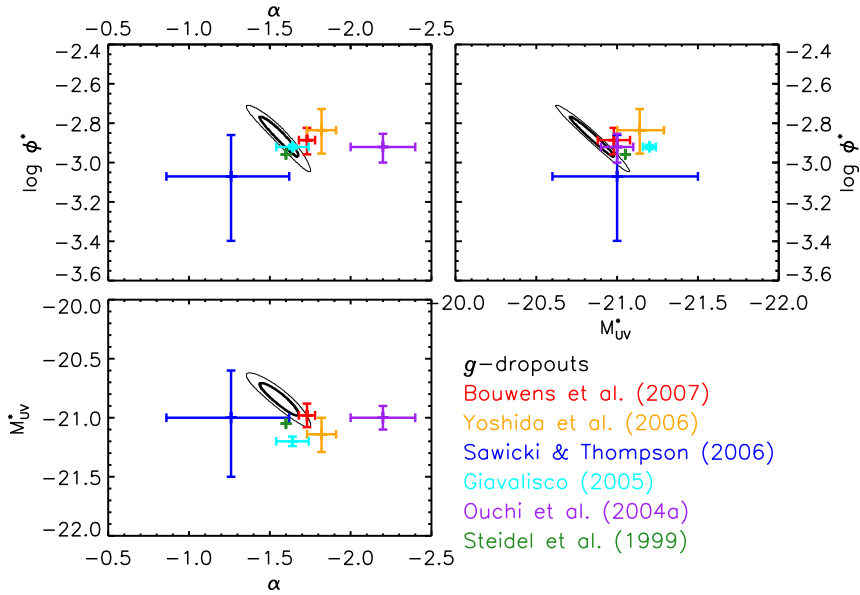


Figure 6.12: Similar as Fig. 6.11, but now a comparison at $z \sim 4$.

survey area is about 60 times smaller than the CFHTLS-Deep. The depth of their observations is slightly deeper than ours, but due to our Eddington bias correction, we are able to probe the LFs down to similar magnitudes. Reddy & Steidel (2009) estimate a LF at $z \sim 3$, from 31 spatially independent fields, having a total area of about a quarter of ours. Their sample contains several thousands of spectroscopic redshifts at $z=2-3$. Arnouts et al. (2005) mainly focussed on the galaxy LF at lower redshifts ($0.2 \leq z \leq 1.2$) from *GALEX*-data, but their redshift range was extended using 173 galaxies at $z \sim 3$ from the HDF sample. Poli et al. (2001) used the HDF-N, HDF-S and NTT-DF samples to estimate the LF in the range $2.5 \leq z \leq 3.5$. Their sample was therefore selected from a very small volume, which makes their results susceptible to cosmic variance. Steidel et al. (1999) pioneered this work, and estimated the UV LF from 0.23 deg^2 of moderately deep data. Their study was supported by a spectroscopic redshift sample. This data is included in the study by Reddy & Steidel (2009).

Our results agree within the $1 - \sigma$ level with the results from previous determinations at $z \sim 3$. Note that the other data points lie in the direction of the elongated ellipse, and therefore in the direction of the degeneracy we find.

6.5.2 Comparison at $z=4$

Our g -dropout sample is compared with the $z \sim 4$ sample from Sawicki & Thompson (2006), selected from the *GRI* filter sets on the Keck telescope. Their area is identical to the one from which the $z \sim 3$ LF was estimated. Steidel et al. (1999) also estimated the $z \sim 4$ LF with a similar filter set as Sawicki & Thompson (2006), but did not probe deep enough to be able to constrain the faint-end slope α . This parameter was set equal to the value found at $z = 3$, namely $\alpha = -1.6$. Yoshida et al. (2006) presented the LF for 3808 BRI^i -selected LBGs, selected from the Subaru Deep Field project. Ouchi et al. (2004a) selected a $z \sim 4$ LBG sample from Subaru imaging, supported by a sample of 85 spectroscopically identified objects. Giavalisco et al. (2004) used a $\sim 0.09 \text{ deg}^2$ sample from the GOODS to estimate a LF for $B_{450}V_{606}z_{850}$ -selected LBGs. Bouwens et al. (2007) used the deep HST ACS fields, including the HUDF and the GOODS, to select a sample of 4671 B-dropouts, from which they estimated the UV LF to $M_{1600,AB} = -16.26$.

With this data set we have been able to measure the Schechter parameters for the g -dropout sample with very high statistical accuracy. Note however that several systematic uncertainties, which we comment upon in Sect. 6.4.3, are not included in our error ellipses. Our results agree within the $1 - \sigma$ level with many of the $z \sim 4$ results in the literature. However, there is still some tension in measurements of the faint-end slope α . The characteristic

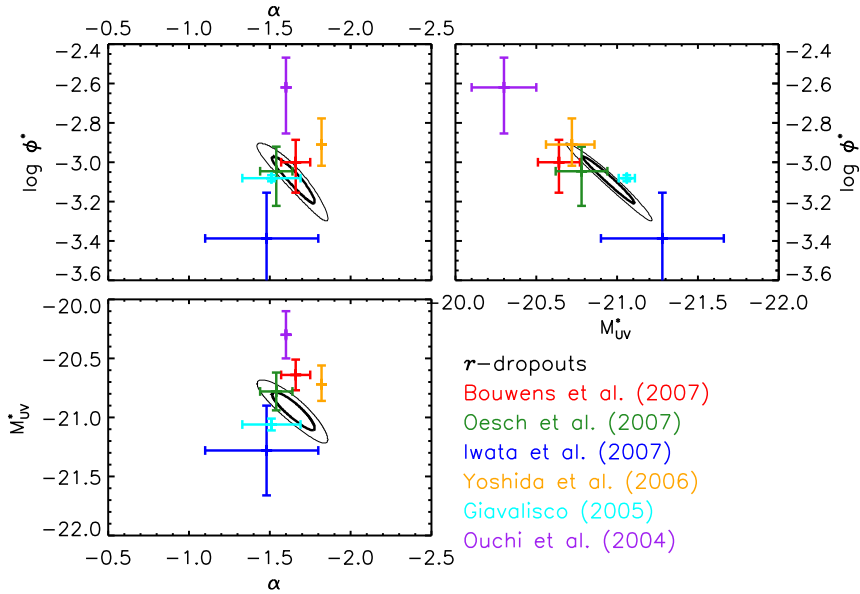


Figure 6.13: Similar as Fig. 6.11, but now a comparison at $z \sim 5$.

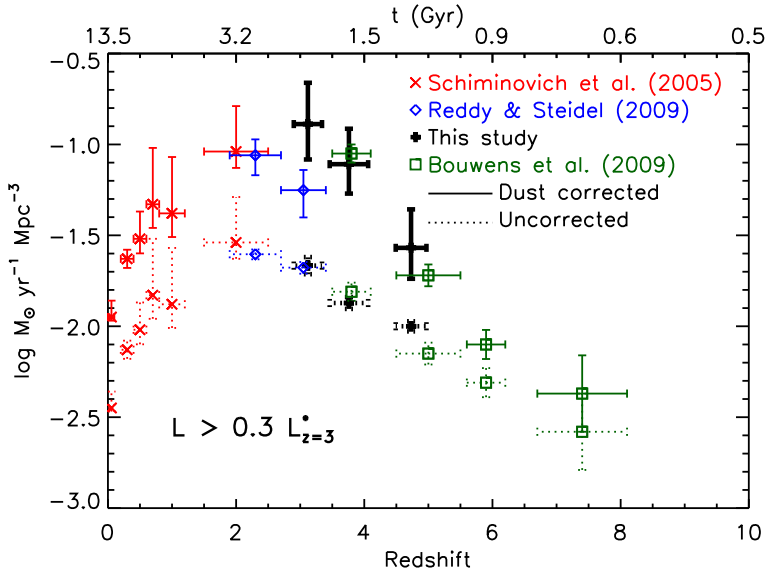


Figure 6.14: ρ_{SFR} as a function of redshift and cosmic time. Dotted: SFRD uncorrected for dust. Solid: the dust corrected SFRD, where we use a luminosity dependent dust correction factor from Bouwens et al. (2009). Note that we included both random and systematic errors in our dust correction, unlike most other studies.

magnitude, M_{UV}^* , we measure, is slightly fainter than the values we found in the literature.

6.5.3 Comparison at $z=5$

At $z \sim 5$, Iwata et al. (2007) reported the UV LF from a combination of HDF and Subaru images, totalling a survey area about 1/9 of ours. Oesch et al. (2007) based their study on approximately 100 LBGs from very deep ACS and NICMOS imaging. Yoshida et al. (2006) also defined a $z \sim 5$ sample from their observations, combining $Vi'z'$ and $Ri'z'$ selected objects, as did Ouchi et al. (2004a). Giavalisco et al. (2004) selected 275 $V_{606}i_{775}z_{850}$ LBGs to estimate a $z \sim 5$ UV LF. Bouwens et al. (2007) also measured a sample of 1416 V -dropouts from their deep HST ACS sample, which resulted in an estimation of the UV LF down to $M_{1600,AB} = -17.16$.

Similar to the Schechter parameters found for $z \sim 4$, there is a large discrepancy in the literature for the Schechter parameters at $z \sim 5$. The statistical uncertainties in the Schechter parameters is very small for our r -dropout sample. Note however that several systematic uncertainties are not included in these error ellipses, see Sect. 6.4.3. Our results agree reasonably well, within the $1 - \sigma$ level, with many previous determinations at $z \sim 5$.

6.5.4 Comparison of the SFR density

In Fig. 6.14 we compare the SFR density values given in Table 6.3 to values reported by Schiminovich et al. (2005), who made use of low- z GALEX data, Reddy & Steidel (2009) at intermediate z , and Bouwens et al. (2009) at high z . The uncorrected SFRDs are in good agreement with each other and show a smooth redshift evolution. However, it is clear that the dust correction is the major uncertainty because of the age-dust degeneracy. We use the same dust correction as Bouwens et al. (2009) and also include systematic uncertainties in the error bars.

6.6 Summary & Conclusions

In this paper we use the CFHT Legacy Survey Deep fields to estimate the UV Luminosity Functions of the largest u -, g -, and r -dropouts samples to date. As our samples are all extracted from the same dataset this study is ideally suited to study a time evolution of the luminosity function in the redshift regime $z = 3 - 5$. Thanks to the large volumes we probe with our 4 square degree survey, cosmic variance plays a negligible role in our analysis. We are now able to study the bright end of the luminosity function with unprecedented accuracy. Furthermore, given the depth of the stacked MegaCam images, we

probe the faint end of the luminosity function with comparable precision as the deepest ground based surveys have done before. This unique combination gives us the opportunity to not only estimate the Schechter parameters for the different luminosity functions, but also to study a possible deviation from this commonly used fit.

In the u -, and g -dropout samples of our survey we are able to measure the UV continuum slope directly from the data. This allows us to simulate sources that have the same distribution of UV slopes, which is important for an accurate estimate of the Schechter parameters.

We find the faint-end slope α to not evolve significantly in the redshift range we probe, and to have a value of around -1.6 . This parameter however, is not very strongly constrained by our ground based survey, as this parameter depends on some of the assumptions made.

We do not find a significant evolution in M_{UV}^* , and argue that this might be due to insufficient knowledge of the redshift distribution of the source galaxies. The conversion of apparent to absolute magnitudes depends strongly on these distributions, and an uncertainty in the distance modulus directly propagates into an equal uncertainty in M_{UV}^* . This parameter is therefore poorly constrained by this study, until a more reliable redshift distribution is available.

We find a strong evolution in ϕ^* , which we argue to be significant. The normalisation of the LBG density, ϕ^* , increases by a factor of ~ 2.5 from $z \approx 5$ to $z \approx 3$, an increase that cannot be explained by any change in the assumptions tested. We therefore conclude that the UV luminosity density is increasing in the corresponding epoch, in a way that does not strongly differ with magnitude.

The SFR Density does increase significantly, by a factor of ~ 3 , between $z \sim 5$ and $z \sim 4$. We find a smaller, but less significant increase between $z \sim 4$ and $z \sim 3$.

With our 4 square degree survey we probe densities that are at least four times lower than any of the studies we compared our results to. We find a substantial deviation from the Schechter function at the bright end for the u -dropouts, where the LBG densities are very low. We find that the deviation can be attributed to magnification effects that arise from inhomogeneities in the matter distribution between the LBGs and the observer. We fit an improved Schechter function that is corrected for magnification and find that the quality of the fit improves significantly. Intrinsically the distribution of luminosities does therefore not deviate significantly from a Schechter model. With this data set we have been the first to be able to measure a hint of this magnification imprint on a $z \sim 3$ LBG sample.

Acknowledgements

We thank Stefan Hilbert for supplying the magnification distribution for sources at our redshift of interest. We are grateful to Konrad Kuijken, Rychard Bouwens, Ludovic van Waerbeke and Marijn Franx for the interesting discussions we had and their suggestions to improve the quality of this research. We thank Henk Hoekstra for the supply of powerful CPU's to perform the simulations with, and useful comments on the paper. We also thank the anonymous referee for a detailed report with nice suggestions for this paper.

Based on observations obtained with MegaPrime/MegaCam, a joint project of CFHT and CEA/DAPNIA, at the Canada-France-Hawaii Telescope (CFHT) which is operated by the National Research Council (NRC) of Canada, the Institut National des Sciences de l'Univers of the Centre National de la Recherche Scientifique (CNRS) of France, and the University of Hawaii. This work is based in part on data products produced at TERAPIX and the Canadian Astronomy Data Centre as part of the Canada-France-Hawaii Telescope Legacy Survey, a collaborative project of NRC and CNRS.

We are grateful to the CFHTLS survey team for conducting the observations and the TERAPIX team for developing software used in this study. We acknowledge use of the Canadian Astronomy Data Centre operated by the Dominion Astrophysical Observatory for the National Research Council of Canada's Herzberg Institute of Astrophysics. HH is supported by the European DUEL RTN, project MRTN-CT-2006-036133. TE is supported by the European DUEL RTN, the German Ministry for Science and Education (BMBF) through the DESY project 'GAVO III', and the Deutsche Forschungsgemeinschaft through the projects SCHN 342/7 - 1 and ER 327/3 - 1 within the Priority Programme 1177.

Bibliography

- Abazajian, K. N., Adelman-McCarthy, J. K., Agüeros, M. A., et al. 2009, *ApJS*, 182, 543
- Ahn, C. P., Alexandroff, R., Allende Prieto, C., et al. 2013, *ArXiv e-prints*
- Andreon, S. 2010, *MNRAS*, 407, 263
- Andreon, S. 2012, *A&A*, 548, A83
- Andreon, S. & Hurn, M. A. 2010, *MNRAS*, 404, 1922
- Arnouts, S., Schiminovich, D., Ilbert, O., et al. 2005, *ApJ*, 619, L43
- Bahé, Y. M., McCarthy, I. G., Balogh, M. L., & Font, A. S. 2013, *MNRAS*, 430, 3017
- Baldry, I. K., Balogh, M. L., Bower, R. G., et al. 2006, *MNRAS*, 373, 469
- Balogh, M. L., Baldry, I. K., Nichol, R., et al. 2004, *ApJ*, 615, L101
- Balogh, M. L., McCarthy, I. G., Bower, R. G., & Eke, V. R. 2008, *MNRAS*, 385, 1003
- Balogh, M. L., McGee, S. L., Wilman, D. J., et al. 2011, *MNRAS*, 412, 2303
- Balogh, M. L., Morris, S. L., Yee, H. K. C., Carlberg, R. G., & Ellingson, E. 1999, *ApJ*, 527, 54
- Bastian, N., Covey, K. R., & Meyer, M. R. 2010, *ARA&A*, 48, 339
- Bauer, A. H., Baltay, C., Ellman, N., et al. 2012, *ApJ*, 749, 56
- Beers, T. C., Flynn, K., & Gebhardt, K. 1990, *AJ*, 100, 32
- Behroozi, P. S., Conroy, C., & Wechsler, R. H. 2010, *ApJ*, 717, 379
- Behroozi, P. S., Wechsler, R. H., & Conroy, C. 2013, *ApJ*, 770, 57
- Bell, E. F. & de Jong, R. S. 2001, *ApJ*, 550, 212
- Bell, E. F., McIntosh, D. H., Katz, N., & Weinberg, M. D. 2003, *ApJS*, 149, 289
- Bennett, C. L., Larson, D., Weiland, J. L., et al. 2013, *ApJS*, 208, 20
- Benson, A. J., Lacey, C. G., Baugh, C. M., Cole, S., & Frenk, C. S. 2002, *MNRAS*, 333, 156
- Bertin, E. 2006, in *Astronomical Society of the Pacific Conference Series*, Vol.

- 351, *Astronomical Data Analysis Software and Systems XV*, ed. C. Gabriel, C. Arviset, D. Ponz, & S. Enrique, 112
- Bertin, E. & Arnouts, S. 1996, *A&AS*, 117, 393
- Bildfell, C., Hoekstra, H., Babul, A., et al. 2012, *MNRAS*, 425, 204
- Binney, J. & Tremaine, S. 2008, *Galactic Dynamics: Second Edition* (Princeton University Press)
- Biviano, A., Katgert, P., Thomas, T., & Adami, C. 2002, *A&A*, 387, 8
- Blakeslee, J. P., Franx, M., Postman, M., et al. 2003, *ApJ*, 596, L143
- Blanton, M. R., Eisenstein, D., Hogg, D. W., Schlegel, D. J., & Brinkmann, J. 2005, *ApJ*, 629, 143
- Bolzonella, M., Kovač, K., Pozzetti, L., et al. 2010, *A&A*, 524, A76
- Borgani, S., Girardi, M., Carlberg, R. G., Yee, H. K. C., & Ellingson, E. 1999, *ApJ*, 527, 561
- Bouwens, R. J., Illingworth, G. D., Blakeslee, J. P., & Franx, M. 2006, *ApJ*, 653, 53
- Bouwens, R. J., Illingworth, G. D., Franx, M., et al. 2009, *ArXiv e-prints*
- Bouwens, R. J., Illingworth, G. D., Franx, M., & Ford, H. 2007, *ApJ*, 670, 928
- Bouwens, R. J., Illingworth, G. D., Oesch, P. A., et al. 2012, *ApJ*, 754, 83
- Bower, R. G., Benson, A. J., & Crain, R. A. 2012, *MNRAS*, 422, 2816
- Bower, R. G., Benson, A. J., Malbon, R., et al. 2006, *MNRAS*, 370, 645
- Boylan-Kolchin, M., Bullock, J. S., & Kaplinghat, M. 2011, *MNRAS*, 415, L40
- Boylan-Kolchin, M., Springel, V., White, S. D. M., Jenkins, A., & Lemson, G. 2009, *MNRAS*, 398, 1150
- Brammer, G. B., van Dokkum, P. G., & Coppi, P. 2008, *ApJ*, 686, 1503
- Brammer, G. B., Whitaker, K. E., van Dokkum, P. G., et al. 2011, *ApJ*, 739, 24
- Bruzual, G. & Charlot, S. 2003, *MNRAS*, 344, 1000
- Bruzual A., G. & Charlot, S. 1993, *ApJ*, 405, 538
- Bryan, G. L. & Norman, M. L. 1998, *ApJ*, 495, 80
- Budzynski, J. M., Kuposov, S. E., McCarthy, I. G., & Belokurov, V. 2013, *MNRAS*
- Budzynski, J. M., Kuposov, S. E., McCarthy, I. G., McGee, S. L., & Belokurov, V. 2012, *MNRAS*, 423, 104
- Bullock, J. S. 2010, *ArXiv e-prints*
- Bundy, K., Ellis, R. S., Conselice, C. J., et al. 2006, *ApJ*, 651, 120
- Burke, C. & Collins, C. A. 2013, *MNRAS*, 434, 2856
- Burke, C., Collins, C. A., Stott, J. P., & Hilton, M. 2012, *MNRAS*, 425, 2058
- Butcher, H. & Oemler, Jr., A. 1978, *ApJ*, 219, 18
- Calzetti, D., Armus, L., Bohlin, R. C., et al. 2000, *ApJ*, 533, 682
- Capak, P., Aussel, H., Ajiki, M., et al. 2007, *ApJS*, 172, 99
- Carilli, C. L. & Walter, F. 2013, *ARA&A*, 51, 105
- Carlberg, R. G., Yee, H. K. C., & Ellingson, E. 1997a, *ApJ*, 478, 462
- Carlberg, R. G., Yee, H. K. C., Ellingson, E., et al. 1996, *ApJ*, 462, 32
- Carlberg, R. G., Yee, H. K. C., Ellingson, E., et al. 1997b, *ApJ*, 485, L13

- Carlberg, R. G., Yee, H. K. C., Ellingson, E., et al. 1997c, *ApJ*, 476, L7
- Cen, R. 2014, *ApJ*, 781, 38
- Chabrier, G. 2003, *PASP*, 115, 763
- Clowe, D., Markevitch, M., Bradač, M., et al. 2012, *ApJ*, 758, 128
- Cole, S., Norberg, P., Baugh, C. M., et al. 2001, *MNRAS*, 326, 255
- Colless, M., Dalton, G., Maddox, S., et al. 2001, *MNRAS*, 328, 1039
- Comerford, J. M. & Natarajan, P. 2007, *MNRAS*, 379, 190
- Contini, E., De Lucia, G., Villalobos, A., & Borgani, S. 2013, *ArXiv e-prints*
- Cooper, M. C., Coil, A. L., Gerke, B. F., et al. 2010, *MNRAS*, 409, 337
- Covey, K. R., Ivezić, Ž., Schlegel, D., et al. 2007, *AJ*, 134, 2398
- Cusworth, S. J., Kay, S. T., Battye, R. A., & Thomas, P. A. 2013, *ArXiv e-prints*
- Dalla Vecchia, C. & Schaye, J. 2008, *MNRAS*, 387, 1431
- De Lucia, G. & Blaizot, J. 2007, *MNRAS*, 375, 2
- De Lucia, G., Weinmann, S., Poggianti, B. M., Aragón-Salamanca, A., & Zaritsky, D. 2012, *MNRAS*, 423, 1277
- Demarco, R., Wilson, G., Muzzin, A., et al. 2010, *ApJ*, 711, 1185
- Diemer, B., More, S., & Kravtsov, A. V. 2013, *ApJ*, 766, 25
- Dolag, K., Borgani, S., Murante, G., & Springel, V. 2009, *MNRAS*, 399, 497
- Dressler, A. 1980, *ApJ*, 236, 351
- Dressler, A., Smail, I., Poggianti, B. M., et al. 1999, *ApJS*, 122, 51
- Duffy, A. R., Schaye, J., Kay, S. T., & Dalla Vecchia, C. 2008, *MNRAS*, 390, L64
- Eddington, A. S. 1913, *MNRAS*, 73, 359
- Efstathiou, G. 2000, *MNRAS*, 317, 697
- Eggen, O. J., Lynden-Bell, D., & Sandage, A. R. 1962, *ApJ*, 136, 748
- Erben, T., Hildebrandt, H., Lerchster, M., et al. 2009, *A&A*, 493, 1197
- Erben, T., Schirmer, M., Dietrich, J. P., et al. 2005, *Astronomische Nachrichten*, 326, 432
- Evrard, A. E., Bialek, J., Busha, M., et al. 2008, *ApJ*, 672, 122
- Fabian, A. C. 2012, *ARA&A*, 50, 455
- Fadda, D., Girardi, M., Giuricin, G., Mardirossian, F., & Mezzetti, M. 1996, *ApJ*, 473, 670
- Ford, J., Hildebrandt, H., Van Waerbeke, L., et al. 2013, *ArXiv e-prints*
- Gamow, G. 1948, *Nature*, 162, 680
- Gao, L., Navarro, J. F., Cole, S., et al. 2008, *MNRAS*, 387, 536
- Ghigna, S., Moore, B., Governato, F., et al. 2000, *ApJ*, 544, 616
- Giavalisco, M. 2002, *ARA&A*, 40, 579
- Giavalisco, M. 2005, *New Astronomy Review*, 49, 440
- Giavalisco, M. & Dickinson, M. 2001, *ApJ*, 550, 177
- Giavalisco, M., Dickinson, M., Ferguson, H. C., et al. 2004, *ApJ*, 600, L103
- Giavalisco, M., Steidel, C. C., & Macchetto, F. D. 1996, *ApJ*, 470, 189
- Illis, B. R., Hudson, M. J., Erben, T., et al. 2013, *MNRAS*, 431, 1439

- Giodini, S., Finoguenov, A., Pierini, D., et al. 2012, *A&A*, 538, A104
- Giodini, S., Pierini, D., Finoguenov, A., et al. 2009, *ApJ*, 703, 982
- Girardi, L., Groenewegen, M. A. T., Hatziminaoglou, E., & da Costa, L. 2005, *A&A*, 436, 895
- Girardi, M., Biviano, A., Giuricin, G., Mardirossian, F., & Mezzetti, M. 1993, *ApJ*, 404, 38
- Girardi, M. & Mezzetti, M. 2001, *ApJ*, 548, 79
- Gladders, M. D. & Yee, H. K. C. 2000, *AJ*, 120, 2148
- Gonzalez, A. H., Sivanandam, S., Zabludoff, A. I., & Zaritsky, D. 2013, *ApJ*, 778, 14
- Gonzalez, A. H., Zaritsky, D., & Zabludoff, A. I. 2007, *ApJ*, 666, 147
- Gunn, J. E. & Gott, III, J. R. 1972, *ApJ*, 176, 1
- Guo, Q., White, S., Li, C., & Boylan-Kolchin, M. 2010, *MNRAS*, 404, 1111
- Haines, C. P., Pereira, M. J., Sanderson, A. J. R., et al. 2012, *ApJ*, 754, 97
- Haines, C. P., Pereira, M. J., Smith, G. P., et al. 2013, *ApJ*, 775, 126
- Henriques, B. M. B., White, S. D. M., Lemson, G., et al. 2012, *MNRAS*, 421, 2904
- High, F. W., Stubbs, C. W., Rest, A., Stalder, B., & Challis, P. 2009, *AJ*, 138, 110
- Hilbert, S., White, S. D. M., Hartlap, J., & Schneider, P. 2007, *MNRAS*, 382, 121
- Hildebrandt, H., Arnouts, S., Capak, P., et al. 2010, *A&A*, 523, A31
- Hildebrandt, H., Bomans, D. J., Erben, T., et al. 2005, *A&A*, 441, 905
- Hildebrandt, H., Erben, T., Dietrich, J. P., et al. 2006, *A&A*, 452, 1121
- Hildebrandt, H., Erben, T., Kuijken, K., et al. 2012, *MNRAS*, 421, 2355
- Hildebrandt, H., Muzzin, A., Erben, T., et al. 2011, *ApJ*, 733, L30
- Hildebrandt, H., Pielorz, J., Erben, T., et al. 2007, *A&A*, 462, 865
- Hildebrandt, H., Pielorz, J., Erben, T., et al. 2009, *A&A*, 498, 725
- Hildebrandt, H., van Waerbeke, L., Scott, D., et al. 2013, *MNRAS*, 429, 3230
- Hilton, M., Hasselfield, M., Sifón, C., et al. 2013, *MNRAS*, 435, 3469
- Hirashita, H., Buat, V., & Inoue, A. K. 2003, *A&A*, 410, 83
- Hoekstra, H. 2007, *MNRAS*, 379, 317
- Hoekstra, H., Donahue, M., Conselice, C. J., McNamara, B. R., & Voit, G. M. 2011, *ApJ*, 726, 48
- Hoekstra, H., Franx, M., & Kuijken, K. 2000, *ApJ*, 532, 88
- Hoekstra, H., Mahdavi, A., Babul, A., & Bildfell, C. 2012, *MNRAS*, 427, 1298
- Hogg, D. W. 1999, *ArXiv Astrophysics e-prints*
- Hu, W. & White, M. 1996, *ApJ*, 471, 30
- Hubble, E. & Humason, M. L. 1931, *ApJ*, 74, 43
- Hubble, E. P. 1926, *ApJ*, 64, 321
- Ilbert, O., Salvato, M., Le Floc'h, E., et al. 2010, *ApJ*, 709, 644
- Iwata, I., Ohta, K., Tamura, N., et al. 2007, *MNRAS*, 376, 1557
- Jain, B. & Lima, M. 2010, *ArXiv e-prints*

- Kapteyn, J. C. 1922, *ApJ*, 55, 302
- Kauffmann, G., Heckman, T. M., White, S. D. M., et al. 2003, *MNRAS*, 341, 33
- Kauffmann, G., White, S. D. M., Heckman, T. M., et al. 2004, *MNRAS*, 353, 713
- Kennicutt, Jr., R. C. 1983, *ApJ*, 272, 54
- Kennicutt, Jr., R. C. 1998, *ARA&A*, 36, 189
- Klypin, A., Kravtsov, A. V., Valenzuela, O., & Prada, F. 1999, *ApJ*, 522, 82
- Knobel, C., Lilly, S. J., Kovač, K., et al. 2013, *ApJ*, 769, 24
- Komatsu, E., Smith, K. M., Dunkley, J., et al. 2010, *ArXiv e-prints*
- Kovač, K., Lilly, S. J., Knobel, C., et al. 2014, *MNRAS*, 438, 717
- Kravtsov, A. V. & Borgani, S. 2012, *ARA&A*, 50, 353
- Kriek, M., van Dokkum, P. G., Labbé, I., et al. 2009, *ApJ*, 700, 221
- Kron, R. G. 1980, *ApJS*, 43, 305
- Kroupa, P. 2001, *MNRAS*, 322, 231
- Kuijken, K. 2006, *A&A*, 456, 827
- Kuijken, K. 2008, *A&A*, 482, 1053
- Laganá, T. F., Martinet, N., Durret, F., et al. 2013, *A&A*, 555, A66
- Laporte, C. F. P., White, S. D. M., Naab, T., & Gao, L. 2013, *MNRAS*, 435, 901
- Larson, R. B., Tinsley, B. M., & Caldwell, C. N. 1980, *ApJ*, 237, 692
- Lasker, B. M., Lattanzi, M. G., McLean, B. J., et al. 2008, *AJ*, 136, 735
- Leauthaud, A., George, M. R., Behroozi, P. S., et al. 2012a, *ApJ*, 746, 95
- Leauthaud, A., Tinker, J., Bundy, K., et al. 2012b, *ApJ*, 744, 159
- Lidman, C., Iacobuta, G., Bauer, A. E., et al. 2013, *MNRAS*, 433, 825
- Lidman, C., Suherli, J., Muzzin, A., et al. 2012, *MNRAS*, 427, 550
- Lilly, S. J., Le Fevre, O., Hammer, F., & Crampton, D. 1996, *ApJ*, 460, L1
- Lin, Y.-T. & Mohr, J. J. 2004, *ApJ*, 617, 879
- Lin, Y.-T., Mohr, J. J., & Stanford, S. A. 2004, *ApJ*, 610, 745
- Lin, Y.-T., Stanford, S. A., Eisenhardt, P. R. M., et al. 2012, *ApJ*, 745, L3
- Lonsdale, C. J., Smith, H. E., Rowan-Robinson, M., et al. 2003, *PASP*, 115, 897
- Madau, P. 1995, *ApJ*, 441, 18
- Madau, P., Ferguson, H. C., Dickinson, M. E., et al. 1996, *MNRAS*, 283, 1388
- Madau, P., Pozzetti, L., & Dickinson, M. 1998, *ApJ*, 498, 106
- Magnier, E. A. & Cuillandre, J.-C. 2004, *PASP*, 116, 449
- Mahajan, S., Mamon, G. A., & Raychaudhury, S. 2011, *MNRAS*, 416, 2882
- Mahdavi, A., Hoekstra, H., Babul, A., Balam, D. D., & Capak, P. L. 2007, *ApJ*, 668, 806
- Mandelbaum, R., Seljak, U., & Hirata, C. M. 2008, *J. Cosmology Astropart. Phys.*, 8, 6
- Marchesini, D., van Dokkum, P. G., Förster Schreiber, N. M., et al. 2009, *ApJ*, 701, 1765
- Martel, H., Barai, P., & Brito, W. 2012, *ApJ*, 757, 48
- Martin, D. C., Fanson, J., Schiminovich, D., et al. 2005, *ApJ*, 619, L1

- McCarthy, I. G., Frenk, C. S., Font, A. S., et al. 2008, *MNRAS*, 383, 593
- McCracken, H. J., Milvang-Jensen, B., Dunlop, J., et al. 2012, *A&A*, 544, A156
- McGee, S. L., Balogh, M. L., Bower, R. G., Font, A. S., & McCarthy, I. G. 2009, *MNRAS*, 400, 937
- McGee, S. L., Balogh, M. L., Wilman, D. J., et al. 2011, *MNRAS*, 413, 996
- Meurer, G. R., Heckman, T. M., & Calzetti, D. 1999, *ApJ*, 521, 64
- Miller, G. E. & Scalo, J. M. 1979, *ApJS*, 41, 513
- Mok, A., Balogh, M. L., McGee, S. L., et al. 2013, *MNRAS*, 431, 1090
- Moore, B., Katz, N., Lake, G., Dressler, A., & Oemler, A. 1996, *Nature*, 379, 613
- Moran, S. M., Ellis, R. S., Treu, T., et al. 2007, *ApJ*, 671, 1503
- Moster, B. P., Naab, T., & White, S. D. M. 2013, *MNRAS*, 428, 3121
- Moster, B. P., Somerville, R. S., Maulbetsch, C., et al. 2010, *ApJ*, 710, 903
- Mullis, C. R., Rosati, P., Lamer, G., et al. 2005, *ApJ*, 623, L85
- Munari, E., Biviano, A., Borgani, S., Murante, G., & Fabjan, D. 2013, *MNRAS*, 430, 2638
- Muzzin, A., Marchesini, D., Stefanon, M., et al. 2013a, *ApJ*, 777, 18
- Muzzin, A., Marchesini, D., Stefanon, M., et al. 2013b, *ApJS*, 206, 8
- Muzzin, A., Wilson, G., Lacy, M., Yee, H. K. C., & Stanford, S. A. 2008, *ApJ*, 686, 966
- Muzzin, A., Wilson, G., Yee, H. K. C., et al. 2012, *ApJ*, 746, 188 (M12)
- Muzzin, A., Wilson, G., Yee, H. K. C., et al. 2009, *ApJ*, 698, 1934
- Muzzin, A., Yee, H. K. C., Hall, P. B., Ellingson, E., & Lin, H. 2007, *ApJ*, 659, 1106
- Nagai, D. & Kravtsov, A. V. 2005, *ApJ*, 618, 557
- Nantais, J. B., Rettura, A., Lidman, C., et al. 2013, *A&A*, 556, A112
- Natarajan, P., Kneib, J.-P., & Smail, I. 2002, *ApJ*, 580, L11
- Navarro, J. F., Frenk, C. S., & White, S. D. M. 1997, *ApJ*, 490, 493
- Navarro, J. F., Ludlow, A., Springel, V., et al. 2010, *MNRAS*, 402, 21
- Neto, A. F., Gao, L., Bett, P., et al. 2007, *MNRAS*, 381, 1450
- Newman, A. B., Treu, T., Ellis, R. S., & Sand, D. J. 2013, *ApJ*, 765, 25
- Noble, A. G., Webb, T. M. A., Muzzin, A., et al. 2013, *ApJ*, 768, 118
- Noeske, K. G., Weiner, B. J., Faber, S. M., et al. 2007, *ApJ*, 660, L43
- Oesch, P. A., Stiavelli, M., Carollo, C. M., et al. 2007, *ApJ*, 671, 1212
- Oke, J. B. & Gunn, J. E. 1983, *ApJ*, 266, 713
- Oman, K. A., Hudson, M. J., & Behroozi, P. S. 2013, *MNRAS*, 431, 2307
- Ouchi, M., Shimasaku, K., Okamura, S., et al. 2004a, *ApJ*, 611, 660
- Ouchi, M., Shimasaku, K., Okamura, S., et al. 2004b, *ApJ*, 611, 685
- Papovich, C., Dickinson, M., & Ferguson, H. C. 2001, *ApJ*, 559, 620
- Patel, S. G., Holden, B. P., Kelson, D. D., et al. 2012, *ApJ*, 748, L27
- Patel, S. G., Holden, B. P., Kelson, D. D., Illingworth, G. D., & Franx, M. 2009, *ApJ*, 705, L67

- Peng, Y.-j., Lilly, S. J., Kovač, K., et al. 2010, *ApJ*, 721, 193
- Peng, Y.-j., Lilly, S. J., Renzini, A., & Carollo, M. 2012, *ApJ*, 757, 4
- Pérez-González, P. G., Rieke, G. H., Villar, V., et al. 2008, *ApJ*, 675, 234
- Perlmutter, S., Aldering, G., Goldhaber, G., et al. 1999, *ApJ*, 517, 565
- Pirzkal, N., Malhotra, S., Rhoads, J. R., & Chun, X. 2005, in *Bulletin of the American Astronomical Society*, Vol. 37, *Bulletin of the American Astronomical Society*, 1195–+
- Planelles, S., Borgani, S., Dolag, K., et al. 2013, *MNRAS*, 431, 1487
- Poggianti, B. M., Aragón-Salamanca, A., Zaritsky, D., et al. 2009, *ApJ*, 693, 112
- Poggianti, B. M., Bridges, T. J., Komiyama, Y., et al. 2004, *ApJ*, 601, 197
- Poggianti, B. M., Smail, I., Dressler, A., et al. 1999, *ApJ*, 518, 576
- Poli, F., Menci, N., Giallongo, E., et al. 2001, *ApJ*, 551, L45
- Press, W. H. & Schechter, P. 1974, *ApJ*, 187, 425
- Raichoor, A. & Andreon, S. 2012, *A&A*, 543, A19
- Rasmussen, J., Mulchaey, J. S., Bai, L., et al. 2012, *ApJ*, 757, 122
- Reddy, N. A. & Steidel, C. C. 2009, *ApJ*, 692, 778
- Reddy, N. A., Steidel, C. C., Pettini, M., et al. 2008, *ApJS*, 175, 48
- Refregier, A. 2003, *MNRAS*, 338, 35
- Riess, A. G., Filippenko, A. V., Challis, P., et al. 1998, *AJ*, 116, 1009
- Rines, K., Geller, M. J., Diaferio, A., & Kurtz, M. J. 2013, *ApJ*, 767, 15
- Rubin, V. C. & Ford, Jr., W. K. 1970, *ApJ*, 159, 379
- Rudnick, G., von der Linden, A., Pelló, R., et al. 2009, *ApJ*, 700, 1559
- Salpeter, E. E. 1955, *ApJ*, 121, 161
- Sand, D. J., Graham, M. L., Bildfell, C., et al. 2011, *ApJ*, 729, 142
- Sanders, D. B., Salvato, M., Aussel, H., et al. 2007, *ApJS*, 172, 86
- Saro, A., Mohr, J. J., Bazin, G., & Dolag, K. 2013, *ApJ*, 772, 47
- Sawicki, M. & Thompson, D. 2006, *ApJ*, 642, 653
- Schawinski, K., Thomas, D., Sarzi, M., et al. 2007, *MNRAS*, 382, 1415
- Schaye, J., Dalla Vecchia, C., Booth, C. M., et al. 2010, *MNRAS*, 402, 1536
- Schechter, P. 1976, *ApJ*, 203, 297
- Schiminovich, D., Ilbert, O., Arnouts, S., et al. 2005, *ApJ*, 619, L47
- Schlegel, D. J., Finkbeiner, D. P., & Davis, M. 1998, *ApJ*, 500, 525
- Scoville, N., Aussel, H., Benson, A., et al. 2007, *ApJS*, 172, 150
- Sereno, M. & Covone, G. 2013, *MNRAS*
- Shapley, A. E., Steidel, C. C., Pettini, M., & Adelberger, K. L. 2003, *ApJ*, 588, 65
- Sheldon, E. S., Johnston, D. E., Masjedi, M., et al. 2009, *ApJ*, 703, 2232
- Sifón, C., Menanteau, F., Hasselfield, M., et al. 2013, *ApJ*, 772, 25
- Smith, G. P., Khosroshahi, H. G., Dariush, A., et al. 2010a, *MNRAS*, 409, 169
- Smith, R. J., Lucey, J. R., Hammer, D., et al. 2010b, *MNRAS*, 408, 1417
- Sobral, D., Best, P. N., Smail, I., et al. 2011, *MNRAS*, 411, 675
- Somerville, R. S., Lee, K., Ferguson, H. C., et al. 2004, *ApJ*, 600, L171

- Springel, V., White, S. D. M., Jenkins, A., et al. 2005, *Nature*, 435, 629
- Steidel, C. C., Adelberger, K. L., Giavalisco, M., Dickinson, M., & Pettini, M. 1999, *ApJ*, 519, 1
- Steidel, C. C., Adelberger, K. L., Shapley, A. E., et al. 2003, *ApJ*, 592, 728
- Steidel, C. C., Giavalisco, M., Pettini, M., Dickinson, M., & Adelberger, K. L. 1996, *ApJ*, 462, L17+
- Steidel, C. C., Shapley, A. E., Pettini, M., et al. 2004, *ApJ*, 604, 534
- Tal, T., van Dokkum, P. G., Franx, M., et al. 2013, *ApJ*, 769, 31
- Taranu, D. S., Hudson, M. J., Balogh, M. L., et al. 2012, *ArXiv e-prints*
- Teerikorpi, P. 2004, *A&A*, 424, 73
- Thomas, D., Maraston, C., Schawinski, K., Sarzi, M., & Silk, J. 2010, *MNRAS*, 404, 1775
- Tinker, J., Kravtsov, A. V., Klypin, A., et al. 2008, *ApJ*, 688, 709
- Tran, K.-V. H., Franx, M., Illingworth, G. D., et al. 2007, *ApJ*, 661, 750
- Trenti, M. & Stiavelli, M. 2008, *ApJ*, 676, 767
- Treu, T., Ellis, R. S., Kneib, J.-P., et al. 2003, *ApJ*, 591, 53
- van Daalen, M. P., Schaye, J., Booth, C. M., & Dalla Vecchia, C. 2011, *MNRAS*, 415, 3649
- van den Bosch, F. C., Aquino, D., Yang, X., et al. 2008, *MNRAS*, 387, 79
- van der Burg, R. F. J., Hildebrandt, H., & Erben, T. 2010, *A&A*, 523, A74
- van der Burg, R. F. J., Muzzin, A., Hoekstra, H., et al. 2013, *A&A*, 557, A15 (vdB13)
- van der Burg, R. F. J., Muzzin, A., Hoekstra, H., et al. 2014, *A&A*, 561, A79 (vdB14)
- van Dokkum, P. G. 2001, *PASP*, 113, 1420
- van Dokkum, P. G., Franx, M., Fabricant, D., Kelson, D. D., & Illingworth, G. D. 1999, *ApJ*, 520, L95
- Vulcani, B., Poggianti, B. M., Aragón-Salamanca, A., et al. 2011, *MNRAS*, 412, 246
- Vulcani, B., Poggianti, B. M., Fasano, G., et al. 2012, *MNRAS*, 420, 1481
- Vulcani, B., Poggianti, B. M., Finn, R. A., et al. 2010, *ApJ*, 710, L1
- Vulcani, B., Poggianti, B. M., Oemler, A., et al. 2013, *A&A*, 550, A58
- Wechsler, R. H., Bullock, J. S., Primack, J. R., Kravtsov, A. V., & Dekel, A. 2002, *ApJ*, 568, 52
- Weinmann, S. M., Kauffmann, G., von der Linden, A., & De Lucia, G. 2010, *MNRAS*, 406, 2249
- Weinmann, S. M., Pasquali, A., Oppenheimer, B. D., et al. 2012, *ArXiv e-prints*
- Wetzell, A. R., Tinker, J. L., & Conroy, C. 2012, *MNRAS*, 424, 232
- Wetzell, A. R., Tinker, J. L., Conroy, C., & van den Bosch, F. C. 2013, *MNRAS*, 432, 336
- Whitaker, K. E., Labbé, I., van Dokkum, P. G., et al. 2011, *ApJ*, 735, 86
- White, S. D. M. & Rees, M. J. 1978, *MNRAS*, 183, 341

- Williams, R. J., Quadri, R. F., Franx, M., van Dokkum, P., & Labbé, I. 2009, *ApJ*, 691, 1879
- Wilson, G., Muzzin, A., Yee, H. K. C., et al. 2009, *ApJ*, 698, 1943
- Woo, J., Dekel, A., Faber, S. M., et al. 2013, *MNRAS*, 428, 3306
- Worthey, G. 1994, *ApJS*, 95, 107
- Wu, P.-F., Gal, R. R., Lemaux, B. C., et al. 2013, *ArXiv e-prints*
- Wuyts, S., Labbé, I., Franx, M., et al. 2007, *ApJ*, 655, 51
- Yan, R., Newman, J. A., Faber, S. M., et al. 2009, *MNRAS*, 398, 735
- Yee, H. K. C., Ellingson, E., & Carlberg, R. G. 1996, *ApJS*, 102, 269
- Yoshida, M., Shimasaku, K., Kashikawa, N., et al. 2006, *ApJ*, 653, 988
- Zibetti, S., White, S. D. M., Schneider, D. P., & Brinkmann, J. 2005, *MNRAS*, 358, 949
- Zwicky, F. 1933, *Helvetica Physica Acta*, 6, 110

Nederlandse Samenvatting

"Als je iets niet op een eenvoudige manier kunt uitleggen dan begrijp je het niet goed genoeg."

-Albert Einstein

Onze plaats in het heelal

Ons perspectief op de plaats van de mensheid in het universum heeft zich de afgelopen eeuwen sterk ontwikkeld. Tot minder dan 25 menselijke generaties geleden was het geocentrische model, waarin de Aarde het centrum van het universum inneemt, nog de algemeen aangenomen beschrijving van het heelal. Sindsdien hebben nieuwe inzichten tot een geheel ander beeld geleid. Zo werd in de 16de eeuw het heliocentrische model, waarin de planeten zich rond een stationaire Zon bewegen, geformuleerd door o.a. Nicolaas Copernicus en Galileo Galilei. Dit model voorziet in een eenvoudigere en elegantere beschrijving van de planeetbanen in het zonnestelsel. Ook weten we nu dat de andere sterren aan de hemel eigenschappen hebben die vergelijkbaar zijn met de kenmerken van onze Zon, alhoewel ze op aanzienlijk grotere afstanden staan.

Om de enorme afstanden in het heelal te beschrijven is het gebruikelijk deze uit te drukken met behulp van de lichtsnelheid. Als een lichtstraal in de lege ruimte van het heelal reist, legt deze per seconde een indrukwekkende afstand af van ongeveer 300.000 km. De afstand naar de Maan is zo'n 380.000 km, oftewel ruim één lichtseconde. De Zon staat op zo'n acht lichtminuten, wat betekent dat we de Zon eigenlijk zien zoals hij acht minuten geleden straalde. De afstand tot de eerstvolgende ster is meer dan vier lichtjaar, een treffende illustratie van de uitgestrektheid van het heelal. Deze eindigheid van de lichtsnelheid zorgt er ook voor dat we binnen de sterrenkunde effectief terugkijken in de tijd als we het verre heelal bestuderen.

De Melkweg bestaat uit zo'n 100 miljard sterren, verdeeld over een dunne

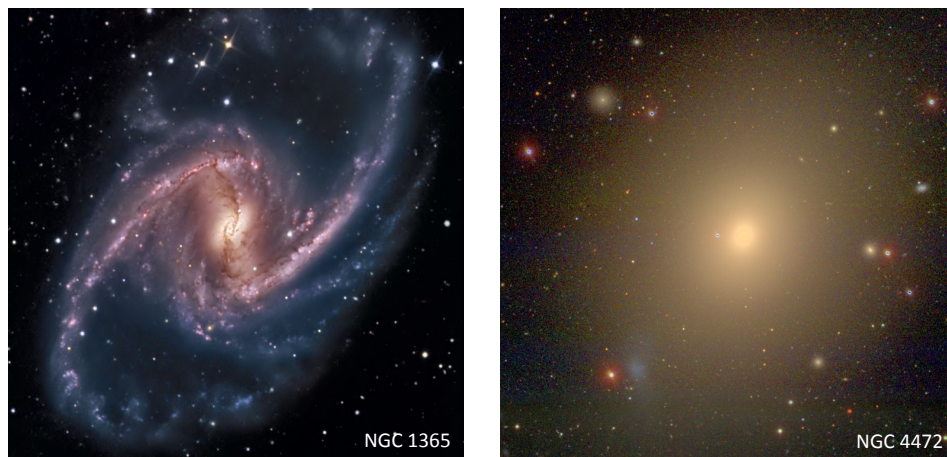
schijf met een diameter van ongeveer 100.000 lichtjaar. De Zon bevindt zich in één van de spiraalarmen binnen deze schijf. In de twintiger jaren van de vorige eeuw werd duidelijk dat de Melkweg niet uniek is, maar dat er vele sterrenstelsels bestaan op nog grotere afstanden. De Andromedanevel is het meest nabije sterrenstelsel dat van vergelijkbare grootte is als de Melkweg, en staat op een afstand van zo'n 2,5 miljoen lichtjaar. Met deze ontdekking vond men ook dat nagenoeg alle sterrenstelsels van ons af bewegen, en wel met een snelheid die lineair toeneemt met hun afstand. De implicatie van deze waargenomen uitdijing van het heelal is dat de bestanddelen van het heelal in het verleden dichter op elkaar gepakt moeten hebben gezeten, en dit heeft geleid tot de oerknaltheorie.

De oerknaltheorie is in de loop van de jaren verfijnd door verschillende waarnemingen te combineren. Volgens deze theorie is het heelal zo'n 13,8 miljard jaar geleden uit een singulariteit ontstaan, en is sindsdien afgekoeld en in omvang toegenomen tot het huidige heelal. Hierbij zijn alle structuren gevormd die het heelal rijk is; van de grootste verzameling sterrenstelsels tot planeten zoals de Aarde. Alhoewel dit model in eerste instantie misschien bizar zal klinken, kunnen veel waargenomen verschijnselen in het heelal hierdoor verklaard worden. Zo heeft de meting van de gloed van de oerknal, in de vorm van kosmische achtergrondstraling, in 2006 de Nobelprijs voor de Natuurkunde opgeleverd, en dit wordt gezien als het belangrijkste argument voor de oerknaltheorie. Sinds de oerknal heeft de zwaartekracht ervoor gezorgd dat het contrast tussen hoge en lage dichtheidsgebieden in de loop van de tijd steeds groter is geworden, en ook dit is waargenomen in de verdeling van materie in het heelal.

Halverwege de 20ste eeuw werd nog een andere grote ontdekking gedaan. De beweging van sterren in sterrenstelsels en de beweging van sterrenstelsels in clusters van sterrenstelsels, kunnen alleen begrepen worden als er buiten de materie die we kunnen zien, een aanzienlijke hoeveelheid materie aanwezig is die niet direct waarneembaar is. Aangezien deze donkere materie geen licht uitstraalt, is het bestaan ervan uitsluitend af te leiden aan de hand van de zwaartekracht. Door verschillende metingen te combineren wordt geschat dat 80% van de massa in het heelal de eigenschappen van donkere materie heeft.

Structuurformatie met behulp van donkere materie

Volgens het standaardmodel binnen de kosmologie (de oerknaltheorie) speelt donkere materie een belangrijke rol bij het vormen van structuren in het heelal dankzij de bijzondere eigenschap dat donkeremateriedeeltjes niet kunnen botsen. Deze eigenschap zorgt er ook voor dat de vorming van structuren met donkere materie relatief makkelijk te simuleren is met de computer. Op de omslag van dit proefschrift zijn twee gesimuleerde verdelingen van donkere



Figuur 7.1: *Links:* Voorbeeld van een spiraalvormig stelsel in het nabije heelal, waarin actief sterren worden gevormd. Ook de Melkweg behoort tot dit type. *Rechts:* Voorbeeld van een passief stelsel in het nabije heelal, waarin praktisch geen nieuwe sterren ontstaan.

materie op de achtergrond te zien. De voorzijde toont de gesimuleerde verdeling binnen een groot volume in het huidige heelal, terwijl de achterzijde de verdeling in hetzelfde volume toont, maar dan op het moment dat het gesimuleerde heelal minder dan vijf miljard jaar oud is. Als we deze beide zijden met elkaar vergelijken blijkt inderdaad dat het contrast tussen hoge en lage dichtheidsgebieden toeneemt met de tijd. De donkeremateriewolken (ook halo's genoemd) die ontstaan binnen deze simulatie zijn verdeeld langs filamenten, en deze verdeling heeft iets weg van een spinnenweb. Alhoewel de verdeling van donkere materie niet direct waar te nemen is in het heelal, blijkt de verdeling van sterrenstelsels op grote schaal goed overeen te komen met de gesimuleerde verdeling van donkere materie. Volgens de theorie bevinden de sterrenstelsels in ons heelal zich dus in halo's van donkere materie. Ook dit vermoeden wordt bevestigd door indirecte metingen.

Op relatief kleinere schaal, de schaal van de sterrenstelsels zelf, zijn de eigenschappen van baryonische materie (zoals de deeltjes waar wij van gemaakt zijn) van grote invloed op het vormen van sterren, planeten en uiteindelijk ook de levensvormen op Aarde. Door kernreacties in de centra van sterren worden voortdurend nieuwe elementen gevormd, en door stellaire winden en supernova-ontploffingen worden deze deeltjes het heelal in geblazen. Door dergelijke processen wordt het vormen van nieuwe sterren beïnvloed, alsmede door de energetische straling die wordt uitgezonden wanneer zwarte gaten in de centra van sterrenstelsels groeien door de aanwas van nieuwe materie. Het samenspel tussen deze processen en de natuurkundige principes die hierbij een rol spelen zijn zodanig complex dat er nog veel open vragen zijn betreffende de formatie en evolutie van sterrenstelsels.

Gegeven ons uitgestrekte heelal en de enorme hoeveelheid sterrenstelsels (naar schatting rond de 100 miljard, met elk ook ruwweg 100 miljard sterren), is het opmerkelijk dat sterrenstelsels grofweg in twee soorten te classificeren zijn, zie Fig. 7.1. Spiraalvormige stelsels zijn actief in het vormen van sterren; zo vormt de Melkweg tegenwoordig enkele nieuwe sterren per jaar. De aanwezigheid van deze jonge sterren geeft spiraalvormige stelsels een blauwe kleur. Het tweede type bestaat uit sterrenstelsels met een vaak elliptische vorm, waarin niet of nauwelijks nieuwe sterren worden gevormd. Door het gebrek aan jonge sterren hebben deze passieve stelsels een rode kleur. Verschillende factoren bepalen van welk type een gegeven sterrenstelsel is. Vooral de massa van een stelsel en de hoeveelheid naburige sterrenstelsels spelen hierbij een belangrijke rol, maar ook de leeftijd van het heelal op het moment dat we een sterrenstelsel waarnemen is van invloed. In het algemeen geldt dat sterrenstelsels een grotere kans hebben om passief te zijn naarmate hun massa hoger is, ze meer naburige sterrenstelsels hebben en het heelal ouder is (dus wanneer we in het nabijgelegen heelal kijken). Dergelijke metingen zijn belangrijk voor het verfijnen van ons begrip van de natuurkundige processen die ten grondslag liggen aan het transformeren van blauwe actieve sterrenstelsels naar rode passieve sterrenstelsels.

Dit proefschrift

Om te begrijpen hoe sterrenstelsels gevormd worden in dit door donkere materie gedomineerde heelal, en omdat de transformatie van sterrenstelsels van verschillende factoren afhankelijk is, is het van belang om de invloed van massa, omgeving en de leeftijd van het heelal los van elkaar te beschouwen. Zo is het bijvoorbeeld nog onduidelijk welke processen precies zorgen voor het doven (d.w.z. rood worden) van blauwe sterrenstelsels in gebieden met een hoge dichtheid (d.w.z. sterrenstelsels met veel burens). Een gerelateerde vraag is wat precies het verband is tussen de verdeling van stellaire materie en de verdeling van donkere materie. In dit proefschrift richten we ons op dergelijke vragen en gebruiken we precieze waarnemingen van de meeste massieve structuren die gevormd zijn in het heelal, namelijk clusters van sterrenstelsels, om onze huidige theorieën te kunnen toetsen en verder te verfijnen. Specifiek staat de vraag centraal wat de invloed van zulke extreme omgevingen is op de evolutie van sterrenstelsels.

In **Hoofdstuk 1** geven we meer achtergrondinformatie en introduceren we begrippen waar in de rest van het proefschrift op voortgebouwd wordt. Centraal in dit proefschrift staat het karakteriseren van sterrenstelsels aan de hand van hun stellaire massa. Deze kunnen we schatten door te kijken hoeveel licht een sterrenstelsel uitstraalt in verschillende kleuren. Alhoewel de stellaire massa maar een klein deel is van de totale massa (welke wordt gedomineerd

door donkere materie en gas tussen de sterren), geeft dit veel informatie over natuurkundige processen die een rol spelen bij het vormen van sterren.

In de **Hoofdstukken 2-4** bestuderen we de verdeling van stellaire materie in tien clusters in het jonge heelal, toen het heelal ongeveer de helft van zijn huidige leeftijd had. Het gebruik van gevoelige waarnemingen van telescopen op Chili, Hawaï en ook de Spitzer ruimtetelescoop, geeft ons een gedetailleerde kijk op deze jonge systemen die tot dusver ongeëvenaard is in de literatuur. De achterzijde van dit proefschrift toont een foto van één van deze clusters, geconstrueerd door meerdere waarnemingen te combineren.

In **Hoofdstuk 2** bestuderen we specifiek de verdeling van sterrenstelsels in deze clusters als functie van hun stellaire massa en vergelijken dit met sterrenstelsels erbuiten. We vinden dat deze massaverdelingen significant van elkaar verschillen. Echter, wanneer we de twee typen sterrenstelsels los van elkaar beschouwen, zien we dat elk type wordt beschreven door een verdeling die onafhankelijk is van de omgeving. Het verschil in de totale massaverdeling wordt derhalve veroorzaakt doordat de clusters ook in het jonge heelal al een relatief hoog aantal passieve sterrenstelsels bevatten. We vergelijken deze metingen met een model dat het doven van sterrenstelsels beschrijft en vinden hiermee een goede beschrijving van de data.

Het model dat het doven van sterrenstelsels beschrijft, voorspelt in onze clusters de aanwezigheid van een populatie sterrenstelsels die recentelijk en abrupt uitgedoofd zijn. Deze recent uitgedoofde sterrenstelsels hebben specifieke kenmerken, en in **Hoofdstuk 3** identificeren we deze stelsels in onze tien clusters in het jonge heelal. We vinden dat sterrenstelsels van dit type kenmerkende relatieve snelheden en posities hebben ten opzichte van de clustercentra. Dit heeft mogelijk te maken met een plotselinge verwijdering van heet gas uit deze sterrenstelsels, dat daardoor niet meer beschikbaar is voor het vormen van sterren. Door deze studie kunnen we zo meer leren over het proces dat ten grondslag ligt aan het doven van sterrenstelsels in hoge dichtheidsgebieden.

In **Hoofdstuk 4** verschuift onze focus van de individuele sterrenstelsels binnen de clusters naar de eigenschappen van de clusters zelf. Op de schaal van clusters verwachten we dat ongeveer 80% van de massa de eigenschappen heeft van donkere materie, en dat de baryonische fractie (bestaande uit gas en sterren) dus nagenoeg gelijk is aan de gemiddelde waarde in het heelal. Door de totale hoeveelheid donkere materie, die we middels indirecte methodes kunnen bepalen, en de stellaire materie te vergelijken, kunnen we zo iets leren over de efficiëntie waarmee sterren zich vormen in clusters van sterrenstelsels. Ook kijken we naar de ruimtelijke verdeling van stellaire materie in deze clusters en vinden dat de profielen die deze verdeling beschrijven meer gepiekt zijn dan de verdeling van donkere materie voor dergelijke clusters in de simulaties.

In **Hoofdstuk 5** bouwen we hierop voort, en beschrijven een meting van de ruimtelijke verdeling van stellaire materie binnen tien clusters van sterrenstelsels in het nabije heelal, op basis van waarnemingen gedaan in Hawaï en

op La Palma. De voorzijde van dit proefschrift laat een kleurenfoto van één van deze clusters zien. Omdat deze tien clusters in het nabije heelal staan, hebben ze bijna de gehele leeftijd van het heelal gehad om zich tot deze staat te ontwikkelen. Door deze clusters te vergelijken met de clusters uit het jonge heelal (d.w.z. degene die we bestudeerd hebben de in de hoofdstukken 2-4), kunnen we bestuderen hoe de ruimtelijke verdeling van stellaire materie evolueert in de loop van de tijd. Vergeleken met de evoluerende verdeling van donkere materie in simulaties, nemen we een significant andere evolutie waar in de verdeling van stellaire materie. We beschouwen verschillende scenario's om deze verschillen te kunnen verklaren. Zo is het mogelijk dat de voorspellingen van simulaties herzien moeten worden door het toevoegen van baryonische processen, of dat we een deel van de sterren niet kunnen waarnemen doordat ze te diffuus verdeeld zijn tussen de sterrenstelsels in.

In **Hoofdstuk 6** bestuderen we het heelal zoals het er minder dan twee miljard jaar na de oerknal uit zag, een periode waarin sterrenstelsels zeer actief waren in het vormen van sterren. Door specifiek te focussen op het uitgestraalde ultraviolette licht door deze sterrenstelsels, kunnen we een inventarisatie maken van de hoeveelheid sterren die gevormd wordt per sterrenstelsel. Vergeleken met voorgaande metingen in de literatuur, maken we gebruik van waarnemingen van een groter stuk aan de hemel, wat een statistisch betere representatie geeft van het totale heelal. Met behulp van deze meting kunnen we dergelijke verafgelegen sterrenstelsels zelfs gebruiken om iets te leren over de donkerematerieverdeling in het tussenliggende heelal. Wat hieraan ten grondslag ligt is het vermogen van massa om lichtstralen af te buigen, wat leidt tot een waargenomen helderheidsverdeling die anders is dan de intrinsieke verdeling.

Door de waarnemingen die beschreven staan in de hoofdstukken van dit proefschrift met modellen en steeds geavanceerdere simulaties te vergelijken, leren we meer over de natuurkundige processen die een rol spelen bij het ontstaan van structuur in het heelal en de evolutie van sterrenstelsels.

Curriculum Vitae

Op 30 april 1986 ben ik geboren in Leiderdorp, waarna ik in het dorpje Benthuizen opgroeide. In September 2004 begon ik mijn studie sterrenkunde aan de Universiteit Leiden, waar ik vijf jaar later *cum laude* afstudeerde. Gedurende deze jaren heb ik kennis gemaakt met verschillende onderzoeksrichtingen binnen de sterrenkunde. Zo heb ik tijdens mijn Bacheloronderzoek in de onderzoeksgroep van Dr. Ignas Snellen een zoektocht naar exoplaneten ondernomen, en met succes afgesloten. Een jaar later volgde een nieuwe uitdaging in de groep van Dr. Michiel Hogerheijde, waarbij ik het gedrag en de samenwerking tussen gas en stof in de schijven rond jonge sterren onderzocht. In het kader van dit onderzoek ondernam ik een waarneemreis naar Hawaï. Tijdens mijn laatste en meeste uitgebreide onderzoek maakte ik kennis met de extragalactische sterrenkunde, onder leiding van Dr. Hendrik Hildebrandt en Prof.dr. Koendaad Kuijken. De ontelbare sterrenstelsels in de uitgestrektheid van het heelal prikkelden mijn nieuwsgierigheid.

In 2009 kreeg ik in de onderzoeksgroep van Dr. Henk Hoekstra de mogelijkheid om me middels een promotiepositie verder te ontwikkelen op het gebied van de extragalactische sterrenkunde. Mijn wetenschappelijke resultaten van de daaropvolgende jaren staan in dit proefschrift beschreven. Ook heb ik de kans gekregen deze te presenteren gedurende internationale conferenties in Schotland, Duitsland, Italië en Spanje. Verder heb ik enkele malen een bezoek gebracht aan de Verenigde Staten om intensief samen te werken met collega's daar. Gedurende 36 nachten, verdeeld over de jaren 2010 en 2011, heb ik astronomische waarnemingen verricht op de Isaac Newton Telescoop in La Palma. De komende jaren zal ik mijn carrière voortzetten in CEA Saclay, Frankrijk, in de onderzoeksgroep van Dr. Monique Arnaud.

Naast het leveren van deze bijdrage aan de wetenschap heb ik me ook op andere gebieden verder kunnen ontwikkelen. Zo heb ik me jaren lang als roeier en coach ingezet bij Asopos de Vliet, en heb ik hardgelopen bij LUHV Currimus. Ook brachten mijn gitaar en piano de nodige afleiding en inspiratie.

Nawoord

Nu het schrijven van dit proefschrift achter de rug is, kijk ik terug op een interessante tijd en leerzame jaren. Het onderzoek wat hier beschreven staat had ik nooit kunnen uitvoeren zonder de onvergetelijke steun van mijn collega's, vrienden en familie. Graag bedank ik mijn naasten hieronder voor hun bijdragen aan mijn persoonlijke ontwikkeling.

Allereerst mijn collega's van de Sterrewacht Leiden, en in het bijzonder de onderzoeksgroep waar ik deel van heb mogen uitmaken. Hendrik, it has been a great pleasure to work with you. I learned a lot, especially from your working efficiency, and this has been a strong motivation for me to join the PhD program. Berenice, I very much appreciated working together with you for several months :-). Edo, Malin, Elisabetta, Stefania, Tim, Merijn, Cristóbal, Fabian, Jeroen, Ricardo, Massimo, Marcello, Jelte, Margot, Martin; thanks for the fun, and your contributions to a great working environment.

Also I would like to thank all my former office-mates, in particular Adam and Jayne. Adam, it was great fun to work with you, and I highly value all science discussions we had during the last few years. Also I will long remember our blackjack games in Las Vegas, our hikes along some steep cliffs, and your ever-continuing complaints about the Dutch weather and food. Jayne, it has been great to get to know you on a more personal level, outside the office. I consider myself lucky that I met such a special person with such a warm personality! Further I would like to thank all other colleagues, especially Jesse, Daniël, Rob, Shannon, Renske, Allison and Mattia. Without you the coffee and lunch breaks would never have been the same! Tenslotte gaat mijn dank uit naar David, Erik, Evelijn, Liesbeth, Anita en Aart voor hun praktische ondersteuning op de Sterrewacht.

In de loop van mijn PhD heb ik ook internationaal een onderzoeksnetwerk kunnen opbouwen. I would like to thank my international colleagues of the KiDS team, and also the SPARCS/GCLASS collaboration: in particular Gil-

lian, Chris, Howard, Tracy, Allison, Michael, Dennis, and Julie. And directly related to the thesis itself; Suzanne, many thanks for your help in designing such a wonderful thesis cover!

Buiten de Sterrewacht gaan mijn gedachten uit naar de mannen van WicKY voor de epische gevechten die we samen per roeiboort op menig woest water hebben uitgevchten. De bananen 8+, wat in theorie een onoverwinnelijk gezelschap was. Een gezelschap was het zeker :-). Alle roeiploegjes die de afgelopen jaren naar mijn wijze raad wilden luisteren. In het bijzonder de mannen van Tovergieter en de Club8+ genaamd YOLO. Ook mijn mede-coaches en alle andere leden voor de tweewekelijkse borrels in het clubgebouw. Mijn maatjes van Currimus voor een aantal mooie hardloop-estafettes, met als hoogtepunt onze deelname aan de RoPaRun in 2013: Het was een fantastische ervaring, waarbij zeker de heldendaden van team blauw niet vergeten mogen worden! Karli, Timo, Niels, Mark, Thijs en Julius; onze hike-tochten in Schotland, Zweden, de Pyreneeën, IJsland en Bulgarije waren te episch voor woorden. Het blijft bijzonder hoe snel je een hechte band opbouwt bij het samen doorstaan van ontberingen! En ook mijn fiets-buddy's en onze aanstaande derde reis naar de alpen voor een weekje bergen beklimmen en bbq'en.

Ook mag ik mezelf gelukkig prijzen met een fantastische familie. Mijn lieve oma, ondanks haar mooie leeftijd nog altijd haarscherp van geest, daar heb ik veel bewondering voor. Maar bovenal de steun en onvoorwaardelijke liefde van mijn ouders hebben ervoor gezorgd dat ik kon opgroeien tot wie ik nu ben. Mijn dankbaarheid gaat naar hen uit, en ook naar mijn liefvallige zusje die me als paranimf terzijde zal staan.

Remco F.J. van der Burg
Maart 2014.

The time will come
when, with elation
you will greet yourself arriving
at your own door, in your own mirror
and each will smile at the other's welcome,
and say, sit here. Eat.
You will love again the stranger who was your self.
Give wine. Give bread. Give back your heart
to itself, to the stranger who has loved you
all your life, whom you ignored
for another, who knows you by heart.
Take down the love letters from the bookshelf,
the photographs, the desperate notes,
peel your own image from the mirror.
Sit. Feast on your life.

Derek Walcott

